

GEOLOGICA ULTRAIECTINA

MEDEDELINGEN VAN DE
FACULTEIT AARDWETENSCHAPPEN
UNIVERSITEIT UTRECHT

No. 225

**Geochemistry and environmental mineralogy of the
iron–sulphur–arsenic system**

Mariëtte Wolthers

**Geochemistry and environmental mineralogy of the
iron–sulphur–arsenic system**

**Geochemie en milieumineralogie van het
ijzer–zwavel–arseen systeem**

(met een samenvatting in het Nederlands)

PROEFSCHRIFT

ter verkrijging van de graad van doctor aan de Universiteit Utrecht
op gezag van de Rector Magnificus, Prof. Dr. W.H. Gispen, ingevolge
het besluit van het College voor Promoties in het openbaar te verdedigen
op maandag 31 maart 2003 des middags te 2:30 uur

door

Mariëtte Wolthers

geboren op 9 juni 1974, te Opmeer

Promotoren: Prof. Dr. C.H. Van der Weijden
Department of Geochemistry
Faculty of Earth Sciences
Utrecht University

Prof. Dr. D. Rickard
Department of Earth Sciences
Cardiff University

Co-promotor: Dr. P.R. Van der Linde
University of Professional Education Leiden

This research was conducted at the Department of Geochemistry, Faculty of Earth Sciences, Utrecht University, the Netherlands and at the Department of Earth Sciences, Cardiff University, Wales, United Kingdom. This study was supported by the Netherlands Organization of Scientific Research (NWO/ALW grant 750.197.06).

Printing: Grafisch bedrijf Ponsen & Looijen, Wageningen

Cover art: Carola Maas

ISBN 90-5744-083-0

I was just guessing at numbers and figures
Pulling your puzzles apart
Questions of science, science and progress
Do not speak as loud as my heart
Tell me you love me, come back and haunt me
Oh and I rush to the start
Running in circles, chasing our tails
Coming back as we are

Nobody said it was easy
Oh it's such a shame for us to part
Nobody said it was easy
No one ever said it would be so hard
I'm going back to the start

Coldplay

Voor Rutger

Contents

	Voorwoord	9
	Samenvatting	13
	Introduction	17
Chapter 1	The iron–sulphur–arsenic system	19
Chapter 2	A surface and structural model describing the environmental reactivity of disordered mackinawite	37
Chapter 3	Surface chemistry of disordered mackinawite	61
Chapter 4	Arsenic mobility in the ambient sulphidic environment: sorption of arsenic(V) and arsenic(III) onto disordered mackinawite	85
Chapter 5	Arsenic in iron sulphides: sorption and incorporation	109
Chapter 6	Arsenic incorporation into pyrite at ambient environmental conditions: a continuous-flow experiment	145
Chapter 7	Synthesis	163
	References	167
	Curriculum Vitae	185

Voorwoord

Vol enthousiasme en goede moed begon ik in september 1997 aan het promotie-onderzoek dat heeft geleid tot dit proefschrift. Toch liep het, vooral de eerste twee jaar, anders dan gehoopt. Zonder alle hulp en steun die ik heb mogen krijgen had ik dit onderzoek nooit tot een goed einde kunnen volbrengen. Om dat te benadrukken begin ik het proefschrift dan ook met dit dankwoord.

Er zijn veel mensen die het verdienen om hier als eerste genoemd te worden. Bijvoorbeeld Kees van der Weijden, voor het geven van de letterlijke en figuurlijke ruimte en tijd die ik nodig had om het, onder zijn begeleiding, op mijn manier te kunnen doen. Of Peter van der Linde, voor de onmisbare persoonlijke begeleiding, vooral in de eerste twee jaar, naast het "puntjes op scheikundige i's" zetten. Dave Rickard equally well deserves to be first-mentioned in this thesis for inspiring me and making sure I was scientifically happy. I had a great time, working within his research group, and I could never have finished writing up the way I did without his and Kees' sacrifices around Christmas time. Furthermore, at the final stage of my PhD, the members of the dissertation committee played a crucial role: Dr. Ian Butler, Prof. Dr. Bernard de Jong, Prof. Dr. George Luther, Prof. Dr. Martin Schoonen and Prof. Dr. Philippe Van Cappellen.

Several scientists helped to improve this thesis with their advise and co-operation: Thilo Behrends, Liane Benning, Jacqueline Claessens, Hans Huisman, Sieger van der Laan, George Luther, Paul Mason, Gernot Nehrke, Denis Rancourt, Hilde Passier, Philippe Van Cappellen, Kees Woensdrecht and Enno Zinngrebe. Laurent Charlet guided me through the surface chemistry research, like a third promotor. Ook de kristallografische kennis van, maar vooral de prettige samenwerking met, Sjerry van der Gaast was onmisbaar bij de aanleg van de basis van dit proefschrift. Last, but definitely not least, playing in and around the Cardiff labs hadn't been fun, instructive and constructive without my office/lab/teammates Ian "RTFB" Butler, Steve "celery lover" Grimes, Tony "shut up" Oldroyd and Clare "did you have curry last night?" Cottnam.

Gedurende de vele experimenten, analyses en andere praktische zaken, die lang niet allemaal in dit proefschrift zijn beland, kon ik rekenen op Mark van Alphen, Paul Anten, Jaco Bergenhenegouwen, Tilly Bouten, Hans de Bresser, Jan Drenth, Igno Dur, Boudewijn 't Hart, Wil den Hartog, Marijke de Kleijn, Pieter "sorcier" Kleingeld, Peter van Krieken, Dorinda van der Linden, Hans Meeldijk, Dineke van de Meent, Ronald van Miltenburg, Pien van Minnen, Wim Nieuwenhuis, Paul van Oudenallen, Herman van Roermund, Sander Roosendaal, Izaack Santoe, Tony Senior, Otto Stiekema, Marnella van der Tol, Fred Trappenburg, Arjen Vredenberg, Helen de Waard en Ton Zalm; Jan Jansen, Marcel Stelling en overige bibliotheekmedewerk(st)ers (UU); Wim Boer (KNIOZ); Lawrence Badham, Peter Fisher, Sarah Goldschmidt en Colin Lewis (CU).

De sociale kant van onderzoek doen is minstens zo belangrijk als de inhoudelijke. Heel wat lief, leed, koffie, thee en lekkers heb ik kunnen delen met mijn kamergenoten: Arthur Schmidt, Thomas Keijzer, Niels Hartog, Anja Reitz en Laurent Voitel. Nog meer koffie of thee drinken, lunchen, borrelen, wachten op printjes of kopietjes, praten over (wetenschappelijke) koetjes of kalfjes, congressen afreizen — zonder mijn (oud)collega's zou dit alles een stuk minder leuk zijn geweest. Tja, dat wordt een lange lijst, maar laat ik het eens proberen: David Aguilera, Ron Baarends, Thilo Behrends, Gerard van den Berg, Pim van Bergen, Steeve Bonneville, Erica Broeder, Rick Canavan, Jacqueline Claessens, Emelina Corrales, Anke Dählmann, Mark Dekkers, Arnold van Dijk, Charon Duermeijer, Jasper Griffioen, Ralf Haese, Hans Hage, Boudewijn 't Hart, Andreas Hübner, Christelle Hyacinthe, Jan Jansen, Parisa Jourabchi, Gerard Klaver, Marijke de Kleijn, Rinske Knoop, Johan Kool, Gert de Lange, Annet Laverman, Anke Leenders, Dorinda van der Linden, Yvonne van Lith, Guus Loch, Debby Los, Lucas Lourens, Christof Meile, Diana Menzel, Jack Middelburg, Pien van Minnen, Gerben Mol, Dennis Naafs, Gernot Nehrke, Ivar Nijenhuis, Gijs Nobbe, Ingeborg van Oorschot, Bertil van Os, Céline Pallud, Hilde Passier, Peter Pruyzers, Imogen Poole, Pierre Regnier, Gert-Jan Reichart, Katja Richter, Michiel de Roo, Arrian Rutten, Sjoerd Schenau, Olaf Schuiling, Caroline Slomp, Claudette Spiteri, Kagan Tuncay, Simon Vriend, de al eerder genoemde en misschien toch ook nog ongenoemde collega's.

Of course, life in Cardiff wouldn't have been the same without the good company of, and especially the endless dinners with, my housemates Simon

Beavington-Penney and Kate Habgood. Getting started in and around Cardiff University would have been much harder without Liesbeth Diaz, Vera Walters and Amin Barzanji. The lunch, pub and other sociable talk kept going thanks to my Cardiff colleagues, in particular: Andrew Barnett, Laurence Coogan, Sarah Goldschmidt, Duncan Irving, Fiona Knight, Paul and Anisa Knutz, Kirsty Meldrum, Jenny Pike, Brice Rea, Richard Thomas, Simon Wakefield and, of course, my housemates and my partners in sulphide crime.

De volgorde die ik in dit voorwoord heb aangehouden, is zo'n beetje standaard voor het dankwoord bij een proefschrift. Maar zoals ik al schreef, velen verdienen het om hier als eerste genoemd te worden. Niet in de laatste plaats mijn familie: mijn moeder, vader en broer(tje) — en mijn schoonfamilie: Ruud, Thea, Renske en Arlette — voor hun onverdeeld begrip en vertrouwen, "het mij mijn gang laten gaan". Of mijn vrienden. Biertje, filmpje, concert of achtbaan meepikken, uitwaaien of squashen, klussen of kletsen, noem maar op, zonder hen had ik niet steeds weer mijn batterij kunnen opladen: Carola, Arnoud, Karin, Eelco, Stella, Olaf, Marcia, Friso, Hero, Martijn, Helma, Peter en Sandra, maar ook diegenen die hun naam hier niet zien staan. Maar wie het nog het allermeest verdient om als eerste genoemd te worden is Rutger. Voor alles wat hij voor mij gedaan heeft en van mij geaccepteerd heeft, zou ik een proefschriftlang dankwoord moeten schrijven. Vandaar dat ik dit proefschrift aan hem opdraag.

Samenvatting

Wat is het belang van een studie naar de geochemie en milieumineralogie van het ijzer–zwavel–arseen systeem? "Arseen" en "gif" zijn voor veel mensen bijna synoniem. Voor ontevreden echtgenoten en de politiek ambitieuzen is het al duizenden jaren beschikbaar geweest als een goedkoop en effectief middel tegen de netelige situaties die kunnen ontstaan bij intermenselijke relaties (vrijvertaald naar een citaat van Penrose, 1974). Tegenwoordig wordt arseen wereldwijd beschouwd als een van de meest problematische anorganische vervuilingen van grondwater voor drinkwater productie. Bangladesh is een alarmerend voorbeeld van deze problemen met arseen in het grondwater. In een groot aantal van de miljoenen recentelijk aangelegde drinkwater putten, bevat het water arseen in hoge concentraties (Smedley en Kinniburgh, 2002). Deze putten onttrekken water van zuurstofloze waterhoudende lagen. De processen achter de effectief hoge mobiliteit van arseen in deze en andere zuurstofarme en zuurstofloze milieus zijn slecht bekend (Smedley en Kinniburgh, 2002; Harvey e.a., 2002). Kennis van deze processen is essentieel voor het begrijpen en voorspellen van het gedrag van arseen in deze milieus. Doordat, onder uiteenlopende omstandigheden in het poriewater van sediment, de oplosbaarheid van arseenoxiden en arseensulfiden relatief groot is, zal de mobiliteit van arseen het sterkst beïnvloed worden door sorptie aan andere, minder oplosbare, oxiden en sulfiden. IJzeroxiden en ijzersulfiden zijn minder oplosbaar en daardoor veel voorkomende vaste fasen in sedimentaire milieus. In tegenstelling tot de intensief bestudeerde sorptie van arseen aan ijzeroxiden, is de sorptie van arseen aan ijzersulfiden nog niet uitgebreid bestudeerd.

In dit proefschrift wordt een bijdrage geleverd aan het begrip van het gedrag van arseen in zuurstofarme en zuurstofloze milieus. Dit wordt gedaan door middel van het bestuderen van de sorptie van arseen aan zwak kristallijne mackinawiet, of FeS_{am} , en de associatie van arseen met ijzersulfiden gedurende de vorming van pyriet. Als basis voor deze studie werden de eigenschappen van zowel de bulk als het oppervlak van synthetische FeS_{am} bepaald.

Synthetische FeS_{am} bestaat uit nanometergrote kristalletjes en vertoont een verwrongen tetragonale mackinawiet structuur. Het heeft een opgeblazen kristalrooster, voornamelijk langs de c as waar, ingebed tussen de roosterlagen,

watermolekulen voorkomen. Mogelijk komen ook hydroxylgroepen met geassocieerde protonen, kationen of weggelaten zwavelatomen voor, die de lading balanceren. FeS_{am} kan worden beschreven als een mengsel van twee eindleden met zowel een andere gemiddelde deeltjesgrootte als een verschillende mate van kristalliniteit. De vorming van twee FeS_{am} fasen komt overeen met de twee concurrerende reactiepaden voor de vorming van FeS_{am} vanuit de waterige oplossing (Rickard, 1995). De reactiviteit van FeS_{am} is afhankelijk van de relatieve verhouding van de twee eindleden. Deze verhouding is op haar beurt afhankelijk van de omstandigheden gedurende de vorming van FeS_{am} , in het bijzonder van de zuurgraad, en van de leeftijd van het neerslag. Deze bevindingen verklaren deels de eerder gerapporteerde verschillen in FeS_{am} reactiviteit in zowel experimenten als in het milieu.

De oplosbaarheid van FeS_{am} in het neutrale tot basische pH-bereik is $K_{\text{s}}^{\text{app}} = \{\text{Fe}^{2+}\} \cdot \{\text{H}_2\text{S}(\text{aq})\} \cdot \{\text{H}^+\}^{-2} = 10^{+4.87 \pm 0.27}$. Dit is de eerste studie waarin de $K_{\text{s}}^{\text{app}}$ bepaald is voor het neutrale tot basische pH-bereik. Zuur-base titraties tonen aan dat het nulpunt van de oppervlaktelading (PZC) van FeS_{am} bij pH ~ 7.5 ligt. Het gehydrateerde oppervlak wordt gekarakteriseerd door sterk zure enkelvoudig gecoördineerde zwavelgroepen en zwak zure drievoudig gecoördineerde zwavelgroepen. Beide typen oppervlaktegroepen hebben een concentratie van 1.2×10^{-3} mol per gram FeS_{am} . De zuur-base eigenschappen worden bepaald door de enkelvoudig gecoördineerde zwavelgroepen bij pH < PZC en door de drievoudig gecoördineerde zwavelgroepen bij hogere pH. De totale dichtheid van de oppervlaktegroepen is 4 groepen per vierkante nanometer.

De modelbeschrijving van het oppervlak van FeS_{am} is toegepast op de experimentele arseensorptiedata. Sorptie van arsenaat, As(V), op synthetische FeS_{am} is snel en sterk pH-afhankelijk. As(V) vormt dominant een monodentaat complex op het oppervlak, waar het bindt met de geprotoneerde enkelvoudig gecoördineerde zwavelgroep. Sorptie van arseniet, As(III), is niet sterk pH-afhankelijk en kan beschreven worden met behulp van een Freundlich isotherm. Dit impliceert dat As(III) op verschillende oppervlaktegroepen sorbeert. Sorptie is snel, hoewel niet zo snel als As(V) sorptie. Sterkere sorptie van As(V) dan van As(III), en derhalve een hogere As(III) mobiliteit, kan tot uitdrukking komen in natuurlijke milieus wanneer FeS_{am} de mobiliteit van arseen controleert.

Het gedrag van arseen gedurende de reactie van FeS_{am} naar pyriet werd bestudeerd in batch experimenten. De opname van arseen in de vaste fase kan beschreven worden door sorptie van As(V) en As(III) op FeS_{am} . In deze batch experimenten speelt nucleatiekinetiek in de pyrietvorming een belangrijke rol, omdat de oplossingen sterk oververzadigd waren ten opzichte van pyriet (vergelijk Butler en Rickard, 2000). De nucleatie van pyriet wordt vertraagd in de aanwezigheid van opgelost arseen, en zelfs verhinderd bij hoge concentraties van arseen, door sorptie van arseen op het oppervlak van FeS_{am} en/of door reactie met het opgeloste $\text{FeS}(\text{aq})$ complex (zie Rickard en Luther, 1997); bovendien oxideert As(V) ijzersulfide. Met andere woorden, arseen beïnvloedt de nucleatie van pyriet sterk. In een opstelling onder continue doorstroming van de oplossing, werd pyriet ook gesynthetiseerd in oplossingen met As(III) concentraties die natuurlijke concentraties benaderen. In deze minder sterk oververzadigde experimenten is kristalgroei van pyriet dominant ten opzichte van nucleatie van pyriet. Gedurende de kristalgroei van pyriet in deze continue experimenten werd een doorgaande inbouw van arseen waargenomen. Deze resultaten tonen zodoende aan dat, terwijl de nucleatie van pyriet een sterke invloed ondervindt van de aanwezigheid van opgelost arseen, de kristalgroei van pyriet niet waarneembaar beïnvloed wordt.

De gevolgen van deze laatste conclusie zijn tweeledig. Ten eerste zal in milieus die sterk oververzadigd zijn ten opzichte van pyriet, waar nucleatie relatief sneller is dan kristalgroei, inbouw van arseen in pyriet niet de voorkeur hebben, aangezien arseen de vorming van pyriet remt. Daarom zal sorptie van arseen op FeS_{am} in dit geval een belangrijker mechanisme zijn voor de vastlegging van arseen vanuit de oplossing. Het op deze manier vastgelegde arseen kan niet beschouwd worden als immobiel omdat de gastheer zelf metastabiel is en de mogelijkheid van desorptie bestaat. Ten tweede zal arseen wel in pyriet worden ingebouwd in milieus waar pyriet zich vormt uit een oplossing die minder sterk oververzadigd is ten opzichte van pyriet. In deze milieus is de snelheid van kristalgroei hoger dan de nucleatiesnelheid en kristalgroei wordt niet waarneembaar gehinderd door arseen, waardoor arseen in substantiële hoeveelheden in pyriet ingebouwd kan worden. In deze milieus zal een relatief stabiele vastlegging van arseen plaatsvinden, die alleen onstabiel wordt door oxidatie.

Vanuit dit proefschrift komen verschillende vragen naar voren, die in toekomstig onderzoek beantwoord zouden moeten worden. Ten eerste: „Zal de

PZC van het FeS_{am} oppervlak veranderen met rijping van de FeS_{am} ?" Zo'n verandering wordt verwacht, aangezien de PZC van kristallijne mackinawiet onder pH 3 ligt (Bebié et al., 1998). Bovendien is in hoofdstuk 2 aangetoond dat de kristalstructuur verandert met de ouderdom van het precipitaat wanneer de ordening van het kristalrooster over grotere afstand (in nanometers) uitbreidt. Zoals bediscussieerd in hoofdstuk 3 zal voor silicaten zo'n structurering van het rooster een versterking van de zure oppervlaktegroepen tot gevolg hebben en derhalve een verlaging van de PZC. Een dergelijk effect zou van belang zijn voor milieustudies, aangezien een oppervlak met een andere lading bij dezelfde pH andere sorptie eigenschappen bezit en preferent kationen of anionen zal sorberen. Ten tweede: „Wat is het mechanisme dat de oplosbaarheid van FeS_{am} controleert in het neutrale tot basische pH-bereik?” Een gedetailleerde studie naar de ijzersulfidespeciëatie in oplossing in relatie tot de oplosbaarheid van FeS_{am} is daarbij vereist, omdat de resultaten die gepresenteerd zijn in hoofdstuk 3 aantonen dat de mechanismen die de oplosbaarheid controleren veranderen met pH. Ten derde: „Wat zijn de reductiemechanismen van As(V) en As(III) in ijzersulfidesystemen?” Deze vraag zou beantwoord kunnen worden met behulp van experimenteel onderzoek naar de sorptie van arseen op FeS_{am} en pyriet met reactietijden tot een paar weken, gecombineerd met zowel analyses op de macroschaal als spectroscopie studies op atomair niveau van aan het oppervlak gesorbeerde complexen. Zoals besproken als hypothese in hoofdstuk 5 zou de reductie kunnen verlopen via intermediären zoals thioarsenaat- en thioarsenietcomplexen binnen vier weken bij pH 6. De reductie van arseen naar nominaal As(-I) en de inbouw daarvan in pyriet is een belangrijke stap in de meest stabiele vastlegging van arseen in zuurstofarme en zuurstofloze milieus. Tot slot: „Kan de inbouw van arseen in pyriet gedurende continue experimenten gekwantificeerd worden?” Om deze vraag te kunnen beantwoorden zullen meer soortgelijke experimenten uitgevoerd moeten worden, met daaraan gekoppelde gedetailleerde analyses van de opgeloste species waaronder mogelijk ijzersulfidecomplexen, thioarsenaten en thioarsenieten en zelfs ijzer-arseen-sulfidecomplexen. De beste benadering zou zijn om experimenten te doen bij natuurlijke concentraties en de speciëatie in oplossing te meten met behulp van polarografische analysetechnieken. Op deze manier worden de natuurlijke omstandigheden van de vorming van arseenhoudende pyriet het meest nauwkeurig nagebootst.

Introduction

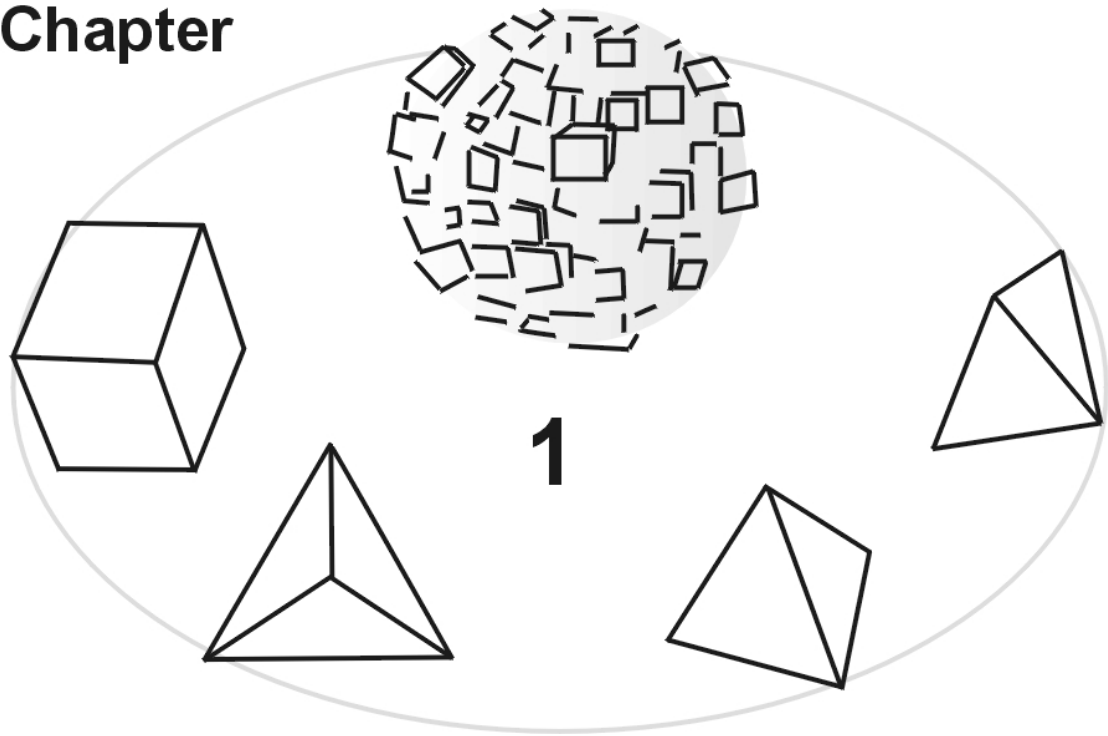
Why study the geochemistry and environmental mineralogy of the iron-sulphur-arsenic system? In the minds of most people, "arsenic" and "poison" are almost synonyms. It has been available to dissatisfied spouses and the politically ambitious for thousands of years, a cheap and effective solution to many of the awkward situations that develop in human affairs (quote from Penrose, 1974). Presently, arsenic is recognised as one of the most serious inorganic contaminants in drinking water on a worldwide basis. An alarming example of arsenic problems in groundwater is Bangladesh, where many of the recently installed millions of drinking water wells contain high concentrations of arsenic (Smedley and Kinniburgh, 2002). These wells withdraw water from suboxic aquifers. The processes behind the effectively high arsenic mobility in this and other suboxic and anoxic environments are poorly understood (Smedley and Kinniburgh, 2002; Harvey et al., 2002). Knowledge of such processes is essential to understand and predict the behaviour of arsenic in these environments. The solubility of arsenic oxides and sulphides is relatively high under a wide range of pH and redox conditions. The most important process reducing arsenic mobility in the environment is sorption onto other, less soluble, oxides and sulphides. Iron oxides and sulphides are ubiquitous phases in sedimentary environments. While arsenic sorption onto iron oxides has been studied intensively over the past few years, its sorption onto Fe(II) sulphides has not been widely investigated.

The scope of this thesis is to study arsenic sorption onto disordered mackinawite, FeS_{am} , and the association of As with Fe(II) sulphides during the formation of pyrite, FeS_2 . At ambient temperatures and pressures, several iron-sulphide phases can be formed. However, in anoxic sulphidic environments at pH values higher than 5, pyrite is the most stable and ubiquitous phase formed. Generally, pyrite formation is preceded by the precipitation of metastable disordered mackinawite, FeS_{am} . Since, in sedimentary settings, arsenic is present as dissolved As(III) or As(V), the behaviour of both As(V) and As(III) in the presence of FeS_{am} and during the reaction to pyrite is studied.

As a background to this thesis, a brief overview of the literature on (disordered) mackinawite, pyrite and arsenic is provided in *Chapter 1*. In

Chapters 2 and 3, the bulk characteristics, crystallinity and surface properties of synthetic FeS_{am} are determined. The constructed surface model is applied in *Chapter 4* to experimental arsenic sorption data. In *Chapter 5*, the behaviour of arsenic during the transformation of FeS_{am} to pyrite is studied in batch experiments and results are interpreted in relation to the sorption reactions proposed in Chapter 4. Subsequently, pyrite formation in the presence of As(III) at concentrations approaching those in ambient environments is explored in *Chapter 6*, using a continuous-flow reaction system. Lastly, *Chapter 7* is the synthesis of the thesis, in which conclusions are discussed and environmental implications of the study considered.

Chapter



The iron–sulphur–arsenic system

In this chapter, background information is provided on the geochemistry and environmental mineralogy of Fe(II) sulphides and on the geochemistry of arsenic. Rather than giving a comprehensive review, the aim of this chapter is building the relevant background to this thesis. Therefore, the discussion on Fe(II) sulphides is focused on FeS_{am} and pyrite and the section on arsenic geochemistry concentrates on sulphidic environments.

1 Iron (II) sulphides

In increasingly anoxic waters in marine and freshwater sediments, soils, and aquifers, a well-known sequence of microbially-facilitated reduction reactions occurs (Berner, 1981; Stumm and Morgan, 1995; Langmuir, 1997). This sequence begins with O_2 consumption and CO_2 production from the decomposition of organic matter. Next, nitrate is reduced to nitrite, N_2O and N_2 . Manganic oxides dissolve by reduction to soluble Mn(II) and hydrous ferric oxides are reductively dissolved to Fe(II). These processes are followed by sulphate reduction to S(-II), CH_4 production from fermentation and methanogenesis, and, finally, reduction of N_2 to ammonium. During sulphate reduction, the resulting S(-II) reacts with any available Fe(II) to produce Fe(II) sulphides. Arsenic(V) reduction would normally be expected to occur after Fe(III) reduction, but before sulphate reduction.

1.1. Fe(II) monosulphide

Anoxic marine sediment pore waters are saturated with respect to disordered mackinawite (Berner, 1967). It is the first iron sulphide to form in most ambient aqueous environments and with time it reacts to form more stable iron sulphide phases such as ordered mackinawite, greigite and ultimately pyrite or pyrrhotite. In this thesis, disordered mackinawite is defined as the first precipitated Fe(II) monosulphide phase formed through the reaction between aqueous Fe(II) and S(-II) under ambient conditions. This phase is sometimes referred to as “amorphous FeS”; here, this phase is referred to as FeS_{am} .

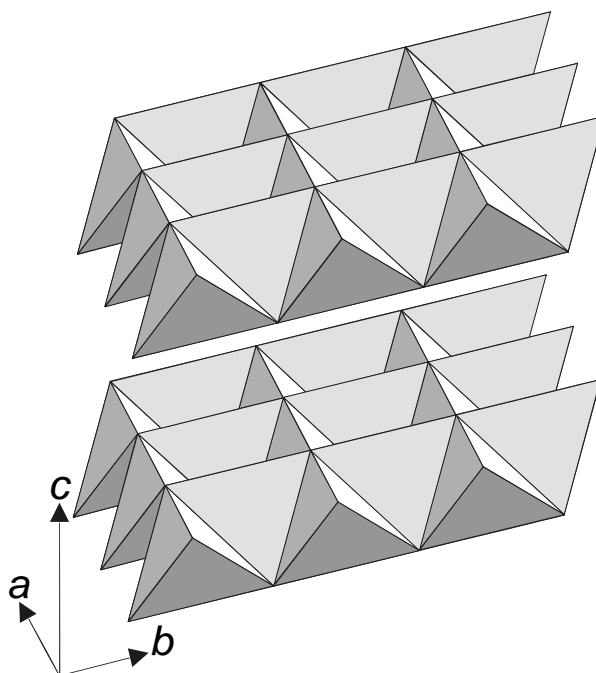


Figure 1. The structure of mackinawite (after Uda, 1968). The lattice parameters are the ribs of the unit cell: a and b within the x - y plane of the tetrahedral sheets and c perpendicular to the sheets.

1.1.1. Properties of FeS_{am}

Lennie and Vaughan (1996) showed that FeS_{am} displays long-range mackinawite ordering. Mackinawite possesses a tetragonal layer structure (Figure 1), where the iron atoms are linked in a tetrahedral coordination to four equidistant sulphur atoms. By sharing edges, these tetrahedra form sheets which are stacked along the c axis, with Van der Waals forces holding the sheets together (Vaughan and Craig, 1978). This unusual layer structure permits very close metal–metal distances in the basal plane (0.256–0.259 nm; Lennie and Vaughan, 1996) and may account for the metallic properties of mackinawite (Kjekshus et al., 1972). Along the c -axis the occurrence of double layers of sulphur atoms makes the metal–metal distances very large by comparison with those in the basal plane.

Non-stoichiometry of mackinawite results from sulphur deficiency; its composition is FeS_{1-x} (Taylor and Finger, 1970) with $0 < x < 0.07$ (Vaughan and Craig, 1978). Sweeney and Kaplan (1973) found that FeS_{am} has a similar composition of $\text{FeS}_{0.87-0.92}$, while Berner (1964) and Rickard (1969) found

Table 1. Particle size and SSA values for freeze-dried FeS_{am} measured and *calculated* (using a density of 4.1 g cm^{-3} ; approximate values, given in *italic*) from: [1] Widler and Seward (2002), [2] Benning et al. (2000), [3] Rickard (1997), [4] Kornicker (1988), [5] Taylor et al. (1979), [6] Rickard (1975). BET = the gas adsorption method; XRPD = X-ray powder diffraction; SEM = scanning electron microscopy.

Method	SSA ($\text{m}^2 \text{g}^{-1}$)	Diameter (nm)	Reference
BET	80	18	[1]
BET	16 – 21	70 – 90	[2]
XRPD + SEM	40 – 140	10 – 35	[3]
BET	36.5	40	[3]
BET	53.0 ± 46.3	28 (15 – 220)	[4]
BET	7	210	[5]
Microscopy	44	33	[6]

higher upper sulphur content of $\text{FeS}_{1.1}$. The higher sulphur content was attributed to adsorption of hydrogen sulphide (cf. Morse et al., 1987). While mackinawite and FeS_{am} are pure phases in the iron–sulphur system, mackinawite in sulphide-ore deposits shows considerable contents of other transition metals (e.g. Morse et al., 1987) and scavenging of trace elements by FeS_{am} is reportedly an important pathway for removal of these elements from solution in anoxic environments (Kornicker, 1988; Morse and Arakaki, 1993; Arakaki and Morse, 1993; Morse and Luther, 1999; Wharton et al., 2000).

As discussed in Rickard and Luther (1997), there appears to be a continuum of FeS_{am} sizes down to electroactive FeS_{am} less than 5 nm in size which can be treated as soluble species. Table 1 gives an overview of reported particle-size and specific surface-area (SSA) measurements, estimates and calculations. This broad range of particle sizes and SSA measurements has been determined or calculated from properties of dried and therefore strongly aggregated disordered mackinawite and may be artefactual (cf. Morse et al., 1987; Kornicker, 1988).

Characterisation studies of sulphide surfaces are rare in general and the fundamental surface acid–base properties for FeS_{am} have not been investigated. Kornicker’s (1988) attempt to determine the surface charge of FeS_{am} by acid–base titrations failed due to the rapid dissolution of the mineral below about pH 7. Dekkers and Schoonen (1994) and Bebié et al. (1998) employed

Table 2. Potentiometrically determined pH_{PZC} for Fe(II) sulphides and the site density for gold hydrosulphide sorption onto each Fe(II) sulphide (from Widler and Seward, 2002).

Mineral	pH_{PZC}	Sorption sites nm^{-1}
Pyrite (synthetic)	2.0	0.26
Pyrite (natural)	2.4	0.057
Pyrrhotite (synthetic)	2.7	0.086
Mackinawite (synthetic)	2.9	0.018

Table 3. Apparent solubility products $K_{\text{S}}^{\text{app}}$ for the synthetic Fe(II) monosulphides, where $K_{\text{S}}^{\text{app}} = \{\text{Fe(II)(aq)}\} \cdot \{\text{H}_2\text{S(aq)}\} \cdot \{\text{H}^+(\text{aq})\}^{-2}$. [1] at 20°C, Davison et al. (1999); [2] at 25°C, Benning et al. (2000); [3] at 25°C, Davison (1991). *Literature data where $K_{\text{S}}^{\text{app}}$ was defined as $\{\text{Fe(II)(aq)}\} \cdot \{\text{HS}^-(\text{aq})\} \cdot \{\text{H}^+(\text{aq})\}^{-1}$ were recalculated by adding $K_1 = \{\text{H}_2\text{S(aq)}\} \cdot \{\text{HS}^-(\text{aq})\}^{-1} \cdot \{\text{H}^+(\text{aq})\}^{-1} = 10^{+6.98}$ (Suleimonov and Seward, 1997).

Mineral	$\log K_{\text{S}}^{\text{app}}$	Reference
FeS_{am}	3.98 ± 0.12	[1]*
Aged (2–15 days) FeS_{am}	3.15 ± 0.05	[2]
Mackinawite	3.38 ± 0.2	[3]*
Pyrrhotite	1.88 ± 0.15	[3]
Troilite	1.73 ± 0.2	[3]

electrophoresis to study the surface charge as a function of pH. They found that the isoelectrical points (i.e.p.) for several crystalline metal sulphides, including the crystalline Fe(II) monosulphide, pyrrhotite, lie below $\text{pH} \sim 3.3$. This means that, at pH values higher than their $\text{pH}_{\text{i.e.p.}}$ in solutions with protons as the only surface potential determining ions, the surfaces of crystalline metal sulphides will be negatively charged. Bebić et al. (1998) found that differences in bulk chemical composition and crystal structure result in only minor differences in surface charge development with pH and proposed that surface sulphur groups govern the metal–sulphide surface chemistry.

Potentiometrically derived surface charge data exist for crystalline iron sulphides (Widler and Seward, 2002), zinc sulphide (Rönngrén et al., 1991), lead sulphide (Sun et al., 1991), arsenic and antimony sulphide (Renders and Seward, 1989). Widler and Seward (2002) reported that only with no added salt charging of the crystalline mackinawite surface could be observed. Table 2 lists the potentiometrically determined points of zero charge (pH_{PZC}) and the

density of gold-hydrosulphide sorption sites for iron sulphides obtained by Widler and Seward (2002).

Davison (1991) critically evaluated literature values for the solubility products of various iron sulphide phases, and reappraised the value for FeS_{am} in 1999 (Davison et al., 1999). In Table 3, these and other values are listed. For FeS_{am} the values refer to measurements at $\text{pH} < 6$. Benning et al. (2000) noted that the solubility of FeS_{am} in the important neutral and alkaline pH range ($6 > \text{pH} < 8$) was poorly constrained and found values for $\log K_{\text{s}}^{\text{app}}$ of +6.55 and +7.31 at 80°C. At $\text{pH} < 6$, the temperature dependence of the solubility product of FeS_{am} was determined experimentally by Benning et al. (2000). They report:

$$(1) \quad \log K_{\text{s}}^{\text{app}} = 2848.799T^{-1} - 6.347$$

for the temperature (T) range of 25–95°C, and measured $\log K_{\text{s}}^{\text{app}} = +3.15 \pm 0.05$ at 25°C compared with Davison et al.'s revised value of $\log K_{\text{s}}^{\text{app}} = +3.98 \pm 0.12$ at 20°C. FeS_{am} is an extremely sensitive material. It varies with both environmental conditions and age. In Table 3, information is listed about the nature of the FeS_{am} reactant used in the solubility measurements.

Davison (1991) showed that, in anoxic freshwater environments where solid phase iron sulphides were present, FeS_{am} is generally the phase controlling the iron–sulphide activity product while mackinawite or greigite may be the controlling phases in seawater.

1.1.2. Formation of FeS_{am}

There are broadly three ways of synthesising mackinawite at low temperature: by the reaction of aqueous S(–II) solutions with either (i) Fe(0) or (ii) Fe(II) (Berner, 1964; Rickard, 1969; Lennie and Vaughan, 1996) or (iii) via sulphate-reducing bacteria (Rickard, 1968; Watson et al., 2000). The reaction of Fe(0) with aqueous S(–II) results in a more crystalline mackinawite than the reactions (ii) and (iii) (Lennie and Vaughan, 1996; Mullet et al., 2002), while the reaction of Fe(II) with inorganic and bacterial aqueous S(–II) produces disordered mackinawite which is very similar to natural disordered mackinawite (Berner, 1967; Spadini et al., submitted).

Rickard (1995) examined the kinetics and mechanism of synthetic FeS_{am} formation in detail. He demonstrated that FeS_{am} precipitation follows Eigen–Wilkins kinetics with two competing mechanisms resulting from the pH dependence of aqueous S(–II) speciation:



where reaction (1) is dominant at $\text{pH} < 7$ and (2) is dominant at $\text{pH} > 7$. With HS^- , the reaction involves the formation of an inner-sphere bisulphide complex, $[\text{Fe}(\text{HS})\cdot(\text{H}_2\text{O})_5]^+$, followed by the condensation of the inner-sphere complex to FeS_{am} according to overall reaction (1). In contrast, aqueous H_2S reacts via an outer-sphere complex to form FeS_{am} directly. The relative importance of the two routes is pH-dependent, since the $\text{H}_2\text{S}:\text{HS}^-$ ratio is pH-dependent. The pathway involving HS^- results in the formation of an intermediate zero-charged Fe(II) sulphide or bisulphide complex. Wei and Osseo–Asare (1995) also observed an intermediate product at $\text{pH} > 7$ during FeS_{am} precipitation. Theberge and Luther (1997) showed that this complex was an aqueous FeS cluster complex. Rickard (1995) found that FeS_{am} formed very rapidly within milliseconds at ambient temperature. This rapid formation of FeS_{am} explains why this material is formed first in environments where the aqueous Fe(II) and S(-II) activity product equals or exceeds the FeS_{am} solubility product. The more stable phases, such as pyrite, are relatively slow to form and thus the most soluble, least stable phase is produced. This is an example of the Ostwald Step Rule (Morse and Casey, 1988; Steefel and Van Cappellen, 1990).

1.2. Pyrite

1.2.1. Properties of pyrite

Pyrite, FeS_2 , is the most stable and ubiquitous authigenic Fe(II) sulphide phase in Earth-surface environments. It is a cubic Fe(II) disulphide, in which iron is coordinated in a slightly distorted octahedron to six $\text{S}_2(-\text{II})$ sulphur dianions (Figure 2). The midpoints of the $\text{S}_2(-\text{II})$ groups occupy the corners of the octahedra and the octahedra share corners.

Kullerud and Yoder (1959) proposed that the composition of pure pyrite is $\text{FeS}_{2.00}$ and that deviations from this stoichiometry are caused by the presence of impurities. Authigenic pyrite can contain large amounts of trace elements and, hence, is an important sink for many trace elements in anoxic

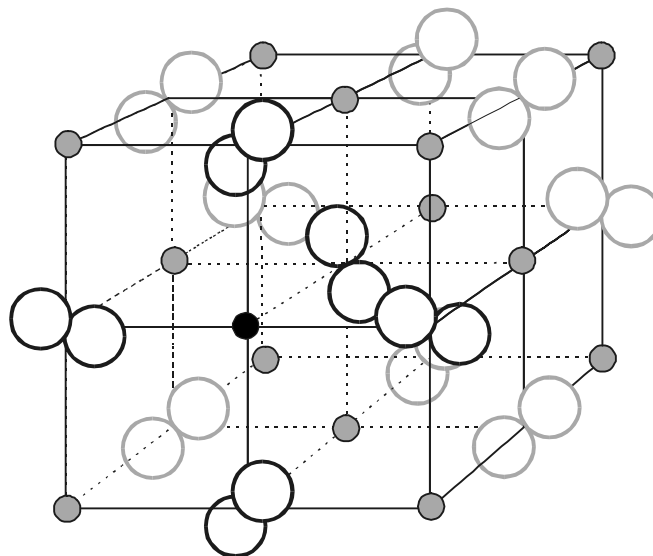


Figure 2. The crystal structure of pyrite (after Morse et al., 1987).

sulphidic sediments (e.g. Huerta–Diaz and Morse, 1992; Morse and Luther, 1999; Dellwig et al., 2002). Impurities in natural pyrite can lead to *n*- or *p*-type semiconducting behaviour. The former is more common and usually arises from cobalt, nickel or copper substitution for Fe(II), whereas the latter arises from arsenic substitution for sulphur in the $S_2(-II)$ group (cf. Rosso, 2001).

While hydrothermal pyrite can form cm-sized crystals and larger aggregates, authigenic pyrite generally forms (sub)micrometer-sized euhedra or micrometer-sized framboids (e.g. Passier et al., 1997). Diagenetic pyrite overgrowths may be hundreds of microns large. Kornicker and Morse (1991) determined the specific surface area of synthetic pyrite by BET adsorption and found that the SSA was $5.14 \pm 2.27 \text{ m}^2 \text{ g}^{-1}$. Furthermore, they estimated the density of available surface sites from sorption isotherms of Ca(II), Ni(II), and Co(II) onto their synthetic pyrite. The estimated site densities they reported lie between 11 and $14 \mu\text{mol g}^{-1}$, which corresponds to a site density of 1.3–1.6 sites nm^{-2} . The theoretical broken-bond density on the (100) and (111) planes of pyrite, calculated from crystallography, are much higher: the (100) plane consists of 14 broken Fe–S bonds per square nm, whereas the (111) surface consists of 10 broken Fe–S and 7 broken S–S bonds per square nm (Rosso, 2001) This suggests that approximately ten percent of the theoretical reactive sites are specific sorption sites.

Dekkers and Schoonen (1994) and Bebié et al. (1998) found that the i.e.p. for pyrite, lies below pH ~ 3.3 and showed that the sulphide surface was largely dominated by sulphide groups. Widler and Seward (2002) performed

potentiometric titrations of the surface of synthetic and natural pyrite. Similar to their titration of crystalline mackinawite, they observed one inflection point in the surface charge curve for natural pyrite and assumed this represents the pH_{PZC} (Table 2). In contrast, two asymmetrical inflection points were found in the case of synthetic pyrite, one at pH 2.0 and one at pH 3.0. Widler and Seward (2002) suggested two different explanations for the two inflections: (i) site-specific sensitivity where two different sites are protonated at different pH values; (ii) the further protonation of a surface site that was already partially protonated in an earlier step. They assumed that the inflection point, at pH 2.0, represents the pH_{PZC} (Table 2). However, these two inflection points and the possible explanations could actually indicate a trajectory of zero charge between the two inflection points. In that case, the inflection point at pH 3.0 represents the neutralisation of all negative surface sites by protonation and the inflection point at pH 2.0 represents the protonation of the neutral sites, resulting in a positively charged surface. Even so, their results are in general agreement with the electrophoretic measurements of Bebié et al. (1998).

The low solubility of pyrite makes direct measurement of the solubility product difficult. Therefore, Davison (1991) proposed to calculate the thermodynamic solubility product from the free energies of formation of the components in the dissolution reaction:



Using the critical compilation of Bard et al. (1985), he suggested the consensus value of $\log K_s^{\text{calc}} = -16.4 \pm 1.2$. This is generally accepted. However, the uncertainty is greater than the stated precision because of the debate over the free energy for hexaquoiron(II) and the problem with equating S_0 with S_8 .

1.2.2. Formation of pyrite

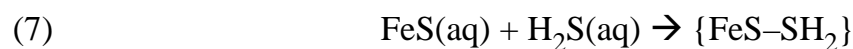
Different reactions for pyrite formation have been suggested (e.g. Rickard, 1975; Taylor et al., 1979; Luther, 1991; Rickard and Luther, 1997; Wilkin and Barnes, 1997), but a general conclusion is that the formation of the relatively oxidised $\text{S}_2(-\text{II})$ disulphide is a prerequisite for any pyrite forming reaction. Nucleation of pyrite has been demonstrated to occur on existing pyrite surfaces (Harmandes et al., 1999, Butler et al., submitted), by organic surfaces (Grimes et al., 2001) and, possibly, by defects on the precursor FeS_{am} surface (Wang and Morse, 1996).

With the notable exception of Rickard (1975, 1997), Luther (1991) and Rickard and Luther (1997), no kinetic and mechanistic studies on the formation of pyrite have been performed. Rickard (1975) and Luther (1991) investigated the role of polysulphide species in pyrite formation. Rickard (1975) showed that increased polysulfide concentrations increased the rate of pyrite formation. Rickard's mechanism for the rate controlling reaction with polysulfide was refined by Luther (1991). This mechanism can be applied to Fe(II) sulphide surface species as well as solution complexes. For the FeSH^+ solution complex, the reaction is as follows (Luther, 1991):



where S_5^{2-} and S_4^{2-} are polysulphide species (see Luther (1991) for a detailed discussion on the kinetics and mechanism of this reaction).

Rickard and Luther (1997) unravelled the problem of the formation of pyrite in strictly anoxic conditions, which has been widely observed in the natural environment. They demonstrated that aqueous H_2S oxidised FeS_{am} . The mechanism of reaction between FeS_{am} and H_2S is :



where $\text{FeS}(\text{aq})$ is the dissolved electroactive Fe(II) monosulphide cluster complex mentioned in section 1.1.2. This mechanism and its kinetics have been discussed in detail by Rickard (1997), Rickard and Luther (1997) and Butler and Rickard (2000).

2. Arsenic geochemistry

Over the past decades, the geochemistry of arsenic has been the subject of several reviews (Ferguson and Gavis, 1972; Cullen and Reimer, 1989; Korte and Fernando, 1991; Smedley and Kinniburgh, 2002). The most recent review, by Smedley and Kinniburgh (2002), gives an excellent overview of the aqueous geochemistry, the sources and the macroscale mineral–water interaction with relevance to groundwater environments and arsenic problem areas.

2.1. Arsenic abundance in natural waters

Natural sources of arsenic in nature are volcanism, hydrothermal exhalations and hydrothermal water–rock interactions (e.g. Pokrovski et al., 2002). Examples of important anthropogenic inputs are through mining and smelting activities (e.g. Meyer et al., 1999) and industry (e.g. Andreae et al., 1983) and through the use of pesticides (e.g. Basu et al., 2001) wood preservatives (e.g. Hingston et al., 2002).

Although anthropogenic sources are locally important, most environmental As problems are the result of mobilisation under natural conditions (Smedley and Kinniburgh, 2002). Next to fluorine, arsenic is now recognised as the most serious inorganic contaminant in drinking water on a worldwide basis. One of the most alarming examples of an arsenic problem in groundwater is Bangladesh, where many of the recently installed millions of drinking water wells contain high concentrations of arsenic (Smedley and Kinniburgh, 2002). Harvey et al. (2002) studied the arsenic mobility in an aquifer in southern Bangladesh and proposed that arsenic mobilisation is associated with recent inflow of labile carbon through either organic-carbon driven reduction or displacement by carbonate.

In general, the concentration of arsenic in fresh and estuarine water shows considerable variation with the geological composition of the drainage area and the extent of anthropogenic input (Andreae et al., 1983; Andreae and Froelich, 1984), while oceanic constituents tend to be less variable (Broecker and Peng, 1982) (Table 4).

Table 4. Arsenic concentrations in natural waters. [1] Andreae (1980); [2] Scudlark and Church (1988); [3] Barbaris and Betterton (1996); [4] Andreae et al. (1983); [5] Froelich et al. (1985); [6] Seyler and Martin (1991); [7] Azcue et al. (1994, 1995); [8] Azcue and Nriagu (1995); [9] Seyler and Martin (1989); [10] Baur and Onishi (1969); [11] Reuther (1992); [12] Abdullah et al. (1995); [13] Peterson and Carpenter (1983); [14] Seyler and Martin (1990); [15] Cullen and Reimer (1989); [16] Yusof et al. (1994); [17] Navarro et al. (1993); [18] Maher (1985); [19] Widerlund and Ingri (1995); [20] Yan et al. (2000); [21] Sullivan and Aller (1996) (from Smedley and Kinniburgh, 2002)

Water body	Range ($\times 10^{-6}$ M)	References
Rain water	<0.01	[1]–[3]
River water	0.002–0.028	[4]–[6]
Lake water	0.001–0.123	[7]–[11]
Estuarine water	0.009–0.051	[6], [12]–[14]
Seawater	0.007–0.049	[15]–[18]
Sediment pore water	0.017–4.005	[19]–[21]

2.2. Aqueous arsenic speciation

In nature, arsenic can be found in four oxidation states: the (–III) state, the metallic (0) state, the (III) and (V) states. However, arsenic dissolved in natural waters is predominantly inorganic As(V) and/or As(III) (Figure 3). Because of the high charges on the (III) and (V) states of arsenic, and hence the rapid hydrolysis of these states in aqueous solutions, there is practically no cationic chemistry of arsenic except in extremely strong acidic solutions (Boyle and Jonasson, 1973).

In oxygenated waters, the following As(V) species are stable with increasing pH: H_3AsO_4 , H_2AsO_4^- , HAsO_4^{2-} , and AsO_4^{3-} (Figure 4a). In reducing waters, As(V) is reduced to a large extent to As(III) (e.g. Andreae, 1979; Sadiq, 1990; Kuhn and Sigg, 1993; Abdullah et al., 1995; Gonzalez Soto et al., 1996; Yan et al., 2000). The As(III) species H_3AsO_3 , H_2AsO_3^- and HAsO_3^{2-} (Figure 4b) are generally dominant under reducing conditions. As(III) may also form stable oligomers such as $\text{As}_6\text{O}_6(\text{OH})_6$ and $\text{As}_3\text{O}_3(\text{OH})_3$ (Pokrovski et al., 1996; Tossell, 1997) and, in the presence of high S(–II) concentrations, thioarsenite monomers $\text{AsS}(\text{SH})_2^-$ and $\text{AsS}_2(\text{SH})_2^{2-}$ and trimer $\text{As}_3\text{S}_4(\text{SH})_2^-$ (Helz et al., 1995). Additionally, arsenic may be mobile in the form of arsenic oxide and

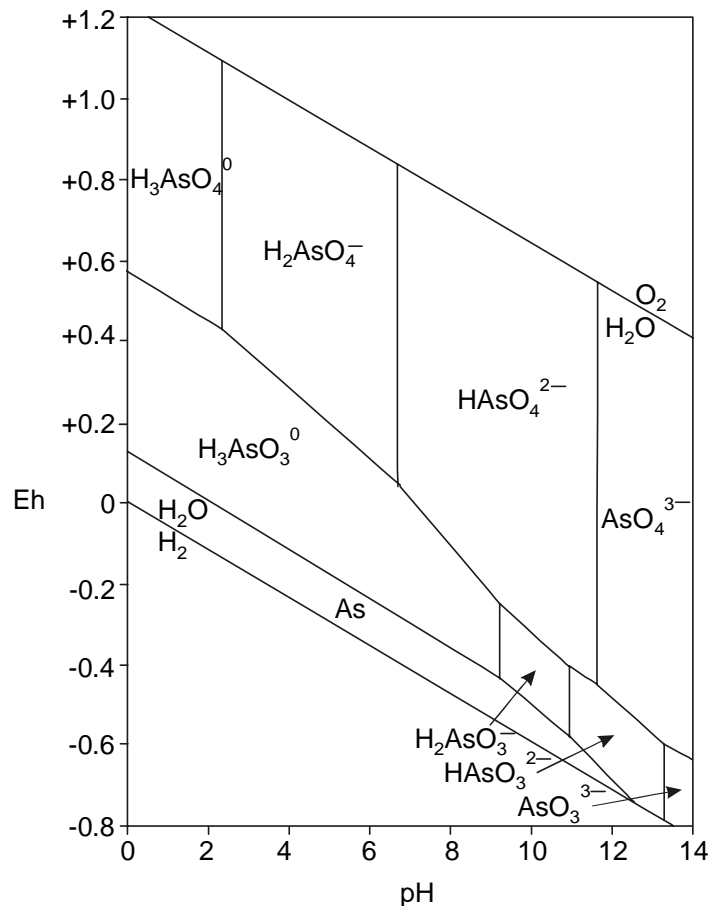


Figure 3. Eh–pH diagram for the As–O–H system at 25°C, 1 atm and a total arsenic concentration of 10^{-6} M (adapted from Vink, 1996).

arsenic sulphide colloids, adsorbed to hydrous iron oxide, silicate and humic colloids, and in a variety of chelated and other organic compounds (Boyle and Jonasson, 1973).

2.3. Oxidation–reduction transformations and kinetics

The oxidation–reduction potential is an important factor controlling the behaviour of arsenic. According to thermodynamic equilibrium calculations, As(V) concentrations should be greater than As(III) concentrations under all conditions in redox sequences above the onset of sulphate-reduction.. However, in natural waters such behaviour is not necessarily followed (e.g. Kuhn and Sigg, 1993). Inorganic oxidation of As(III) in solution has a half-life of several months to years (e.g. Eary and Schramke, 1990), but is catalysed by manganese oxide particles (e.g. Tournassat et al., 2002) and by micro-organisms (e.g. Oremland et al., 2000).

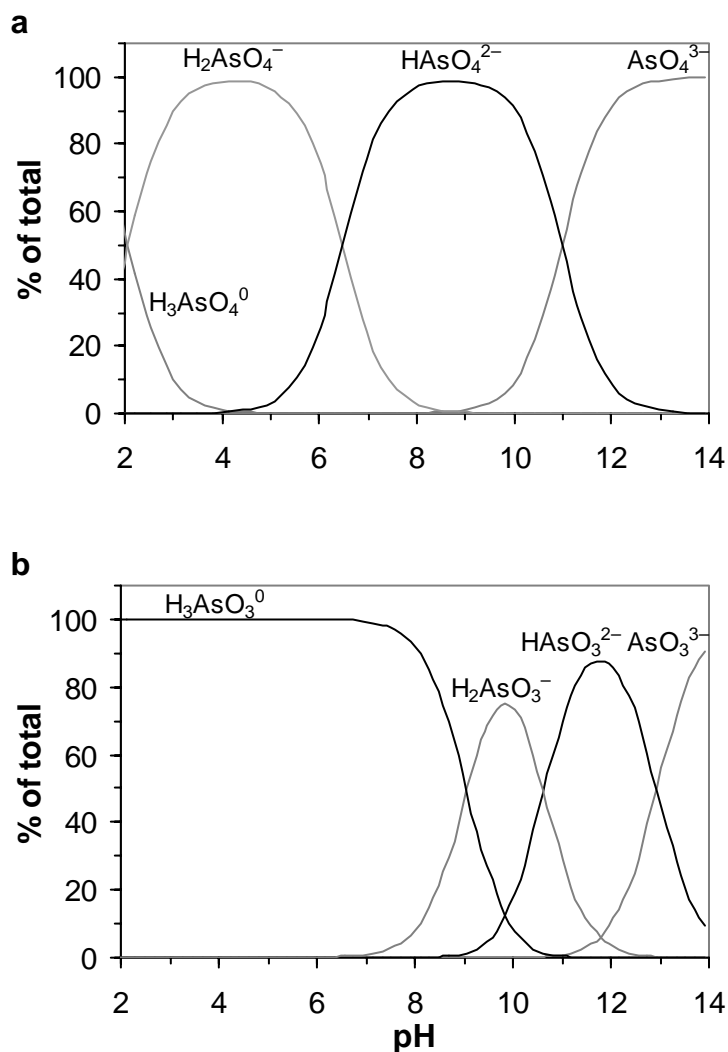


Figure 4. (a) Arsenate and (b) arsenite speciation at 0.05M ionic strength. Thermodynamic constants are taken from Table 1 in chapter 4.

Of particular interest to this thesis is the study by Rochette et al. (2000). They studied abiotic arsenate reduction kinetics by hydrogen sulphide in solution and postulated a reduction mechanism. At pH 4, they found arsenate reduction to be rapid and conform to a second order rate constant, $k = 3.2 * 10^2 \text{ M}^{-1} \text{ h}^{-1}$. At pH 7, they observed that essentially no reduction had occurred after 7 days. They described the first two steps in the reaction mechanism as ligand exchanges where oxo groups are replaced by sulphide groups to form thioarsenate and dithioarsenate. Within 75 hours of their experiments, approximately all arsenate was converted to (di)thioarsenate. The actual reduction reaction Rochette et al. (2000) propose is an electron transfer within the dithioarsenate and formation of thioarsenite by release of the S(0).

Table 5. Overview of As concentrations in sedimentary pyrites from various types of sediments (adapted from Huerta–Diaz, 1992). [1] Hickmott and Baldrige (1995); [2] Huerta–Diaz (1992); [3] Belzile and Lebel (1986); [4] Raiswell and Plant (1980); [5] Ferguson and Gavis (1972); [6] Keith and Degens (1959); [7] Krauskopf (1955); [8] Fleisher (1955).

Origin	As (wt.%)	Reference
Coal Macerals	15–3,420	[1]
Anoxic non-sulphidic sediment	<0.004–0.925	[2]
Euxinic, hypersaline sediment	0.164–0.527	[2]
Anoxic sulphidic sediment	115–0.243	[2]
Laurentian trough sediments	0.075	[3]
Marine biogenesis film	0.009–0.010	[4]
Sediment	0.120	[5]
Fresh water shale	0.210–0.400	[6]
Fresh water sandstone	<0.002	[6]
Fresh water limestone	0.340–0.850	[6]
Marine shale	<0.002–0.037	[6]
Marine sandstone	<0.002	[6]
Marine limestone	0.002–0.130	[6]
Sediment	0.480	[7]
Sediment	0.096–0.140	[8]

Subsequently, the thioarsenite is thought to undergo ligand exchange to either dithioarsenite or arsenite, depending on the S(–II) concentration.

2.4. Arsenic in pyrite

Large arsenic concentrations tend to occur in Fe(II) sulphide minerals. Huerta–Diaz and Morse (1992) found concentrations of arsenic in marine sedimentary pyrites up to 0.93 wt.%. Their results indicate that sedimentary pyrite is an important sink for arsenic, even if only minor pyrite formation has taken place. Table 5 lists arsenic concentrations in various authigenic pyrites reported in literature.

In studies on auriferous pyrites from hydrothermal deposits, several authors proposed that arsenic substitutes for sulphur in pyrite (e.g. Fleet et al., 1993; Tingle et al., 1996; Fleet and Mumin, 1997; Savage et al., 2000) while

Table 6. Parameters obtained from XAS data fitting of the As *K*-edge spectra for As(V) sorbed on mackinawite and pyrite (results from Farquhar et al., 2002). Mk = mackinawite; Py = pyrite; *N* = the coordination number; *r* = the interatomic distance (± 0.02 Å), $2\sigma^2$ = the Debye–Waller factor (± 25 %) and *R* = the overall goodness of fit (Binsted et al., 1992).

Sample (initial solution concentration)	Shell no.	Atom type	N ± 1	<i>r</i> (Å)	$2\sigma^2$ (Å ²)	R
As(V) + Mk (0.04×10^{-3} M)	1	O	4.0	1.70	0.005	29.9
	2	S	1.0	3.11	0.004	
	3	Fe	1.0	3.51	0.010	
As(V) + Mk (0.20×10^{-3} M)	1	O	4.0	1.70	0.005	23.1
	2	S	1.0	3.09	0.005	
	3	Fe	1.0	3.38	0.012	
As(V) + Mk (5.5×10^{-3} M)	1	S	3.0	2.23	0.008	45.6
	2	S	2.0	2.69	0.008	
As(V) + Mk (55.0×10^{-3} M)	1	O	2.5	1.70	0.004	27.9
	2	S	1.5	2.33	0.021	
	3	As	4.0	3.35	0.029	
As(V) + Py (0.20×10^{-3} M)	1	O	4.0	1.69	0.005	39.9
	2	Fe	2.0	3.35	0.010	

others proposed that arsenopyrite, FeAsS, lamellae are present in the hydrothermal pyrite (Griffin et al., 1991). Fleet and Mumin (1997) found an apparent full range of metastability from FeS₂ to near FeAsS in the Deep Star gold deposit, Nevada, with an arsenic concentration ranging from zero to approximately 35 at.%, and a negative As to S atomic correlation, suggesting substitution of As for S. It must be noted that the crystal structure within this range changed from the pyrite structure via the marcasite structure to the arsenopyrite structure and that the arsenopyrite structure is a derivative of the marcasite structure (Tossell et al., 1981).

Tossell et al. (1981) used molecular orbital theory to predict the electronic structure of the dianions in pyrite and arsenopyrite. The best description, according to Tossell et al. (1981), is AsS(–II) for the dianion in arsenopyrite and S₂(–II) in pyrite, with a nominal valence of sulphur and

Table 7. Parameters obtained from XAS data fitting of the As *K*-edge spectra for As(III) sorbed on mackinawite and pyrite (results from Farquhar et al., 2002). Mk = mackinawite; Py = pyrite; *N* = the coordination number; *r* = the interatomic distance (± 0.02 Å), $2\sigma^2$ = the Debye–Waller factor (± 25 %) and *R* = the overall goodness of fit (Binsted et al., 1992).

Sample (initial solution concentration)	Shell no.	Atom type	N ± 1	<i>r</i> (Å)	$2\sigma^2$ (Å ²)	R
As(III) + Mk (0.04×10^{-3} M)	1	O	4.0	1.76	0.0014	39.1
	2	S	1.0	3.09	0.010	
	3	Fe	1.0	3.40	0.010	
As(III) + Mk (0.20×10^{-3} M)	1	O	4.0	1.72	0.014	28.0
	2	O	2.0	2.29	0.005	
	3	Fe/S?	1.0	2.87	0.028	
	4	Fe	1.0	3.32	0.013	
As(III) + Mk (50.6×10^{-3} M)	1	O	1.0	1.79	0.003	30.2
	2	S	1.0	2.30	0.009	
	3	S	0.5	2.73	0.009	
	4	S	0.5	3.16	0.011	
As(III) + Py (0.20×10^{-3} M)	1	O	4.0	1.73	0.013	40.9
	2	S	1.0	3.02	0.011	
	3	Fe	1.0	3.41	0.020	

arsenic in the dianions of -1 . Tingle et al. (1996) and Savage et al. (2000) measured the As *K*-edge with X-ray absorption spectroscopy (XAS) and reported a nominal valence of -1 of arsenic in arsenian pyrite. The nearest-neighbour environment information from the XAS data and high resolution transmission electron microscopy supported As substitution for S instead of (sub)microscopic inclusions of arsenopyrite (Savage et al., 2000).

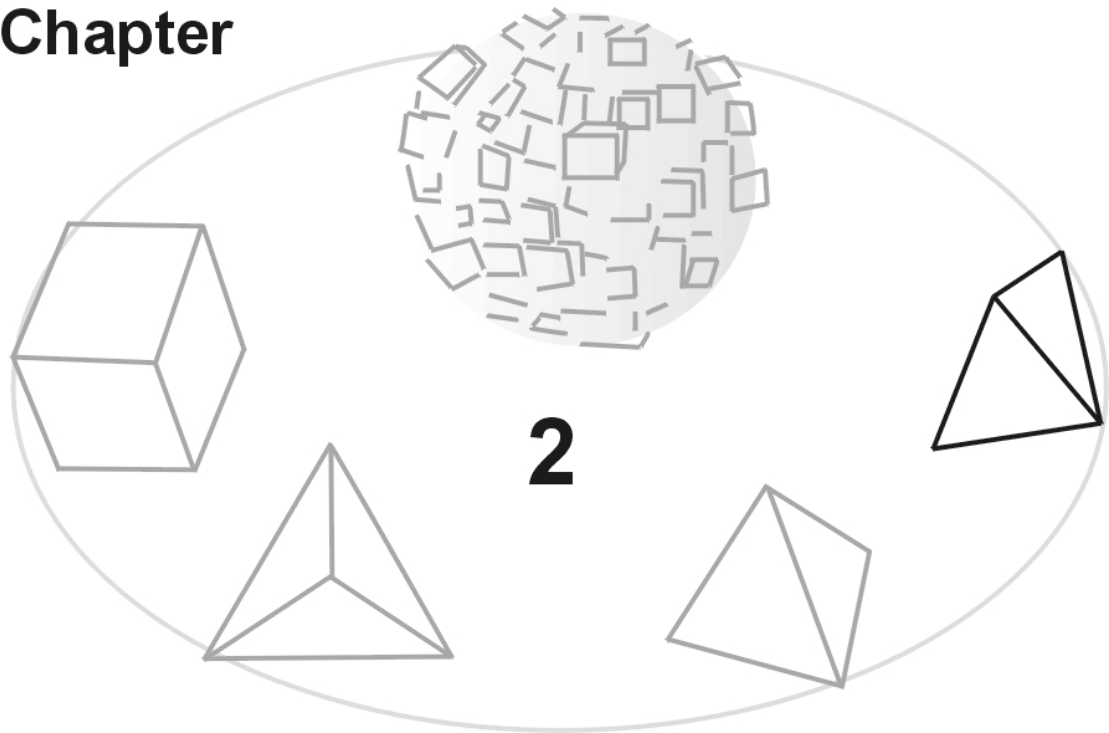
The results for hydrothermal iron(II) disulphides with increasing amounts of arsenic incorporated show that there is no solid solution over the full range from FeS₂ to near FeAsS, since the mineral structure changes. The arsenic concentrations in arsenian pyrite studied by Savage et al. (2000) is on average 1.2 wt.%, with local As concentrations ranging from ~ 0 to 5 wt.%. These concentrations were insufficient to cause local structural transformation of pyrite to arsenopyrite. Fleet and Mumin (1997) reported that arsenian pyrite

contained up to 7.7 wt.% As. Iron(II) sulphides with 10–13 wt.% As were characterised as arsenian marcasite and, in the range of 24–54 wt.% As, the solid possessed the structure of arsenopyrite.

2.5. Arsenic sorption

Arsenic sorption onto metal oxides has been examined intensively (e.g. Pierce and Moore, 1982; Waychunas et al., 1996; Fendorf et al., 1997; Hiemstra and Van Riemsdijk, 1999; Swedlund and Webster, 1999; Ding et al., 2000). Contrastingly, only one study on the sorption of arsenic onto Fe(II) sulphides was reported (Farquhar et al., 2002). They investigated the mechanisms whereby As(III) and As(V) in aqueous solution (pH 5.5–6.5) interact with the surfaces of goethite, lepidocrocite, mackinawite and pyrite using As *K*-edge XAS. Their results are summarised in Table 6 for As(V) and Table 7 for As(III) sorption onto mackinawite and pyrite. At low As(V) and As(III) concentrations, they observed similar surface complex structure with four oxygen atoms in the first shell of both arsenic species. This suggests that As(III) oxidised to As(V), which may have occurred during measurements in the high-energy beam (L. Charlet, personal communication). At higher As(V) and As(III) concentrations, different surface complexes seem to form along with poorly crystalline arsenic sulphide.

Chapter



A surface and structural model describing the environmental reactivity of disordered mackinawite*

* Submitted for publication as: Wolther M., Van der Gaast S.J., Charlet L., Rickard D., *American Mineralogist*.

Abstract

Synthetic iron(II) monosulphide, FeS_{am} , displays a disordered tetragonal mackinawite structure. It is nanocrystalline, with an average primary particle size equivalent to a crystallite size of 4 nm and a corresponding specific surface area of $350 \text{ m}^2 \text{ g}^{-1}$. It can be described in terms of a mixture of two end-member phases with different long-range ordering, which we term MkA and MkB. MkA has an average primary particle size of $2.2 \times 1.7 \text{ nm}$ and lattice parameters $a = b = 0.40 \text{ nm}$, $c = 0.67 \pm 0.01 \text{ nm}$. MkB has an average primary particle size of $7.4 \times 2.9 \text{ nm}$ and lattice parameters $a = b = 0.36 \text{ nm}$, $c = 0.53 \pm 0.02 \text{ nm}$. A typical disordered mackinawite precipitate consist of 30% MkA and 70% MkB and the proportion of MkA decreases on ageing. Lattice expansions relative to crystalline mackinawite ($a = b = 0.37 \text{ nm}$, $c = 0.50 \text{ nm}$.) are explained by intercalation of water molecules between the tetrahedral sheets and by lattice relaxation due to small crystallite size. The hydrated FeS_{am} surface can be best described by strong mono-coordinated and weak tri-coordinated sulphur sites as the surface reactive sites.

The formation of two phases of FeS_{am} is consistent with competing pathways involved in its formation from aqueous solution. MkA may be equivalent to sheet-like precipitated $\text{FeS}(\text{aq})$ clusters. The reactivity of FeS_{am} is dependent on the proportion of the two end-member phases. These in turn are dependent on the conditions of formation, especially pH, and the age of the precipitate. These observations partly explain the reported differences in FeS_{am} reactivity in experimentation and in the environment. The presented surface and structural model has implications for the behaviour of natural acid volatile sulphides in scavenging elements from solution in natural environments.

1. Introduction

Disordered mackinawite is a highly reactive phase with a high adsorptive capacity for divalent metals (e.g., Kornicker, 1988; Morse and Arakaki, 1993; Arakaki and Morse, 1993; Wharton et al., 2000). Anoxic marine sediment pore waters are saturated with respect to disordered mackinawite (Berner, 1967). It

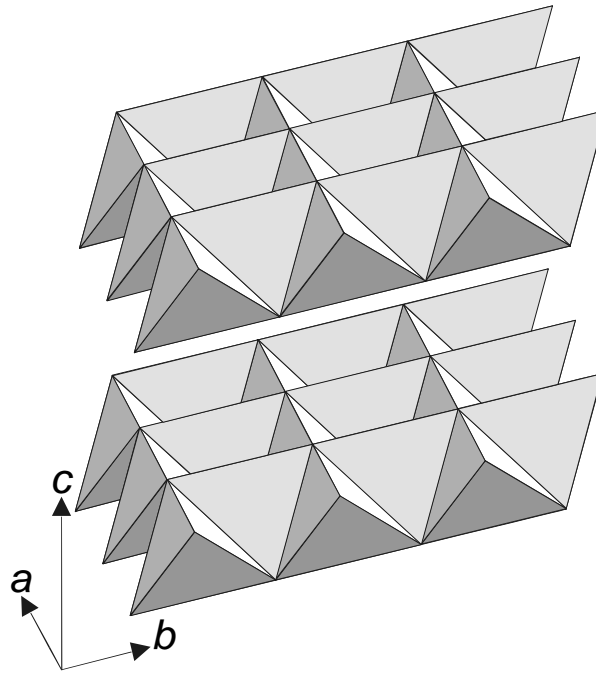


Figure 1. The structure of mackinawite (after Uda, 1968). The lattice parameters are the ribs of the unit cell: a and b within the x - y plane of the tetrahedral sheets and c perpendicular to the sheets.

is the first iron sulphide to form in most ambient aqueous environments and with time it reacts to form more stable iron sulphide phases such as ordered mackinawite, greigite and ultimately pyrite or pyrrhotite. The mackinawite structure possesses a tetragonal layer structure (Figure 1), where the iron atoms are linked in a tetrahedral coordination to four equidistant sulphur atoms. By sharing edges, these tetrahedra form sheets which are stacked along the c axis, with Van der Waals forces holding the sheets together (Vaughan and Craig, 1978). Non-stoichiometry results from sulphur deficiency; its composition is FeS_{1-x} (Taylor and Finger, 1970) with $0 < x < 0.07$ (Vaughan and Craig, 1978).

The bulk properties of synthetic disordered mackinawite have been described by several authors. There are roughly three ways of synthesising mackinawite at low temperature: by the reaction of aqueous sulphide solutions with either (i) metallic iron or (ii) ferrous iron (Berner, 1964; Rickard, 1969; Lennie and Vaughan, 1996) or (iii) via sulphate-reducing bacteria (Rickard, 1968; Watson et al., 2000). The reaction of metallic iron with aqueous sulphide results in a more crystalline mackinawite than the reaction (ii) and (iii) (Lennie and Vaughan, 1996; Mullet et al., 2002). With the notable exception of the one by Watson et al. (2000), all recent studies aiming to describe the bulk disordered mackinawite properties, pertained to the more crystalline solid

(Lennie and Vaughan, 1996; Mullet et al., 2002). However, the reaction of iron(II) with inorganic and bacterial aqueous sulphide produces disordered mackinawite which is very similar to natural disordered mackinawite (Berner, 1967; Spadini et al., submitted).

In this paper, disordered mackinawite is defined as the first precipitated iron(II) monosulphide phase formed through the reaction between aqueous Fe(II) or metallic iron and S(-II) under ambient conditions. Lennie and Vaughan (1996) showed that this phase, which is sometimes referred to as “amorphous FeS”, displays long-range mackinawite ordering. This phase is referred to as FeS_{am} in the present paper.

Rickard (1995) showed that the rate of precipitation is fast and follows Eigen–Wilkins kinetics with two competing mechanisms resulting from the pH dependence of aqueous sulphide speciation:



where reaction 1 is dominant at pH < 7 and 2 is dominant at pH > 7.

This study is the first to describe the bulk crystal and surface structure of disordered mackinawite. The objective is to develop a model for the surface and structural properties of the disordered mackinawite produced by reacting aqueous Fe(II) with aqueous S(-II). Low-angle X-ray powder diffraction (LAXRPD) analyses are used to measure the average diameter of the primary particles of freeze-dried FeS_{am} and compare these results with transmission electron microscopy (TEM) results and specific surface area measurements from freeze-dried FeS_{am}. Furthermore, from the conventional X-ray powder diffraction (XRPD) data the size of the crystalline domains (i.e., portions of the structure that diffract X-rays coherently) is estimated for freeze-dried and suspended FeS_{am}. Finally, a surface and structure-based model for disordered mackinawite is suggested.

2. Materials and Methods

2.1. Chemicals

All chemicals were of analytical grade and used without further purification; solutions were prepared from Milli-QTM water and purged for at least 30

minutes with O_2 -free N_2 gas before use. Solutions of S(-II) and Fe(II) were prepared before every experiment by dissolving $\text{Na}_2\text{S}\cdot 9\text{H}_2\text{O}$ (Fisher ChemicalsTM) and Mohr's salt ($\text{Fe}(\text{NH}_4)_2(\text{SO}_4)_2\cdot 4\text{H}_2\text{O}$; MerckTM), which is relatively resistant to oxidation, in either purged Milli-QTM water or background electrolyte of varying KNO_3 (Fisher ChemicalTM) concentration. Syntheses were run under O_2 -free conditions by directly flushing the reaction vessel with N_2 , purified by bubbling through a succession of two 15 wt.% pyrogallol in 50 wt.% KOH solutions to remove O_2 , a ChrompackTM O_2 and sulphide scrubber for additional cleaning and Milli-QTM water to saturate the N_2 with water. The O_2 concentration in the reaction vessels was below 1×10^{-6} M (0.03 ppm), which is the detection limit of the OrionTM oxygen probe 850 used to measure O_2 in solution.

2.2. Materials

Disordered mackinawite was synthesised in two ways. (i) FeS_{am} was prepared in advance and freeze-dried. This material was used for the bulk solid characterisation and determination of the specific surface area by the N_2 -BET adsorption method. Freeze-dried FeS_{am} was prepared less than a week in advance by mixing 100 mL Mohr's salt solution (0.6 M) with 100 mL sulphide solution (0.6 M $\text{Na}_2\text{S}\cdot 9\text{H}_2\text{O}$) under N_2 , filtering the suspension through a WhatmanTM No.1 filter, and freeze drying the product for 3 to 4 days. Effectively, the freeze-dried FeS_{am} was aged for less than half an hour. After freeze drying, the FeS_{am} was stored under N_2 atmosphere at -18°C upon use. (ii) *suspended* FeS_{am} was precipitated *in situ* for XRPD measurements by adding a 40×10^{-3} M Mohr's salt solution to a 40×10^{-3} M disodium sulphide solution while constantly flushing with N_2 ; flocculated FeS_{am} formed rapidly and was left to age for varying times prior to analysis.

2.3. Solid characterisations

TEM images, selected-area electron diffraction patterns (SAED) and energy-dispersive X-ray (EDX) analyses of freeze-dried FeS_{am} were collected on a PhilipsTM CM200 FEG-TEM (200 kV). Approximately 0.5 mg of freeze-dried FeS_{am} dispersed in acetone was quickly loaded in air onto a copper grid with a thin biofilm, carbon coated, and loaded into a low-background specimen

microscope holder. SAED patterns and TEM images were recorded photographically. Since the particles may be smaller than the interaction volume of the 200 kV electron beam and since no calibration could be done, the EDX data were used qualitatively.

XRPD was carried out using a self built θ - θ goniometer equipped with a long-fine-focus X-ray tube (CuK α radiation, 40 kV, 40 mA), variable divergence and anti-scatter slits, and a KeveX solid-state Si(Li) detector. Approximately 0.5 g of freeze-dried FeS_{am} was loaded under a nitrogen atmosphere within a glove bag into a 1 mm deep depression in a metal support and then the surface of the material was carefully levelled with the top of the specimen holder using light pressure from a glass slide. The specimen was placed in an environmental chamber with MylarTM windows which was mounted on the goniometer. The chamber was constantly flushed with dry N₂ to prevent oxidation of the specimen. A series of 12 XRPD patterns, in the range of 1–60° 2 θ , were collected using the following settings: 20 mm irradiated specimen length, 0.3 mm receiving slit, 3 s/0.05° 2 θ counting time. The 2 θ range chosen facilitates the determination of both primary particle size, through the diffraction by stacked particles with LAXRPD, and lattice d -spacing and crystalline domain size, through conventional XRPD. Afterwards, the XRPD patterns were carefully checked for temporal variability due to oxidation or ageing during analysis. No significant differences between the 12 patterns were found and therefore they could be summed to give one pattern over the 1–60° 2 θ range with a net counting time of 36 s per step of 0.05° 2 θ . The detection limit of a phase is estimated to be ~1%.

XRPD patterns were corrected for the Lorentz–polarization factor (McEwan et al., 1961) and for the diffracting specimen volume. Peak positions and widths were obtained by fitting Pearson-IV-functions (PEAKFIT 4.0, Jandell[®]). The average diameter of the primary particles of the disordered mackinawite was obtained by either multiplying the LAXRPD peak position by a factor of 1.225 based on the approximation that the particles are hexagonally close-packed or by assuming the particles to be regularly stacked platy particles, that is, no correction factor. The primary particle diameter was taken as the average of the two obtained values.

Additionally, XRPD patterns were collected from a thick (settled and decanted) FeS_{am} suspension quickly loaded in air onto a low background sample holder (silicon wafer), and covered with a 2.5 μ m thick MylarTM foil. A

series of XRPD patterns, in the range of 9–24° 2 θ , were collected from the suspended FeS_{am} using the following settings: 20 mm irradiated specimen length, 0.4 mm receiving slit, 1° antiscatter slit, 30 s/0.1° 2 θ counting time. Blank patterns of a thick calcite suspension loaded on the low background holder were collected with the same settings, and subtracted from the FeS_{am} patterns in order to correct for the interference from water. A conservative estimate of the detection limit is ~5%.

The average diameters of the crystalline domains were determined from the conventional XRPD patterns by applying the Scherrer equation:

$$(3) \quad L = K\lambda (\beta \cos \theta)^{-1}$$

to the (001) peak, where L is the average diameter of the domain, K is the factor 0.91 (Brindley, 1980), λ is the wavelength of the applied X-rays (0.154 nm for CuK α), β is the full width (in radians) at half maximum (FWHM) of the peak, and θ is the angle of the position of the peak.

The specific surface area (SSA) of freeze-dried FeS_{am} was determined in triplicate following the N₂-BET adsorption method, using a MicromeriticsTM Tristar 3000. Approximately 400 mg samples were loaded into the appropriate sample holder, dried for 12 hours at 60°C under gently flowing N₂ and evacuated via the Tristar 3000. The free surface area was measured with He gas prior to N₂-BET adsorption. MicromeriticsTM kaolinite with a specific surface area of 16.2 ± 0.8 m² g⁻¹ was used as a reference standard. In order to compare the measured specific surface area to the bulk solid characterisations, the particle size was estimated from the measured SSA assuming a spherical particle shape and a density of 4.1 g cm⁻³.

3. Results

The initial examination of freeze-dried FeS_{am} was performed using TEM (Figure 2). The FeS_{am} occurs as micrometer-sized aggregates consisting of smaller subparticles. This aggregation resulted from filtration and subsequent freeze drying of an FeS_{am} suspension. The subparticle sizes roughly fall into a range of 20–400 nm diameter, although it was difficult to clearly identify individual subparticles within the aggregates. Calculating the specific surface area based on the minimum particle size yields ~73 m² g⁻¹ and based on the maximum particle size yields ~4 m² g⁻¹ (Table 1). EDX measurements were

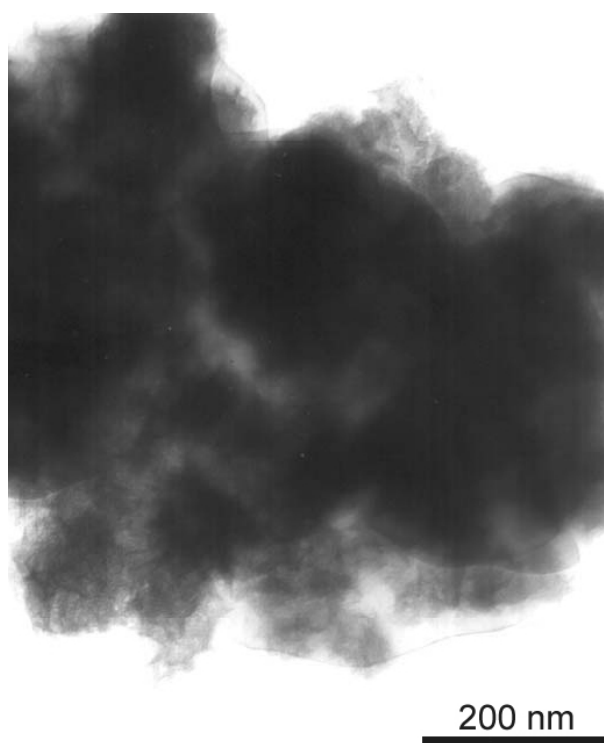


Figure 2. TEM image of freeze-dried FeS_{am}.

Table 1. Particle size and SSA values for freeze-dried FeS_{am} measured and *calculated* (using a density of 4.1 g cm⁻³; approximate values, given in *italic*) from: [1] this study, [2] Widler and Seward (2002), [3] Benning et al (2000), [4] Rickard (1997), [5] Kornicker (1988), [6] Taylor et al. (1979), [7] Rickard (1975). SEM = scanning electron microscopy.

Method	SSA (m ² g ⁻¹)	Diameter (nm)	Reference
TEM	4 – 73	20 – 400	[1]
BET	47 ± 1	31	[1]
LAXRPD	350	4.2 ± 0.2	[1]
BET	80	18	[2]
BET	16 – 21	70 – 90	[3]
XRPD + SEM	40 – 140	10 – 35	[4]
BET	36.5	40	[4]
BET	53.0 ± 46.3	28 (15 – 220)	[5]
BET	7	210	[6]
Microscopy	44	33	[7]

made on several individual FeS_{am} aggregates and yielded an approximate Fe:S ratio of 1, indicating a mackinawite-like composition. No other phases were observed in the TEM analyses. The FeS_{am} aggregates showed weak rings in SAED, confirming the disordered character of FeS_{am}.

In the conventional XRPD pattern from freeze-dried FeS_{am} (Figure 3a, spectrum at an angle $> 10^\circ 2\theta$) the broad peaks are indicative of a disordered phase, with peak intensities and positions in reasonable agreement with previously reported data for mackinawite (Kuovo et al., 1963; Rickard, 1969). At approximately $42^\circ 2\theta$ there is a small contribution from the brass specimen holder. The best fit ($R^2 = 0.994$) to the diffraction pattern was found with a minimum of two peak sets and is given as the smooth curve displayed below the experimental data in Figure 3a. The relevant individual peaks of the fit are also shown in Figure 3a and the crystallographic data extracted from this fit, assuming the conventional tetragonal unit cell for mackinawite, are listed in Table 2. The $50^\circ 2\theta$ peak is rather complex and its fit is omitted from the discussion. However, even though the sensitivity of the fit of this peak is low, and peak assignment is obscure, for the sake of completeness the crystallographic data for the *hkl* reflections in this part of the pattern are listed in Table 2.

The low-angle XRPD pattern (Figure 3a, $< \sim 10^\circ 2\theta$) shows a distinct maximum between $1\text{--}8^\circ 2\theta$ for freeze-dried FeS_{am}. Comparable low-angle reflections were found for different clay particles (Van der Gaast et al., 1985, 1986) and for ferrihydrite particles (Parfitt et al., 1992). The low-angle peak position indicates the average primary particle size. In our pattern, the tail of the peak towards higher angles is caused by a poor stacking of the particles and (or) the grain size distribution. If the FeS_{am} particles are assumed to be hexagonally close-packed spheres, then the LAXRD maximum indicates an average diameter of 4.6 nm (correction factor 1.225). If the FeS_{am} particles are assumed to be regularly stacked platy particles, then the maximum indicates an average diameter of 3.7 nm (no correction factor). Thus, on average, the primary particle size will be 4.2 ± 0.5 nm. Estimation of the specific surface area based on this average primary particle size yields 350 ± 40 m² g⁻¹ (Table 1).

The diffraction patterns collected from *in situ* prepared suspended FeS_{am} (Figures 3b and 3c) show a similar broad (001) peak for precipitated FeS_{am} around $15^\circ 2\theta$ as for freeze-dried FeS_{am} (Figure 3a). In Figure 3b, the

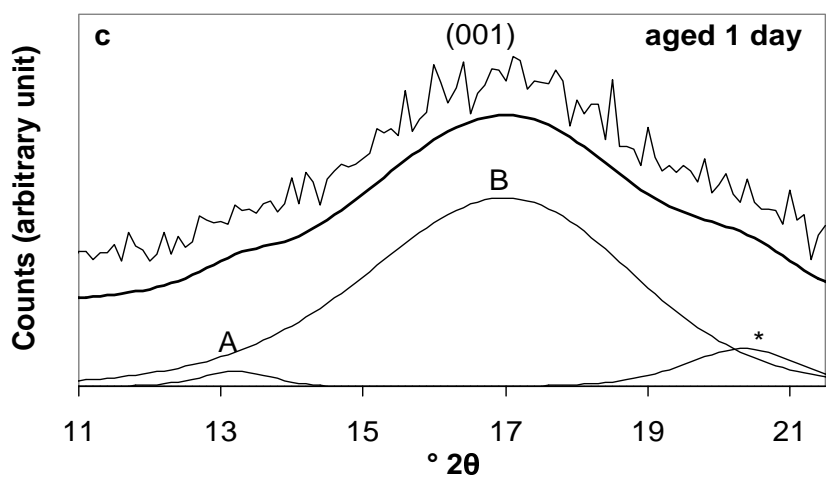
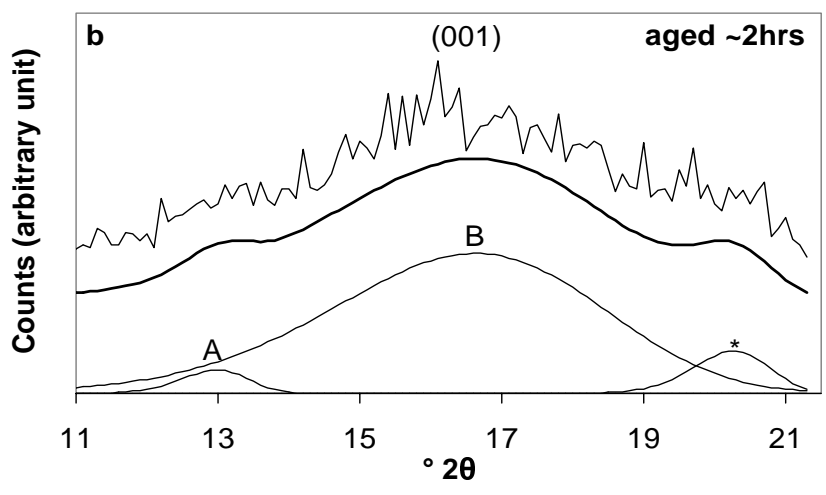
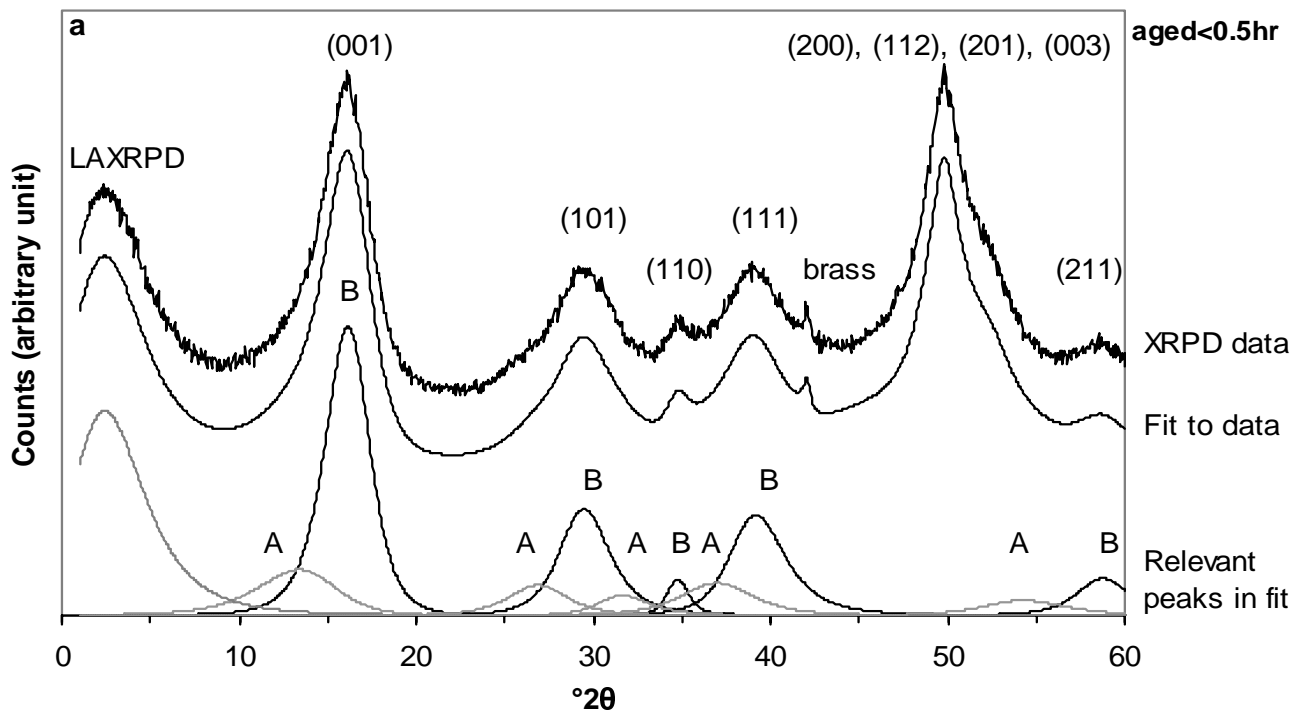


Figure 3 (previous page). Conventional and LAXRPD pattern and the corresponding fit for freeze-dried disordered mackinawite (a). XRPD patterns and fits for a freshly prepared disordered mackinawite suspensions aged for ~ 2 hrs (b) and 1 day (c). Crystallographic data derived from the fits are listed in Tables 2 to 4. A and B in the spectra correspond to disordered mackinawite phases MkA and MkB respectively (see text). * in (b) and (c) is introduced by the (102) calcite d -spacing (see text).

Table 2. Conventional XRPD data for disordered mackinawite from freeze-dried FeS_{am} MkA and MkB (see text) compared with crystalline reference mackinawite (JCPDS 15–0037, Kuovo et al., 1963). The first column gives the hkl planes. For each phase, the d -spacings with the relative intensities (peak surface area) are given.

hkl	Reference Mk		Freeze-dried MkA		Freeze-dried MkB	
	d (nm)	I	d (nm)	I	d (nm)	I
001	0.503	100	0.660	100	0.548	100
101	0.297	80	0.333	51	0.336	41
110	0.260	5	0.284	27	0.258	7
111	0.231	8	0.242	41	0.230	47
200	0.184	40	0.200	35	0.195	10
112	0.181	80	0.188	52	0.183	29
201	0.173	40	0.177	50	0.173	23
003	0.167	20	0.184	44	0.181	30
211	0.156	30	0.163	21	0.157	12

diffraction pattern is shown for suspended FeS_{am} which has been aged for ~ 2 hours; the diffraction pattern depicted in Figure 3c is from 1 day old suspended FeS_{am} . The low signal-to-background ratio permitted the measurement of the most intense (001) peak only. The diffraction patterns were fitted graphically and the best fit ($R^2 = 0.93$ for Figure 3b and $R^2 = 0.95$ for Figure 3c) is given as a smooth curve below the raw patterns together with the individual peaks of the fit. Based on the fit of the freeze-dried FeS_{am} (Figure 3a), the suspended- FeS_{am} patterns were fitted with two peaks as well. The relative contribution of low-amplitude peaks to the total diffracted signal is less in Figures 3b and 3c than in Figure 3a. The third peak in Figures 3b and 3c is an artificial one, introduced by (102) d -spacing of calcite at 23.01° 2θ from the blank pattern after correction. The crystallographical data extracted from this fit are listed in Table 3.

Table 3. X-ray data for disordered mackinawite from the XRPD analyses of ageing suspended FeS_{am} MkA and MkB (see text) compared with freeze-dried FeS_{am} (JCPDS 15–0037, Kuovo et al., 1963). The relative intensities are in % peak surface area of the (001) signal.

	MkA		MkB	
	(001) <i>d</i> (nm)	<i>I</i> (%)	(001) <i>d</i> (nm)	<i>I</i> (%)
Freeze-dried FeS _{am} , <0.5 hr	0.660	22	0.548	78
Suspended FeS _{am} , ~2 hrs	0.68	4	0.53	96
Suspended FeS _{am} , 1 day	0.67	2	0.52	98

Table 4. Lattice parameters for disordered mackinawite from: [1] this study, [2] Mullet et al. (2000), [3] Lennie and Vaughan (1996), [4] Rickard (1969), [5] Kuovo et al. (1963). n.d. = not determined.

	<i>a</i> = <i>b</i> (nm)	<i>c</i> (nm)	Reference
Freeze-dried MkA (<0.5 hr)	0.402	0.660	[1]
Suspended MkA (~2 hrs)	n.d.	0.68	[1]
Suspended MkA (~1 day)	n.d.	0.67	[1]
Freeze-dried MkB (<0.5 hr)	0.365	0.548	[1]
Suspended MkB (~2 hrs)	n.d.	0.53	[1]
Suspended MkB (~1 day)	n.d.	0.52	[1]
Freeze-dried	0.367	0.505	[2]
Vacuum-dried	0.367	0.503	[3]
Suspended	0.368	0.503	[4]
Crystalline	0.368	0.504	[5]

The XRPD patterns collected from the freeze-dried FeS_{am} (Figure 3a) and from the suspended FeS_{am} (Figures 3b and 3c) could be fitted with a minimum of two peak sets, because of a tailing of peaks towards low angles. Such a tailing was also found in patterns of freeze-dried FeS_{am} from other batches, in patterns collected at different instrument settings, and in patterns from both freeze-dried and suspended FeS_{am}. The fact that the patterns could be fitted with a minimum of two peak sets indicates that the material is a mixture of at least two disordered mackinawite phases, referred to as MkA and MkB, with varying *d*-spacing and crystallinity. The low-amplitude peak set of the freeze-dried material (Figure 3a) represents the *d*-spacings for MkA; the high-amplitude peak set in Figure 3a represents the *d*-spacings for MkB. The

relative proportions of MkA and MkB vary with age (Table 3). The unit cell parameters derived from the XRPD patterns are listed in Table 4.

The average dimensions of the crystalline domains were determined from the FWHM values of the (001) and (110) peaks by applying the Scherrer equation (Eq. 3). From the pattern of the freeze-dried MkA phase (Figure 3a), the calculated domain size is 2.2 nm along the a and b crystallographic axes and 1.7 nm along the c axis (that is, 5 by 5 by 3 unit cells in one MkA domain; Figure 4a). For the MkB phase (Figure 3a), the domain sizes is 7.4 nm along the a and b axes and 2.9 nm along the c axis (i.e., 20 by 20 by 5 unit cells in one MkB domain; Figure 4b). For suspended MkA and MkB, only the domain dimensions along the c axis could be established, since only the (001) peak was measured (Figures 3b and c). Due to the low signal-to-background ratio, the FWHM values are not as accurate as for the ones from the freeze-dried material. The domain size here is ~ 2 nm for MkA and ~ 3 nm for MkB.

4. Discussion

4.1. Primary particle size and specific surface area

The primary particle sizes and corresponding specific surface areas (SSA) listed in Table 1, show a large variance. The particle-size range from the TEM imaging is broad owing to the difficulty to distinguish individual particles in the strongly aggregated freeze-dried material. The lower end of the size range is comparable with the particle size calculated from the BET-measured specific surface area ($47 \pm 1 \text{ m}^2 \text{ g}^{-1}$) and with most other reported or calculated diameters. A much smaller size, $4.2 \pm 0.5 \text{ nm}$, yielding a SSA of $350 \pm 40 \text{ m}^2 \text{ g}^{-1}$, was measured by LAXRPD.

This broad range of particle sizes and specific surface area measurements has been determined on, or calculated from, properties of dried and therefore strongly aggregated disordered mackinawite. Kornicker (1988) reported a $53.0 \pm 46.3 \text{ m}^2 \text{ g}^{-1}$ BET surface area for disordered mackinawite and explained the large standard deviation by drying artefacts. Watson et al. (2000) described similar effects of freeze-drying on an iron sulphide mixture, consisting of disordered mackinawite and greigite, formed by sulphate-reducing bacteria. Based on magnetic measurements, they suggested that the material collapsed during the freeze-drying process, forming a porous material

composed of 2–3 nm sized magnetic particles and holes with an average diameter of 2 nm. Watson et al. (2000) found a BET specific surface area of $18.4 \text{ m}^2 \text{ g}^{-1}$ while magnetic properties, neutron scattering and the adsorption isotherms of a number of heavy metals indicated a specific surface area of the order of $400\text{--}500 \text{ m}^2 \text{ g}^{-1}$. They explained this disagreement by inaccessibility of the 2 nm pores towards the N_2 gas they used in the BET adsorption method, resulting in an underestimation of the SSA. In the present study, pure disordered mackinawite may suffer similarly from the freeze-drying process, leading to underestimation of the specific surface area.

Compared to the nanoparticulate iron sulphide mixture from Watson et al. (2000) and other fine-grained amorphous materials, the SSA estimated from the LAXRPD analyses seems the most realistic. Hydrous ferric oxide, for example, reportedly has a SSA ranging from $159\text{--}720 \text{ m}^2 \text{ g}^{-1}$ (see Dzombak and Morel, 1990) and amorphous silica $100\text{--}200 \text{ m}^2 \text{ g}^{-1}$ (Dixit and Van Cappellen, 2002). It is therefore proposed that disordered mackinawite has a specific surface area of the order of $350 \text{ m}^2 \text{ g}^{-1}$ and a corresponding average primary particle size of ~ 4 nm. This is consistent with the suggestion of Rickard and Luther (1997) that a continuum of FeS-sizes down to electroactive FeS(aq) clusters less than 5 nm in size exists. Thus, disordered mackinawite particles are nanoparticles, possibly nanocrystals (section 4.2), according to the definitions of Waychunas (2001).

4.2. Crystal structural properties

The XRPD patterns for freeze-dried and suspended FeS_{am} show that the material is a mixture of at least two phases of different crystallinity (Figure 3, Tables 2 and 3). The pattern for freeze-dried FeS_{am} is dominated by the more crystalline phase, MkB, forming $\sim 78\%$ of the (001) peak. The domain size for MkB extends over 2000 unit cells (Figure 4b). If the crystalline domain is assumed to be spherical, its average diameter is 6.4 nm. Approximately 22% of the (001) peak for freeze-dried FeS_{am} consists of the less crystalline MkA. The MkA domain consists of 75 unit cells (Figure 4a). Approximating the crystalline domain as spherical, its average diameter would be 2.0 nm. If the crystalline domains of MkA are also primary particles, analogous to MkB, then this particle size is equal to the average particle size of 2–3 nm Watson et al.

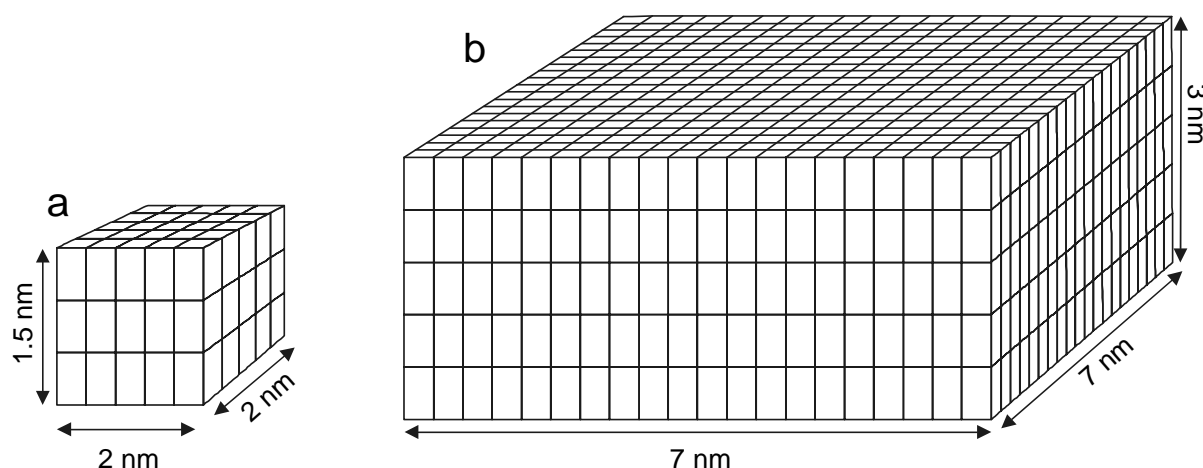


Figure 4. Models for the crystalline domains in disordered mackinawite as discussed in section 4.2. (a) one crystalline MkA domain, consisting of 75 unit cells, and (b) one crystalline MkB domain, consisting of 2000 unit cells. The size of the unit cell is the same for MkA and MkB in this sketch, actual values of the unit cells are listed in Table 4.

(2000) found for their mackinawite–greigite mixture precipitated by SRB's. A mixture of 78% MkB with a (spherical) domain size of 6.4 nm and 22% MkA with 2.0 nm gives an average diameter of 5.4 nm, which is close to the average primary particle size established with LAXRPD. This suggests that each primary particle is one domain and thus a nanocrystal (Waychunas, 2001). In suspended FeS_{am} , the domain size for MkA and MkB ranges from 2 to 3 nm respectively, which is comparable to the domains for freeze-dried disordered mackinawite.

It can be concluded that disordered mackinawite consists of at least two phases of different long-range ordering, the size of MkA domains being smaller to that of MkB domains. It is likely that the FeS_{am} mixture in fact consists of a much larger variety of phases than just two, ranging from FeS_{am} clusters (cf. Rickard and Luther, 1997) and nanoparticulate FeS_{am} to more crystalline mackinawite. Indeed, the XRPD pattern in Figure 3a can be fitted with many more peak sets. Even so, the most simple two-phase model fits the pattern ($R^2 = 0.995$), and describes the crystal structure of disordered mackinawite equally well. In fact, MkA and MkB can be regarded as end-members of a domain size and crystallinity distribution. Precipitated FeS_{am} ripens within days to more crystalline mackinawite (Kornicker, 1988), through aggregation and secondary growth. The decrease of the proportion of MkA with ageing (Table 3) is consistent with this process.

Table 5. Summary of the characteristics of MkA and MkB end-members in precipitated and freeze-dried FeS_{am}.

	MkA	MkB
average crystallite size (nm)	2.0	5.4
surface area (m ² g ⁻¹)	~750	~300
lattice parameters	$a = b = 0.402$	$a = b = 0.365$
	$c = 0.660$	$c = 0.548$
crystallinity (% unit cell expansion)	54%	4%
density (g cm ⁻³)	3.3	4.4

Why can disordered mackinawite be represented by two end-member phases with differing crystallinities? The domain size distribution is consistent with the two competing mechanisms of FeS_{am} precipitation described by Rickard (1995), one involving H₂S (Eq. 1) and the other aqueous HS⁻ (Eq. 2). With HS⁻, the reaction involves the formation of an inner-sphere bisulphide complex, [Fe(HS)·(H₂O)₅]⁺, followed by the condensation of the inner-sphere complex to FeS_{am} according to overall reaction 1. Aqueous H₂S reacts via an outer-sphere complex to form FeS_{am} directly. The relative importance of the two routes is pH-dependent, since the H₂S:HS⁻ ratio is pH-dependent. The pathway involving HS⁻ results in the formation of an intermediate zero-charged Fe(II) sulphide or bisulphide complex. Theberge and Luther (1997) showed that this complex was an FeS(aq) cluster. This intermediate cluster subsequently precipitates as an iron(II) monosulphide. In this experimentation, the pH regime ranged between 6 and 8, where both the H₂S and HS⁻ mechanisms occur. The net result is the direct formation of FeS_{am} via the H₂S mechanism and the formation of FeS(aq) clusters via the HS⁻ mechanism. The presence of two competing pathways for FeS_{am} formation in aqueous solutions is consistent with the observation of two forms of FeS_{am} in this experimentation: MkA being the precipitated clusters (Eq. 2) and MkB resulting from the more rapid direct precipitation route (Eq. 1).

Aqueous metal sulphide cluster complexes have structures similar to the first formed metal sulphide precipitates (Luther et al., 1999, 2001). The structure and stoichiometry of the FeS(aq) cluster (Theberge and Luther, 1997) have not been determined as yet. However, molecular models suggest that it should have a structure similar to mackinawite. FeS(aq) clusters are abundant in experimental (e.g. Theberge and Luther, 1997) and natural systems (e.g.

Rickard et al., 1999; Luther et al., 2001). Freeze-drying itself would act to increase the solution concentrations of the aqueous clusters through loss of water. The size of MkA is consistent with the suggestion that this material may represent sheet-like precipitated $\text{FeS}(\text{aq})$ clusters.

4.3. Lattice spacings

The lattice parameters for disordered mackinawite decrease with age and with drying (Table 4). Freeze-dried FeS_{am} is essentially the first precipitate, since it was filtered and dried immediately after precipitation, thus it has aged for less than half an hour. It showed all strong mackinawite reflections, in keeping with results from Lennie and Vaughan (1996) and Rickard (1969), indicating that the tetrahedral sheets form and start ordering (Figure 1) within one hour after precipitation. Lattice parameters a and b of the freeze-dried MkB fraction are indistinguishable from crystalline mackinawite, although c is slightly larger. For the MkB fraction, c decreases with age towards the crystalline-mackinawite value (Table 4). Freeze-dried MkA has an expanded lattice along the three crystallographical axes relative to crystalline mackinawite. Lattice parameter c of the suspended MkA decreases with age and with freeze drying. Apparently, the controlling factor of this lattice expansion is also influenced by the freeze-drying process.

Expansion along the c axis implies that the tetrahedral sheets lie further apart, while expansion along the a and b axes implies that the tetrahedra within the sheets are either dislocated or distorted relative to crystalline mackinawite (Figure 1). In the past, expansions of the crystalline mackinawite lattice have been explained by excess cation uptake between sulphur–sulphur layers, in tetrahedral coordination with sulphur (Vaughan, 1970). Additionally, Murowchick and Rickard (1997) explained (i) lattice expansions in young synthetic mackinawite, formed from alpha-iron corrosion, by repulsion between the adjacent S–Fe–S layers and (ii) different reflection intensity ratios by tetrahedral sheet offsets. In general, the MkA and MkB lattices can expand relative to the crystalline standard for several reasons. For example, lattice relaxation through expansion or contraction with decreasing nanocrystallite size has been reported (see Waychunas, 2001). Since disordered mackinawite is nanocrystalline, lattice expansion purely caused by small crystallite size affects lattice parameters a , b and c . MkA has a more expanded lattice (Table 5) and a

smaller crystalline domain size, which may support lattice relaxation. Alternatively, lattice parameters can vary owing to lattice defects, substitutions, impurities and (or) hydration. Dang et al. (1998) performed a thorough study of several synthetic tetragonal hematite-like materials and they concluded that these hematites differ from pure bulk hematite in their precise lattice parameters due to incorporated structural water molecules or OH⁻-groups with associated vacancies to balance charge. A similar scenario can be envisaged for disordered mackinawite. Based on Kornicker's (1988) finding that drying changes the physical properties of mackinawite, Morse et al. (1987) concluded that disordered mackinawite may be a hydrate. For example, within the structure of crystalline mackinawite water molecules can partly occupy the cavities enclosed by four tetrahedra (Figure 1); lattice parameter c would then increase with 0.043 nm as is the case for freeze-dried MkB (Table 4). Complete occupation of the cavities and approximately one additional layer of H₂O molecules between the sheets would increase c with 0.16 nm as is the case for freeze-dried MkA. Possibly, some of this "intra sheet" water is expelled during freeze-drying, as a slightly smaller value for c is observed in freeze-dried MkA relative to suspended MkA suggests (Table 4). The variation in lattice parameters found may thus be explained by various amounts of intercalated water. Analogous to the hematite-like materials of Dang et al. (1998), OH⁻-groups might be structurally incorporated as well, if associated with either incorporated protons or cations, or sulphide vacancies to balance local charge deficits. This would have a similar effect on the lattice parameters as intercalated water. Obviously, the observed lattice contraction will proceed, with time, towards water-free crystalline mackinawite as was shown by Kornicker (1988). If the lattice, and thus unit cell, expansion relative to crystalline mackinawite is caused by hydration, then the density of the solid can be estimated. The density of crystalline mackinawite is 4.5 g cm⁻³. The freeze-dried FeS_{am} density calculated from the unit cell expansions and relative contributions of MkA and MkB is 4.1 g cm⁻³. This is similar to the density found by Watson et al. (2000) of 3.9 g cm⁻³ for their mackinawite–greigite mixture.

The XRDP data point to at least two of the explanations for lattice expansion: lattice relaxation is supported by the negative correlation between domain size and lattice expansion, while hydration is supported by the effects of drying on lattice parameter c and the SSA. It is likely that several

explanations apply, since disordered mackinawite originates in the reaction between a hexaquoiron(II) and either a hydrogen sulphide molecule or a bisulphide ion within the milliseconds preceding precipitation (Rickard, 1995). Hydration seems to have the largest effect on the disordered mackinawite lattice. The variation in lattice parameter c indicates that increasing amounts of water are intercalated with decreasing degree of crystallinity. It is proposed, therefore, that disordered mackinawite is a hydrated phase. Future work on the characterisation of disordered mackinawite should include methods to test the possibility of hydration, such as weight loss measurements (DTA/DTG) or infrared spectroscopy.

4.4. Surface reactive sites

At iron sulphide surfaces, two possible functional groups have previously been suggested: an iron(II) hydroxyl functional group, $\equiv\text{FeOH}^0$, and a sulphide functional group, $\equiv\text{SH}^0$ (Kornicker, 1991; Bebié et al., 1998). However, in solutions saturated with respect to FeS_{am} , the aqueous FeSH^+ complex is dominant over the FeOH^+ complex at $\text{pH} < \sim 10$. Thus, the Fe–SH bond is expected to be favoured over Fe–OH bond, i.e. surface hydrolysis of metal atoms is not expected to occur. Analogous to the multi-site complexation model for metal (hydr)oxides (Hiemstra et al., 1996), a model describing the proton affinity of the FeS_{am} reactive surface groups can be developed.

At a local level, the structure of disordered mackinawite is similar to the layered structure of crystalline mackinawite, as shown by the XRPD data. In each layer FeS_4 tetrahedra are linked by edge sharing to four neighbouring tetrahedra and by corner sharing to four neighbouring tetrahedra (Figure 1). The Fe–S distance is 2.230 Å and the S–Fe–S angle is that of a regular tetrahedron, i.e. 109° (Taylor and Finger, 1970). At a terminal edge on the surface of crystalline mackinawite, two types of sulphur atoms are present: terminal S coordinated to only one Fe atom, (FeS), and S coordinated to three Fe atoms, (Fe_3S), as shown in Figure 5. At a hydrated iron(II) sulphide surface in a solution saturated with respect to disordered mackinawite, these two types of sulphur atoms are expected to persist below $\text{pH} \sim 10$. Therefore, it is proposed that the hydrated disordered mackinawite surface can be described by mono- and tri-coordinated sulphur sites as the surface reactive sites rather than the tri-coordinated iron and sulphur sites from a truncated mackinawite lattice.

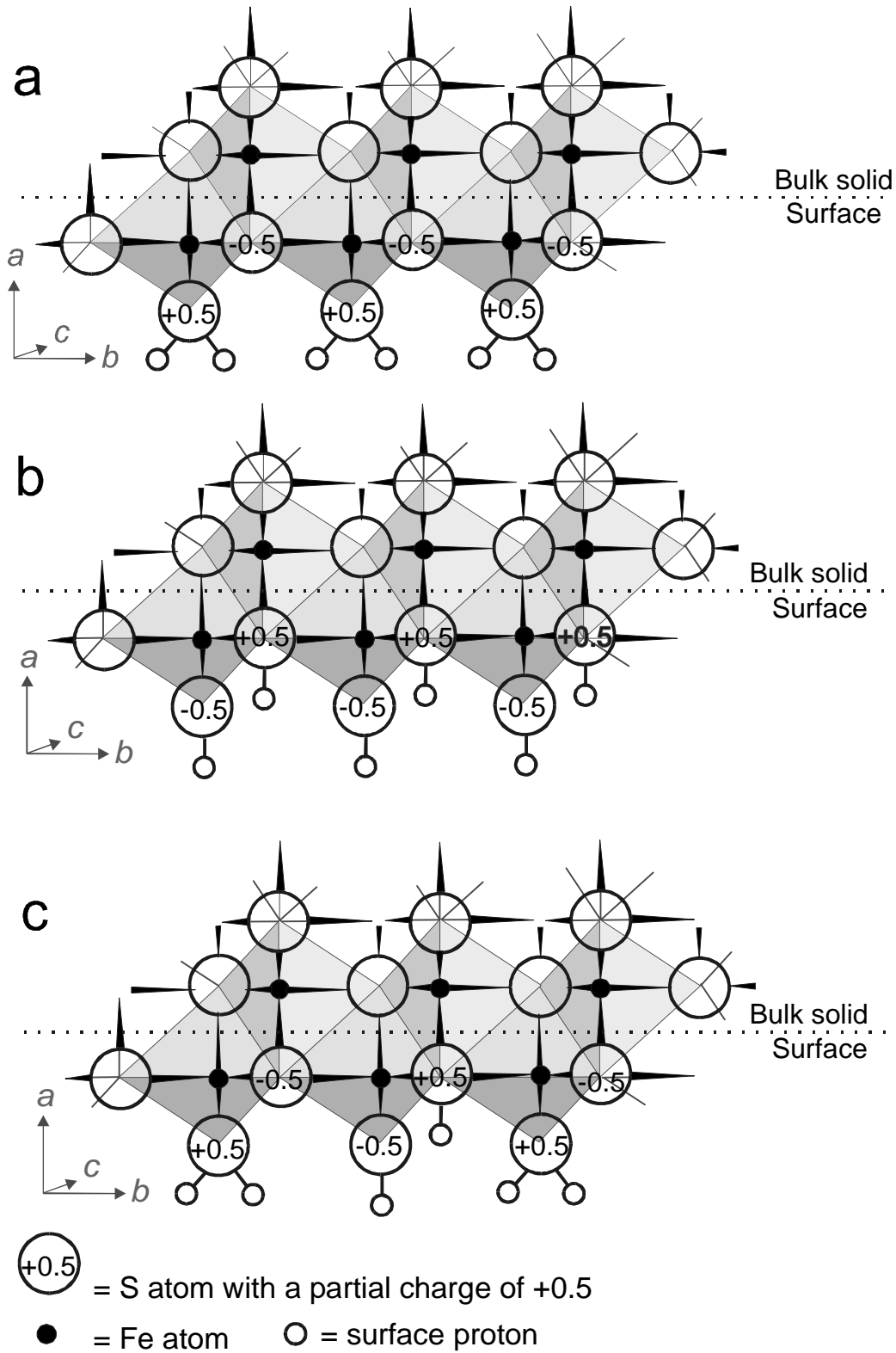


Figure 5. Surface structural model at the point of zero net proton charge. The representation of the sulphide surface is largely notional because relevant detailed surface spectroscopic data to support the presence of these various groups is lacking.

Hiemstra et al. (1996) showed that, for stable ionic solids, the charge distribution over surface groups can be described using Pauling's bond valence theory (1939, 1960), even though the actual charge will deviate from the charge predicted by the bond valence theory. This deviation will be stronger for disordered mackinawite, a solid with dominantly covalent bonds (Pauling, 1970). Nevertheless, Pauling's bond valence theory will be used here to estimate the average charge distribution at the surface of disordered mackinawite. The bond valence is +0.5 for each iron and -0.5 for each sulphur, and thus the terminal mono-coordinated sulphur has a partial charge of -1.5, that is, -2 for the charge of a sulphide ion plus +0.5 for the S-Fe bond. Accordingly, the sulphur atom coordinated to three Fe atoms has a valence charge of -0.5. Upon hydrolysis, the terminal sulphur atoms will be protonated and the point of zero net proton charge (PZNPC) could be represented by two different configurations (Figure 5a and 5b) or a combination of both (Figure 5c). Macroscopically the three configurations in Figure 5 are equivalent.

Hiemstra et al. (1996) have established a microscopic model for the surface of goethite. The goethite structure consists of double chains of edge-sharing octhedra. At the goethite surface, the mono- and tri-coordinated oxygen proton-reactive sites have very different proton affinities (Hiemstra et al., 1996). At low pH ($\text{pH} < \text{PZNPC}$), the surface charge is determined by changes in the speciation of the strong, mono-coordinated surface group, while at high pH changes in the surface charge are governed by speciation changes of the weak, tri-coordinated surface group. Accordingly, the mono- and tri-coordinated sulphur atoms at the disordered mackinawite surface are expected to have very different proton affinities. The mono-coordinated sulphur site is expected to be the strong surface site and determine the acid-base properties of the FeS_{am} at $\text{pH} < \text{PZNPC}$, while at higher pH the weaker, tri-coordinated sulphur is thought to determine the surface charge. The hydrated sulphide surface can thus be represented by a uniform array of strong and weak surface sites with equal concentrations. This does not mean that all strong surface sites or weak surface sites must be microscopically identical, but rather that it is possible to assign macroscopically meaningful average properties to the sites.

The crystal faces present at the surface of the disordered mackinawite will influence the relative concentrations of the two site types. Mackinawite has a platy habit, which is determined by two (001) faces, two (100) and two (010) faces—the latter two are in fact identical—and it is assumed that disordered

mackinawite consists of nano-sized crystals of the same habit. Of the freeze-dried FeS_{am} , 78% is MkB, which consists of $7.4 \times 7.4 \times 2.9$ nm crystals (Figure 4b) with 2 (001) faces consisting of 324 (Fe_4S) surface groups each and 2 (100) and 2 (101) faces with zero (Fe_4S), 90 (Fe_3S), 5 (Fe_2S) and 100 (FeS) surface groups each. The (Fe_4S) are saturated and will not protonate, the (Fe_2S) are insignificant in amount compared to the (Fe_3S) and (FeS) groups. The latter two therefore determine the surface reactivity, as discussed above, and the ratio of the concentrations of these two groups is approximately one to one. The overall reactive-site density is $4.0 \text{ sites nm}^{-2}$, for the reactive (100) and (010) edge faces only it is $9.1 \text{ sites nm}^{-2}$.

Implications for the reactivity of disordered mackinawite

Disordered mackinawite is a major component of the acid volatile sulphide fraction of sediments (Berner, 1970). Scavenging of trace elements by FeS_{am} is an important pathway for removal of these elements from solution in anoxic environments (Kornicker, 1988 ; Morse and Arakaki, 1993; Arakaki and Morse, 1993; Morse and Luther, 1999; Wharton et al., 2000). The structural and surface model presented here shows that disordered mackinawite is nanocrystalline and thus has a very high reactive surface area. It has an expanded lattice, in particular along the *c* axis, with intercalated water molecules between the tetrahedral sheets and possibly intercalated hydroxyl groups with associated protons, cations or sulphide vacancies to balance charge. In such a flexible lattice relatively large amounts of trace elements could be taken up, while at the reactive edge faces more trace elements could adsorb. Our work suggests that the particle size reactivity and surface state of FeS_{am} will depend on its composition in terms of the two end-member disordered mackinawite phases. The properties of the two end-member forms of disordered mackinawite, summarized in Table 5, are significantly different. This means that disordered mackinawite will react differently depending on the proportions of these two end-member forms. The proportion of the two end-member phases depends in turn on the conditions under which FeS_{am} is precipitated and on its age. The master variables determining the reactivity of disordered mackinawite in ambient temperature aqueous solutions are thus pH and time.

The experimental reactivity of FeS_{am} has been observed to vary and this, in turn, is partly explained by the age and preparation conditions of the precipitate. For example, Benning et al. (2000) showed that their freeze-dried FeS_{am} would only form pyrite in the reaction with H_2S if it was oxidised. In contrast, Rickard (1997) showed that freeze-dried FeS_{am} reacts quite readily with H_2S to form pyrite and that the stoichiometry of the reaction precluded O_2 as playing a substantive role. Our results show that freeze-dried FeS_{am} contains varying proportions of 2.0 nm and 6.4 nm particles depending on the formation conditions and the age of the FeS_{am} precipitate when freeze-dried. This will lead to different reactivities as the proportion of the highly reactive 2 nm MKA decreases, for example, with time. These observations may explain the differences in reactivity found in the experimentations described above and in the environment.

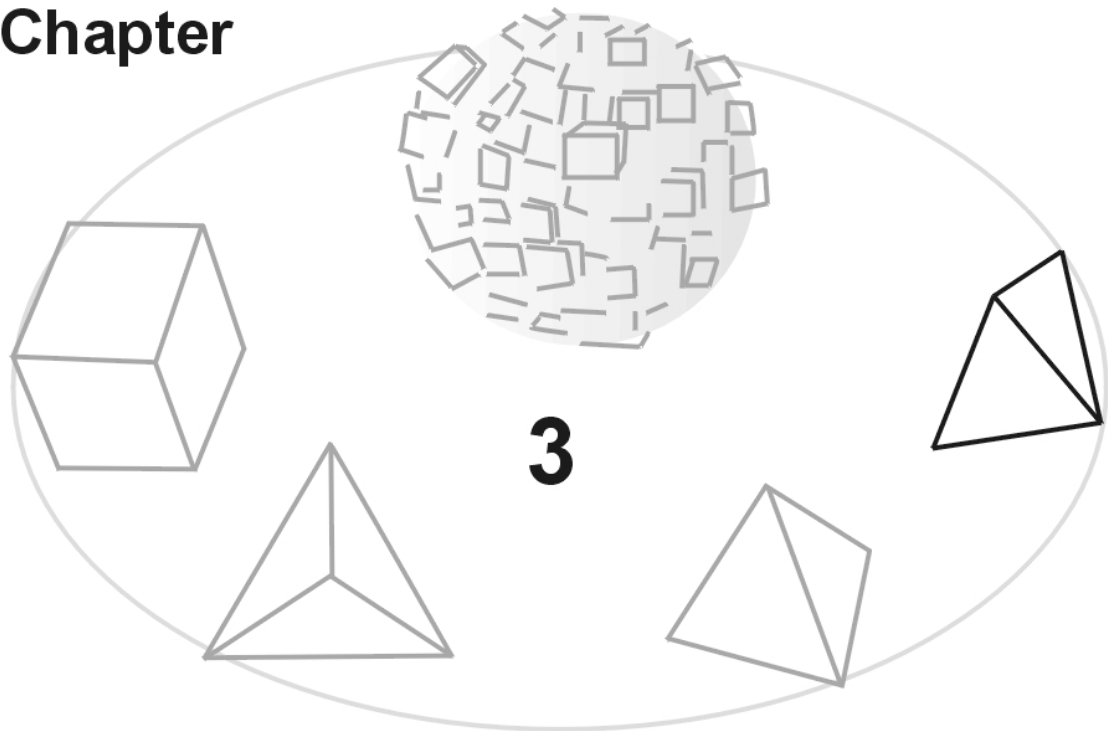
The effect of ageing on the structure of FeS_{am} has been well established. After periods of days to months in aqueous solutions, crystalline mackinawite develops (Rickard, 1969; Kornicker, 1988). The development of crystalline mackinawite is also enhanced at elevated temperatures (Rickard, 1997). Both observations are consistent with the results of this experimentation which demonstrates that ageing results in a decrease of nanoparticulate MKA and a decrease in the degree of hydration of the material. The result of these changes with time and temperature is to decrease the reactivity of FeS_{am} towards oxidation and pyrite formation. It partly explains why mackinawite can last metastably for considerable periods of time in sedimentary environments (e.g. Berner, 1974; Hurtgen et al., 1999) and hydrothermal and magmatic ore deposits (e.g. Kuovo et al., 1963; Evans et al., 1964; Browne and Wood, 1974).

Acknowledgements

We thank Lorenzo Spadini (Grenoble University) for generously sharing data and contributing to the surface structural model discussion. Philippe Van Cappellen and Cornelis H. van der Weijden (Utrecht University) provided insightful discussions over the course of this study. We thank Wim Boer (NIOZ) for performing the BET measurements. This research was supported by the Netherlands Organization of Scientific Research (NWO/ALW grant 750.197.06 to M.W.), by Donder's Chair grant (Utrecht University) to L.C. and

by NERC grant NERLS200000611 to D.R. This research was conducted under the program of the Netherlands Research School of Sedimentary Geology.

Chapter



Surface chemistry of disordered mackinawite^{*}

^{*} To be submitted as: Wolthers M., Charlet L., Van der Linde P.R., Van der Weijden C.H., Rickard D., *Aquatic Geochemistry*.

Abstract

Disordered mackinawite, FeS_{am} , is the first formed iron sulphide in ambient sulphidic environments. Its solubility in the neutral pH-range can be described by $K_s^{\text{app}} = \{\text{Fe}^{2+}\} \cdot \{\text{H}_2\text{S}(\text{aq})\} \cdot \{\text{H}^+\}^{-2} = 10^{+4.87 \pm 0.27}$. Acid–base titrations show that the point of zero charge (PZC) of disordered mackinawite lies at pH ~ 7.5 . The hydrated disordered mackinawite surface can be best described by strong mono-coordinated and weak tri-coordinated sulphurs as the reactive sites. The mono-coordinated sulphur site determines the acid–base properties at $\text{pH} < \text{PZC}$ and has a concentration of 1.2×10^{-3} mol per gram FeS_{am} . At higher pH the tri-coordinated sulphur, which has a concentration of 1.2×10^{-3} mol per gram FeS_{am} as well, determines surface charge changes. Total site density is 4 sites nm^{-2} .

1. Introduction

Disordered mackinawite is a highly reactive phase with a high adsorptive capacity for divalent metals (e.g., Kornicker, 1988; Arakaki and Morse, 1993; Morse and Arakaki, 1993; Wharton et al., 2000). Anoxic marine sediment pore waters are saturated with disordered mackinawite (Berner, 1967; Spadini et al., submitted). It is the first iron sulphide to form in most ambient environments and with time it reacts to form more stable iron sulphide phases such as ordered mackinawite, greigite and ultimately pyrite or pyrrhotite. In this paper, disordered mackinawite is defined as the first precipitated iron(II) monosulphide phase formed through the reaction between aqueous Fe(II) and sulphide under ambient conditions. Lennie and Vaughan (1996) showed that this phase, which is sometimes referred to as “amorphous FeS”, displays long-range mackinawite ordering. Here, this phase is referred to as FeS_{am} .

Fundamental surface properties have not been reported for disordered mackinawite. In fact, experimental characterisation studies of sulphide surfaces are rare in general. Potentiometrically derived point of zero charge (pH_{PZC}) data exist for crystalline iron sulphides (Widler and Seward, 2002), zinc sulphide (Rönngrén et al., 1991), lead sulphide (Sun et al., 1991), arsenic and antimony sulphide (Renders and Seward, 1989). Other studies on the charge

Table 1. Properties of disordered mackinawite(Chapter 2). SSA = specific surface area; average diameter = the average primary particle size, site density = the density of sites at the surface; $[≡FeS]$ = the concentration of mono-coordinated sulphur sites at the surface; $[≡Fe_3S]$ = the concentration of tri-coordinated sulphur sites at the surface.

SSA ($m^2 g^{-1}$)	Average diameter (nm)	Site density (sites nm^{-2})	$[≡FeS]$ ($mmol g^{-1}FeS$)	$[≡Fe_3S]$ ($mmol g^{-1}FeS$)
350	4.2 ± 0.2	4.0	1.2	1.2

development of sulphides have employed electrophoresis or flocculation methods to study the surface charge as a function of pH. Dekkers and Schoonen (1994) and Bebié et al. (1998) employed electrophoresis to study the surface charge as a function of pH. They found that the isoelectrical points for several crystalline metal sulphides lie below pH ~ 3.3 and showed that the sulphide surface was largely dominated by sulphide groups. In Chapter 2, X-ray powder diffraction measurements were used to construct a structure-based model describing FeS_{am} . It was shown that synthetic FeS_{am} displays a disordered tetragonal mackinawite structure and that it is nanocrystalline, with an average primary particle size equivalent to a crystallite size of 4 nm and a corresponding specific surface area of $350 m^2 g^{-1}$ (Table 1). FeS_{am} was described in terms of a mixture of two end-member phases with different long-range ordering, with the relative proportions of the end-members varying with age and, probably, with formation conditions. Lattice expansions of up to 54 vol.% relative to crystalline mackinawite are explained by intercalation of water molecules between the tetrahedral sheets and by lattice relaxation due to small crystallite size. The hydrated FeS_{am} surface can be best described by strong mono-coordinated and weak tri-coordinated sulphurs as the reactive sites (Table 1, Figure 1).

The objective of this study is to describe the experimentally determined surface properties of synthetic FeS_{am} produced by reacting aqueous Fe(II) with aqueous sulphide. The solubility of FeS_{am} in the neutral pH range is addressed and the acid–base properties of the FeS_{am} surface are characterised using potentiometric titrations. Subsequently, a surface complexation model is proposed using the potentiometric titration data in combination with the structural surface model presented in Chapter 2.

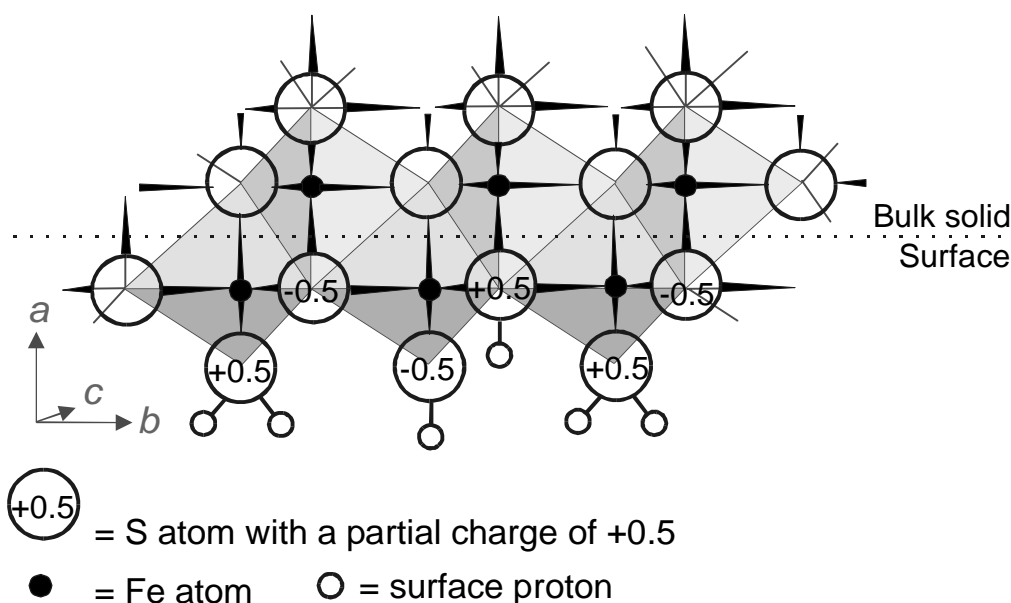


Figure 1. Surface structural model at the point of zero net proton charge, after Chapter 2.

2. Materials and Methods

2.1. Materials

All chemicals were of analytical grade and used without further purification; solutions were prepared from Milli-QTM water and purged for at least 30 minutes with O₂-free N₂ before use. Solutions of S(-II) and Fe(II) were prepared before every experiment by dissolving Na₂S·9H₂O (Fisher ChemicalsTM) and Mohr's salt (Fe(NH₄)₂(SO₄)₂·4H₂O; MerckTM), which is relatively resistant to oxidation, in background electrolyte of varying KNO₃ (Fisher ChemicalsTM) concentration. Because the salts are hydrates, the Fe and S concentrations were checked regularly by ICP-OES analysis, where the Na concentration in the sulphide solution was assumed representative of the sulphide concentration.

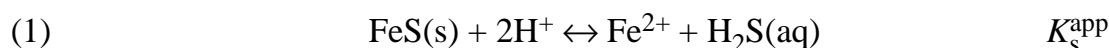
Experiments were run under O₂-free conditions by directly flushing the reaction vessel with N₂, purified by bubbling through a succession of two 15 wt.% pyrogallol in 50 wt.% KOH solutions to remove O₂, a ChrompackTM oxygen and sulphide scrubber for additional cleaning and Milli-QTM water to saturate the N₂ with water vapour. The O₂ concentration in the reaction vessels was below 1×10^{-6} M, which is the detection limit of the OrionTM oxygen probe (850).

Fresh FeS_{am} suspensions for potentiometric titrations were synthesised *in situ* by adding a 1×10^{-3} M S(-II) solution to a 1×10^{-3} M Fe(II) solution in the reaction vessel while constantly flushing with N₂. FeS_{am} formed rapidly and was left to age in the reaction vessel for at least half an hour before the initial pH was set, and one hour before experimentation started. The suspensions were stirred magnetically with a TeflonTM-coated stirring bar.

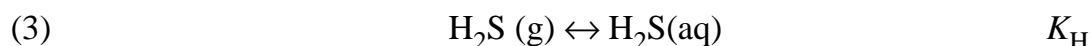
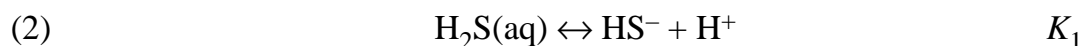
2.2. Solubility

Since the solubility will depend on the method of synthesis (e.g. Davison, 1991) and dissolution of the solid will influence the proton balance determined in the potentiometric titration, the solubility of the synthetic FeS_{am} used in this study needs to be determined. Note that all species are aqueous unless otherwise indicated and that equilibrium is assumed between all solution species and with the solid.

The solubility of FeS_{am} can be expressed by reaction (1):



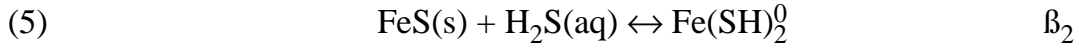
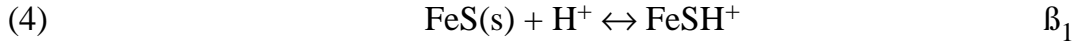
K_s^{app} is the apparent solubility constant at zero ionic strength which is derived from the experimental pH and total dissolved Fe data and compared to the solubility $K_s^* = 10^{+3.98 \pm 0.12}$ from Davison et al. (1999), recalculated from their $K_s^* = \{\text{Fe}^{2+}\} \cdot \{\text{HS}^-\} \cdot \{\text{H}^+\}^{-1} = 10^{-3.00 \pm 0.12}$ by adding $K_1 = \{\text{H}_2\text{S(aq)}\} \cdot \{\text{HS}^-(\text{aq})\}^{-1} \cdot \{\text{H}^+(\text{aq})\}^{-1} = 10^{+6.98}$ (Suleimonov and Seward, 1997). A 1:1 iron to sulphide stoichiometry is assumed based on EDX spectra collected on freeze-dried FeS_{am} particles (Chapter 2). Furthermore, dissolution is assumed to be congruent. The aqueous sulphide chemistry is represented by the following reactions:



where $K_1 = 10^{-6.98}$ (Suleimonov and Seward, 1997) and $K_H = \{\text{H}_2\text{S(aq)}\} P_{\text{H}_2\text{S}}^{-1} = 10^{+0.99}$ (Morel and Hering, 1993) at zero ionic strength. A closed-system equilibrium with respect to hydrogen sulphide gas is assumed. Accordingly, reaction (3) will be ignored in further calculations.

Aqueous iron–sulphide complexation plays an important role in this pH range (Rickard, 1989; Davison, 1991; Luther, 1991; Luther and Ferdelman,

1993; Zhang and Millero, 1994; Rickard, 1995; Luther et al., 1996; Davison et al., 1999). The two most simple complexation reactions reported are:



where $\beta_1 = 10^{+2.05 \pm 0.5}$ (Luther et al., 1996), $\beta_2 = 10^{-3.43 \pm 0.1}$ (Davison et al., 1999). The way reactions (4), (5) and (1) are written simplifies further derivations; no assumptions about the actual reactive species are made. Davison et al. (1999) determined a much lower value for β_1 , i.e. $\beta_1 = 10^{+0.05 \pm 0.1}$. There is still considerable disagreement on aqueous iron–sulphide complexation reactions and their thermodynamic constants, the latter should therefore be treated with caution (Davison et al., 1999). It may be that the iron–sulphide complexation is sensitive to FeS_{am} characteristics, which in turn are sensitive to the preparation method (Davison, 1991). Since in this study FeS_{am} was prepared using the same method as Luther et al. (1996), their higher β_1 value is adopted.

From (1) to (5) the definitions for the activities of the sulphide species and aqueous iron(II)–sulphide complexes can be derived:

$$(6) \quad \{\text{H}_2\text{S(aq)}\} = \frac{K_s^{\text{app}} \{\text{H}^+\}^2}{\{\text{Fe}^{2+}\}}$$

$$(7) \quad \{\text{HS}^-\} = \frac{K_1 \{\text{H}_2\text{S(aq)}\}}{\{\text{H}^+\}} = \frac{K_1 K_s^{\text{app}} \{\text{H}^+\}}{\{\text{Fe}^{2+}\}}$$

$$(8) \quad \{\text{FeSH}^+\} = \beta_1 \{\text{H}^+\}$$

$$(9) \quad \{\text{Fe(SH)}_2^0\} = \beta_2 \{\text{H}_2\text{S(aq)}\} = \frac{\beta_2 K_s^{\text{app}} \{\text{H}^+\}^2}{\{\text{Fe}^{2+}\}}$$

Furthermore, the expressions for total iron (10) and total sulphide (11) in the system are known and it is assumed that the two are equal as a first approximation (12):

$$(10) \quad \text{Fe}_T = [\text{Fe}^{2+}] + [\text{FeSH}^+] + [\text{Fe(SH)}_2^0] + [\text{FeS(s)}]$$

$$(11) \quad \text{S}_T = [\text{HS}^-] + [\text{H}_2\text{S(aq)}] + [\text{FeSH}^+] + 2[\text{Fe(SH)}_2^0] + [\text{FeS(s)}]$$

$$(12) \quad [\text{Fe}^{2+}] = [\text{HS}^-] + [\text{H}_2\text{S(aq)}] + [\text{Fe(SH)}_2^0]$$

Combining (6) to (12), an expression for the Fe(II) activity is obtained as follows:

$$\frac{\{\text{Fe}^{2+}\}}{\gamma_{\text{Fe}}} = \frac{\{\text{H}_2\text{S}(\text{aq})\}}{\gamma_{\text{H}_2\text{S}}} + \frac{\{\text{HS}^-\}}{\gamma_{\text{HS}}} + \frac{\{\text{Fe}(\text{SH})_2^0\}}{\gamma_{\text{Fe}(\text{SH})_2}}$$

$$\frac{\{\text{Fe}^{2+}\}}{\gamma_{\text{Fe}}} = \frac{K_s^{\text{app}} \{\text{H}^+\}^2}{\gamma_{\text{H}_2\text{S}} \{\text{Fe}^{2+}\}} + \frac{K_1 K_s^{\text{app}} \{\text{H}^+\}}{\gamma_{\text{HS}} \{\text{Fe}^{2+}\}} + \frac{\beta_2 K_s^{\text{app}} \{\text{H}^+\}^2}{\gamma_{\text{Fe}(\text{SH})_2} \{\text{Fe}^{2+}\}}$$

$$(13) \quad \{\text{Fe}^{2+}\} = \sqrt{\gamma_{\text{Fe}} K_s^{\text{app}} \left(\frac{\{\text{H}^+\}^2}{\gamma_{\text{H}_2\text{S}}} + \frac{K_1 \{\text{H}^+\}}{\gamma_{\text{HS}}} + \frac{\beta_2 \{\text{H}^+\}^2}{\gamma_{\text{Fe}(\text{SH})_2}} \right)}$$

To compare the experimental solubility to the literature solubility, it is assumed that the total dissolved iron, $[\text{Fe}(\text{aq})_T]$, can be equated by:

$$(14) \quad [\text{Fe}(\text{aq})_T] = [\text{Fe}^{2+}] + [\text{FeSH}^+] + [\text{Fe}(\text{SH})_2^0]$$

Substituting equations (8), (9) and (13) into (14) and taking the literature values for the equilibrium constants, equation (14) can be solved for any pH value. Extrapolation to zero theoretical ionic strength (cf. Davison, 1991) facilitates comparison of the solubility calculated here to the literature solubility; the corrections of the experimental titration data is done with the appropriate activity coefficients. The K_s^{app} was determined by the best fit method, calculated by multiple least-squares estimation and multiple linear correlation; the error in the solubility constant was taken as twice the standard error of estimate.

2.3. Surface characterisations

The aim of the potentiometric titration was to determine the balance of adsorbed and desorbed protons on the surface of the disordered mackinawite as a function of pH, within the pH range of 6 to 8. The FeS_{am} titrations were conducted on *in situ* precipitated FeS_{am} , thus in a background electrolyte solution containing sodium, sulphate and ammonium as well as the 0.005 M, 0.05 M, or 0.1 M KNO_3 ionic medium, giving total ionic strengths of 0.0078 M, 0.053 M, or 0.103 M. The titrations were performed from pH 8 to 6 to prevent back precipitation reactions to occur as pH increases (the FeS_{am} solubility decreases with increasing pH). This would have interfered with the surface acid–base reactions. Afterwards, reversibility of the titrations was

tested by increasing the pH back to 8. The freshly precipitated 0.044 g L^{-1} FeS_{am} suspension was prepared as described above and kept at $23.2 \pm 0.4^\circ\text{C}$. In the course of the titrations, 1 mL samples were taken from the suspension and filtered through $0.2 \mu\text{m}$ AcrodiscTM filter discs. The total dissolved iron in the filtrates was measured spectrophotometrically by the ferrozine method (Viollier et al., 2000) using a UnicamTM UV1 spectrophotometer, to check for mineral dissolution during titrations. Two blank titrations were performed on supernatants which had been collected after filtrating FeS_{am} suspensions at pH 8 or 6 through a $0.2 \mu\text{m}$ MilliporeTM filter. In this way, not only contributions to the surface charge by matrix species is accounted for, but also possible contributions by equilibrium concentrations of Fe(II) and sulphide, which increase with decreasing pH, are taken into account. The pH 8 supernatant was titrated to pH 6 and back to 8; the pH 6 supernatant was titrated to pH 8. No significant difference between the two blanks was found, so for blank corrections the data from the blank titration performed down to pH 6 after filtration of the suspension at pH 8 were used.

The pH of the suspension in the air-tight 500 mL titration cell was controlled via an automated system, consisting of a MetrohmTM 736 GP Titrino for base delivery ($[\text{NaOH}] = 0.01 \text{ M}$) and a MetrohmTM 685 Dosimat for acid delivery ($[\text{HCl}] = 0.1 \text{ M}$) coupled to a PC equipped with TiNet[®] 2.4 software. In order to minimise local OH^- or H^+ excess, acid and base were added at a rate of 0.05 mL min^{-1} . Throughout the experiment, pH was measured using a MetrohmTM 6.0233.100 combined LL pH glass electrode incorporated in the titration cell. Prior to use, the electrode was calibrated in CALITECHTM pH 4, 7 and 10 buffers traceable to NIST (National Institute of Standards and Technology) standards and after use, the electrode was checked for drift in the pH 7 buffer. The drift of the electrode during a run was always less than 0.01 pH unit. The pH of the suspension was adjusted to an initial value of 8 by base addition, before start of the potentiometric titration. Titrations were performed by decreasing the pH to a value of 6 and then back again to a value of 8. After each acid or base addition, the pH reading was allowed to stabilise before the next addition. A potential drift of less than 0.5 mV min^{-1} was used as a criterion for stable readings, or a maximum equilibration time of 30 minutes was allowed if a stable reading was not reached.

The proton balance on the solid surface, Q (in mol per g FeS_{am}), was calculated from the potentiometric acid titration by correcting the total proton

balance in the system ($C_A - C_B$) for all matrix impurities and dissolution of the solid as follows:

$$(15) \quad Q = \frac{C_A - C_B - Q_{\text{blank}} - [H^+]_c}{N}$$

where C_A and C_B are acid and base concentrations added per litre, N is the amount of solid (in $g L^{-1}$). Q_{blank} , in M, is the proton balance as a function of pH derived from the blank potentiometric titration as follows (Stumm, 1991):

$$(16) \quad Q_{\text{blank}} = C_A - C_B + [OH^-] - [H^+]$$

Q_{blank} includes all protolytic components in the matrix such as ammonia and aqueous bisulphide. The H^+ concentration is calculated from the measured pH and $[OH^-] = K_w \{H^+\}^{-1} \gamma_{OH^-}^{-1}$. The term $[H^+]_c$ in equation (15) describes the proton consumption by solid dissolution depending on pH. This correction of Q is necessary because of the high solubility of FeS_{am} , especially towards lower pH values. In order to derive an expression for $[H^+]_c$, a mass balance relating the consumed protons to the produced iron and sulphide species needs to be made (17):

$$(17) \quad [H^+]_c = [HS^-]_p + 2[H_2S(aq)]_p + [FeSH^+]_p + 2[Fe(SH)_2^0]_p$$

For each bisulphide and $FeSH^+$ complex produced during dissolution one proton is consumed; for each $H_2S(aq)$ and $Fe(SH)_2^0$ produced two protons are consumed. Combining mass balances (12) and (17) results in (18):

$$(18) \quad [H^+]_c = [Fe^{2+}] - [Fe^{2+}]_i + [H_2S(aq)] - [H_2S(aq)]_i + [FeSH^+] - [FeSH^+]_i + [Fe(SH)_2^0] - [Fe(SH)_2^0]_i$$

where the suffixes c indicates consumed, p indicates produced by dissolution and i indicates initially in solution, i.e. at pH 8. Converting mass balance (18) to include activities for all species and filling in (6), (8), (9) and (13), an expression for $[H^+]_c$ can be derived as follows:

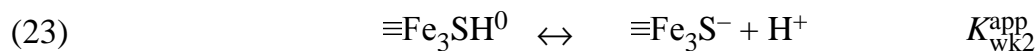
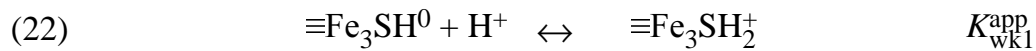
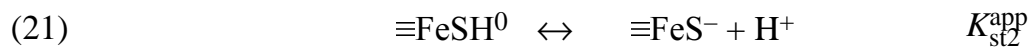
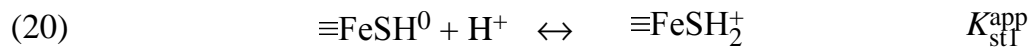
$$(18b) \quad \frac{\{H^+\}_c}{\gamma_H} = \frac{\{Fe^{2+}\}}{\gamma_{Fe}} - \frac{\{Fe^{2+}\}_i}{\gamma_{Fe}} + \frac{\{H_2S(aq)\}}{\gamma_{H_2S}} - \frac{\{H_2S(aq)\}_i}{\gamma_{H_2S}} + \frac{\{FeSH^+\}}{\gamma_{FeSH}} - \frac{\{FeSH^+\}_i}{\gamma_{FeSH}} + \frac{\{Fe(SH)_2^0\}}{\gamma_{Fe(SH)_2}} - \frac{\{Fe(SH)_2^0\}_i}{\gamma_{Fe(SH)_2}}$$

$$(19) \quad [H^+]_c = \sqrt{\frac{K_s^{app}}{\gamma_{Fe}} \left(\frac{\{H^+\}^2}{\gamma_{H_2S}} + \frac{K_1\{H^+\}}{\gamma_{HS}} + \frac{\beta_2\{H^+\}^2}{\gamma_{Fe(SH)_2}} \right) - \frac{\{Fe^{2+}\}_i}{\gamma_{Fe}} + \frac{K_s^{app} \{H^+\}^2}{\gamma_{Fe} K_s^{app} \left(\frac{\{H^+\}^2}{\gamma_{H_2S}} + \frac{K_1\{H^+\}}{\gamma_{HS}} + \frac{\beta_2\{H^+\}^2}{\gamma_{Fe(SH)_2}} \right) - \frac{\{H_2S(aq)\}_i}{\gamma_{H_2S}} + \frac{\beta_1\{H^+\}}{\gamma_{FeSH}} - \frac{\{FeSH^+\}_i}{\gamma_{FeSH}} + \frac{\beta_2 K_s^{app} \{H^+\}^2}{\gamma_{Fe(SH)_2} \sqrt{\gamma_{Fe} K_s^{app} \left(\frac{\{H^+\}^2}{\gamma_{H_2S}} + \frac{K_1\{H^+\}}{\gamma_{HS}} + \frac{\beta_2\{H^+\}^2}{\gamma_{Fe(SH)_2}} \right) - \frac{\{Fe(SH)_2^0\}_i}{\gamma_{Fe(SH)_2}}}}$$

where $\{Fe^{2+}\}_i = 10^{-5.45}$, $\{H_2S(aq)\}_i = 10^{-6.51}$, $\{FeSH^+\}_i = 10^{-5.95}$ and $\{Fe(SH)_2^0\}_i = 10^{-9.9}$. With this expression (19), the amount of protons consumed can be calculated at any pH for all ionic strengths by dissolution of synthetic FeS_{am} . All activity corrections were calculated using the Davies equation. In the pH range of the experiments, the increase in solution species due to dissolution of the solid has a negligible effect on the ionic strength. Thus, the activity coefficients remain constant up to two decimals over the pH ranges of all experiments.

2.4. Surface complexation modelling

According to surface complexation theory, reactions between surface functional groups and solute species control the nonpermanent surface charge and specific adsorption properties of minerals in aqueous solutions (Dzombak and Morel, 1990; Stumm, 1991). The hydrated FeS_{am} surface can be best described by strong mono-coordinated and weak tri-coordinated sulphur sites as the surface reactive sites (Chapter 2). In a first approach, both sites were assumed to protonate and deprotonate according to the following surface protonation reactions:



where $\equiv\text{FeSH}^0$ is the neutral, strongly acidic mono-coordinated surface functional sulphide group which can protonate (reaction 20) and deprotonate (reaction 21) and $\equiv\text{Fe}_3\text{SH}^0$ is a neutral, weakly acidic tri-coordinated sulphur sites which can protonate (reaction 22) and deprotonate (reaction 23). $K_{\text{stf}}^{\text{app}}$, $K_{\text{stf}2}^{\text{app}}$, $K_{\text{wk1}}^{\text{app}}$ and $K_{\text{wk2}}^{\text{app}}$ are the apparent surface acidity constants and are variable model parameters.

A stepwise approach to modelling the surface protonation curve (Q versus pH), derived from the titration data was adopted by considering the simple, chemically reasonable, model given by equations (20) – (23) and finding a best fit by eye to the titration curve. In each step, first the computer program MINEQL+[®] 4.06 was used to calculate the surface speciation from estimated K values for Equations 20 – 23, using the constant capacitance model with a specific capacitance of 1 Fm^{-2} . From the modelled surface speciation the surface charge was calculated as follows:

$$(24) \quad Q_{\text{MINEQL}} = [\equiv\text{FeSH}_2^+] + [\equiv\text{Fe}_3\text{SH}_2^+] - [\equiv\text{FeS}^-] - [\equiv\text{Fe}_3\text{S}^-]$$

and compared to experimental values. Through trial and error a set of apparent surface acidity constants for equations (20) – (23) corresponding to the best fit of the experimental surface charge was obtained.

3. Results

3.1. Solubility

Figure 2 shows the total dissolved Fe(II), $\log[\text{Fe}(\text{aq})_{\text{T}}]$, with pH. The total dissolved iron, including both free and complexed Fe(II), was measured in aliquots taken during the titrations. The total dissolved iron increased with decreasing pH due to dissolution of the solid. Equation (14) is the expression for the total dissolved iron as a function of pH. The dotted line in Figure 2 describes the calculated total dissolved iron as a function of pH if it is assumed that equilibrium is established between all solution species and with the solid, that H_2S degassing is insignificant, that FeS_{am} is stoichiometric and dissolves congruently according to reaction (1) with an apparent solubility constant of $K_s^{\text{app}} = 10^{+3.98 \pm 0.12}$ (Davison et al., 1999). To fit the measured total dissolved iron concentrations, the value for K_s^{app} was varied by trial and error. The best fit

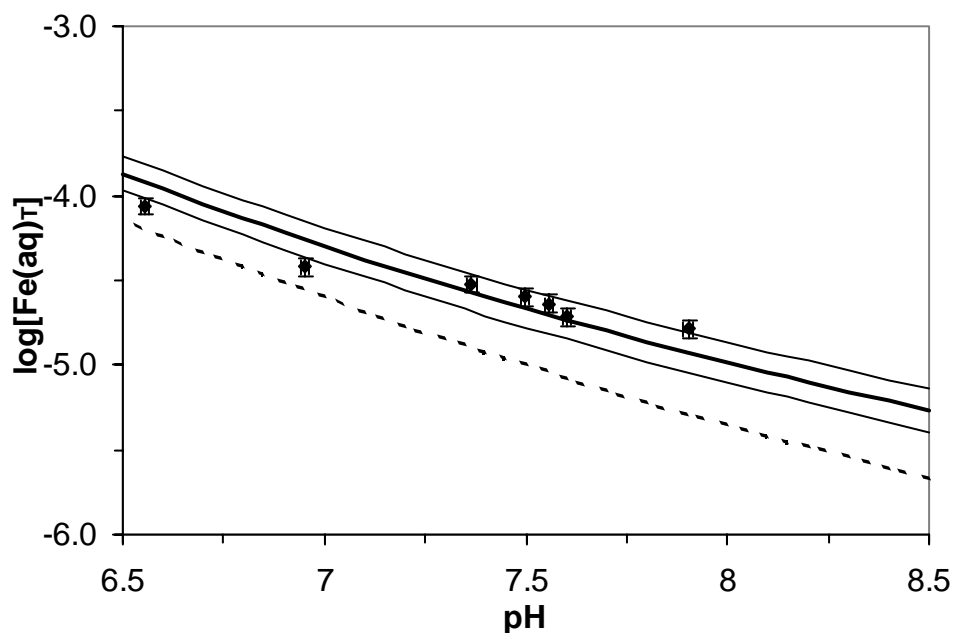


Figure 2. Total dissolved Fe(II), $\log[\text{Fe}(\text{aq})_{\text{T}}]$, plotted versus pH. Filled diamonds are measured values; the dotted line is the predicted total dissolved iron using the solubility $K_{\text{s}}^* = 10^{+3.98}$ (Davison et al., 1999) and the solid lines using $K_{\text{s}}^{\text{app}} = 10^{+4.87 \pm 0.27}$, fitting the $\log[\text{Fe}(\text{aq})_{\text{T}}]$ data with $R^2 = 0.90$ (see sections 2.2 and 3.1).

was found with $K_{\text{s}}^{\text{app}} = 10^{+4.87 \pm 0.27}$, fitting the total dissolved iron data with an R^2 of 0.90, resulting in the band of solid lines in Figure 2. This is higher than the value of $K_{\text{s}}^{\text{app}} = 10^{+3.98 \pm 0.12}$ modified from Davison et al. (1999).

3.2. Potentiometric titrations

The proton balances from the acid–base titrations were calculated through equation (15), that is, they have been corrected for proton consumption by: (i) protolytic components in solution, (ii) the dissociation of water, (iii) solid dissolution using $K_{\text{s}}^{\text{app}} = 10^{+4.87}$ and (iv) aqueous iron–sulphide complexation. Therefore, the surface protonation data, plotted as Q in mmol per gram FeS_{am} versus pH as circle, triangle and square symbols in Figures 3a and 3b, represent the proton balances at the surface of disordered mackinawite at 0.053, 0.0078, or 0.103 M ionic strengths respectively. Since these surface protonation curves have a common inflection point at pH value: 7.5 ± 0.2 , they have been shifted vertically so as to intersect each other and the $Q = 0 \text{ mmol g}^{-1} \text{ FeS}_{\text{am}}$ at the

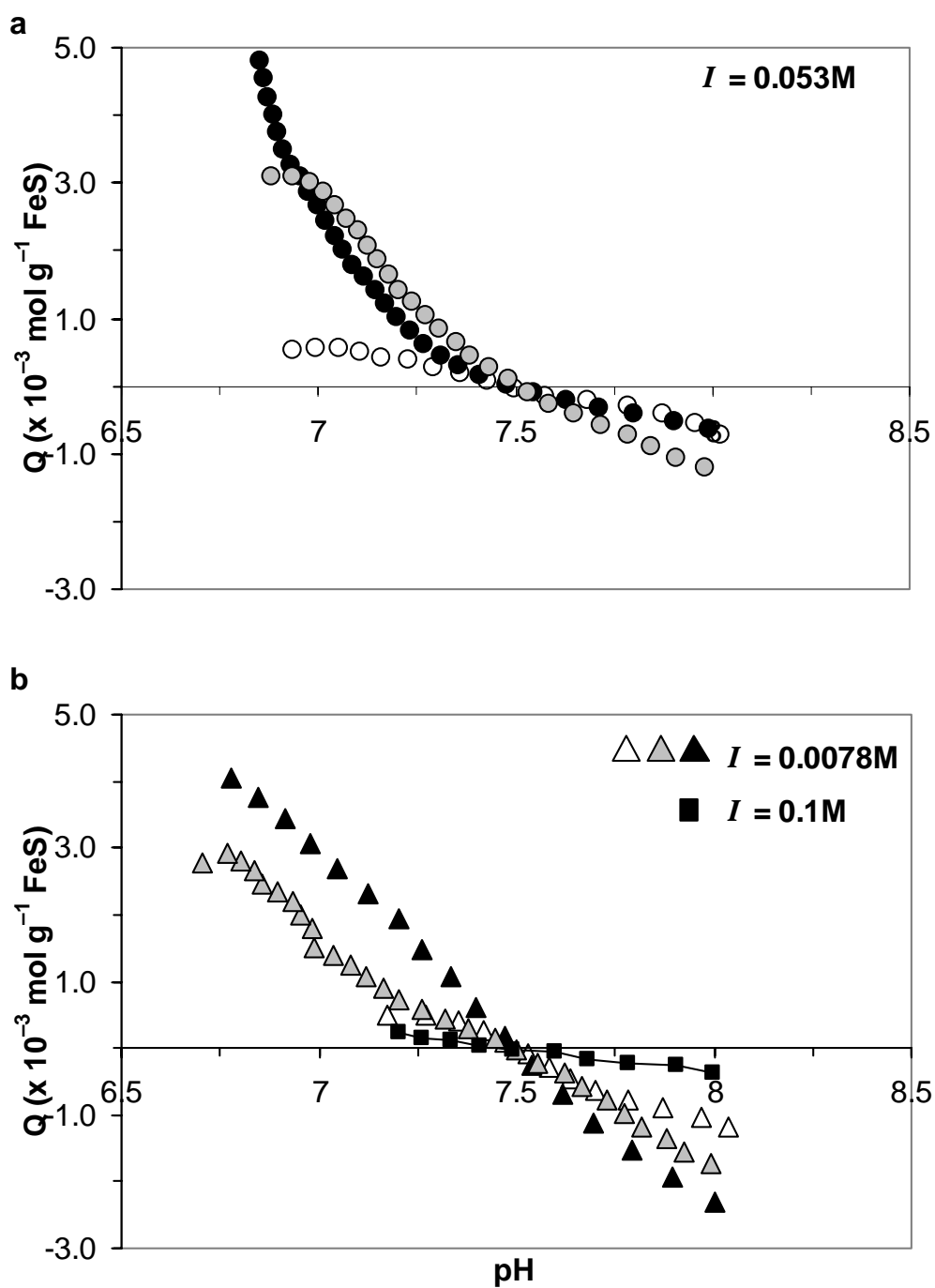


Figure 3. Proton balances from the disordered mackinawite surface titrations: (a) experimental proton balance Q calculated according to equation (2) from the titrations performed at $I = 0.053 \text{ M}$ plotted versus pH; (b) Q calculated from $I = 0.0078 \text{ M}$ (open triangles) and $I = 0.103 \text{ M}$ (filled squares, duplicate experiment plotted as one) titrations versus pH.

Table 2. Model surface protonation reactions and their estimated apparent equilibrium constants derived from the model fit shown in Figure 4a. The surface speciation based on these data is shown in Figure 4b.

Model reactions	LogK
$\equiv\text{FeSH}^0 + \text{H}^+ \leftrightarrow \equiv\text{FeSH}_2^+$	$\text{LogK}_{\text{st1}}^{\text{app}} = +8.0 \pm 0.1$
$\equiv\text{FeSH}^0 \leftrightarrow \equiv\text{FeS}^- + \text{H}^+$	$\text{LogK}_{\text{st2}}^{\text{app}} = -6.5 \pm 0.1$
$\equiv\text{Fe}_3\text{SH}^0 + \text{H}^+ \leftrightarrow \equiv\text{Fe}_3\text{SH}_2^+$	$\text{LogK}_{\text{wk1}}^{\text{app}} = +7.85 \pm 0.05$
$\equiv\text{Fe}_3\text{SH}^0 \leftrightarrow \equiv\text{Fe}_3\text{S}^- + \text{H}^+$	$\text{LogK}_{\text{wk2}}^{\text{app}} = < -9.5$

common inflection point. This common inflection point represents the pH value where the surface has a zero charge (pH_{PZC}). Thus, at $\text{pH} > \sim 7.5$ the surface becomes increasingly negatively charged, approaching saturation at high pH values. At $\text{pH} < \sim 7.5$ the surface becomes increasingly positively charged until the surface approaches saturation at $\text{pH} \approx 6.5$ (Figures 3a and 3b). Significant hysteresis was observed between consecutive acid and base titrations (data not shown); the base titration was shifted as much as 1.5 pH unit higher than the acid titration. For hydrous ferric oxide, similar hysteresis is observed between the acid and base titrations (cf. Dzombak and Morel, 1990).

3.3. Surface complexation modelling

The surface protonation data derived from a titration at 0.053 M ionic strength was fitted with the MINEQL+ model. In Chapter 2, an estimated total reactive-site density of 4.0 sites nm^{-2} and a specific surface area of 350 $\text{m}^2 \text{g}^{-1}$ for disordered mackinawite was proposed. Furthermore, it was estimated that the relative site-density ratio $\equiv\text{FeSH}^0:\equiv\text{Fe}_3\text{SH}^0$ is approximately 1:1. From these data, the concentration of both reactive sites can be calculated: $[\equiv\text{FeSH}^0] = [\equiv\text{Fe}_3\text{SH}^0] \approx 1.2 \text{ mmol g}^{-1} \text{ FeS}_{\text{am}}$. This was used as input into the surface complexation model. The surface speciation as a function of pH was calculated by varying the surface acidity constants for equations (20) – (23). The best fit to the surface protonation curve, shown as a solid line in Figure 4a, was obtained with the surface speciation given in Figure 4b using the apparent surface acidity constants listed in Table 2. Modelling was performed throughout at the actual FeS_{am} concentrations.

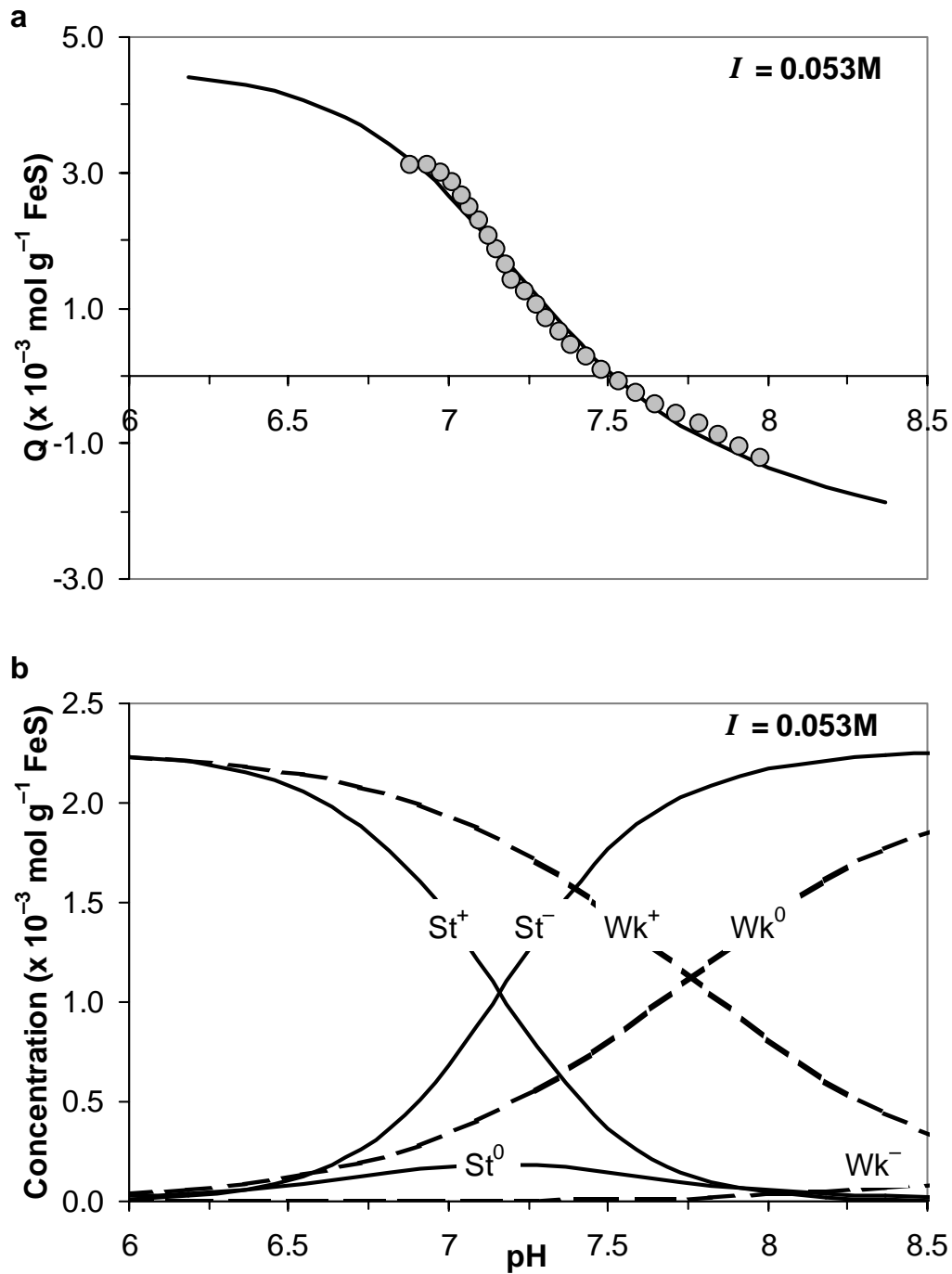


Figure 4. Surface complexation model fit to an experimental proton balance at $I = 0.053 \text{ M}$. (a) experimental Q (open circles) from an $I = 0.053 \text{ M}$ titration fitted with Q_{MINEQL} (solid line) from equation (9); (b) surface speciation calculated in MINEQL+ which sums up to Q_{MINEQL} fitting the experimental data in Figure 4c; $\text{St}^+ = \equiv\text{FeSH}_2^+$; $\text{St}^0 = \equiv\text{FeSH}^0$; $\text{St}^- = \equiv\text{FeS}^-$; $\text{Wk}^+ = \equiv\text{Fe}_3\text{SH}_2^+$; $\text{Wk}^0 = \equiv\text{Fe}_3\text{SH}^0$; $\text{Wk}^- = \equiv\text{Fe}_3\text{S}^-$.

4. Discussion

4.1. Solubility

The solubility of FeS_{am} was determined in order to correct for dissolution effects during the acid–base titrations. The derived apparent solubility constant is $K_s^{\text{app}} = \{\text{Fe}^{2+}\} \cdot \{\text{H}_2\text{S}(\text{aq})\} \cdot \{\text{H}^+\}^{-2} = 10^{+4.87 \pm 0.27}$ (25°C). Benning et al. (2000) noted that the solubility of FeS_{am} in the important neutral and alkaline pH range ($6 > \text{pH} < 8.5$) was poorly constrained and found values for K_s^{app} at 80°C of $10^{+6.55}$ (pH 8.15) and $10^{+7.31}$ (pH 7.39). The divergence observed for K_s^{app} in the present study is, therefore, well within the uncertainty at pH 6–8. Benning et al. (2000) also noted that the variation in their measurements in this pH range suggested that a detailed study of FeS solubility at neutral to alkaline pH was urgently required. Although not a detailed study, the present solubility determination for FeS_{am} is the first to result in a designation of K_s^{app} at neutral to alkaline pH.

The apparent solubility constant derived here is higher than the 20°C solubility constant $K_s^* = 10^{+3.98 \pm 0.12}$ recalculated from Davison et al. (1999; see section 2.2) (Figure 2). Preparation methods have often been named as controlling bulk characteristics as, for example, particle size (cf. Morse et al, 1987; Davison, 1991; Chapter 2) and, consequently, may control FeS_{am} reactivity and solubility. Furthermore, in Chapter 2, it was shown that FeS_{am} may contain structurally incorporated water molecules, a property which is likely to influence solubility.

The total dissolved iron versus pH plots presented here (Figure 2) shows a pH dependence of $\log[\text{Fe}(\text{aq})_{\text{T}}]$ with an approximate average slope of -0.5 when fitted linearly. When reaction (1) controls FeS_{am} solubility in the pH 6–8 range, then the slope in Figure 2 would be -1 , assuming that $\{\text{Fe}^{2+}(\text{aq})\}$ is equal to $\{\text{H}_2\text{S}(\text{aq})\}$. Similarly, when reactions (1) and (2) control FeS_{am} solubility, then the slope is -0.5 . Furthermore, if the complexation reactions (4) or (5) would control FeS_{am} solubility, then the slope would be -1 or -2 , respectively. However, while the average observed slope is -0.5 , a close inspection of Figure 2 shows that the slope tends to level off towards zero with increasing pH. In fact, this change in slope with pH suggests that the aqueous FeS cluster complex forms an important part of the total dissolved iron with

increasing pH, because (i) its formation is pH independent and (ii) its size is too small to allow removal by filtration through the 0.2 μm filter discs used (cf. Chapter 2). Therefore, from Figure 2, it is concluded that the solubility is not simply controlled by one of the reactions (1), (2), (4) or (5), and that the dominant dissolution reaction changes with pH. Determining the dissolution mechanism or the generic solubility product for FeS_{am} in the neutral to alkaline pH range, is beyond the scope of the present thesis. The determined $K_{\text{s}}^{\text{app}}$ allows correction for proton consumption during the potentiometric titration and, thus, serves the present purpose.

4.2. Surface chemistry

4.2.1. Surface charge versus pH

Titration performed with suspensions of *in situ* precipitated stoichiometric iron(II) monosulphide have the advantage of minimising surface oxidation. The conditions can be kept as oxygen free as possible and any treatment such as drying which may alter the surface characteristics is avoided (Herbert et al., 1998; Morse and Arakaki, 1993). The precipitation process results in very small particles, implying a large surface area, which will simulate closely naturally occurring disordered mackinawite. It is expected that titrations performed in solutions with increasing ionic strengths give an increasing slope of the resulting Q versus pH curve (c.f. Dzombak and Morel, 1990). However, the Q versus pH curves in Figures 3a and 3b do not show this trend. The precipitation of FeS_{am} occurs through heterogeneous nucleation followed by growth including lattice contractions. The variability of the titration data may be reflecting this complex stochastic precipitation process.

The trend from the surface protonation curves is nevertheless reproducible, showing an increase in surface charge with decreasing pH and reaching saturation towards high and low pH (Figures 3a and 3b). When only one symmetrical inflection is observed in a solid titration curve, as with hydrous ferric oxide titrations, then the net surface protonation curve represents the protonation of one kind of active surface site. The pH value of this inflection point represents the pH_{PZC} . If the surface charge is solely acquired by proton exchange (protonation and deprotonation), the point of zero charge is pristine and therefore equal to the pH_{PZNPC} (Dzombak and Morel, 1990). The

FeS_{am} surface titrations were performed within a complex solution and adsorption of other potential determining ions cannot be ruled out. Therefore, the common inflection point of the surface protonation curves is referred to as the pH_{PZC}. The surface protonation curves for disordered mackinawite show an asymmetrical inflection around pH ~7.5; this common inflection point is assumed to be the pH_{PZC}. Moreover, in the numerous FeS_{am} syntheses performed during this study (and chapter 4), the supernatant pH was observed to be stable within several minutes after precipitation at a value varying between 7.4 < pH < 7.8. This observation supports a pH_{PZC} ~7.5, given that fresh precipitates tend to drive the supernatant pH towards the pH_{PZC} since a solid with an uncharged surface is the most stable (Stumm et al., 1987; Van Cappellen et al., 1993).

Significant hysteresis was observed between consecutive acid and base titrations; the base titration was shifted as much as 1.5 pH unit higher than the acid titration. For hydrous ferric oxide, similar hysteresis is observed. Sorption and desorption on oxides are governed by two-step kinetics: a fast initial step (minutes) followed by a much slower second step (Dzombak and Morel, 1990). The second step is generally thought to result from exchange within the interior of oxide particles, causing hysteresis between consecutive acid and base titrations. Rapid titrations should therefore be employed, that is, slow enough for the first step to reach equilibrium while fast enough to avoid the second step (c.f. Charlet et al., 1990). Even with fast acid–base titrations, hysteresis is observed. In particular, hysteresis is reported for amorphous oxides where the second step is faster than for more crystalline oxides (Dzombak and Morel, 1990). The fact that similar hysteresis is observed for FeS_{am} suggests that the same two-step kinetics govern the surface protonation and deprotonation reactions. For the acid titration this means that the first step is the rapid surface protonation and the second step a slower diffusion of protons towards the interior of the solid.

Widler and Seward (2002) performed the only previously reported potentiometric titration on the surface of hydrothermally synthesised mackinawite. They obtained a similarly shaped trend with one inflection, shifted to lower pH compared to Figures 3a–c, and they estimated the pH_{PZC} to be 2.9 for crystalline mackinawite from one blank-uncorrected curve. However, no surface deprotonation was found in the base titration, that is, the surface protonation was irreversible, and they observed a surface protonation in zero

ionic strength solutions only. These observations seem to be inconsistent with the data presented here and data for other mineral surfaces. Bebié et al. (1998) performed an electrokinetic study on a range of crystalline metal sulphides, although not on mackinawite, and estimated that the isoelectrical point, the point of zero charge in the shearing plane (Sposito, 1984), for all studied metal sulphides lies below pH 3.3. In general, more alkaline points of zero charge, such as e.g. ~ 8.5 for ZnS from Rönngren et al. (1991), ~ 8.5 for PbS from Sun et al. (1991), ~ 7.7 for CdS from Park and Huang (1987) are thought to be affected by oxidation (Bebié et al., 1998; Widler and Seward, 2002). Although it could be argued that the data reported here must have been affected by oxidation as well, similar discrepancies between proton titration data and electrokinetic data have been reported for other minerals, e.g. silica (Gabriel et al., 2001). Additionally, continuous dissolution of FeS_{am} during the titration renews the FeS_{am} surface while also increasing the S(-II) concentration in solution. The dissolved S(-II) may be more reactive towards O_2 than the FeS_{am} surface and further ensure anoxia. Therefore, it is assumed that the reproducible trends observed and the pH_{PZC} estimated are accurate and unaffected by oxidation.

Features that might affect the pH_{PZC} of disordered mackinawite more strongly than of crystalline mackinawite are proton diffusion and ageing. Proton diffusion from the surface into the solid, e.g. in between the tetrahedral sheets, as indicated by the hysteresis of the acid and base titrations, leads to an overestimated surface charge since the surface explored by protons increases with time (Dzombak and Morel, 1990). Thus, the pH_{PZC} will be shifted to a more alkaline pH due to proton diffusion. Significantly lower pH_{PZC} values were reported for hydrous ferric oxide after long ageing times (Prasad, 1976; Kuo and McNeal, 1984) with the possibility of transformation of hydrous ferric oxide to goethite. Similarly, pH_{PZC} shifts to lower values have been observed for silica surfaces (Foissy and Persello, 1998). The shifts for silica were explained by an increase of surface-site acidity with polymerisation and structuration (Strazhesko et al., 1974; Milonjić, 1987; Foissy and Persello, 1998). Possibly, the acidity of sulphide surface groups increases with crystallinity as well. It is proposed here that the pristine FeS_{am} surface has a $\text{pH}_{\text{PZC}} \sim 7.5$. In natural environments, the FeS_{am} surface charge will further depend on the solution chemistry and cation or ligand adsorption (e.g. Dekkers

Table 3. Recommended surface protonation reactions and estimated apparent equilibrium constants from: [1] this study; [2] Rönngren et al., 1991; [3] Sun et al., 1991.

Reaction	LogK	Reference
$(\equiv\text{FeS})\text{H}^0 + \text{H}^+ \leftrightarrow (\equiv\text{FeS})\text{H}_2^+$	$+8.0 \pm 0.1$	[1]
$(\equiv\text{FeS})\text{H}^0 \leftrightarrow (\equiv\text{FeS})^- + \text{H}^+$	-6.5 ± 0.1	[1]
$(\equiv\text{Fe}_3\text{S})\text{H}^0 + \text{H}^+ \leftrightarrow (\equiv\text{Fe}_3\text{S})\text{H}_2^+$	$+7.85 \pm 0.05$	[1]
$(\equiv\text{Fe}_3\text{S})\text{H}^0 \leftrightarrow (\equiv\text{Fe}_3\text{S})^- + \text{H}^+$	< -9.5	[1]
$\equiv\text{SZn}^0 + 2\text{H}^+ \leftrightarrow \equiv\text{SH}_2^0 + \text{Zn}^{2+}$	9.59 ± 0.03	for synthetic ZnS, [2]
	9.65 ± 0.03	for sphalerite, [2]
$\equiv\text{SZn}^0 + \text{H}_2\text{O} \leftrightarrow \equiv\text{SZnOH}^- + \text{H}^+$	-10.28 ± 0.10	for synthetic ZnS, [2]
	-10.29 ± 0.10	for sphalerite, [2]
$\equiv\text{ZnS}^0 + \text{H}^+ \leftrightarrow \equiv\text{ZnSH}^+$	6.91 ± 0.03	for synthetic ZnS, [2]
	7.14 ± 0.03	for sphalerite, [2]
$\equiv\text{SPb}^0 + 2\text{H}^+ \leftrightarrow \equiv\text{SH}_2^0 + \text{Pb}^{2+}$	9.48 ± 0.027	for synthetic PbS, [3]
	10.21 ± 0.024	for galena, [3]
$\equiv\text{SPb}^0 + \text{H}_2\text{O} \leftrightarrow \equiv\text{SPbOH}^- + \text{H}^+$	-10.0 ± 0.09	for synthetic PbS, [3]
	-10.2 ± 0.09	for galena, [3]
$\equiv\text{PbS}^0 + \text{H}^+ \leftrightarrow \equiv\text{PbSH}^+$	7.11 ± 0.044	for synthetic PbS, [3]
	7.15 ± 0.047	for galena, [3]

and Schoonen, 1994; Bebié et al., 1998). Future work aiming to resolve the existing disagreements on the point of zero charge of metal sulphides should encompass both potentiometric titrations and electrokinetical studies and focus on ageing and exchange effects.

4.2.2. Surface acid–base chemistry

In keeping with the fundamental concepts for all surface complexation models (Dzombak and Morel, 1990), it is assumed that: (i) sorption reactions at the sulphide–water interface takes place at specific coordination sites; (ii) sorption reactions on sulphides can be described quantitatively via mass law equations; (iii) surface charge results from the sorption reactions themselves; and (iv) the effect of surface charge on sorption can be taken into account by applying a correction factor derived from the electric double-layer theory to mass law constants for surface reactions. In the present case, the constant-capacitance

model, a simplified form of the diffuse-layer model, is used to take into account the effect of surface charge on proton sorption.

A model describing the surface protonation with only one type of surface functional group was tested, but provided a poor fit compared to the model with two site types with different proton affinities. It is therefore concluded that the experimental data show the presence of at least two site types. The surface site dominating the larger surface charge change in the pH range 6.5 to ~ 7.5 is expected to be the strong surface site, $\equiv\text{FeSH}^0$, with a high proton affinity, reacting according to equations (20) and (21). There is also evidence for the presence of a second type of site, the weak acid $\equiv\text{Fe}_3\text{SH}^0$, starting to deprotonate (equations 22 and 23) as the slope of the curve flattens above pH ~ 7 . The total concentration of these specific surface sites is $1.2 \text{ mM g}^{-1} \text{ FeS}$ for both the strong and the weak surface sites (calculated from data presented in Chapter 2). The apparent surface acidity constants equations (20) – (23) are interdependent (Table 2). Within a certain range, equally good fits were obtained by simultaneously increasing one apparent surface acidity constant and decreasing another. This interdependence is reflected in the error given for the constants in Table 2.

A limited number of previous studies have described the surface acid–base chemistry of other metal sulphides in terms of surface protonation reactions and surface acidity constants (see Table 3 for a summary). Rönngren et al. (1991) and Sun et al. (1991) constructed comparable models for the surface speciation of zinc and lead sulphides. In their models, the surface is described by: (i) one type of sulphide site, $\equiv\text{ZnS}$ or $\equiv\text{PbS}$, which can take up one proton; (ii) one type of metal site, $\equiv\text{SZn}$ or $\equiv\text{SPb}$, which can hydroxylate; and (iii) an ion exchange reaction where one cation from the solid is exchanged for two protons. They both found the amount of dissolved divalent metal cations to increase linearly with increasing solid concentration. Combined with an observed ratio of adsorbed protons per released cations close to one and a low total dissolved sulphur concentration, this result led them to conclude that the interaction of protons with the hydrous zinc and lead sulphide surfaces involves the desorption of cations. Our data do not support or refute such an ion exchange reaction. However, since the solubility of disordered mackinawite is far higher than of the lead and zinc sulphides they studied, it is expected that congruent dissolution is the dominant iron releasing mechanism.

The value for the surface acidity constant K_{st2}^{app} reported here, $10^{-6.5}$, is comparable with the value found by Rönngren et al. (1991) and Sun et al. (1991) for the same surface protonation reaction on zinc, $10^{-7.0}$, and lead, $10^{-7.1}$, sulphide surfaces (Table 3). The value for K_{wk2}^{app} reported here, $< 10^{-9.5}$, is identical to the value found by Rönngren et al. (1991) and Sun et al. (1991) for the same surface protonation reaction on zinc, $10^{-10.3}$, and lead, $10^{-10.1}$, sulphide surfaces (Table 3). The reactions described by K_1^{app} for the strong and the weak sites have not been observed on zinc and lead sulphide surfaces by Rönngren et al. (1991) and Sun et al. (1991).

4.3. Surface reactive sites

The chemical surface properties of the FeS_{am} suspensions have been described within the framework of the surface complexation model, assuming that the hydrated sulphide surface can be represented by a uniform array of strong and weak surface sites with equal concentrations. This does not mean that all strong surface sites or weak surface sites must be microscopically identical, but rather that it is possible to assign macroscopically meaningful average properties to the sites.

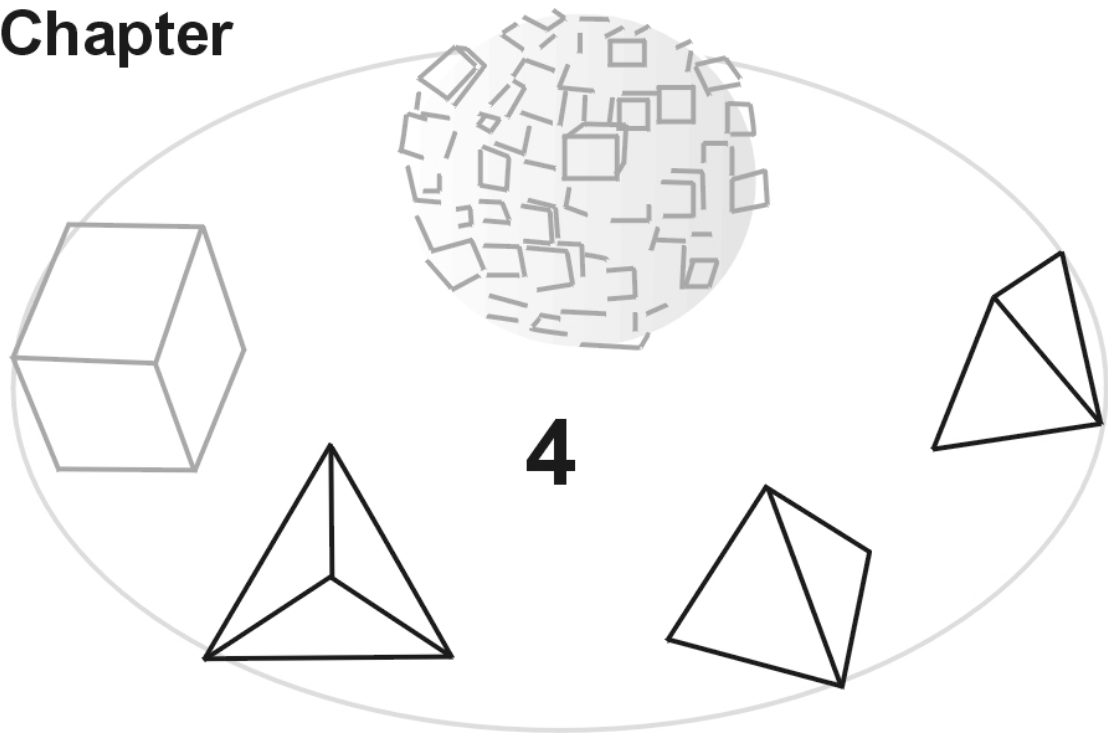
The proposed hypothesis that the hydrated disordered mackinawite surface can be described by mono- and tri-coordinated sulphur sites as the surface reactive sites rather than tri-coordinated iron and sulphur sites (Chapter 2) is confirmed by the presented potentiometric titrations. The asymmetry of the Q versus pH curves (Figure 3) indicates that two sites with different proton affinity control the surface charge. The sketch in Figure 1 is a reasonable representation of the disordered mackinawite surface at pH_{PZC} , showing mono- and tri-coordinated sulphur sites which are, on average, not charged.

Acknowledgements

We thank Lorenzo Spadini (Grenoble University) for generously sharing data and contributing to the surface structural model discussion. Philippe Van Cappellen and Thilo Behrends (Utrecht University) are also gratefully acknowledged for insightful discussions over the course of this study. This research was financially supported by the Netherlands Organization of Scientific Research (NWO/ALW grant 750.197.06 to M.W.), by Donder's

Chair grant (Utrecht University) to L.C. and by NERC grant NERLS200000611 to D.R. This research was conducted under the program of the Netherlands Research School of Sedimentary Geology.

Chapter



Arsenic Mobility in the Ambient Sulphidic Environment: Sorption of Arsenic(V) and Arsenic(III) onto Disordered Mackinawite*

* To be submitted as: Wolthers M., Charlet L., Van der Weijden C.H., Van der Linde P.R., Rickard D., *Geochimica Cosmochimica Acta*.

Abstract

Arsenate, As(V), sorption onto synthetic iron(II) monosulphide, disordered mackinawite (FeS_{am}), is fast. As(V) dominantly forms a monodentate complex at the surface of mackinawite, binding to the protonated mono-coordinated sulphide edge sites. It is not reduced prior to or during sorption. Arsenite, As(III) sorption is not strongly pH-dependent and can be expressed by a Freundlich isotherm. Sorption is fast, although slower than of As(V). As(III) may form a monodentate complex at the surface of mackinawite. Stronger sorption of As(V) than As(III) and thus a higher As(III) mobility may be reflected in natural anoxic sulphidic waters when disordered mackinawite controls arsenic mobility.

1. Introduction

At oxic to anoxic transitions, arsenic is released from reductively dissolving iron hydroxides into the surrounding pore water, groundwater or water body (cf. Smedley and Kinniburgh, 2002). In reducing waters with low sulphide, S(-II), concentrations, arsenic occurs in solutions predominantly as oxyanions of As(V) (Figure 1a) or As(III) (Figure 1b) and as oligomers such as $\text{As}_6\text{O}_6(\text{OH})_6$ and $\text{As}_3\text{O}_3(\text{OH})_3$, the stable As(III) oligomers (Pokrovski et al., 1996; Tossell, 1997). In the presence of high S(-II) concentrations, the dissolved thioarsenite monomers $\text{AsS}(\text{SH})_2^-$ and $\text{AsS}_2(\text{SH})_2^{2-}$ and trimer $\text{As}_3\text{S}_4(\text{SH})_2^-$ may be significant (Helz et al., 1995). While many of the trace metals form insoluble sulphides in sulphide-rich, reducing environments, arsenic is distinctive in being relatively soluble at pH values higher than 5.5, and thus mobile, over a wide range of redox conditions. Hence, a crucial control on the mobility and immobilisation of arsenic is sorption onto particulate phases (Mok and Wai, 1994). In anoxic sulphidic settings, iron(II) sulphides are ubiquitous and are likely to play such a crucial role.

Disordered mackinawite, or FeS_{am} , is thought to be a major component of the acid volatile sulphide fraction of sediments (Berner, 1970, Spadini et al., submitted). It is a precursor phase of pyrite, the most stable and ubiquitous authigenic iron(II) sulphide phase. Scavenging of trace elements by FeS_{am} is an

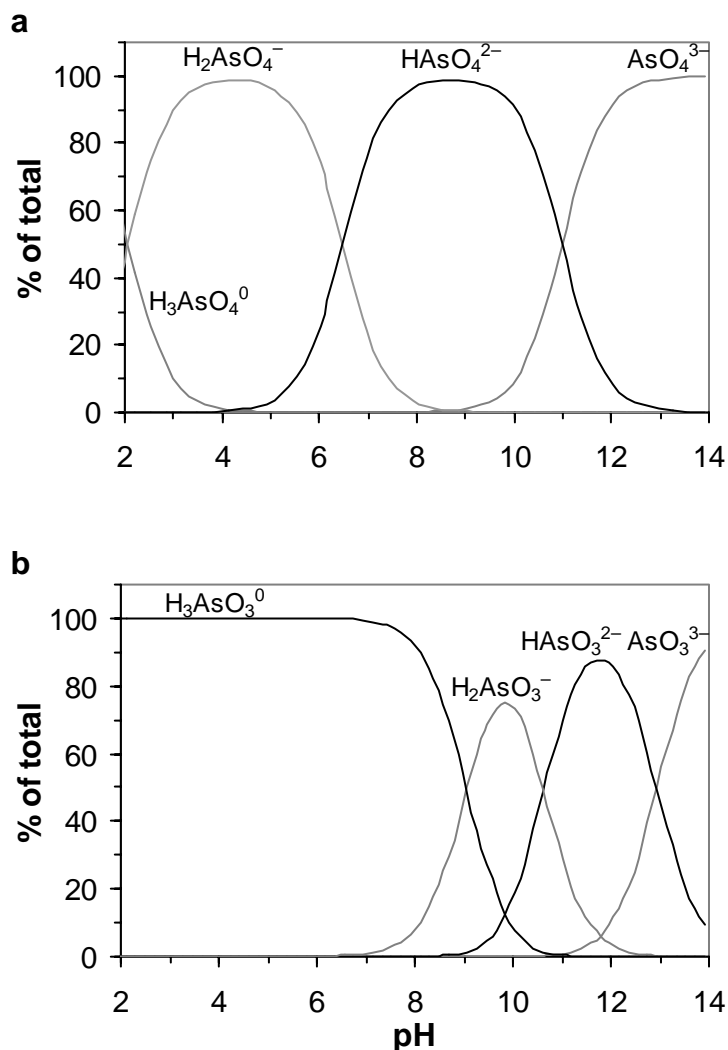


Figure 1. (a) As(V) and (b) As(III) speciation at 0.05 M ionic strength. Thermodynamic constants are taken from Table 1.

important pathway for removal of these elements from solution in anoxic environments (Kornicker, 1988; Morse and Arakaki, 1993; Arakaki and Morse, 1993; Morse and Luther, 1999; Wharton et al., 2000). However, arsenic sorption onto Fe(II) sulphides has not been extensively investigated.

In this chapter, experimentally determined sorption behaviour of As(V) and As(III) onto FeS_{am} is reported. Synthetic FeS_{am} , which was characterised in chapters 2 and 3, was used as a model solid for studying the interaction between aqueous arsenic species and FeS_{am} . The pH-dependence of sorption and the sorption isotherms of As(V) and As(III) were measured. The results are interpreted in terms of the surface complexation model proposed in chapter 3. Additionally, the sorption characteristics and structures are addressed.

Table 1. Aqueous thermodynamic data used in modelling arsenic sorption (I = 0 M; T = 298.15 K). [1] PHREEQC database; [2] Helz et al., 1995; [3] Calculated from Wagman et al., 1982; [3] Eary, 1992.

Hydrolysis reactions	LogK	Reference
$\text{H}_3\text{AsO}_4^0 \leftrightarrow \text{H}_2\text{AsO}_4^- + \text{H}^+$	2.24	[1]
$\text{H}_2\text{AsO}_4^- \leftrightarrow \text{HAsO}_4^{2-} + \text{H}^+$	6.76	[1]
$\text{HAsO}_4^{2-} \leftrightarrow \text{AsO}_4^{3-} + \text{H}^+$	11.60	[1]
$\text{H}_3\text{AsO}_3^0 \leftrightarrow \text{H}_2\text{AsO}_3^- + \text{H}^+$	9.23	[1]
$\text{H}_2\text{AsO}_3^- \leftrightarrow \text{HAsO}_3^{2-} + \text{H}^+$	12.10	[1]
$\text{HAsO}_3^{2-} \leftrightarrow \text{AsO}_3^{3-} + \text{H}^+$	13.41	[1]
Complexation reactions		
$\text{H}_3\text{AsO}_3^0 + 3\text{H}_2\text{S} \leftrightarrow \text{As}(\text{SH})_3^0 + 3\text{H}_2\text{O}$	0.81	[2]
Solubility products		
$\text{As}_2\text{O}_5 + 3\text{H}_2\text{O} \leftrightarrow 2\text{H}_3\text{AsO}_4^0$	6.70	[1]
$\text{As}_2\text{O}_3 + 3\text{H}_2\text{O} \leftrightarrow 2\text{H}_3\text{AsO}_3^0$	-1.79	[1]
$\text{As}_2\text{S}_3(\text{am}) + 6\text{H}_2\text{O} \leftrightarrow 2\text{H}_3\text{AsO}_3^0 + 3\text{H}_2\text{S}$	-11.9	[3]

1.1. Disordered mackinawite properties

Disordered mackinawite refers to the first precipitated iron(II) monosulphide phase formed through the reaction between aqueous Fe(II) or metallic iron and S(-II) under ambient conditions. It is nanocrystalline and displays a disordered tetragonal mackinawite structure (chapter 2). In chapter 2, it was proposed that the hydrated FeS_{am} surface can be described by strong mono-coordinated and weak tri-coordinated sulphur sites as the surface reactive sites. The FeS_{am} solubility in the neutral pH-range could be described by $K_s^{\text{app}} = \{\text{Fe}^{2+}\} \cdot \{\text{H}_2\text{S}(\text{aq})\} \cdot \{\text{H}^+\}^{-2} = 10^{+4.87 \pm 0.27}$ (chapter 3). Furthermore, it was shown with acid–base titrations that the point of zero charge (pH_{PZC}) of FeS_{am} lies at $\text{pH} \sim 7.5$ (chapter 3). The mono-coordinated sulphur sites determine the acid–base properties at $\text{pH} < \text{pH}_{\text{PZC}}$ and have a concentration of $\sim 1.2 \times 10^{-3}$ mol per gram FeS_{am} ; at higher pH, the tri-coordinated sulphur, which has a

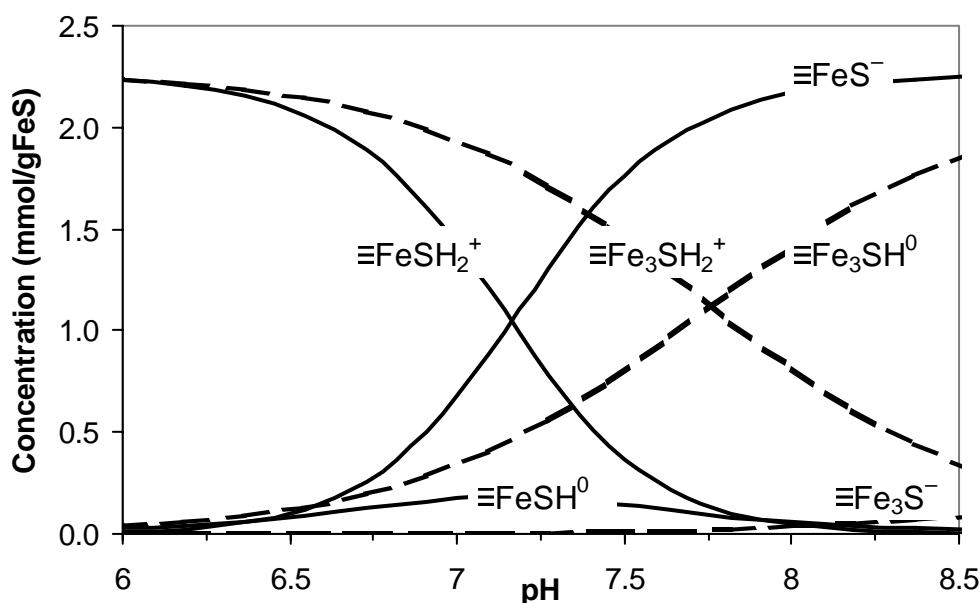


Figure 2. Distribution of species at the hydrated FeS_{am} surface, as predicted by the model proposed in chapter 3 (summarised in Table 2).

concentration of $\sim 1.2 \times 10^{-3}$ mol per gram FeS_{am} as well, determines surface charge changes (Figure 2 and chapters 2 and 3). Total site density is 4.0 sites per square nm (chapter 2).

2. Materials and methods

2.1. Materials

All chemicals were of analytical grade, unless otherwise stated, and used without further purification; solutions were prepared from Milli-QTM water and purged for at least 30 minutes with O_2 -free N_2 before use. The background ionic medium was either 0.05 M KNO_3 (Fisher ChemicalsTM), 3-morpholinopropanesulphonic acid (MOPS, MerckTM) or 2-morpholinoethanesulphonic acid (MES, MerckTM). Preliminary tests showed unambiguously that there was no significant influence of these media on arsenic sorption in the range of experimental conditions used. Fresh stock solutions of As(III) and As(V) were prepared at most five days in advance every week by dissolving $NaAsO_2$ (Fisher ChemicalsTM) and $Na_2HAsO_4 \cdot 7H_2O$ (Fisher ChemicalsTM) in Milli-QTM water or in 0.05 M KNO_3 and checked

daily by ICP-OES or Hydride Generation AAS analysis. For all arsenic solutions the maximum initial As concentration used was at least one order of magnitude less than the solubility limit for $\text{As}_2\text{O}_3(\text{s})$ and $\text{As}_2\text{O}_5(\text{s})$. This condition was chosen to ensure that the starting As solutions were stable.

S(-II) and Fe(II) solutions were prepared before every experiment by dissolving $\text{Na}_2\text{S}\cdot 9\text{H}_2\text{O}$ (Fisher ChemicalsTM) or Mohr's salt ($\text{Fe}(\text{NH}_4)_2(\text{SO}_4)_2\cdot 4\text{H}_2\text{O}$; MerckTM) in the background electrolyte. Because the salt are hydrates, the Fe and S concentrations were checked by ICP-OES analysis, where the Na concentration in the sulphide solution was assumed representative of the S concentration. Experiments were run under O_2 -free conditions by directly flushing the reaction vessel with N_2 gas, which was purified by bubbling through a succession of two 15 wt.% pyrogallol in 50 wt.% KOH solutions to remove O_2 , a ChrompackTM oxygen and sulphide scrubber for additional cleaning and Milli-QTM water to saturate the N_2 with water vapour. The O_2 concentration in the reaction vessels was below 1×10^{-6} M (0.03 ppm), which is the detection limit of the OrionTM O_2 probe (850).

Fresh FeS_{am} was synthesised *in situ* by adding 200 mL of a 1×10^{-3} M S(-II) solution to 200 mL of a 1×10^{-3} M Fe(II) solution in the reaction vessel described in section 2.2 while constantly flushing with O_2 -free N_2 . Disordered mackinawite formed immediately and was left to age in the reaction vessel for one hour before experimentation started.

2.2. Arsenic sorption experiments

Sorption experiments were carried out in duplicate in a 0.05 M ionic strength background electrolyte in four-necked round-bottom flasks. The central neck was used for N_2 purging; O_2 -free N_2 was bubbled through the solution via a Pasteur pipette inserted through a sealed ground-glass joint. The N_2 outflow, via a ground glass connection in the second neck, was led through a washer bottle filled with Milli-QTM water to prevent any O_2 inflow. Purging continued for the entire duration of the experiments. The third and fourth neck were used for temperature and pH monitoring, solution additions and sampling. The suspensions were stirred magnetically with a TeflonTM-coated stirring bar. The temperature in the reaction vessels was not controlled, but never varied more than $\pm 1.5^\circ\text{C}$ during the course of an experiment. Throughout the experiments, pH was measured using an OrionTM Ross combined glass electrode

incorporated in the reaction cell. Prior to use the electrode was calibrated in Calitech™ pH 4, 7 and 10 buffers traceable to NIST (National Institute of Standards and Technology) standards and after use the electrode was checked for drift in the pH 7 buffer. The drift of the electrode during a run was always less than 0.01 pH.

Experiments done in the pH 6–7.5 range were conducted in the 0.05 M MOPS or MES buffer solution to maintain constant pH conditions; experiments in the pH 7–8.5 range were performed in a 0.05 M KNO_3 background ionic medium. The pH of the MOPS and MES buffers was set with 1 M NaOH during preparation of the buffers; the pH of the KNO_3 solution was set to the desired value by small additions of 1 M NaOH or 1 M HCl aliquots after the FeS_{am} suspension had been allowed to equilibrate for one hour. In the overlap of both pH ranges, no difference in experimental results was found showing no significant influence of the MOPS buffer on sorption in the range of experimental conditions used. The concentration of the *in situ* prepared FeS_{am} was 0.5×10^{-3} M, that is $\sim 0.044 \text{ g L}^{-1}$.

The individual pH-dependence experiments were performed for periods of up to six hours; the total As(V) and As(III) concentration was $\sim 3 \times 10^{-5}$ M. Aliquots of the suspension were taken periodically over the course of an experiment; the first aliquot was a blank sample, taken before the arsenic addition. From these experiments the pH-dependence of sorption was established. A stable arsenic concentration in solution was reached within ten minutes for both arsenic species. The sorption isotherms for As(III) and As(V) were measured at pH 7.4. All solutions, including a series of arsenic solutions covering the concentration range required, were freshly prepared before each experiment in a 0.05 M MOPS buffer solution set to pH 7.4. Known amounts of As(III) or As(V) were added to the FeS_{am} suspension and left for half an hour, a time sufficient for the arsenic concentration to stabilise. Aliquots were taken after 30 minutes, before the next arsenic addition. As(V) reduction by FeS_{am} was investigated by acid titrations of FeS_{am} suspensions with arsenic initially sorbed on the surface at pH ~ 7.5 . Subsequently, the pH was lowered to pH 6 by slowly adding 0.1 M HCl solution aliquots, while regularly sampling the suspension.

From the total reaction volume of 400 mL aliquots of 5 mL were taken by pipette and transferred immediately into a syringe for filtration through a $0.45 \mu\text{m}$ pore diameter Acrodisc™ HT Tuffryn filter disc. Subsequently, the

filter membrane was washed with 5 mL 6 M HCl to dissolve FeS_{am} . Sample preparation for analysis was done on the same day as the experiment; the samples were stored at 4°C and analysed within a week.

In order to check for As(III) and As(V) sinks other than FeS_{am} in the set-up, control experiments were conducted without FeS_{am} present. No loss of dissolved arsenic occurred in these control runs. H_2S degassing was negligible over the course of an experiment (Chapter 3). Nevertheless, during experiments at $\text{pH} < 7$, the N_2 outflow from the reaction vessel was bubbled through a concentrated Fe(II) solution. If any $\text{H}_2\text{S}(\text{g})$ bubbled through, the solution would turn black, but no colour was observed.

2.3. Solution analyses

Total dissolved iron in the filtrates was measured spectrophotometrically by the ferrozine method (Viollier et al., 2000) using a UnicamTM UV1 spectrophotometer. Furthermore, samples were routinely analysed for a range of elements including Fe and As concentrations by ICP-OES (Perkin ElmerTM Optima 3000).

Total dissolved arsenic and dissolved As(III) concentrations were determined using a AAS-5100 with a MHS-20 hydride system (Perkin ElmerTM). In the hydride system, only dissolved As(III) is rapidly reduced to arsine, AsH_3 , and analysed. In order to analyse total dissolved arsenic, sample preparation included the reduction of As(V) to As(III). Contrastingly, in the sample preparation for dissolved As(III) analyses, the reduction of As(V) to As(III) was avoided. Thus, depending on the sample preparation before hydride generation, As(III) or total arsenic was determined (Kuhn and Sigg, 1993; Isenbeck-Schröter, 2002). The concentration of As(V) was calculated from the difference between the total As and As(III) concentrations.

The selective determination of As(III) only works in the pH range from 4 to 6 (Kuhn and Sigg, 1993). Therefore, 10 mL samples were mixed with 10 mL of buffer solution to set the pH at 5. The buffer solution consisted of 25 wt.% Citric Acid Monohydrate (MerckTM) and 11 wt.% NaOH in Milli-QTM water (after Kuhn and Sigg, 1993). The calibration solutions were made by a step dilution of a 13.4×10^{-6} M As(III) solution. During the hydride formation, the pH dropped to a minimum of ~ 4 . The pre-reduction step of As(V) to As(III)

Table 2. Summary of site types, site capacities and protolysis constants proposed for FeS_{am} (chapter 3), postulated As(V) surface complexation, and As(III) sorption Freundlich isotherm.

Site types	Site capacities
$\equiv FeSH^0$	1.2 mmol g ⁻¹ FeS_{am}
$\equiv Fe_3SH^0$	1.2 mmol g ⁻¹ FeS_{am}
Surface protonation reactions	logK
$\equiv FeSH^0 + H^+(aq) \leftrightarrow \equiv FeSH_2^+$	$\log K_{st1}^{app} = +8.0 \pm 0.1$
$\equiv FeSH^0 \leftrightarrow \equiv FeS^- + H^+(aq)$	$\log K_{st2}^{app} = -6.5 \pm 0.1$
$\equiv Fe_3SH^0 + H^+(aq) \leftrightarrow \equiv Fe_3SH_2^+$	$\log K_{wk1}^{app} = +7.85 \pm 0.05$
$\equiv Fe_3SH^0 \leftrightarrow \equiv Fe^3S^- + H^+(aq)$	$\log K_{wk2}^{app} < -9.5$
Arsenic sorption	
$\equiv FeSH_2^+ + AsO_3(OH)^{2-} \leftrightarrow \equiv FeS-O-As(OH)_3^-$	$\log K_{ads}^* = +3.2 \pm 0.1$
$[As(III)]_{ads} = 0.074[As(III)]_{aq}^{0.97}$	

required for total As analysis was performed in 15 mL centrifuge tubes (GreinerTM): 10 mL of the sample solution was allowed to react with 3 mL concentrated HCl (MerckTM) and 1 mL of the pre-reducing reagent, a 10 wt.% potassium iodide (MerckTM, suprapur) and 10 wt.% ascorbic acid (MerckTM) in Milli-QTM water (after Kuhn and Sigg, 1993). The calibration solutions were prepared through a step dilution of a 13.4×10^{-6} M As(V) solution. The pre-reduction step was complete within one hour at room temperature. Within the MHS-20 system, the final reduction step of As(III) to arsine prior to analysis was done using a reagent of 0.02 wt.% $NaBH_4$ (FlukaTM) with 0.01 wt.% NaOH (MerckTM); the reducing reagent was stable for two days.

2.4. Surface complexation modelling

The acid–base properties of the FeS_{am} surface can be described by the protonation and deprotonation of two amphoteric site types, the strong $\equiv FeSH^0$ sites and the weak $\equiv Fe_3SH^0$ sites (Table 2, Figure 2; chapter 3). $\equiv FeSH^0$ represents a neutral sulphur functional group coordinated to one bulk-lattice iron and $\equiv Fe_3SH^0$ a neutral tri-coordinated sulphur functional group coordinated to three bulk-lattice irons (chapter 3). In modelling the As sorption data, the basic system parameters applied in chapter 3 were used. This means

that basic surface complexation model parameters such as the site types and protolysis constants are non-adjustable and were all fixed in the subsequent calculations. The uptake of arsenic was computed using MINEQL+[®] (Westall et al., 1976). Modelling was performed throughout at the actual FeS_{am} concentrations using the constant capacitance model with a specific capacitance of 1 F m^{-2} (chapter 3).

3. Results

3.1. Sorption of As(V)

The sorption of As(V) onto disordered mackinawite is strongly dependent on pH (triangles, Figure 3a). With decreasing pH from pH 8.5 sorption first increases strongly, then, below pH 7, a drop in sorption intensity is observed. The scatter in the sorption pH-dependence plot (Figure 3a) can be explained by the variance in specific surface area of the disordered mackinawite over a series of separate experiments (chapter 2). The data were not corrected for FeS_{am} dissolution during the experiments (cf. chapter 3). The strongest sorption, 73% of the total As(V), is found at pH ~ 7.4 where 0.43×10^{-3} mol As(V) sorbed per gram FeS_{am} , or 0.044 mol As per mol suspended FeS_{am} .

The sorption isotherm for As(V), measured at pH 7.5, is depicted as triangles in Figure 3b. Initially, the slope of the isotherm is ~ 1 , however, at higher dissolved As(V) concentrations it levels off. The isotherm can be described as a Langmuir isotherm (Dzombak and Morel, 1990). Figure 3c shows an example of a sorption rate experiment. Within ten minutes after As(V) addition, the amount of arsenic in solution has decreased and stabilised, indicating a rapid sorption reaction. As(V) sorption was found to be associated with a slight increase of pH; no significant change in total dissolved iron was observed with As(V) sorption. No increase in As(III) concentration in either the solution or the solid extract was measured, suggesting insignificant As(V) reduction.

The solid line plotted in Figure 3a represents the pH-dependent concentration of $\equiv\text{FeSH}_2^+$ surface species from the surface model for disordered mackinawite proposed in chapter 3. This curve predicts both the pH-dependent

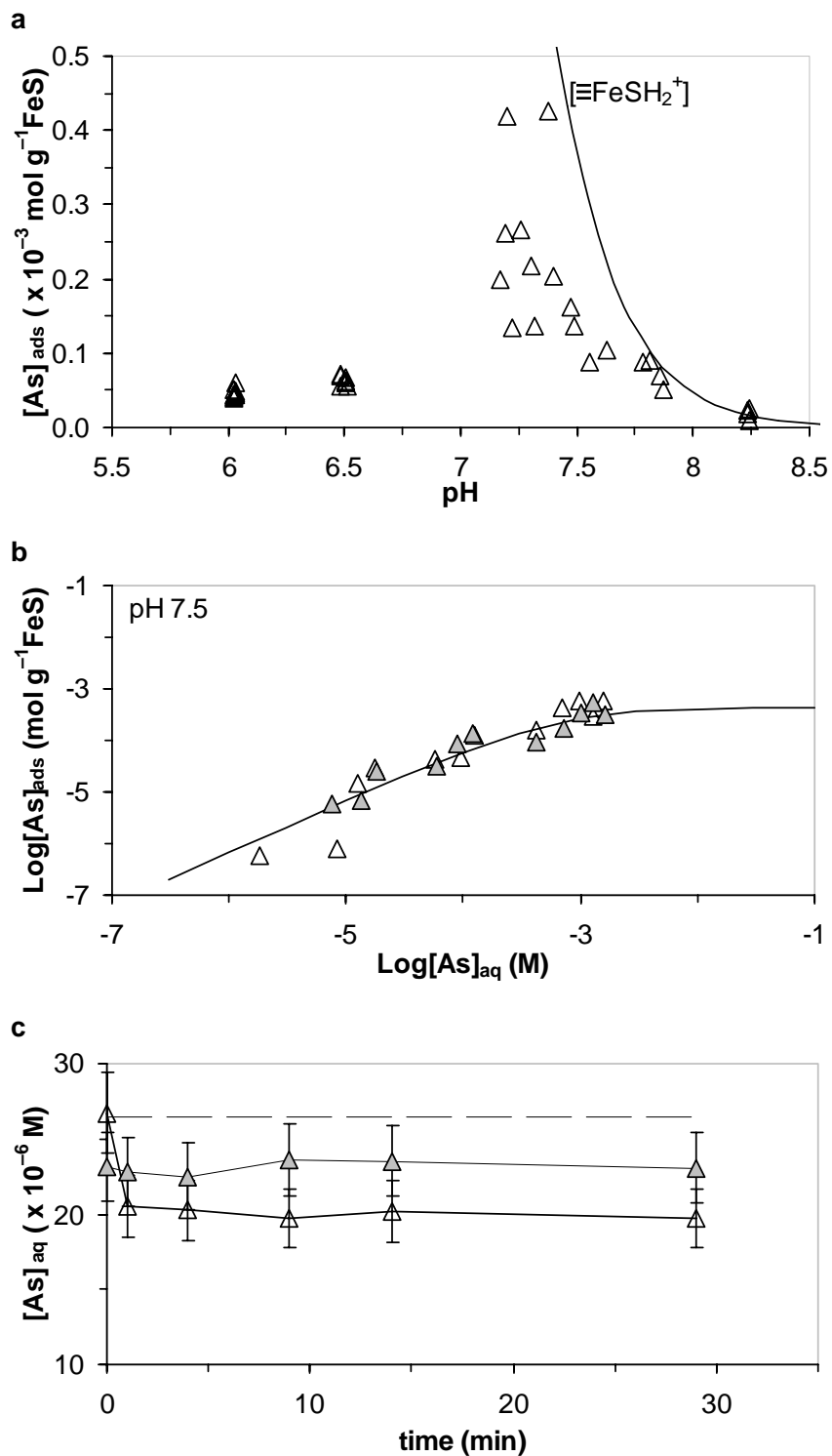


Figure 3. As(V) sorption data, $[\text{FeS}_{\text{am}}] = 5 \times 10^{-4} \text{ M}$ and $[\text{As}]_{\text{tot}} \approx 3 \times 10^{-5} \text{ M}$; (a) experimental data showing the pH-dependence of sorption. Full line is model curve for linear sorption onto $\equiv\text{FeSH}_2^+$ surface species; (b) sorption isotherm at pH 7.5, experimental data (open and filled triangles are duplicate experiments) and model curve according to reaction (1) (full line); (c) example of the first 30 minutes after As(V) addition (dashed line) in a duplicate experiment (open and filled triangles), pH varied from 7.8 to 7.4. In all cases, the suspension contained $0.044 \text{ g FeS}_{\text{am}} \text{ L}^{-1}$.

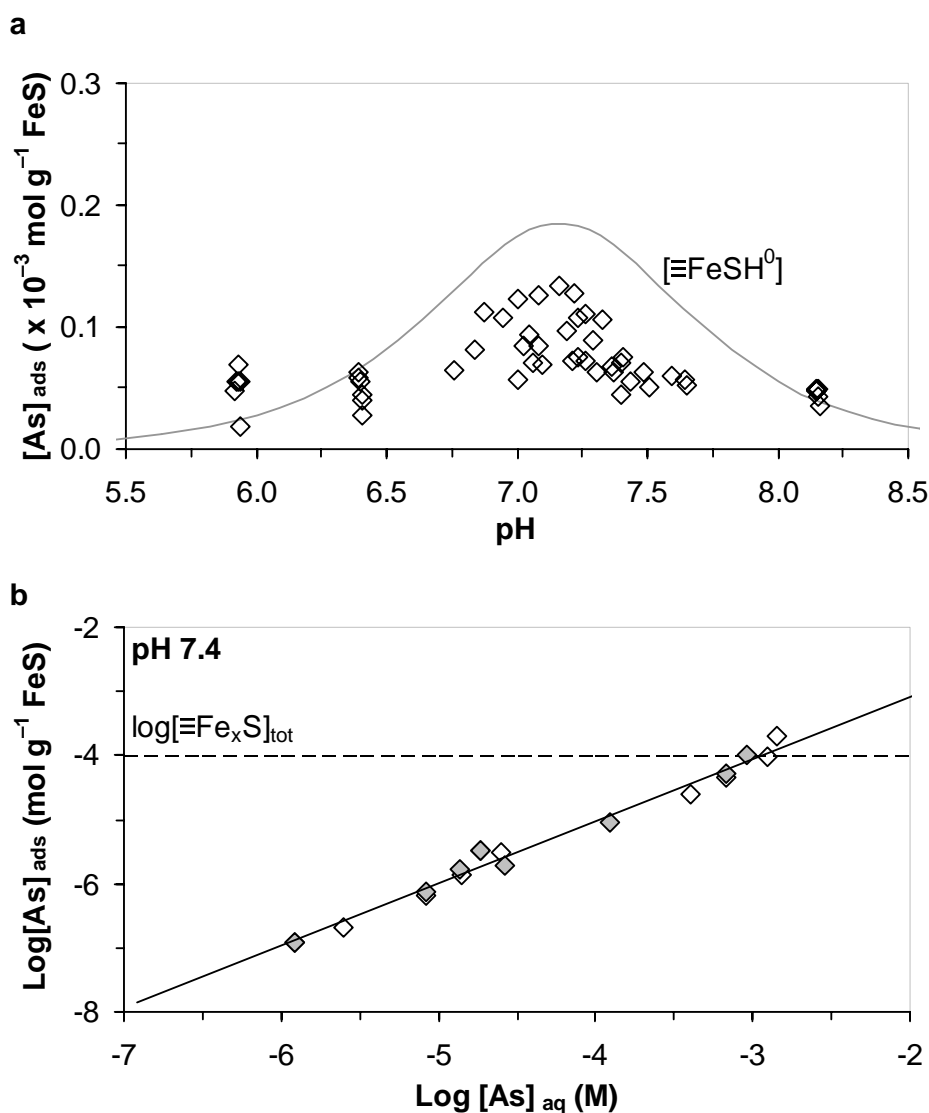


Figure 4. As(III) sorption data, $[FeS_{am}] = 5 \times 10^{-4} \text{ M}$ and $[As]_{tot} \approx 3 \times 10^{-5} \text{ M}$. (a) experimental data showing the pH-dependence of sorption. Dashed line is model curve of $\equiv FeSH^0$ surface species concentration. (b) sorption isotherm at pH 7.4, experimental data (open and filled diamonds are duplicates), the Freundlich isotherm fit according to equation (2) (solid line) and the total concentration of mono- and three-coordinated surface sites $[\equiv Fe_xS]_{tot}$ (horizontal dashed line). In all cases, the suspension contained $0.044 \text{ g FeS L}^{-1}$.

trend of sorption at $\text{pH} > 7$ (Figure 3a) and the Langmuir sorption isotherm (Figure 3b) for As(V) reasonably well. It is important to note that the surface speciation and the protolysis constants (Table 2) are derived solely from potentiometric titration data resulting from the surface protonation as a response to shifts in the pH (chapter 3). Thus, the As(V) sorption pH-

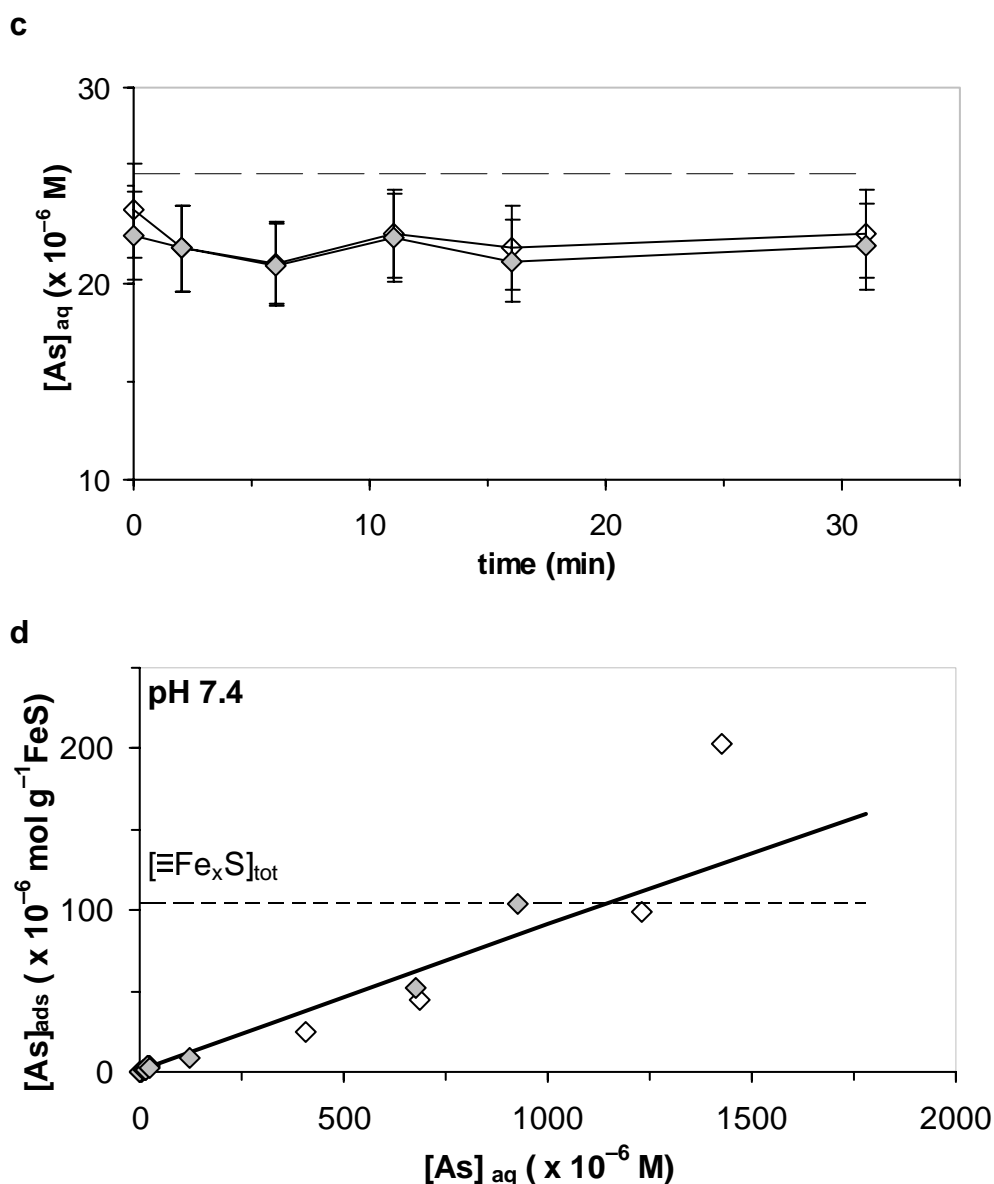


Figure 4 (continued). As(III) sorption data, $[FeS_{am}] = 5 \times 10^{-4}$ M and $[As]_{tot} \approx 3 \times 10^{-5}$ M. (c) example of the first 30 minutes after As(III) addition (dashed line) in a duplicate experiment (open and filled triangles), pH varied from 6.9 to 7.3; (d) non-logarithmic Freundlich isotherm fit to the dissolved arsenite data. In all cases, the suspension contained 0.044 g FeS L^{-1} .

dependence and isotherm, determined from the dissolved As measurements in the filtered supernatant samples, provide independent data to test the proposed surface complexation model suggested in chapter 3. As shown in Figures 3a and 3b, the model correctly predicts the measured sorption edge and isotherm.

3.2. Sorption of As(III)

The sorption of the neutral As(III) complex onto disordered mackinawite is not as strongly pH-dependent as anionic As(V) sorption (diamonds in Figure 4a). There is a weak sorption maximum at pH ~ 7.2 . The data were not corrected for FeS_{am} dissolution during the experiments (cf. chapter 3). The bell shaped curve plotted in Figure 4a (dotted line) represents the concentration of the neutral $\equiv\text{FeSH}^0$ sites, as proposed in the surface model in chapter 3. Similarly to the As(V) data, the scatter in the sorption pH-dependence plot (Figure 4a) can be explained by the variance in the specific surface area of the disordered mackinawite over separate experiments (chapter 2). The strongest sorption, $\sim 23\%$ of the total As(III), is found at pH ~ 7.2 where 0.13×10^{-3} mol As sorbs per gram suspended FeS_{am} , or 0.012 mol As(III) per mol FeS_{am} .

The sorption isotherm for As(III) (diamonds in Figure 4b) at pH 7.4 shows linear sorption. All of the predicted specific surface sites (dashed line in Figure 4b) would be saturated before the highest levels of sorbed As(III) in the isotherm experiment were reached. Figure 4c shows an example of a sorption rate experiment. Within ten minutes after As(III) addition, the amount of arsenic in solution has decreased and stabilised, indicating a rapid sorption reaction. As(III) sorption was found to be associated with a slight increase of pH. No change in total dissolved iron was observed with As(III) sorption, nor was an increase in As(V) concentration in the solution or the solid extract measured.

4. Discussion

4.1. As(V)

4.1.1. pH-dependence of As(V) sorption

Within the experimental pH range, the dominant As(V) species are the negatively charged H_2AsO_4^- and HAsO_4^{2-} (Figure 1a). Generally, sorption of anions is strongest at low pH and gradually decreases as pH increases. For As(V) sorption onto FeS_{am} , such an increase in sorption with decreasing pH is

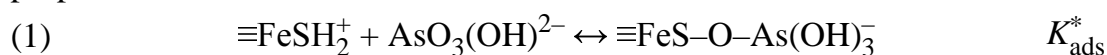
observed initially. However, below pH 7, a decrease in sorption is observed to coincide with an increase in dissolved iron concentration. The solubility of FeS_{am} increases rapidly with decreasing pH (cf. chapter 3). This is supported in the sorption experiments by an increase in total dissolved iron concentration with decreasing pH. Therefore, the unusual drop in As(V) sorption intensity with decreasing pH can be explained by dissolution of the sorbent. Similarly, Widler and Seward (2002), who studied the sorption of the gold(I) hydrosulphide complex $AuHS^0$ onto several iron(II) sulphides, observed a decrease in gold sorption onto crystalline mackinawite and a simultaneous increase of dissolved iron concentration due to solid dissolution at low pH. Thus, the sorption data at $pH < 7$ can be ignored in the discussion.

If As(V) sorption is governed by the presence of a specific surface functional group, then the $\equiv FeSH_2^+$ site is the surface group which describes the pH-dependence of As(V) sorption most suitably of all possible groups (Figure 2), as is illustrated by the solid line in Figure 3a. This suggests that $\equiv FeSH_2^+$ is the As(V) binding site. Farquhar et al. (2002) investigated the mechanisms whereby As(III) and As(V) in aqueous solution (pH 5.5–6.5) interact with the surface of mackinawite using X-ray absorption spectroscopy (XAS). The mackinawite they used was synthesised according to the method of Lennie and Vaughan (1996) and is thus more crystalline than the FeS_{am} used in the present study (chapter 2) and, probably, has surface groups which are more acidic (chapter 3). These differences may influence the amount and pH-dependence of sorption, but are not expected to influence the mechanism and resulting sorption products on the surface. They observed that the complex formed by As(V) at the mackinawite surface has four oxygen atoms in the first shell at 0.170 nm, one sulphur atom in the second shell at 0.311 nm and one iron atom in the third shell at 0.351 nm (Farquhar et al., 2002; Table 6 in chapter 1). This indicates that As(V) forms a monodentate complex at the surface of mackinawite, binding to one surface sulphide group. The fact that there is only one iron in the third shell suggests that the sulphide is coordinated to one iron atom. The XAS data from Farquhar et al. (2002) and the sorption reaction of As(V) with $\equiv FeSH_2^+$ proposed here are clearly in agreement.

4.1.2. Sorption isotherm for As(V)

The As(V) sorption isotherm for FeS_{am} (Figure 3b) is Langmuir, implying a constant sorption affinity until site-saturation is approached and one dominant type of binding site controlling As(V) sorption (cf. Dzombak and Morel, 1990). The isotherm starts to level off at high As(V) concentrations, indicating saturation of the specific binding site. If sorption is monodentate and all specific sites are occupied, then the saturation concentration should indicate the concentration of the specific binding site at the surface. In fitting the Langmuir isotherm, the $\equiv\text{FeSH}_2^+$ concentration at pH 7.5 from the surface model proposed in chapter 3 was used as input. Thus, the Langmuir fit (solid line in Figure 3b) levels off where the $\equiv\text{FeSH}_2^+$ sites would be saturated. As can be seen in Figure 3b, the sorption isotherm data tend to level off at this predicted site concentration. This again suggests that the $\equiv\text{FeSH}_2^+$ site is the specific binding site for monodentate As(V) sorption, confirming the pH-dependence fit described above.

An overall sorption reaction can be derived when combining the following As(V) sorption observations: (i) sorption occurs dominantly at the $\equiv\text{FeSH}_2^+$ site; (ii) As(V) sorbs as a monodentate complex; (iii) no reduction to As(III) prior to or during sorption occurs. Based on these observations and the XAS data from Farquhar et al. (2002), the following sorption reaction can be proposed:



The best fit to the Langmuir sorption isotherm at pH 7.5 is acquired with a $\log K_{\text{ads}}^* = +3.2 \pm 0.1$ for reaction (1).

At higher As(V) concentrations, not reached in the experiments, the sorption isotherm is likely to curve towards a steeper slope, indicative of As(V) coprecipitation. Such behaviour was reported by Farquhar et al. (2002), who observed, in addition to sorption complexes, an arsenic sulphide surface precipitate, probably poorly crystalline As₂S₃. Their data cannot be used to extend the present sorption isotherm, since they worked at a different pH and are likely to have studied a very different mackinawite surface. Nevertheless, it is expected that the solubility of amorphous As₂S₃ would have been reached at higher total arsenic concentrations than in the present sorption experiments (cf. Eary, 1992).

4.1.3. As(V) sorption characteristics

As(V) sorption onto FeS_{am} is found to be fast. Within ten minutes after As(V) addition, the amount of arsenic in solution has decreased and is stable for up to at least five hours. Experiments did not last longer. Dzombak and Morel (1990) set an approximate rule of thumb for sorption kinetics. At low sorbate to sorbent ratios (i.e., less than $0.01 \text{ mol mol}^{-1}$) equilibrium is achieved quickly, while at higher ratios equilibration times for at least a day should be required. The sorbate to sorbent ratio at maximum As(V) sorption is $0.04 \text{ mol mol}^{-1} \text{ FeS}_{\text{am}}$, higher than Dzombak and Morel's ratio. However, such a ratio is also dependent on the specific surface area (SSA) per mol sorbent, and since the SSA of FeS_{am} is relatively high, a higher limiting sorbate to sorbent ratio can be expected. Therefore, it may be assumed that the time between individual As(V) additions in the sorption isotherm experiments, which was 30 minutes, was a sufficient "equilibration" time.

The relatively fast sorption found in this study agrees with limited previous work. Raven et al. (1998) studied As(V) and As(III) sorption onto ferrihydrite and reported that equilibrium was reached in all cases within the first few hours of the experiments. As(V) sorption onto hydrous ferric oxide was found to be rapid: 90% sorption was found to occur in the first hour, 99% sorption was reached in 4 hours (Pierce and Moore, 1982). No kinetics for As(V) sorption onto iron(II) sulphides has been reported in literature. Sorption of gold(I) hydrosulphide complexes onto crystalline mackinawite has been reported to reach equilibrium within half an hour (Widler and Seward, 2002). Morse and Arakaki (1993) reported equilibration times of five to ten minutes for cobalt and nickel sorption onto FeS_{am} . For manganese sorption onto FeS_{am} , they observed equilibration times of less than thirty minutes (Arakaki and Morse, 1993). So, generally, sorption reactions with iron(II) monosulphide surfaces attain equilibrium, or at least steady state, relatively fast.

As(V) sorbs onto FeS_{am} relatively stronger than As(III) (Figures 3a and 4a). No significant reduction of As(V) to As(III) was observed. This is in agreement with Farquhar et al. (2002) who observed in their XAS study that As(V) did not change redox state upon sorption onto the mackinawite surface. Rochette et al. (2000) found As(V) reduction by aqueous S(-II) to be insignificant at pH 7 over a time of 7 days and to increase rapidly in rate with

decreasing pH. The absence of As(V) reduction in the sorption experiments is in agreement with the results of Rochette et al. (2000) and shows that the surface of FeS_{am} does not catalyse As(V) reduction within the timeframe of the experiments.

4.1.4. Structural aspects of As(V) sorption

Farquhar et al. (2002) studied the complex formed by As(V) at the mackinawite surface (see section 4.1.1. and Table 6 in chapter 1). They interpreted these shells as outer sphere complexation distances. However, the As–S distances are in fact comparable to the As–Fe distances reported for monodentate (0.359 nm), mononuclear bidentate (0.285 nm) and binuclear bidentate (0.324 nm) inner sphere complexation of As(V) at the goethite surface (Fendorf et al., 1997). Furthermore, the data presented here clearly indicate inner sphere complexation and generally support Farquhar et al.'s structural data. Thus, their XAS data can be used here to investigate the structural aspects of As(V) sorption onto FeS_{am} through inner sphere complexation.

The As(V) oxyanion sorbs to the $\equiv\text{FeSH}_2^+$ site at the FeS_{am} surface as a monodentate complex with an As–S distance of 0.311 nm (i.e., 0.170 + 0.141 nm; Farquhar et al., 2002). The other three hydroxyl groups of the oxyanion are pointing towards the solution. Geometrically, site saturation can only be achieved by either creating As–O–As corner sharing of adjacent sorbed oxyanion tetrahedra (Figure 5a) and releasing an H_2O molecule or by stereochemical orientation of the tetrahedra (Figure 5b). The formation of such As–O–As bonds as suggested in Figure 5a is comparable to the polymerisation–dehydration reaction proposed by Pokrovski et al. (1996) for concentrated (1–2 molal) As(III) solutions. The As–As distance of 0.335 nm observed by Farquhar et al. (2002) at the highest As(V) concentration (Table 6 in chapter 1) could be explained as such a surface-complex polymerisation, since it is approximately twice the length of the As–O distance. Since the $\equiv\text{FeSH}_2^+$ site is positioned at the edges of the tetragonal layers only (chapter 2), sorption will occur at the edges of the mackinawite lattice and not at the basal (001) plane.

Although the correspondence between the modelled curves and the experimental data using monodentate species was good, the possible formation

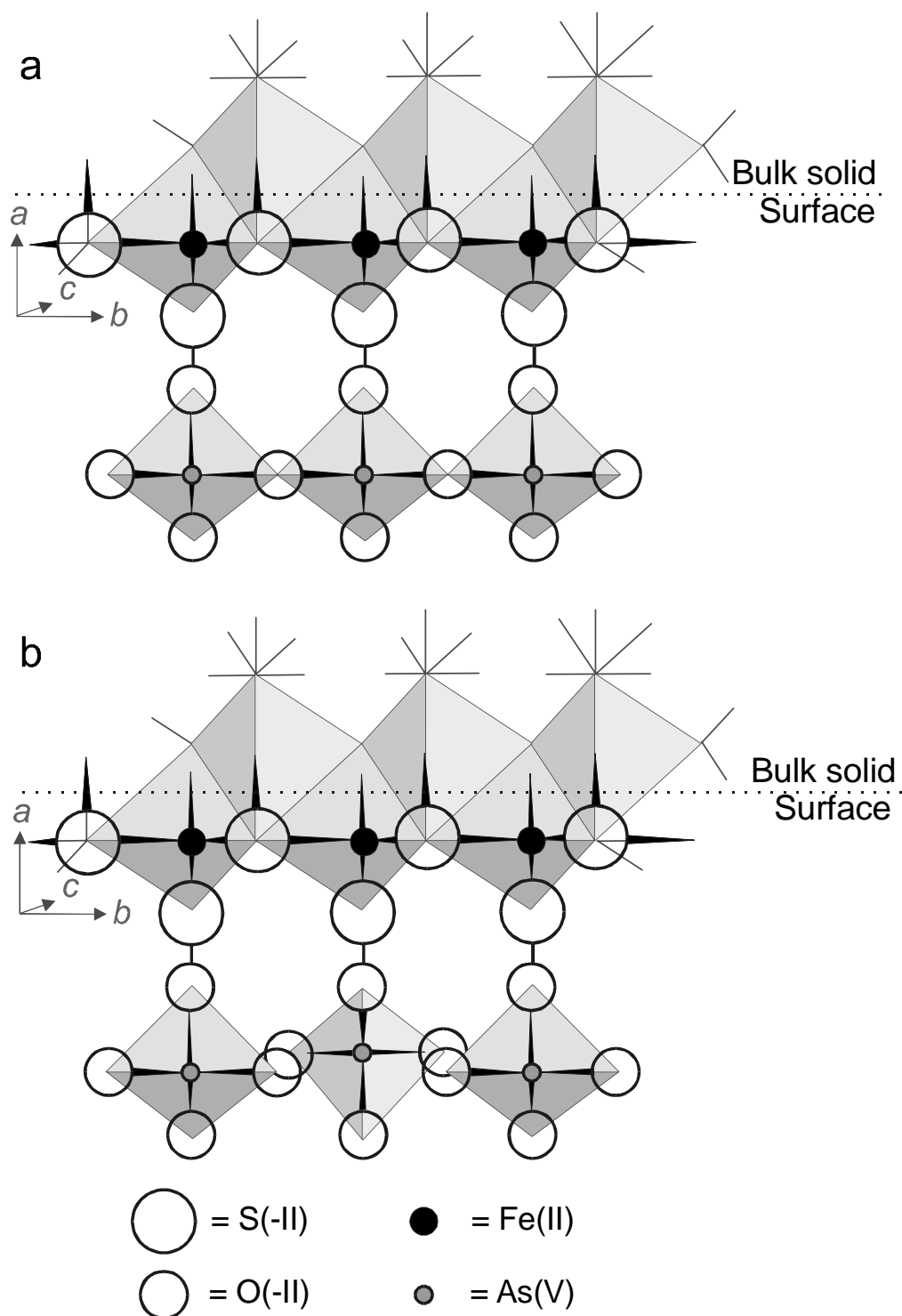


Figure 5. Sketches of possible structures of sorbed As(V) at site-saturation. (a) Polymerised and (b) stereochemically oriented As(V) surface complexes. The structure of disordered mackinawite is assumed to be similar to that of mackinawite (chapter 2). Within the mackinawite lattice, Fe–S distances are 0.223 nm and S–S distances are 0.3622 nm and 0.3680 nm (Uda, 1968). In the surface complex, As–O distances are 0.170 nm, As–S distances are 0.311 nm and O–S distances 0.141 nm (Farquhar et al., 2002).

of bidentate species cannot be ruled out. However, since the XAS data from Farquhar et al. (2002) indicate monodentate sorption of As(V) at the mackinawite surface as well, bidentate sorption is not expected to be important.

4.2. As(III)

4.2.1. pH-dependence of As(III) sorption

Over the experimental pH range, the aqueous As(III) speciation is relatively simple (Figure 1b) compared to As(V) (Figure 1a). The dominant aqueous As(III) species is the neutral H_3AsO_3^0 complex. Sorption of neutral species is generally not strongly pH-dependent. For example, H_3AsO_3^0 sorption onto hydrous ferric oxide is practically independent of pH (Pierce and Moore, 1982; Swedlund and Webster, 1999). Likewise, H_3AsO_3^0 sorption onto FeS_{am} is not strongly pH-dependent (Figure 4a), relative to As(V) sorption.

If As(III) sorption is governed by the presence of a specific surface functional group, then the $\equiv\text{FeSH}^0$ site is the surface group which describes the As(III) sorption pH-dependence most suitably of all possible groups (Figure 2). The bell shaped curve plotted in Figure 4a (dashed line) represents the concentration of the neutral $\equiv\text{FeSH}^0$ sites, as proposed in the surface model in chapter 3. This curve gives the most reasonable fit to the As(III) sorption pH-dependence, since its highest predicted surface site concentration coincides with the weak sorption maximum at pH 7.2 (Figure 4a). However, at higher and lower pH, more As(III) sorbs than can be explained by the surface $\equiv\text{FeSH}^0$ concentration alone. Since As(III) is uncharged, its sorption is not limited by a charged surface site. This may explain the observed sorption at lower and higher pH. Thus, As(III) sorption onto FeS_{am} is probably heterogeneous.

4.2.2. Sorption isotherm for As(III)

The As(III) sorption isotherm for FeS_{am} (Figure 4b) can be interpreted in terms of a Freundlich isotherm. It shows no surface site saturation at high As(III) concentrations, but a linear sorption with a slope of ~ 1.25 . Any of the predicted specific surface sites (chapter 2) would be saturated before the highest levels of sorbed As(III) in the isotherm experiment were reached. This implies sorption

at different site types with different sorption affinities. At the highest As(III) concentrations, all sites are saturated (dashed line in Figure 4b) while As(III) sorption does not tend to level off, indicating a continuum from sorption to coprecipitation. Farquhar et al. (2002) observed, at high As(III) concentrations, the presence of sorption complexes and of a poorly crystalline As_2S_3 phase in the XAS spectra. Such a coprecipitation could explain the high As(III) part of the Freundlich isotherm found in the present study. Since no correlation between total dissolved iron and As(III) sorption was observed, As(III) coprecipitates in an iron-free phase, probably poorly crystalline As_2S_3 .

The association of As(III) with FeS_{am} can be expressed in terms of a Freundlich isotherm, describing the relation between the As(III) concentration at the surface, $[\text{As(III)}]_{\text{ads}}$, and in solution, $[\text{As(III)}]_{\text{aq}}$:

$$(2) \quad [\text{As(III)}]_{\text{ads}} = 0.074[\text{As(III)}]_{\text{aq}}^{0.97}$$

This conditional Freundlich isotherm fits the sorption isotherm data with $R^2 = 0.98$ (Figure 4b). Generally, log-log plots tend to smoothen out scatter and subtle trends in the data. To justify the applicability of the Freundlich isotherm to the dissolved arsenite data, the data are replotted in Figure 4d as $[\text{As}]_{\text{as}}$ versus $[\text{As}]_{\text{aq}}$ with the Freundlich isotherm. As can be seen in Figure 4d, the calculated isotherm (solid line) still fits the data reasonably well. Freundlich sorption isotherms imply heterogeneous sorption, which cannot be described by a single (apparent) equilibrium constant. The applicability of the Freundlich isotherm to the arsenite sorption data therefore indicates that arsenite sorption is heterogeneous.

4.2.3. As(III) sorption characteristics

Similar to As(V), As(III) is found to sorb fast onto FeS_{am} . Within fifteen minutes after As(III) addition, the amount of arsenic in solution has decreased and is stable for up to at least four hours. No longer experiments were run. The sorbate to sorbent ratio at maximum As(III) sorption is $0.012 \text{ mol mol}^{-1} \text{ FeS}_{\text{am}}$, which is comparable to Dzombak and Morel's ratio of $0.01 \text{ mol sorbate per mol sorbent}$ below which sorption kinetics are generally fast. Therefore, it may be assumed that the time between individual As(III) additions in the sorption isotherm experiments, which was 30 minutes, was a sufficient "equilibration"

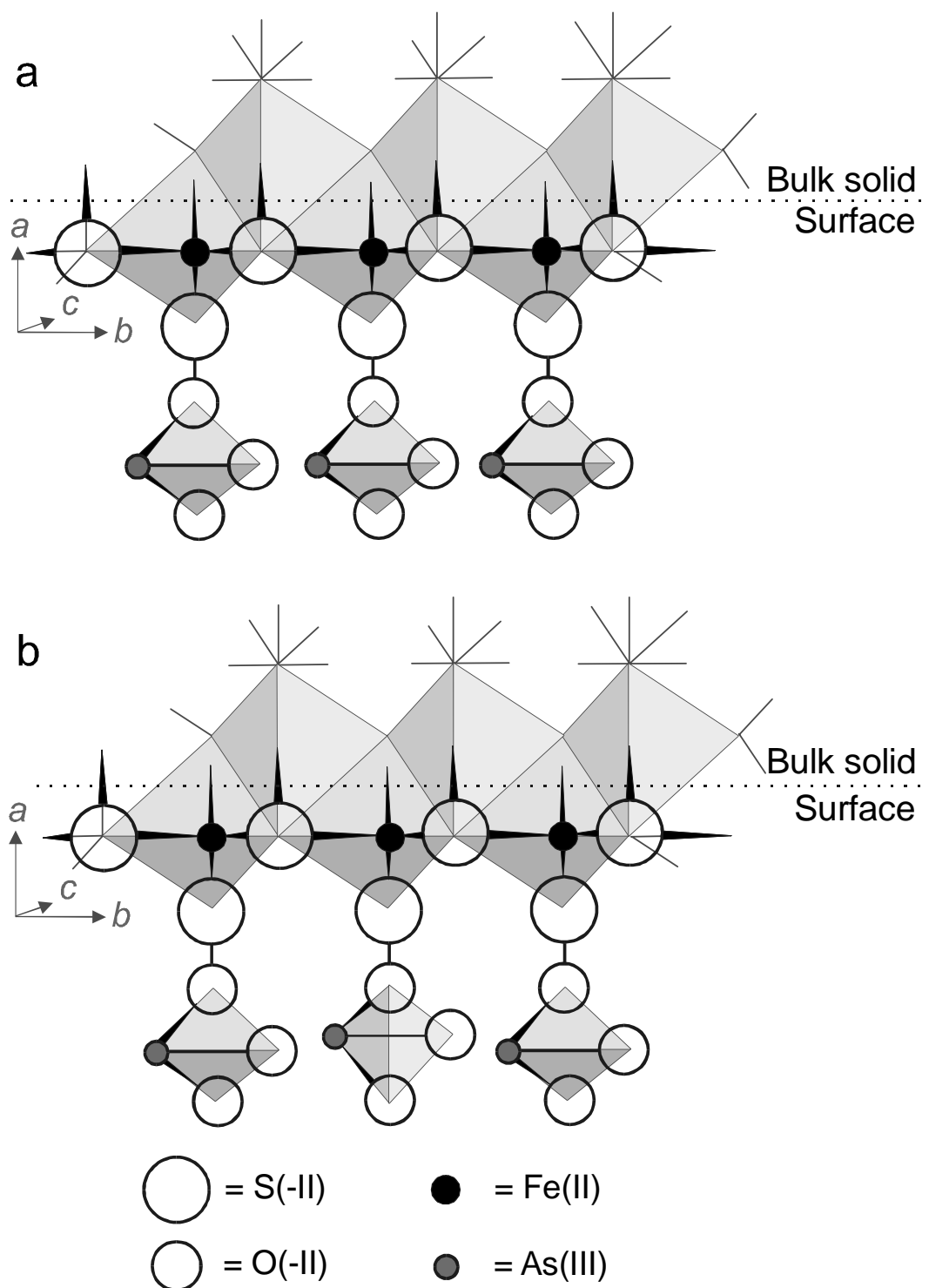


Figure 6. Sketches of possible structures of stereochemically oriented sorbed As(III) tetrahedra at site-saturation. The structure of disordered mackinawite is assumed to be that of mackinawite (chapter 2). Within the mackinawite lattice, Fe–S distances are 0.223 nm and S–S distances are 0.3622 nm and 0.3680 nm (Uda, 1968). In the surface complex, As–O distances are 0.1746 nm (Tossell, 1997) and O–S distances 0.141 nm (Farquhar et al., 2002).

time. The relatively fast sorption found in the present study agrees with limited previous studies of on arsenic sorption, as discussed in section 4.1.3. As(III) sorption onto FeS_{am} is weaker than As(V) sorption (Figures 3a and 4a).

4.2.4. Structural aspects of As(III) sorption

Farquhar et al. (2002) studied As(III) sorption and coprecipitation complexes on the mackinawite surface using XAS. They observed that the complex formed by As(III) at the mackinawite surface is almost identical to the As(V) complex (Tables 6 and 7 in chapter 1). This suggests that As(III) oxidised to As(V), which may have occurred during measurements in the high-energy beam (L. Charlet, personal experience). The fact that they observe an absorption edge indicating As(V) in some spectra of As(III) experiments, supports possible oxidation. However, if this oxidation does not influence the sorption complex structure, then As(III) also sorbs as a monodentate at a mono-coordinated sulphide surface group with two hydroxyl groups pointing towards the solution (Figures 6a and 6b). Sorption will occur at the edges of the mackinawite lattice and not at the basal (001) plane, since the $\equiv\text{FeSH}^0$ site is situated at the edges of the tetragonal layers only (chapter 2).

5. Implications

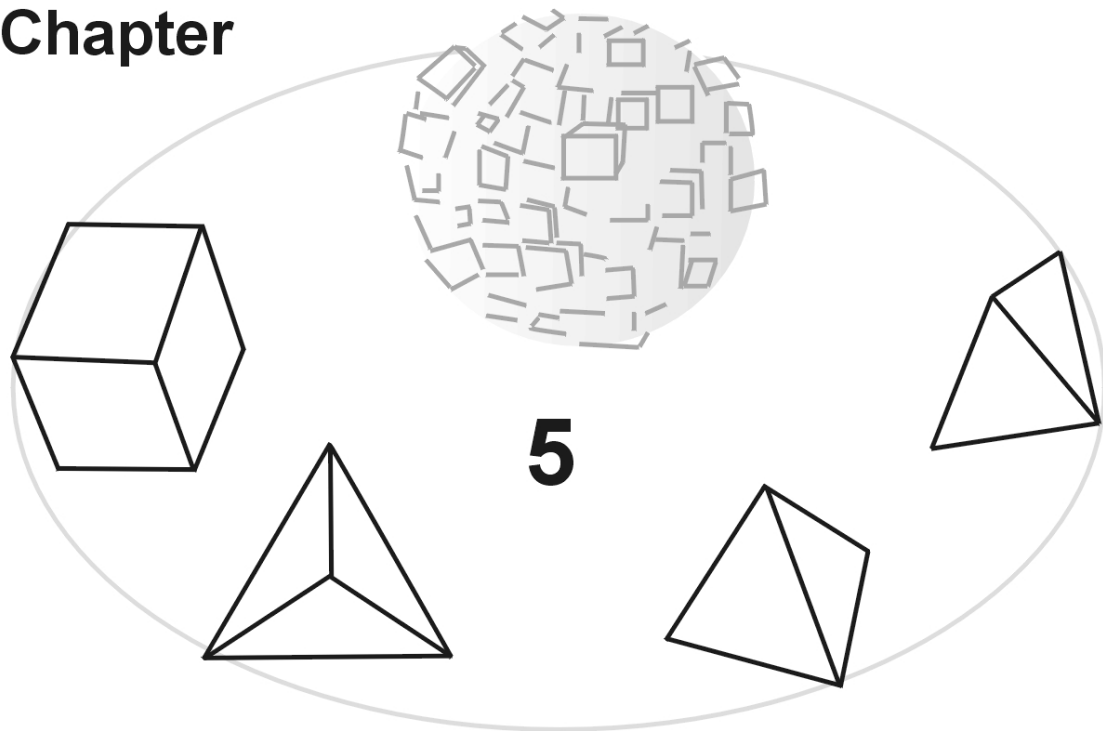
Sorption slows down the transport of a dissolved substance compared to the water flow (Appelo and Postma, 1994) and thus is a controlling factor in the mobility and immobilisation of chemicals. In the case of As(III) sorption onto FeS_{am} , its Freundlich isotherm is a straightforward relation and defines a relatively weakly pH-dependent retardation factor. Contrastingly, in the case of As(V) sorption onto FeS_{am} , its non-linear adsorption isotherm implies that the value of K_{ads}^* varies with As(V) concentration and pH. Furthermore, the strength of sorption varies, with As(V) sorbing more strongly onto FeS_{am} than As(III). It follows from their different sorption behaviour, that As(V) and As(III) will show differential mobility and will travel through an aquifer with different velocities. This will lead to their increased separation along a flow path in a non-steady state situation. Generally, the neutral H_3AsO_3 complex is less strongly sorbed under oxic groundwater settings than As(V) species and may travel five to six times faster than As(V) (Gulens et al., 1979). From the

present study, it may be concluded that a higher As(III) mobility may also be expected if disordered mackinawite controls arsenic mobility.

Acknowledgements

Philippe Van Cappellen (Utrecht University) is gratefully acknowledged for insightful discussions over the course of this study. Lorenzo Spadini (Grenoble University) contributed to the discussion on the structural aspects of sorption. This research was financially supported by the Netherlands Organization of Scientific Research (NWO/ALW grant 750.197.06 to M.W.), by the Donder's Chair grant (Utrecht University) to L.C. and by NERC grant NERLS200000611 to D.R. This study was conducted under the program of the Netherlands Research School of Sedimentary Geology.

Chapter



Arsenic in iron sulphides: sorption and incorporation*

* To be submitted as: Wolthers M., Butler I.B., Benning L., Rickard D., *Geochimica Cosmochimica Acta*.

Abstract

The association of arsenate, As(V), and arsenite, As(III), with disordered iron(II) monosulphide sulphide, FeS_{am} , was studied in sulphide-limited (Fe:S = 1:1) and excess-sulphide (Fe:S = 1:2) batch experiments. In the absence of arsenic, the sulphide-limited experiments produce disordered mackinawite while the excess-sulphide experiments yield pyrite with trace amounts of disordered mackinawite. With increasing initially added As(V) concentrations, $[\text{As(V)}]_0$, the transformation of FeS_{am} to mackinawite and pyrite is retarded. At S:As = 1:1 and 2:1, elemental sulphur, green rust and possibly orpiment are the end products. As(V) oxidises S(-II) in FeS_{am} and (or) in solution to S(0) and Fe(II) in the solid phase to Fe(III). At lower $[\text{As(V)}]_0$ concentrations, the oxidation number of arsenic incorporated in the synthetic pyrite is -1, as suggested by X-ray absorption spectroscopy. Increasing initially added As(III) concentrations inhibit the transformation of FeS_{am} to mackinawite and pyrite. No other oxidation products of FeS_{am} or sulphide, other than pyrite, were observed.

Sorption onto the FeS_{am} surface may be the reaction controlling the uptake of arsenic into the solid phase. Inhibition of iron(II) sulphide transformations due to arsenic sorption suggests that the sorption sites are crucial not only as sorption sites, but also in iron(II) sulphide transformation mechanisms.

1. Introduction

Pyrite, the most stable and ubiquitous authigenic iron(II) sulphide phase in the Earth surface environment, can incorporate relatively large amounts of arsenic (Huerta-Diaz and Morse, 1992; Morse and Luther, 1999), thus retarding the migration of arsenic in the anoxic environment. Huerta-Diaz and Morse (1992) found concentrations of arsenic in marine sedimentary pyrites to range up to 0.93 wt.%. Their results indicate that sedimentary pyrite is an important sink for arsenic, even if only minor pyrite formation has taken place. At high arsenic concentrations (that is, $> 1 \times 10^{-3}$ M) in contaminated sediments, arsenic was found precipitated as an iron-arsenic-sulphide in an approximate 1:1:1 ratio (Rittle et al., 1995). This composition suggests an arsenopyrite, FeAsS ,

precipitate, although this could not be structurally confirmed by X-ray powder diffraction (XRPD).

Since the relevant mineralogy of arsenic containing solid phases in sediments has been mostly inferred from indirect measurements such as selective chemical dissolution of the sediment (cf. Huerta–Diaz and Morse, 1992), structural information on arsenic incorporation into authigenic pyrite is absent. Contrastingly, hydrothermal arsenian, or As-rich, pyrites have been studied in detail. From X-ray absorption spectroscopy studies, it was proposed that arsenic substitutes for sulphur in pyrite (Tingle et al., 1996; Savage et al., 2000). The arsenic concentrations in arsenian pyrite studied by Savage et al. (2000) was on average 1.2 wt.%, with local As concentrations ranging from ~0 to 5 wt.%. These concentrations were insufficient to cause local structural transformation of pyrite to arsenopyrite, although lattice deviations from the cubic symmetry of pyrite towards the orthorhombic structure of arsenopyrite were observed (Savage et al., 2000).

At ambient temperatures, pyrite can be formed via several pathways (cf. Butler and Rickard, 2000), with disordered iron(II) monosulphide often being the initial precipitate (cf. Rickard, 1969; Schoonen and Barnes, 1991b). Synthetic iron(II) monosulphide, FeS_{am} , is a nanocrystalline solid and displays a disordered tetragonal mackinawite structure (chapter 2). The hydrated FeS_{am} surface can be best described by strong mono-coordinated and weak tri-coordinated sulphur sites as the surface reactive sites (chapter 3). In chapter 4, As(V) and As(III) sorption onto FeS_{am} was examined. Analogously to pyrite, FeS_{am} has been recognised as a scavenger of trace elements from solution in anoxic environments (Kornicker, 1988; Morse and Arakaki, 1993; Arakaki and Morse, 1993; Morse and Luther, 1999; Wharton et al., 2000).

At oxic to anoxic transitions, arsenic is released from reductively dissolving iron hydroxides into the surrounding pore water, groundwater or water body. Smedley and Kinniburgh (2002) have shown in their review that there is no clear consensus on the precise mechanisms involved with respect to the roles played by reductive desorption, reductive dissolution and diagenetic changes to the mineral structure of the As-rich iron hydroxides. In reducing waters with low sulphide concentrations, the released arsenic occurs predominantly as oxyanions of As(III) or As(V). In the presence of high sulphide concentrations, the dissolved thioarsenite monomers $\text{AsS}(\text{SH})_2^-$ and $\text{AsS}_2(\text{SH})_2^{2-}$ and trimer $\text{As}_3\text{S}_4(\text{SH})_2^-$ may be significant (Helz et al., 1995).

While many of the trace metals form insoluble sulphides in sulphidic, reducing environments, arsenic is distinctive in being relatively soluble at pH values higher than 5.5, and is therefore mobile over a wide range of redox conditions (Smedley and Kinniburgh, 2002). Consequently, a crucial control on the mobility and immobilisation of arsenic is sorption onto particulate phases (Mok and Wai, 1994), in particular iron(II) sulphides, which are ubiquitous in anoxic sulphidic settings. However, there is no study previously published on the behaviour of arsenic during the conversion of FeS_{am} to mackinawite and pyrite.

In this study, batch experimental techniques were used to study the behaviour and influence of As(V) and As(III) at various concentrations during the transformation of FeS_{am} to mackinawite and the conversion of FeS_{am} to pyrite. The solid end products were characterised by XRPD, transmission electron microscopy (TEM) and X-ray absorption near-edge spectroscopy (XANES) and the supernatant solution chemistry was analysed by inductively coupled plasma mass spectrometry (ICP-MS) and atomic absorption spectroscopy (AAS). The results are interpreted and discussed in terms of arsenic uptake mechanisms, redox reactions and the effect of arsenic uptake on iron(II) sulphide transformation mechanisms.

2. Materials and methods

Two sets of batch experiments were performed: (i) freeze-dried FeS_{am} was reacted with various amounts of As(V) and As(III), and (ii) freeze-dried FeS_{am} was reacted with various amounts of As(V) and As(III) and $\text{H}_2\text{S}(\text{g})$. The first set of experiments, with an Fe(II) to S(-II) ratio of 1:1, are referred to as the *sulphide-limited experiments*. The second set of experiments, with an Fe(II) to S(-II) ratio of set approximately 1:2., are referred to as the *excess-sulphide experiments*.

2.1. Materials

All chemicals were analytical grade Fisher ChemicalsTM and used without further purification. Solutions were prepared from 18 M Ω distilled deionised water which had been rigorously purged for at least 60 minutes with O_2 -free N_2 before use. Analytical-grade O_2 -free N_2 was passed through a pyrogallol scrubber to remove traces of O_2 . A 0.01 M tri-sodium citrate pH-buffer

solution at pH to 6.00 ± 0.01 was used. Stock solutions of the pH buffer were prepared in advance and purged for at least 60 minutes with O_2 -free N_2 gas before use. The initial redox potential was poised with Ti(III) citrate which was prepared using the method of Zehnder and Wuhrman (1976). The Ti(III) citrate stock solution was stored, for a maximum of 6 weeks, under nitrogen in a ground-glass-stoppered bottle. Addition of 2 mL Ti(III) citrate solution poised the initial reaction redox potential below -400 mV (cf. Zehnder and Wuhrman, 1976; Rickard, 1997). However, during the experiment, the redox potential is likely to become controlled by the S(-II)/S(0), the Fe(II)/Fe(III) and—at high arsenic concentrations—by the As(V)/As(III) redox couples.

Freeze-dried FeS_{am} was synthesised from solutions of S(-II) and Fe(II), by dissolving $Na_2S \cdot 9H_2O$ and Mohr's salt ($Fe(NH_4)_2(SO_4)_2 \cdot 4H_2O$), which is relatively resistant to oxidation, in purged $18 M\Omega$ water. Freeze-dried FeS_{am} was prepared less than a week in advance by mixing 100 mL Mohr's salt solution (0.6 M) with 100 mL S(-II) solution (0.6 M $Na_2S \cdot 9H_2O$) under $N_2(g)$, filtering the suspension within minutes after mixing through a WhatmanTM No.1 filter, and freeze drying the product for 3 to 4 days. Effectively, the freeze-dried FeS_{am} has aged for less than half an hour (Chapter 2). After freeze drying, the FeS_{am} was stored under an N_2 atmosphere at $-18^\circ C$ before use.

Arsenite and As(V) solutions were prepared fresh for each batch of experiments by dissolving Na_2AsO_2 and $Na_2HAsO_4 \cdot 7H_2O$ in purged $18 M\Omega$ water while constantly purging with O_2 -free N_2 .

2.2. Batch experimental method

The batch reactions were performed in 100 mL long-necked pyrex ampoules, similar to those used by Richard (1997) and Butler and Rickard (2000). Under a N_2 atmosphere in a glove box, 0.40 g of freeze-dried FeS_{am} was weighed out into the ampoules. Subsequently, the ampoules were filled with 2 mL Ti(III) citrate, 10 mL arsenic solution with the appropriate concentration and valence state, and 40 mL of pH-buffer solution. The reaction ampoule was then attached to the manifold (Figure 1) through an air-tight SwagelokTM ([5] in Figure 1).

The manifold is adapted from the manifold described by Rickard (1997). It permits gases to be added and extracted from the reaction ampoules under

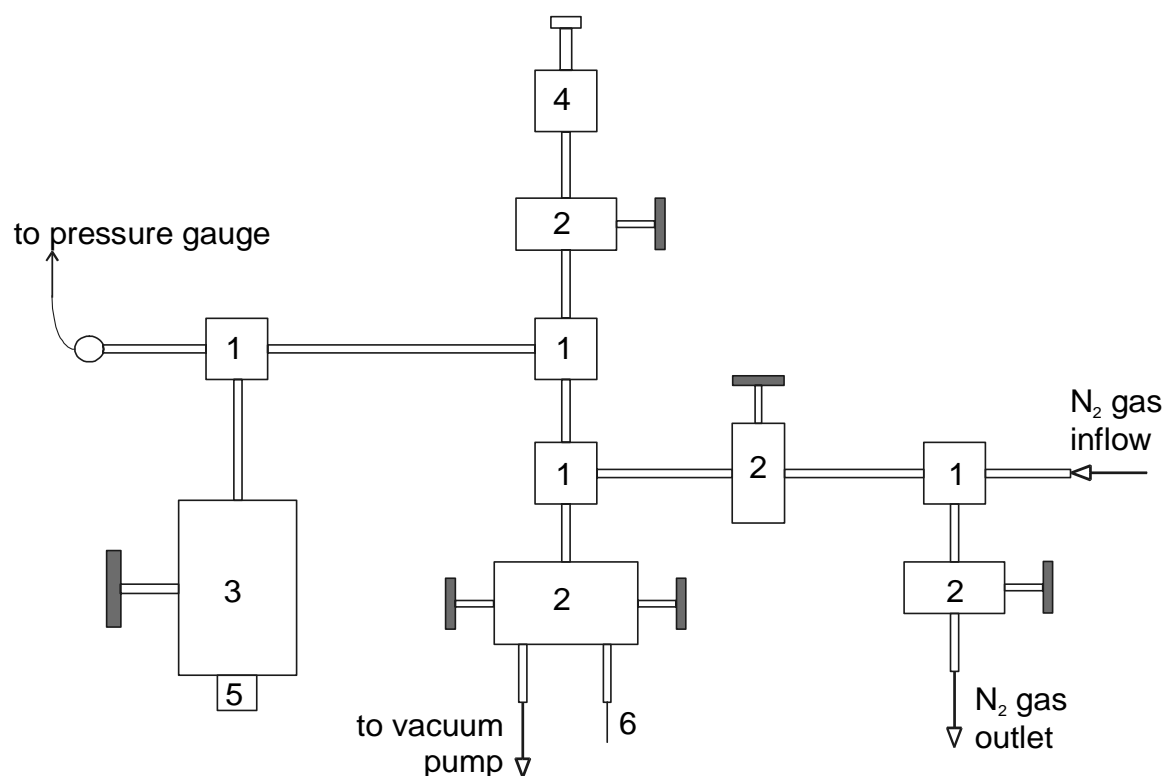


Figure 1. The reaction manifold. Through the manifold, reaction vessels could be evacuated, flushed with nitrogen and filled with $\text{H}_2\text{S}/\text{N}_2$ -gas mixtures. [1] valve junctions; [2] needle valves; [3] large needle-type valve; [4] gas-tight syringe; [5] SwagelokTM air-tight sealing nut with TeflonTM ferrule for reaction vessel attachment; [6] hypodermic needle for serum bottle attachment (adapted from Rickard, 1997).

strictly O_2 -free conditions. Analytical grade N_2 was passed through a SupelcoTM high capacity gas purifier (granular Zr at $> 300^\circ\text{C}$) to remove traces of O_2 prior to flushing through the manifold. After attachment to the manifold, the reaction ampoules were evacuated and flushed with O_2 -free N_2 three times. The third time, the vessel was either filled with N_2 to slightly less than atmospheric pressure (sulphide-limited experiments) or filled with N_2 , evacuated and filled with an $\text{H}_2\text{S}/\text{N}_2$ gas mixture to atmospheric pressure (excess-sulphide experiments). H_2S was generated in serum bottles as follows: sodium sulphide ($\text{Na}_2\text{S}\cdot 9\text{H}_2\text{O}$) was weighed out into a serum bottle; the bottle was fitted to the manifold via a hypodermic needle ([6] in Figure 1) and 50% sulphuric acid was then injected into the bottle to generate the required amount of H_2S . The gas was transferred to the reaction vessel and the gas space made up to slightly less than atmospheric pressure with O_2 -free N_2 . Finally, the reaction ampoule was sealed at the neck with a glass-blowers torch and the ampoule was detached from the manifold. The ampoules were fitted to an

orbital shaker in an oven at 25°C. The orbital shaker was set to ~300 rpm and the experiments were run for four weeks.

At the end of the experiments, the ampoule neck was broken and the contents of the reaction ampoule was filtered using a 0.02 µm Millipore™ filter under a N₂-filled hood. The solid product was freeze-dried for ~24 hrs and stored at -18°C before analysis. The supernatant pH was measured using an Orion™ Ross combined glass electrode. A 5 mL sample of the supernatant was stored in a sealed glass vial at 4°C until acidification and analysis. All experiments were run in duplicate.

2.3. Analyses

2.3.1. Solution analyses

Acidified supernatant samples were analysed for total dissolved arsenic using a Perkin Elmer™ Elan 5000 induced coupled plasma (ICP) mass spectrometer. The detection limit was 6.5×10^{-9} M, taken as the average blank plus five times its standard deviation. Total dissolved iron was measured using a Varian Spectra 300 acetylene–air-flame atomic absorption spectrometer. Since citric acid has been reported to suppress the absorbance by iron up to 50% (Roos and Price, 1971), calibration solutions were made using the tri-sodium citrate pH-buffer solution and were acidified similar to the supernatant samples. The detection limit was 7.4×10^{-9} M, taken as the average blank plus five times its standard deviation.

2.3.2. Solid phase characterisation

XRPD was carried out using a Philips™ PW170 diffractometer (CuKα radiation, 35 kV, 40 mA). Approximately 50 mg of freeze-dried FeS_{am} was dispersed in acetone and loaded onto a glass slide under a N₂ atmosphere within a glove-bag. XRPD patterns, in the range of 3–80° 2θ, were collected under air using the following settings: 0.1 mm receiving slit, 0.4 s/0.02° 2θ counting time.

TEM images, selected-area electron diffraction patterns (SAED) and energy-dispersive X-ray (EDX) analyses of freeze-dried FeS_{am} were collected

on a PhilipsTM CM200 FEG-TEM (200 kV). Approximately 0.5 mg of solid sample dispersed in acetone was quickly loaded in air onto a copper grid with a thin biofilm, carbon coated, and loaded into a low-background specimen microscope holder. Since the particles may be smaller than the interaction volume of the 200 kV electron beam and since no calibration could be done, the EDX data were used qualitatively; the estimated detection limit is 1 wt.% for As. SAED patterns and TEM images were recorded photographically. In the SAED patterns, reciprocal lattice distances were measured manually and converted to lattice d -spacings according to:

$$(1) \quad d = L\lambda R^{-1}$$

where L is the camera or diffraction length of 0.92 m, λ is 2.508×10^{-12} m and R is the measured lattice distance (Grundy and Jones, 1976).

For XANES analysis, 0.5 g synthetic iron(II) sulphide mixture was selected and refined to a pure pyrite sample as follows. The mixture was loaded in a 15 mL GreinerTM tube under N_2 atmosphere in a glove-bag. The sample was washed with 10 mL acetone, centrifuged and decanted three times to remove any elemental sulphur. Then, 10 mL purged 6 M HCl was added. The suspension was purged with N_2 to let most of the $H_2S(g)$ escape before the tube was sealed. HCl was used in order to dissolve the acid volatile iron(II) monosulphides. The tube was loaded on a shaker and the suspension shaken for ~15 hrs. Then, the suspension was centrifuged, decanted and washed with purged Milli-QTM water three times under flowing N_2 . The remaining slurry was frozen and freeze-dried for 3 days. Subsequently, the sample was packed under N_2 for transport to Daresbury where XANES analyses were done.

Prior to XANES analysis, the specimen was ground under air in a pestle and mortar, and loaded into an aluminium sample holder with SellotapeTM windows. Data were collected at the As K -edge at ambient temperature on station 16.5 of the Daresbury Synchrotron Radiation Source, operating at 2 GeV with an average current of 150 mA. A Si(220) double crystal monochromator was used, calibrated using a 5 μ m gold foil. I_0 and I_t were measured using ion chambers filled with a mixture of Ar/He. Fluorescence data were recorded using an OrtecTM 30-element solid state detector. Four scans were taken and summed. Previously recorded data for arsenopyrite and orpiment were used as model compounds for the arsenic analysis in the specimen. The data were processed using the Daresbury EXCALIB program, to

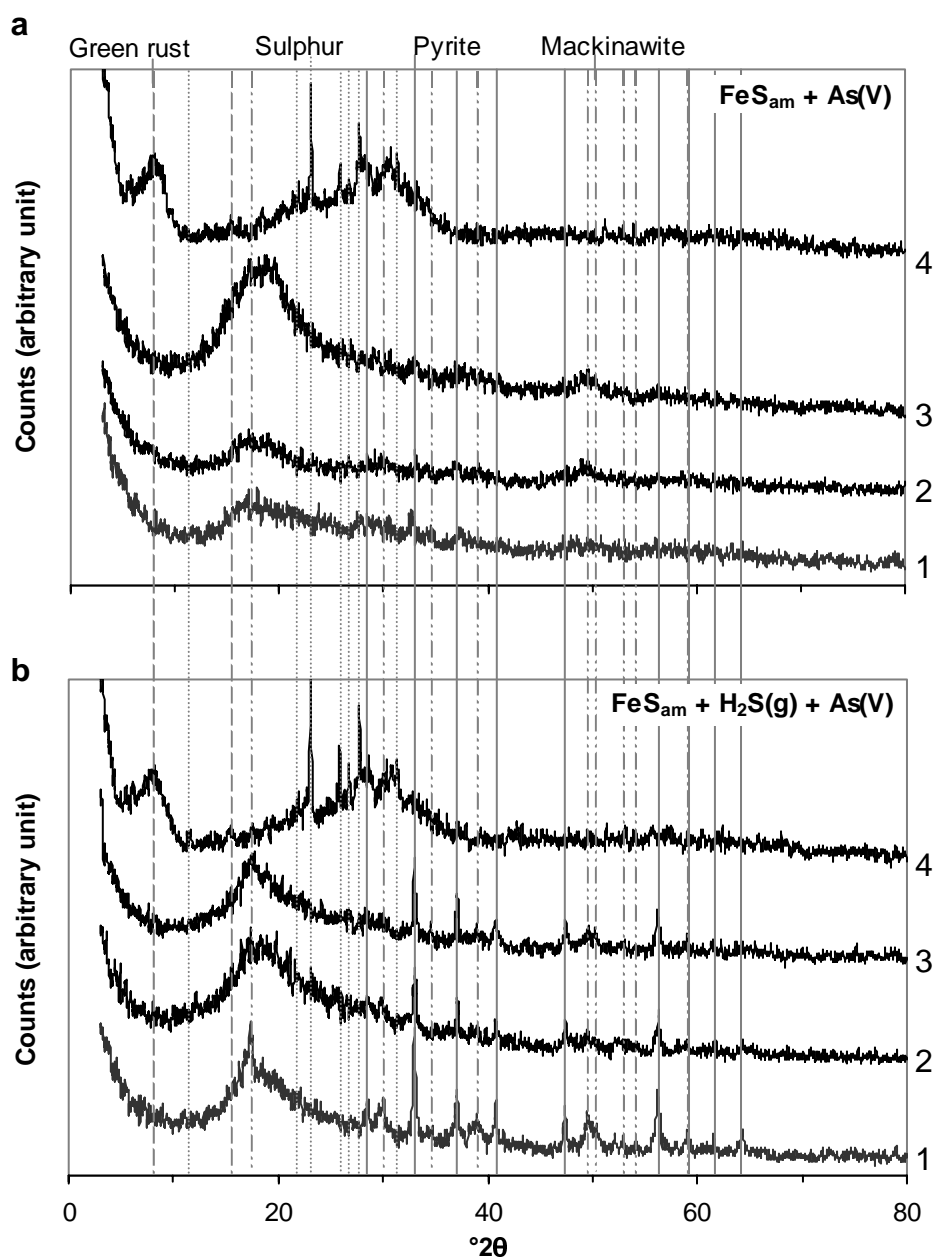


Figure 2. XRPD spectra for the end products of the reactions of various $[\text{As(V)}]_0$ in (a) the sulphide-limited and (b) the excess-sulphide experiments. Spectrum 1: blank experiment; spectrum 2: 1.0 ± 10^{-7} M $[\text{As(V)}]_0$; spectrum [3] = 8.8 ± 10^{-4} M $[\text{As(V)}]_0$; spectrum [4] = 9.2 ± 10^{-2} M $[\text{As(V)}]_0$. Vertical lines indicate 2θ -values for diffraction by pyrite (solid lines; JCPDS file 06-0710), mackinawite (dashed-dotted lines; JCPDS file 15-0037), elemental sulphur (dotted lines; JCPDS file 08-0247) and green rust (dashed lines; JCPDS file 13-0092).

convert the monochromator angle to the corresponding X-ray energy, and to calculate the absorbance from the ion chamber readings as $\ln(I_0/I_t)$ for the transmission spectra, or as (I_f/I_0) for the fluorescence spectra.

3. Results

3.1. As(V)

The supernatant analyses results are listed in Table 1. The amount of arsenic associated with the solid phase, $[As]_s$, was calculated by difference between the amount of As(V) initially added, $[As(V)]_0$, and the concentration measured in the supernatant at the end of the experiments, $[As]_{aq}$. As can be seen in Table 1, $[As]_s$ in the sulphide-limited and excess-sulphide experiments is comparable. The amount decreases with decreasing $[As(V)]_0$. Except for the experiments at highest $[As(V)]_0$, all total dissolved iron concentrations are similar. At the highest $[As(V)]_0$, the iron concentration increases two orders of magnitude.

Typical XRPD patterns for the experiments with different $[As(V)]_0$ are shown in Figure 2. As can be seen in Figure 2a, the acetone-smear method used is not ideal for weakly diffracting disordered materials; it resulted in low signal to noise ratios (chapter 2). A summary of the XRPD results is listed in Table 2. The blank patterns consist of mackinawite (sulphide-limited experiments, Figure 2a) or pyrite and mackinawite (excess-sulphide experiments, Figure 2b). With increasing $[As(V)]_0$, the diffraction patterns increasingly deviate from the blank patterns. The diffraction intensity of the iron(II) sulphides weaken and, at $[As(V)]_0$ concentrations higher than ~1mM, disappear while diffraction peaks of elemental sulphur can be discerned. At the highest $[As(V)]_0$ concentration, a broad diffraction peak at $\sim 9^\circ 2\theta$ appears next to the sharp diffraction peaks of elemental sulphur. This broad diffraction peak at $\sim 9^\circ 2\theta$, corresponding to a diffraction spacing of ~1 nm, is most likely from the Fe(II) Fe(III) oxyhydroxide, green rust. Furthermore, a broad band of diffraction with a maximum around $\sim 30^\circ 2\theta$ was observed in spectrum 4 in Figures 2a and 2b. This may be caused by diffraction of disordered orpiment (As_2S_3 ; JCPDS 19–0084; cf. Eary (1992) for “amorphous” orpiment), which has six major diffraction peaks in the $29\text{--}36^\circ 2\theta$ range. Absence of other peaks makes

Table 1. Total dissolved arsenic and iron concentrations in the As(V) batch experiments. $[\text{As(V)}]_0$ = arsenic concentration added; $[\text{As}]_{\text{aq}}$ = total dissolved arsenic concentration measured (\pm analytical standard deviation, s.d.); $[\text{As}]_s$ = calculated amount of arsenic associated with the solid phase. d.l. = below detection limit (1.7×10^{-6} M when taking dilution steps into account). $[\text{Fe}]_{\text{aq}}$ = total dissolved iron concentration. (* n = 1, \pm 10% s.d. estimate or \pm analytical s.d. if higher; ** n = 2, \pm 10% or \pm s.d. on the average if higher).

Experiment	$[\text{As(V)}]_0$ (M)	$[\text{As}]_{\text{aq}}$ (M)	$[\text{As}]_s$ (M)	$[\text{As}]_s$ ($\text{mol g}^{-1} \text{FeS}_{\text{am}}$)	$[\text{Fe}]_{\text{aq}}$ (M)
Sulphide-limited	9.2×10^{-2}	$7.2 \pm 0.7 \times 10^{-2}$ *	2.0×10^{-2}	3×10^{-3}	$1.4 \pm 0.3 \times 10^{-2}$ *
	8.8×10^{-4}	$1.0 \pm 0.1 \times 10^{-4}$ **	7.8×10^{-4}	1×10^{-4}	$2.0 \pm 0.2 \times 10^{-4}$ **
	8.8×10^{-5}	$2.8 \pm 0.9 \times 10^{-6}$ **	8.5×10^{-5}	1×10^{-5}	$2.5 \pm 0.4 \times 10^{-4}$ **
	1.0×10^{-7}	d.l.			$2.4 \pm 0.2 \times 10^{-4}$ **
	Blank	d.l.			$2.45 \pm 0.2 \times 10^{-4}$ *
Excess-sulphide	9.2×10^{-2}	$7 \pm 1 \times 10^{-2}$ **	2.3×10^{-2}	3×10^{-3}	$1.6 \pm 0.3 \times 10^{-2}$ **
	8.8×10^{-4}	$1.6 \pm 0.2 \times 10^{-4}$ **	7.2×10^{-4}	9×10^{-5}	$3 \pm 1 \times 10^{-6}$ *
	8.8×10^{-5}	d.l.			$4.7 \pm 0.5 \times 10^{-5}$ *
	1.0×10^{-7}	d.l.			$1.9 \pm 0.2 \times 10^{-5}$ *
	Blank	d.l.			$3.6 \pm 0.5 \times 10^{-6}$ *

Table 2. Summary of the XRPD results depicted in Figures 2 and 5. $[\text{As}]_0$ = As(V) or As(III) concentration initially added; py = pyrite; mk = mackinawite; S^0 = elemental sulphur; g.r. = green rust.

	$[\text{As}]_0$ (M)	XRPD products	
		Sulphide-limited	Excess-sulphide
Blank	0	mk	py + mk
As(V)	9.2×10^{-2}	S^0 + g.r.	S^0 + g.r.
	8.8×10^{-4}	FeS_{am}	py + mk + S^0
	8.8×10^{-5}	mk	py + mk
	1.0×10^{-7}	mk	py + mk
As(III)	9.1×10^{-2}	FeS_{am}	FeS_{am}
	9.0×10^{-4}	FeS_{am}	FeS_{am}
	9.0×10^{-7}	FeS_{am}	py + mk
	1.0×10^{-9}	FeS_{am}	py + mk

identification impossible. In summary, the XRPD results show that the diffraction peaks of mackinawite and pyrite weaken and are replaced by elemental sulphur and green-rust peaks with increasing $[\text{As(V)}]_0$.

The colour of the solid end products changed with increasing $[\text{As(V)}]_0$ concentration from black to greyish-green in the sulphide-limited and from greyish-black to yellowish-green in the excess-sulphide experiments. This is consistent with the results from the XRPD observations. In the sulphide-limited experiments at high $[\text{As(V)}]_0$, the black FeS_{am} and mackinawite powders are replaced by elemental sulphur (white), green rust and, possibly, yellow orpiment. In the excess-sulphide experiments at high $[\text{As(V)}]_0$, the greyish-black pyrite and black mackinawite powders are replaced by elemental sulphur, green rust and, possibly, yellow orpiment.

Detailed examination of the iron(II) sulphides which had reacted with 1.0×10^{-7} M $[\text{As(V)}]_0$ was conducted using TEM (Figure 3). Figure 3a shows an example of a rectangular particle from the sulphide-limited experiment. EDX measurement of this particle yielded an Fe:S intensity ratio of 0.99, calculated from the peak surface areas in the spectra. From identification of the SAED pattern (Figure 3b) the crystalline mackinawite identity was determined. In Figure 3c, a crystalline particle formed in the excess-sulphide experiment is

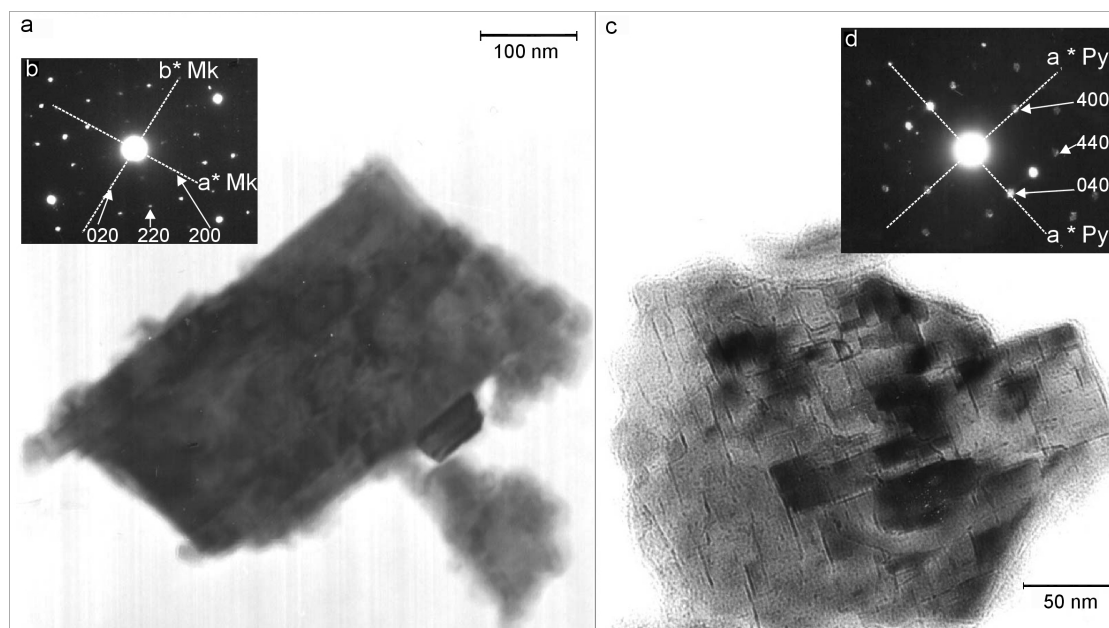


Figure 3. (a) TEM image of a mackinawite crystal from the sulphide-limited reaction with 1.0×10^{-7} M As(V). The Fe:S ratio of this material determined, by EDX analysis, was 0.99. (b) SAED pattern obtained from the crystal in (a) parallel to (001); a^* Mk and b^* Mk are the translation vectors in reciprocal lattice which correspond to tetragonal-lattice parameters a and b for mackinawite and 020, 220 and 200 points in the reciprocal lattice refer to the (hkl) planes in mackinawite. (c) TEM image of a pyrite crystal from the excess-sulphide reaction with 1.0×10^{-7} M As(V). The Fe:S ratio of this material determined by EDX analysis was 0.67. (d) SAED pattern from the crystal in (c) parallel to (001); a_1^* Py and a_2^* Py are the translation vectors in the reciprocal lattice which correspond to cubic-lattice parameters a_1 and a_2 for pyrite and the 400, 440 and 040 points in the reciprocal lattice refer to the (hkl) planes in pyrite.

depicted. EDX measurement of this particle yielded an Fe:S ratio of 0.67, indicating a sulphur-rich composition. Identification of the SAED pattern (Figure 3d) yielded the crystalline pyrite identity. For both particles in Figure 3, the arsenic concentration was below the detection limit of the EDX analyses.

In order to study the oxidation number of arsenic initially added as As(V) and associated with pyrite in the end product, the sample with the largest relative pyrite yield combined with the highest $[\text{As(V)}]_0$ was selected and prepared for XANES analysis. The selected iron(II) sulphide mixture had reacted with 8.8×10^{-5} M $[\text{As(V)}]_0$ in an excess-sulphide experiment. The

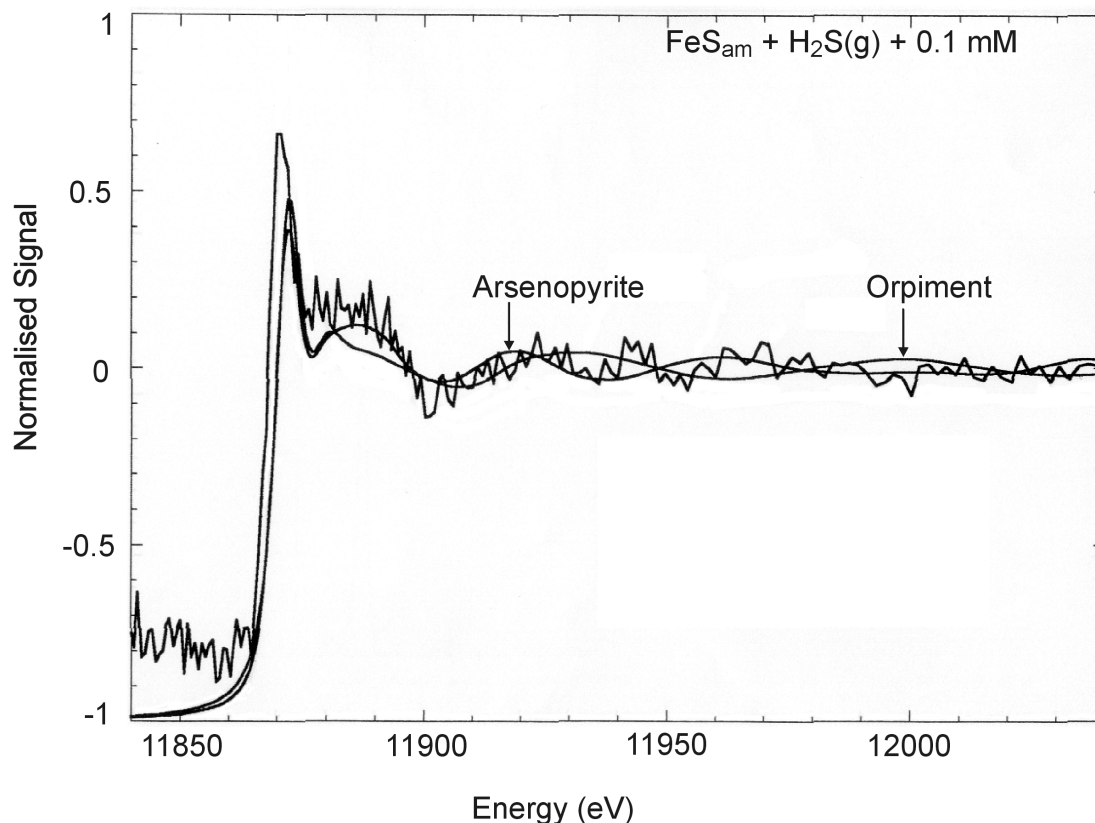


Figure 4. XANES As *K*-edge for batch-experiment solid end products for the excess-sulphide reaction of 8.8×10^{-5} M As(V) and XANES As *K*-edges for reference materials arsenopyrite and orpiment.

arsenic X-ray absorption *K*-edge in the bulk refined pyrite fraction of this mixture was measured. The position of this edge is indicative of its oxidation number. In Figure 4, the As *K*-edge profile obtained from the XANES analysis of the synthetic pyrite is compared to the edge profiles of arsenopyrite and orpiment. Both the edge position and the post-edge signal agree best with the As *K*-edge measured in the model arsenopyrite. Since the oxidation number of arsenic in arsenopyrite is -1 (Tossell et al., 1981), the comparison indicates that the oxidation number of arsenic associated with the synthetic refined pyrite fraction is also -1 .

3.2. As(III)

The amount of As(III) associated with the solid phase from the sulphide-limited and excess-sulphide experiments is similar (Table 3). It decreases with

Table 3. Total dissolved arsenic and iron concentrations in the As(III) batch experiments. $[\text{As(III)}]_0$ = arsenic concentration initially added; $[\text{As}]_{\text{aq}} = \text{total dissolved arsenic concentration measured}$; $[\text{As}]_s$ = calculated amount of arsenic associated with the solid phase. d.l. = below detection limit (1.7×10^{-6} M when taking dilution steps into account). $[\text{Fe}]_{\text{aq}}$ = total dissolved iron concentration. (* n = 1, \pm 10% conservative s.d. estimate or \pm analytical s.d. if higher; ** n = 2, \pm 10% or \pm s.d. on the average if higher).

Experiment	$[\text{As(III)}]_0$ (M)	$[\text{As}]_{\text{aq}}$ (M)	$[\text{As}]_s$ (M)	$[\text{As}]_s$ ($\text{mol g}^{-1} \text{FeS}_{\text{am}}$)	$[\text{Fe}]_{\text{aq}}$ (M)
Sulphide-limited	9.1×10^{-2}	$7.9 \pm 0.8 \times 10^{-2}$ *	1.2×10^{-2}	2×10^{-3}	$3.3 \pm 3 \times 10^{-4}$ **
	9.0×10^{-4}	$5.3 \pm 0.5 \times 10^{-4}$ **	3.7×10^{-4}	5×10^{-5}	$7.0 \pm 1 \times 10^{-3}$ **
	9.0×10^{-7}	d.l.			$8.7 \pm 0.9 \times 10^{-3}$ **
	1.0×10^{-9}	d.l.			$2.2 \pm 0.2 \times 10^{-4}$ **
	blank	d.l.			$2.5 \pm 0.2 \times 10^{-4}$ *
Excess-sulphide	9.1×10^{-2}	$7.5 \pm 0.8 \times 10^{-2}$ **	1.6×10^{-2}	2×10^{-3}	$3.4 \pm 0.6 \times 10^{-5}$ *
	4.5×10^{-4}	$3.8 \pm 0.4 \times 10^{-5}$ *	4.1×10^{-4}	5×10^{-5}	$3.5 \pm 1.4 \times 10^{-4}$ **
	9.0×10^{-7}	d.l.			$1.8 \pm 0.2 \times 10^{-4}$ **
	1.0×10^{-9}	d.l.			$6.0 \pm 2 \times 10^{-6}$ **
	blank	d.l.			$3.6 \pm 0.5 \times 10^{-6}$ *

decreasing the amount of As(III) initially added, $[\text{As(III)}]_0$. These results show the same trends as the As(V) results (Table 1). In contrast, the total dissolved iron results for the As(III) experiments (Table 3) differ from the As(V) experiments (Table 1). With increasing $[\text{As(III)}]_0$ concentration, the iron concentration increases by one to two orders of magnitude before decreasing at the highest $[\text{As(III)}]_0$.

In Figure 5, the XRPD patterns are depicted for the reaction of different amounts of $[\text{As(III)}]_0$ in sulphide-limited (Figure 5a) and excess-sulphide (Figure 5b) experiments. A summary of the XRPD results for both As(III) and As(V) experiments is listed in Table 2. The blank patterns consist of mackinawite (sulphide-limited experiments, Figure 5a) or pyrite and mackinawite (excess-sulphide experiments, Figure 5b). Figure 5a shows that there is a broadening of the diffraction peaks of mackinawite at the lowest $[\text{As(III)}]_0$ and no clear change in the diffraction pattern with increasing $[\text{As(III)}]_0$. In Figure 5b, the diffraction intensity of the iron(II) sulphides weakens relative to the blank patterns with increasing $[\text{As(III)}]_0$. At the highest $[\text{As(III)}]_0$ concentration, only weakened and broadened diffraction peaks of mackinawite, comparable to FeS_{am} diffraction peaks, remain. In summary, the XRPD results show that the diffraction peaks of mackinawite (both sets of experiments; Figures 2a and 2b) weaken and broaden and those of pyrite (excess-sulphide experiments; Figure 2b) disappear with increasing $[\text{As(III)}]_0$.

TEM was used to examine in detail the iron(II) sulphides which had reacted with 9.1×10^{-7} M $[\text{As(III)}]_0$. Figure 6a shows an example of the cloudy material formed from the sulphide-limited experiment. EDX measurement of this particle yielded an Fe:S ratio of 0.85, and the SAED pattern (Figure 6b) shows diffraction rings, indicating an amorphous or very fine grained character of the material. In Figure 6c, a particle formed in the excess-sulphide experiment is depicted. The Fe:S ratio of this aggregate was not determined by EDX. However, on average, the Fe:S ratio in the specimen was 1.2 ± 0.3 (s.d.). This relative iron enrichment, or sulphide loss, may have been caused by oxidation of the material. Since the XRPD pattern in Figure 5 did not reveal oxidation products of iron (II) sulphides such as greigite or Fe(III) oxides, it can be concluded that the material was oxidised during TEM-specimen preparation and storage: the As(III)-specimens were accidentally exposed to air at room temperature for a week in between two analyses sessions.

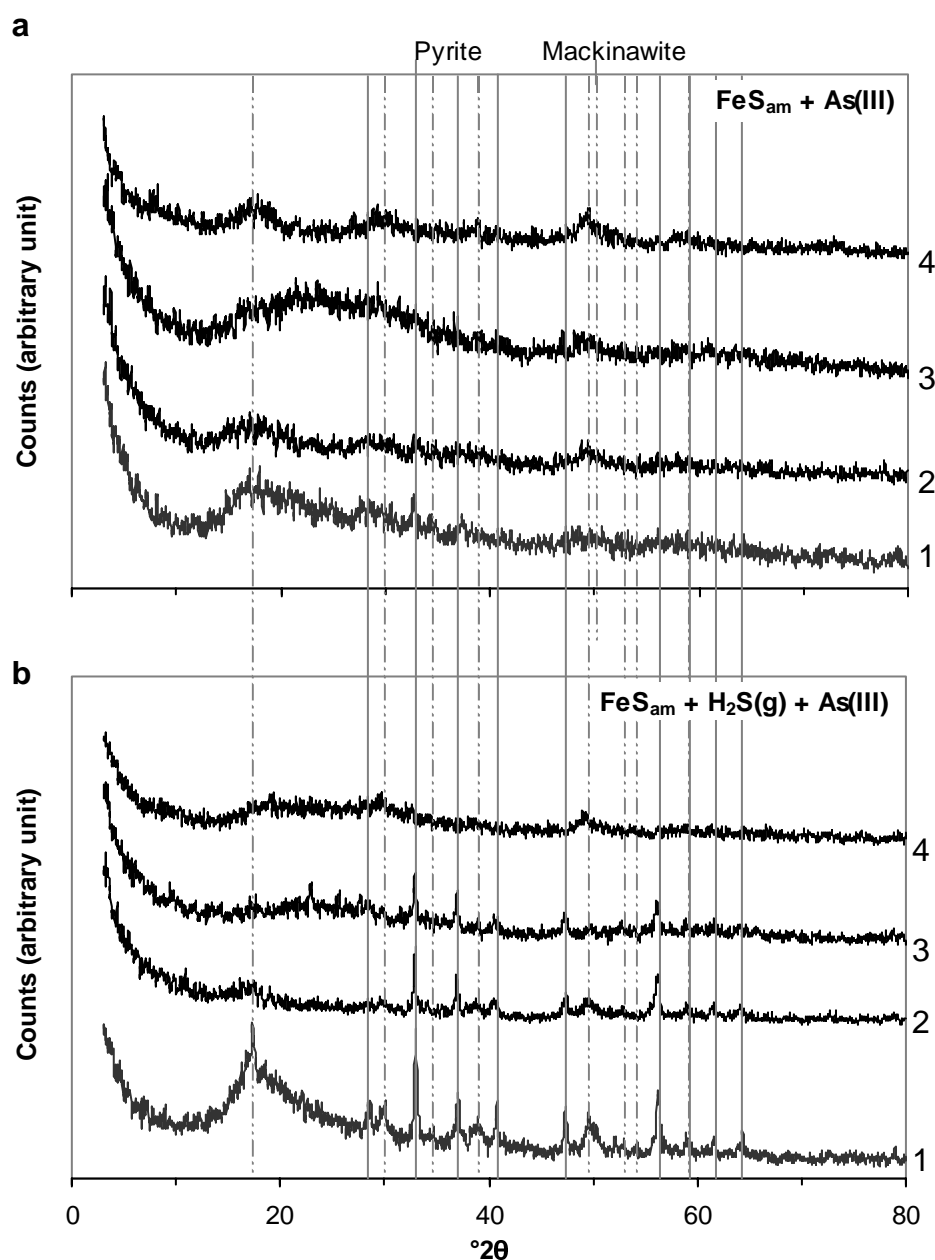


Figure 5. XRPD patterns for batch-experiment end product from the reactions at various $[\text{As(III)}]_0$ in (a) the sulphide-limited and (b) the excess-sulphide experiments. spectrum [1] = blank experiment; spectrum [2] = 1.0 ± 10^{-9} M As(III); spectrum [3] = 9.1 ± 10^{-7} M As(III); spectrum [4] = 9.1 ± 10^{-2} M As(III). Vertical lines indicate 2θ -values for diffraction by pyrite (solid lines; JCPDS file 06-0710) and mackinawite (dashed-dotted lines; JCPDS file 15-0037).

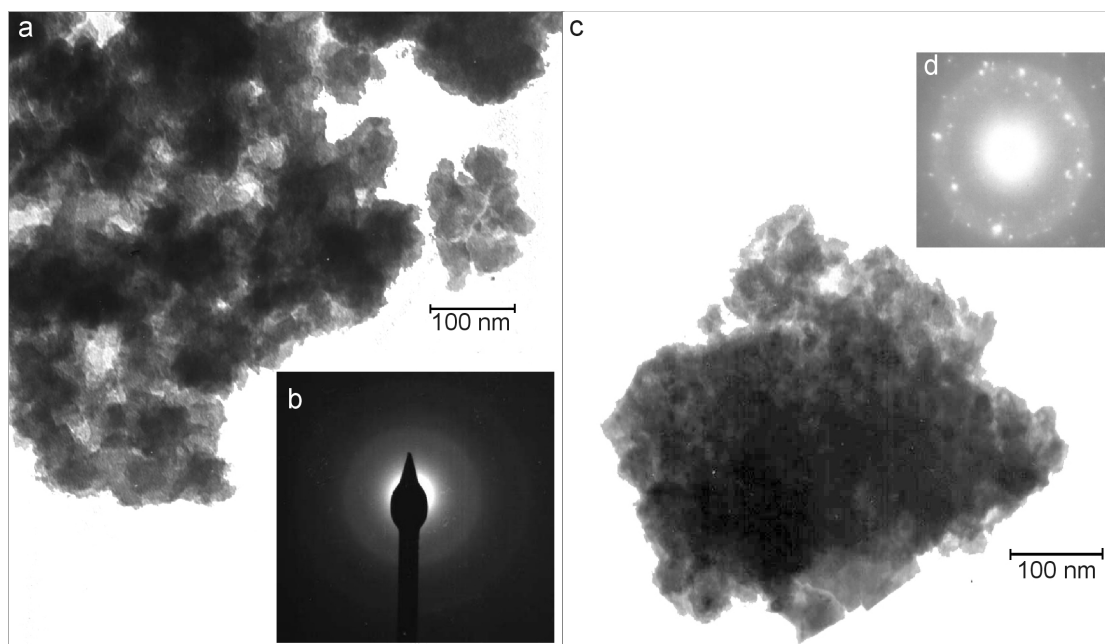


Figure 6. (a) TEM image and (b) SAED rings pattern for the FeS_{ami} end product from the sulphide-limited reaction with 9.1×10^{-7} M As(III). The Fe:S ratio of this material determined by EDX analysis was 0.85. (c) TEM image and (d) polyphase SAED pattern from the excess-sulphide reaction with 9.1×10^{-7} M As(III). The Fe:S ratio of this aggregate was not determined, on average, the Fe:S ratio in end product, determined by EDX analysis, was 1.2.

Identification of the SAED pattern (Figure 6d) was not possible for this particle nor for any particle in the specimen. All particles studied showed polycrystalline diffraction patterns similar to Figure 6d. Thus, the particles are polycrystalline or are transforming to different crystals (cf. Lennie et al., 1997), for example due to oxidation. For both particles in Figure 6, the arsenic concentration was below the detection limit of the EDX analyses.

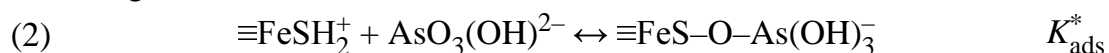
4. Discussion

4.1. As(V)

4.1.1. Aqueous As(V)

The amount of arsenic associated with the solid phase in the end product of the As(V) experiments depends on the total arsenic concentration alone (Table 1). The fact that it does not depend on excess H_2S suggests that pyrite formation is

not responsible for extra uptake of As(V). Thus, the uptake of As(V) may be controlled by the FeS_{am} starting material, or by the more crystalline mackinawite to which it converts during the batch experiments (Figures 2b, 3a and 3b). In chapter 3, a surface model was constructed for FeS_{am} , describing the surface acid–base properties and site concentrations of freshly precipitated FeS_{am} . This model was successfully applied to the sorption of As(V) onto FeS_{am} in chapter 4. As(V) sorption onto FeS_{am} could be described with the following reaction:



where $\log K_{\text{ads}}^* = +3.2 \pm 0.1$ at pH 7.5 (Figure 7) and the sorption site $\equiv\text{FeSH}_2^+$ is the positively charged sulphide surface group which is mono-coordinated to one bulk lattice iron (see chapters 2 and 3).

In order to test if As(V) uptake by the solid phase in the present batch experiments is controlled by the same sorption reaction of As(V) onto the FeS_{am} surface, the data in Table 1 for both the sulphide-limited and excess-sulphide experiments were plotted on a sorption isotherm graph (Figure 7). From the model proposed in chapter 3, the concentration of the specific surface site [$\equiv\text{FeSH}_2^+$] at pH 6.0 was taken as the maximum amount of sorption sites for As(V). Together with $\log K_{\text{ads}}^*$, this was used to calculate the Langmuir isotherm which describes As(V) uptake by the solid phase in the batch experiments, provided this was controlled by sorption onto FeS_{am} . The result is a reasonably good fit, which could be improved by using $\log K_{\text{ads}}^* = +2.8 \pm 0.4$ at pH 6 (solid line in Figure 7), which is consistent with $\log K_{\text{ads}}^* = +3.2 \pm 0.1$ at pH 7.5, obtained in chapter 4. Therefore, it is concluded that As(V) sorption onto FeS_{am} is the reaction controlling the uptake into the solid phase in the present batch experiments.

4.1.2. Solid characteristics

4.1.2.1. Sulphide-limited experiments

At the lowest $[\text{As}(\text{V})]_0$ concentration, the XRPD pattern is similar to the blank diffraction pattern and consists dominantly of mackinawite (Figure 2a).

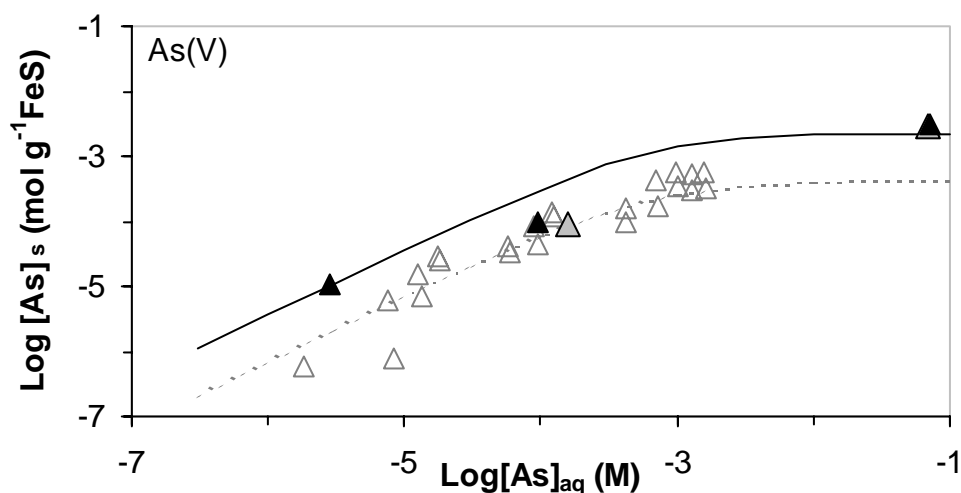


Figure 7. Sorption-isotherm graph for the As(V) data listed in Table 1. Black triangles are the sulphide-limited data; grey-filled triangles are the excess-sulphide data; the solid line is the Langmuir isotherm, equation (2) with $\log K_{\text{ads}}^* = +2.8$. The grey open triangles are the As(V) sorption data from chapter 4; the dashed line is the Langmuir isotherm, equation (2) with $\log K_{\text{ads}}^* = +3.2$. See section 4.1.1 for details.

Imaging, SAED and EDX analysis using the TEM confirmed this observation (Figures 3a and 3b). Traces of pyrite were also observed in the XRPD patterns, however, not reproducibly. With increasing $[\text{As(V)}]_0$, the diffraction peaks for mackinawite weaken and are replaced by elemental sulphur and green-rust peaks (Figure 2a). The total dissolved iron concentrations (Table 1) were constant over a wide range of $[\text{As(V)}]_0$ concentrations. Only at the highest $[\text{As(V)}]_0$, an increase in iron concentration of two orders of magnitude was found. The XRPD and dissolved iron data unambiguously show that $[\text{As(V)}]_0$ at concentrations higher than $\sim 1 \times 10^{-3}$ M, causes dissociation of the iron(II) sulphides and oxidation of the S(-II) to elemental sulphur and Fe(II) to Fe(III). In section 4.1.1., it was proposed that As(V) uptake by the solid phase is controlled by the sorption reaction (Eq. 2) onto FeS_{am} . At pH 6.0, the $\equiv\text{FeSH}_2^+$ site concentration is 2.25×10^{-3} mol per gram FeS_{am} . Thus, in the $\sim 1 \times 10^{-3}$ M $[\text{As(V)}]_0$ experiment (pattern 3 in Figure 2a), only $\sim 4\%$ of the surface sites are occupied. Contrastingly, at the highest $[\text{As(V)}]_0$ (pattern 4 in Figure 2a), all $\equiv\text{FeSH}_2^+$ sites at the FeS_{am} surface were occupied at the start of the experiment. This indicates that, at surface-site saturation, FeS_{am} is converted to elemental sulphur and green rust. Possible oxidation pathways are discussed in section 4.3.

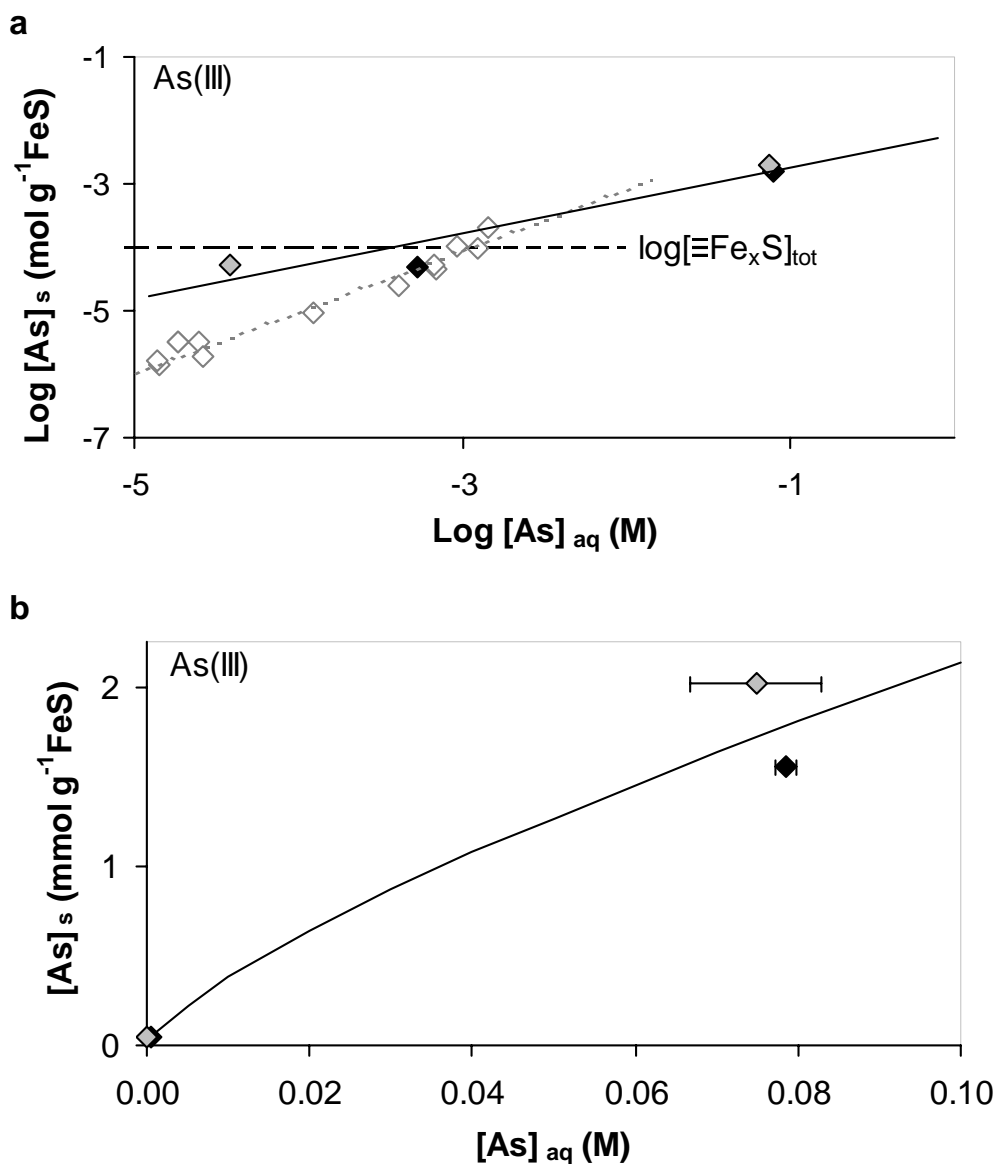


Figure 8. Sorption-isotherm graphs for the As(III) data listed in Table 3. (a) is the traditional log–log plot; (b) shows the same data as concentrations versus concentrations. Black diamonds are the sulphide-limited data; grey-filled diamonds are the excess-sulphide data; the solid line is the Freundlich isotherm from equation (4). The grey open triangles are the As(III) sorption data from chapter 4; the dashed line is the Freundlich isotherm from equation (3). See section 4.2.1 for details.

4.1.2.2. Excess-sulphide experiments

Even at the lowest $[\text{As(V)}]_0$, there are noticeable differences in the XRPD pattern relative to the blank diffraction pattern (Figure 2b). The pyrite diffraction peaks have decreased in intensity and the mackinawite peaks have weakened and broadened, which means that less pyrite and less crystalline mackinawite is formed relative to the blank experiment. This trend continues up to $\sim 1 \times 10^{-3}$ M $[\text{As(V)}]_0$ (pattern 3 in Figure 2b), when $\sim 4\%$ of the $\equiv\text{FeSH}_2^+$ sites are occupied. The fact that both FeS_{am} ripening towards mackinawite and FeS_{am} conversion to pyrite are retarded or inhibited, suggests that the $\equiv\text{FeSH}_2^+$ sites are crucial in iron(II) sulphide transformation mechanisms. This is discussed in detail in section 5.1.

Imaging, SAED and EDX analysis by TEM was performed on pyrite from the 1×10^{-7} M $[\text{As(V)}]_0$ experiment (Figures 3c and 3d). The SAED pattern of pyrite did not show the presence of forbidden h -odd reflections, only h -even $hk0$ reflections (Figure 3d). Weak forbidden h -odd reflections have been found for hydrothermal pyrite with 1.36–1.67 wt.% arsenic (Savage et al., 2000). Such reflections are interpreted as lattice deviations, in for example arsenic-rich lamellae, from the cubic symmetry of pyrite towards the marcasite-type structure (orthorhombic) of arsenopyrite (Pauling, 1978, Bayliss, 1989; Pósfai and Buseck, 1997; Savage et al., 2000). The absence of such forbidden reflections in the SAED pattern of Figure 3d indicates that the arsenic concentration in the pyrite is too low and evenly distributed to cause such structural deviations. A rough estimate of the As concentration in the pyrite, assuming all of the solid-phase As is present in pyrite and that $\sim 60\%$ of the solid phase is pyrite, yields an As concentration in the ppb range. This explains both the absence of the forbidden reflections and of As peaks in the EDX spectra.

Similar to the limited-sulphide experimental results, all iron(II) sulphide is converted to elemental sulphur and green rust (pattern 4 in Figure 2b), at initial reactive-site saturation on the FeS_{am} surface. Likewise, the total dissolved iron concentrations (Table 1) were constant over the whole range of $[\text{As(V)}]_0$ concentrations except at the highest $[\text{As(V)}]_0$. This again shows that As(V), at concentrations higher than $\sim 1 \times 10^{-3}$ M, causes dissociation of the iron(II) sulphides and oxidation of the S(–II) to S(0) and Fe(II) to Fe(III).

4.2. As(III)

4.2.1. Aqueous As(III)

Similar to the As(V) experiments, the amount of arsenic associated with the solid phase in the end product of the As(III) experiments does not depend on excess sulphide (Table 3). Thus, the uptake of As(III) is controlled by the freeze-dried FeS_{am} starting material. In chapter 4, As(III) sorption onto FeS_{am} was found to be heterogeneous and was described in terms of a Freundlich isotherm:

$$(3) \quad [\text{As}]_{\text{ads}} = 0.74[\text{As}]_{\text{aq}}^{0.97} \quad \text{pH} = 7.4$$

where $[\text{As}]_{\text{ads}}$ is the amount of sorbed As(III) and $[\text{As}]_{\text{aq}}$ is the dissolved As(III) concentration (Figure 8a). If the data from the present batch experiments (Table 3) for both the sulphide-limited and excess-sulphide experiments are plotted on a logarithmic sorption isotherm graph (Figure 8a), a similar linear behaviour is suggested. This linear behaviour can be described in terms of a Freundlich isotherm:

$$(4) \quad [\text{As}]_{\text{s}} = 0.01[\text{As}]_{\text{aq}}^{0.75} \quad \text{pH} = 6$$

Generally, log–log plots tend to smooth out scatter and subtle trends in the data. To justify the applicability of the Freundlich isotherm to the dissolved As(III) data, the data are replotted in Figure 8b as $[\text{As}]_{\text{s}}$ versus $[\text{As}]_{\text{aq}}$ with the Freundlich isotherm (Eq. 4). As can be seen in Figure 8b, the calculated isotherm (solid line) still describes the data reasonably well.

The association of As(III) with the solid phase in the present batch experiments can thus be described in terms of a Freundlich isotherm, implying that sorption may occur at different site types with different sorption affinities (cf. Dzombak and Morel, 1990). From this result, no conclusions can be drawn with respect to the phase controlling As(III) uptake by the solid. However, combining the observed H_2S -independent uptake of As(III) (Table 3) with the implied heterogeneous sorption, it can be concluded that As(III) sorption onto FeS_{am} may well be the reaction controlling the uptake into the solid phase in the present batch experiments.

4.2.2. Solid characteristics

4.2.2.1. Sulphide-limited experiments

With increasing $[\text{As(III)}]_0$, no clear change in the diffraction patterns is observed (Figure 5a). At the highest $[\text{As(III)}]_0$, a slight increase in diffraction intensity is observed, although this may be caused by a more optimal sample loading on the glass slide. All patterns can be described as FeS_{am} diffraction patterns. TEM imaging, SAED and EDX analysis confirmed this observation (Figures 6a and 6b). The total dissolved iron concentrations (Table 3) increased one order of magnitude with increasing $[\text{As(III)}]_0$ before decreasing to blank level at the highest $[\text{As(III)}]_0$. The same total dissolved iron trend was observed in the excess-sulphide experiments with As(III). At pH 6.0, the $\equiv\text{FeSH}_2^+$ site concentration is 2.25×10^{-3} mol per gram FeS_{am} and the total surface site concentration is 4.5×10^{-3} mol per gram FeS_{am} (chapter 3). Thus, at the start of the experiment with the highest $[\text{As(III)}]_0$ (pattern 4 in Figures 5a and 5b), approximately all $\equiv\text{FeSH}_2^+$ sites or ~50% of all sites at the FeS_{am} surface were occupied. It may be concluded that low sorption density of As(III) at the FeS_{am} surface increases Fe(II) loss from the solid reflecting a relative increase in FeS_{am} solubility. An explanation for this observation could be, for example, thioarsenite complex formation in solution. This trend is reversed at 50% site coverage, when possibly all $\equiv\text{FeSH}_2^+$ sites are occupied by As(III) and dissolution may be inhibited by blocking of the reactive sites. Additionally, at higher $[\text{As(III)}]_0$, the reduction to As(0) and the formation of less soluble Fe(As,S)_2 may become favourable.

4.2.2.2. Excess-sulphide experiments

Relative to the blank patterns, the diffraction intensity of the iron(II) sulphides weaken with increasing $[\text{As(III)}]_0$ (Figure 5b). At the highest $[\text{As(III)}]_0$, only weakened and broadened diffraction peaks of mackinawite, comparable to FeS_{am} diffraction peaks, remain. The total dissolved iron concentrations (Table 3) increased two orders of magnitude with increasing $[\text{As(III)}]_0$ before decreasing to blank level at the highest $[\text{As(III)}]_0$. Apparently, pyrite formation

is inhibited, possibly due to stabilisation of FeS_{am} by sorption at the FeS_{am} surface. Implications of these results for pyrite formation pathways are discussed in section 5.1.2.

4.3. Redox reactions

4.3.1. Thermodynamic calculations

In the As(V) experiments, the XRPD results clearly show the oxidation of S(-II) and Fe(II), and the reduction of As(V) was suggested from the XANES analyses. In order to test which redox reactions are thermodynamically favourable in the batch experiments, the changes in Gibbs energy were estimated for several potential redox reactions. Table 4 lists the reduction reactions for As(V) and for As(III) by S(-II) and Fe(II), with the standard Gibbs-energy changes and the reaction quotients. The changes in Gibbs energy listed in Table 5 were calculated from the estimated initial reaction conditions (see caption, Table 5). Note that these values are mere indications of the directions likely to be taken by the redox reactions in the solution.

The thermodynamic calculations suggest that initially: (i) S(-II) oxidation by As(V) was energetically favourable in all As(V) experiments; (ii) S(-II) oxidation by As(III) was energetically favourable only in the excess-sulphide experiments at initially added arsenic concentration higher than $\sim 1 \times 10^{-4}$ M; and (iii) Fe(II) oxidation by arsenic was never energetically favourable. It can be concluded that As(V) reduction by S(-II) in solution may have occurred at the start of all As(V) experiments. Under specific conditions (Table 5), As(III) reduction by S(-II) may have occurred in solution. However, the formation of green rust was most likely a reduction in the solid phase, that is, oxidation of iron(II) sulphide by As(V).

4.3.2. Arsenic oxidation state in pyrite

From the As *K*-edge profile obtained from the XANES analysis (Figure 4), it could be concluded that the oxidation number of arsenic associated with the

Table 4. Possible reduction reactions in the Fe–S–As system, the standard changes in Gibbs energy, ΔG_r^0 , for the reactions, and the reaction quotient. Thermodynamic data for the reactions were calculated from half reactions listed in the Wateq4f database in PHREEQC (Parkhurst and Appelo, 1999). r_1 – r_4 are reaction numbers referred to in Table 5.

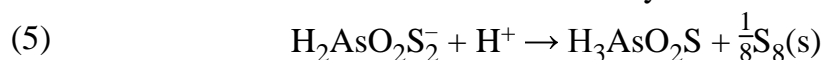
		Reduction reaction	ΔG_r^0 (kJ mol ⁻¹)	Reaction quotient
As(V) to As(III)	r_1	$\text{H}_2\text{AsO}_4^- + \text{H}_2\text{S} + \text{H}^+ = \text{H}_3\text{AsO}_3^0 + \text{S}^0 + \text{H}_2\text{O}$	-92.8	$\frac{\{\text{H}_3\text{AsO}_3^0\}}{\{\text{H}_2\text{AsO}_4^-\} \{\text{H}_2\text{S}\} \{\text{H}^+\}}$
	r_2	$\text{H}_2\text{AsO}_4^- + 2\text{Fe}^{2+} + 3\text{H}^+ = \text{H}_3\text{AsO}_3^0 + 2\text{Fe}^{3+} + \text{H}_2\text{O}$	+28.0	$\frac{\{\text{H}_3\text{AsO}_3^0\} \{\text{Fe}^{3+}\}^2}{\{\text{H}_2\text{AsO}_4^-\} \{\text{Fe}^{2+}\}^2 \{\text{H}^+\}^3}$
As(III) to As(0)	r_3	$2\text{H}_3\text{AsO}_3^0 + 3\text{H}_2\text{S} = 2\text{As}^0 + 3\text{S}^0 + 6\text{H}_2\text{O}$	-55.33	$\frac{1}{\{\text{H}_3\text{AsO}_3^0\}^2 \{\text{H}_2\text{S}\}^3}$
	r_4	$\text{H}_3\text{AsO}_3^0 + 3\text{Fe}^{2+} + 3\text{H}^+ = \text{As}^0 + 3\text{Fe}^{3+} + 3\text{H}_2\text{O}$	+153.49	$\frac{\{\text{Fe}^{3+}\}^3}{\{\text{H}_3\text{AsO}_3^0\} \{\text{Fe}^{2+}\}^3 \{\text{H}^+\}^3}$

synthetic refined pyrite fraction is -1 . This is in agreement with results from Tingle et al. (1996) and Savage et al. (2000), who found an oxidation number of -1 of arsenic in arsenian pyrite.

The As concentration in the pyrite sample is too low for EXAFS analysis of the nearest neighbour environment of As in the pyrite structure. Savage et al. (2000) found good support from their EXAFS data that As in their arsenian pyrite substitutes for S. Tossell et al. (1981) used molecular orbital theory to predict the electronic structure of the dianions in pyrite and arsenopyrite. The best description, according to Tossell et al. (1981), is $\text{AsS}(-\text{II})$ for the dianion in arsenopyrite and $\text{S}_2(-\text{II})$ in pyrite, with an oxidation number of sulphur and arsenic in the dianions of -1 . Thus, it may be assumed that the observed oxidation number of -1 for arsenic in the present synthetic pyrite results from the substitution by As for S in the covalently bonded dianion.

An $\text{AsS}(-\text{II})$ dianion may be formed from the binding between an $\text{S}(-\text{II})$ and an $\text{As}(0)$. The reduction of $\text{As}(\text{III})$ to $\text{As}(0)$ is energetically favourable only in the excess-sulphide experiments at added arsenic concentration higher than $\sim 1 \times 10^{-4}$ M (Table 5). The pyrite containing $\text{As}(-\text{I})$ was formed at $[\text{As}(\text{V})]_0 = 8.8 \times 10^{-5}$ M, when, according to the thermodynamic calculations, $\text{As}(0)$ formation according to the aqueous reduction reaction listed in Table 5 was not favourable. In this reaction $\text{As}(0)$ and $\text{S}(0)$ are produced. If these reaction products are consumed in a subsequent reaction, this will, of course, influence the thermodynamics of the overall reaction. The $\text{As}(\text{III})$ reduction reaction may occur, when the sum of the changes in Gibbs energy of the reduction reaction and the subsequent reaction is negative. Both $\text{As}(0)$ and $\text{S}(0)$ are consumed in the formation of the $\text{S}_2(-\text{II})$ and $\text{AsS}(-\text{II})$ dianions. So, the driving force behind the reduction of $\text{As}(\text{III})$ to $\text{As}(0)$ necessary for arsenic incorporation in the pyrite structure may, in fact, be pyrite formation itself. Alternatively, the reduction of arsenic may follow a different pathway than the simple solution reactions listed in Table 4, with, consequently, different reaction energetics. Nonetheless, it can be inferred that $\text{As}(\text{III})$ reduction is likely to occur at the iron(II) sulphide surface since: (i) the total $\text{As}(\text{V})$ and $\text{As}(\text{III})$ uptake by the solid is controlled by sorption; (ii) the formation of green rust points to $\text{As}(\text{V})$ reduction at the iron(II) sulphide surface; and (iii) arsenic incorporated in pyrite has been reduced to form $\text{AsS}(-\text{II})$.

Iron(II) sulphide oxidation by As(V) or As(III) has not previously been reported. Contrastingly, S(-II) oxidation by As(V) in the aqueous phase has been reported in literature. Rochette et al. (2000) have studied the rate and mechanism of As(V) reduction by S(-II) at pH 4 and S:As = (266:133) $\times 10^{-6}$ M. They describe the first two steps in the reaction mechanism as ligand exchanges where oxo groups are replaced by sulphide groups to form thioarsenate and dithioarsenate. Within 75 hours of their experiments, essentially all As(V) was converted to (di)thioarsenate. The actual reduction reaction Rochette et al. (2000) propose is an electron transfer within the dithioarsenate and formation of thioarsenite by release of the S(0):



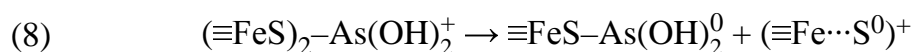
Subsequently, thioarsenite is thought to undergo ligand exchange to either dithioarsenite or As(III), depending on the S(-II) concentration. The concentration of As(III) was found to increase extensively after the first ~50 hours of their experiments. Furthermore, they observed orpiment, As_2S_3 , and small quantities of realgar, AsS, polysulphides and elemental sulphur in the Raman spectra of the solid phase after 330 hours (~2 weeks) of reaction.

If, in the present experiments, As(V) reduction occurs at the FeS_{am} -surface via a similar mechanism as postulated by Rochette et al. (2000), then the first steps in the mechanism would be for the As(V) surface complex from equation (2) to undergo ligand exchange, for example, as follows:



Probably, a second sulphur surface site is involved in reaction (6). The first ligand exchange, reaction (6), could explain the slight pH increase observed in the As(V) sorption experiments reported in chapter 4. The formation of a monodentate dithioarsenate surface complex (that is, by ligand exchange of an oxo group for an aqueous sulphide), instead of the bidentate complex, cannot explain the oxidation observed in the sulphide-limited experiments. Therefore, a bidentate dithioarsenate complex is suggested in reaction (7).

The next step in the reaction mechanism, provided it is similar to the mechanism postulated by Rochette et al. (2000), would be the actual reduction of dithioarsenate to thioarsenite:



The resulting complex is a monodentate thioarsenite surface complex. The elemental sulphur formed may be released from the surface, as is suggested by the XRPD data. S(0) release would create a reactive $\equiv\text{Fe}^+$ site for H_2S sorption and, therefore, cause regeneration of an $\equiv\text{FeSH}_2^+$ site. Hence, this reaction mechanism may be surface catalysed.

The surface complexes suggested in reactions (6) to (8) may have been observed by Farquhar et al. (2002), who studied As(V) and As(III) sorption and coprecipitation onto mackinawite and pyrite using X-ray absorption spectroscopy (XAS). In their coprecipitation experiments with an initially added sulphide, $[\text{S}(-\text{II})]_0$, to $[\text{As}(\text{V})]_0$ ratio of approximately 2:1, they observed arsenic coordination to 2.5 oxygen atoms in the first shell at 0.170 nm, to 1.5 sulphur atoms in the second shell at 0.233 nm and four arsenic atoms in the third shell at 0.335 nm (Table 6 in chapter 1). This can be explained by a mixture of thioarsenate and dithioarsenate species at the surface of mackinawite. Note that the observed As–S distance would result in a S–As–S angle of 107° for the bidentate dithioarsenate surface complex formed in reaction (5), since the S–S distance between two $\equiv\text{FeS}$ -groups is 0.368 nm (Uda, 1968). The resulting surface-complex structure is identical to $\text{As}(\text{SH})_3$ (Helz et al., 1995) and is therefore structurally feasible. In their experiments with $[\text{S}(-\text{II})]_0:[\text{As}(\text{V})]_0 \approx 20:1$, Farquhar et al. (2002) observed arsenic coordination to 3 sulphur atoms at 0.223 nm in the first shell, and 2 sulphur atoms at 0.269 nm in the second shell and explained this by As_2S_3 -precipitation at the surface. Furthermore, in their $[\text{S}]_{\text{ad}}:[\text{As}(\text{III})]_{\text{ad}} \approx 2:1$ As(III) experiment, they observed arsenic coordination to 1 oxygen atom at 0.179 nm in the first shell, to 1 sulphur atom at 0.230 nm in the second shell, to 0.5 sulphur at 0.273 nm in the third shell and to 0.5 sulphur in the fourth shell at 0.316 nm (Table 7 in chapter 1). This can be explained as a dithioarsenite species at the surface of mackinawite. In summary, the proposed reaction mechanism for the reduction of As(V) to As(III) by S(-II) in FeS_{am} , based on the mechanism postulated by Rochette et al. (2000) for the reduction of As(V) by aqueous sulphide, seems to be supported by the XAS results from Farquhar et al. (2002).

The formation of a thioarsenite complex (reaction 8) will change the free energy of change for the reduction of As(III) to As(0) (Tables 4 and 5), possibly in favour of the formation of As(0). Furthermore, the reduction of thioarsenite may occur at the surface or within the solid. No relevant data are available in the literature on potential reduction mechanisms or structures, nor

on reduction rates. The way to test potential reduction mechanisms, in particular for As(III), would be by detailed kinetic experiments, supported by XAS measurements of oxidation states and nearest-neighbour environment changes of As at iron(II) sulphide surfaces. Such experiments should run for several weeks, since As(V) reduction is slow at pH values of 6–8.5 (cf. chapter 4 and Rochette et al., 2000).

From the above discussions, it can be concluded that the reduction of As(V) in the batch experiments may occur through three different reduction reactions occurring. (i) The thermodynamic calculations suggests reduction by S(–II) in solution. (ii) The XRPD results in combination with the thermodynamic calculations points to the reduction by Fe(II) in the solid phase. (iii) The discussion based on the work from Farquhar et al. (2002) and Rochette et al. (2000) shows that reduction by S(–II) at the FeS_{am} surface is possible.

4.4. Limitations

Batch experiments have the advantage of the ease of setting up and running many experiments at the same time. However, they are in general limited by high reactant concentrations and intermediate data points; the present experiments are no exception. At initiation of the experiments, reactants, buffers and poises were mixed, the ampoule was sealed and, after four weeks, the solid end products and the supernatant were analysed. No information about intermediate reaction conditions or products could be collected, except for possible colour changes in the supernatant and solid. The oxidation-reduction potential in the system is likely to change during the experiments, as was discussed in section 2.1. Furthermore, the concentration and thus distribution of all species vary strongly over the course of an experiment and, consequently, the ionic strength and mineral saturation states co-vary. Estimating the ionic strength, I , at the start and end of the As(V) experiments, by assuming aqueous species are not complexed, shows variations of $0.06 < I < 0.08$ M in the highest $[\text{As(V)}]_0$ experiments and $I \approx 0.015$ M in the other As(V) experiments. In the As(III) experiments, higher ionic strengths are caused by the increase in dissolved iron: $0.106 < I < 0.107$ M at highest $[\text{As(III)}]_0$, and I decreases with decreasing $[\text{As(III)}]_0$ concentration from $0.016 < I < 0.03$ M to $I \approx 0.015$ M.

Nevertheless, the As(V) and As(III) sorption data presented in chapter 4 could be successfully extrapolated to the results of the batch experiments.

Furthermore, the As(V) reduction mechanism from Rochette et al. (2000) and the XAS data of coprecipitated As(V) and As(III) at the surface of mackinawite (Farquhar et al., 2002) were studied at similar S(-II) to arsenic ratios and could be used to enhance the interpretation of the batch experimental results. In conclusion, even though the interpretation of the batch results in itself is limited by the lack of control on the reaction conditions and intermediaries, the results are in agreement with and, thus, supported by results from several different lines of experiments and analysis.

5. Implications

5.1. Iron(II) sulphide transformations

Even at the lowest As(V) and As(III) concentrations, there are noticeable differences in the XRPD pattern relative to the blank diffraction (pattern 2 in Figure 2b for As(V) and pattern 2 in Figure 5b for As(III)). The pyrite diffraction peaks have decreased in intensity and the mackinawite peaks have weakened and broadened. The fact that both FeS_{am} ripening towards mackinawite and FeS_{am} conversion towards pyrite are slowed down or prevented to run to completion, suggests that the sorption sites for As(V) and As(III) are crucial not only as sorption sites, but also in iron(II) sulphide transformation mechanisms.

5.1.1. Ageing of FeS_{am} to mackinawite

Sorption of protons onto iron(II) disulphide surface has been reported to distort the S geometry around Fe and thus cause the pH dependent formation of marcasite in preference to stable pyrite (Tossell et al., 1981). Similarly, Lennie and Vaughan (1996) proposed the pH dependent occurrence of cubic FeS and troilite by interaction of surface bound protons with the electronic structure in the solid.

As(V) sorption has been found to stabilise hydrous ferric oxides (HFO) with respect to transformations to more stable crystalline phases due to the modification of the local environment of a significant fraction of the iron in the solid (Waychunas et al., 1996; Rancourt et al., 2001). Rancourt et al. (2001)

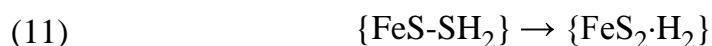
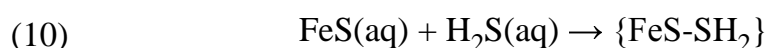
account for the distortion of the local iron environment by perturbation of the Fe(III) electronic orbitals.

FeS_{am} ages to mackinawite (Berner, 1964; Rickard, 1989; Lennie and Vaughan, 1996; Benning et al., 2000) through a solid-state recrystallisation. Possibly, sorption of As(V) and As(III) influence the electronic structure of FeS_{am} in a similar way as As(V) sorption onto HFO and hence prevent the transformation of FeS_{am} to mackinawite.

5.1.2. The mechanism of pyrite formation

All the reaction mechanisms determined for pyrite formation in aqueous solutions at ambient temperatures involve a dissolved stage (Rickard, 1975; Luther 1991; Rickard and Luther, 1997). Any process that affects the dissolved intermediates or the solubility of the disordered mackinawite reactant, will therefore also affect the kinetics of pyrite formation. This has been demonstrated by Rickard et al. (2001).

In this study, pyrite synthesis followed the method of Rickard (1997). According to Rickard and Luther (1997), pyrite formation occurs via the H₂S-oxidation pathway in the blank experimental conditions (pattern 1 in Figures 2b and 3b). The mechanism they proposed consists of four steps:



where FeS(aq) is a highly reactive, dissolved FeS cluster complex (chapter 2). Important to the present study is reaction (9), which involves the dissolution of FeS_{am} to form the FeS cluster complex FeS(aq).

Rickard et al. (2001) showed that C=O in trace amounts inhibits pyrite formation by attacking, or preventing the formation of, FeS(aq). Similarly, As(V) and As(III) may affect the reaction mechanism given above. For example, the reactivity of the FeS_{am} surface will be changed by As(V) or As(III) sorption at the high-affinity sites. Moreover, the labile FeS(aq) cluster complex is likely to react rapidly with As(V) or As(III) near the FeS_{am} surface to form iron(II)-sulphide-arsenic complexes. This would inhibit pyrite formation. Likewise, As(V) and As(III) sorption onto the reactant FeS_{am}

surface may affect pyrite formation by decreasing the solubility of the reactant FeS_{am} , and, in the case of As(V), by oxidation of FeS_{am} . If the surface of the precursor is modified, and the $\text{FeS}(\text{aq})$ cluster complex is attacked or its formation is inhibited, then the rate of pyrite formation is affected.

Nucleation kinetics played an important role in the pyrite formation during these experiments (cf. Butler and Rickard, 2000). The reactant concentrations were high and, therefore, the solutions were initially highly supersaturated with respect to pyrite. Therefore, nucleation was likely to be fast relative to crystal growth. The fact that arsenic retards and inhibits pyrite formation which is dominated by nucleation indicates a strong effect of arsenic on pyrite nucleation.

5.2. Arsenic mobility in the anoxic environment

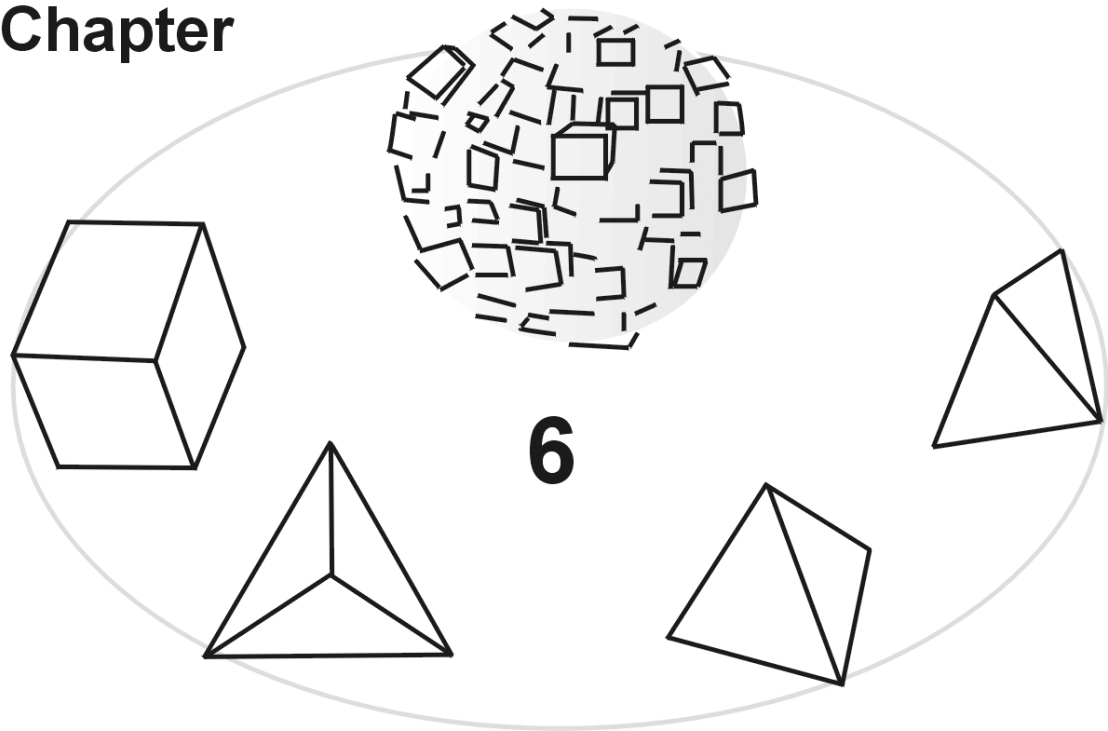
Arsenic uptake by mixture of the environmentally most-abundant iron(II) sulphides is controlled by the most reactive solid phase, that is, FeS_{am} . This uptake can be described using sorption isotherm notations. Such isotherm data can be used in arsenic transport modelling, to predict the mobility and immobilisation of arsenic in the anoxic sulphidic environment. Furthermore, results from this study suggest that the transformation of the precursor FeS_{am} to the most stable and ubiquitous iron(II) sulphide pyrite is retarded by As(V) and As(III) sorption, even at natural levels of aqueous arsenic (cf. Table 4 in chapter 1). In this way, arsenic sorption retards the rate of formation of a relatively more stable natural As sink.

Acknowledgements

We gratefully acknowledge Anthony Oldroyd for his assistance with the experiments and XRPD measurements, John Charnock for assistance with the XANES measurements, Sarah Goldsmith for performing the ICP–MS analyses, Colin Lewis for conducting the AAS measurements and Herman van Roermund for his assistance with the TEM. Cornelis H. van der Weijden (Utrecht University) and Peter van der Linde (University of Professional Education Leiden) provided insightful discussions over the course of this study. This research was supported by the Netherlands Organization of Scientific Research (NWO/ALW grant 750.197.06 to M.W) and by NERC grant

NERLS200000611 to D.R. This research was conducted under the program of the Netherlands Research School of Sedimentary Geology.

Chapter



Arsenic incorporation into pyrite at ambient environmental conditions: a continuous-flow experiment*

* Authors: Wolthers M., Butler I.B., Rickard D., Mason P.R.D.

Abstract

Pyrite was synthesised in the presence of As(III) at concentrations approaching those in ambient environments, under controlled, monitored, anoxic conditions in a continuous-flow reaction system at pH 6 and 25°C. The pyrite textures formed were strongly influenced by the surface quality of the pyrite seeds used and possibly by other subtle differences between runs. No effect of As(III) on the amount of pyrite or on the textures formed was observed. Pyrite crystal growth dominated nucleation during most of the experiment time. During the continuous pyrite growth in these experiments, a continued uptake and incorporation of arsenic by pyrite was observed. So, the experimental results indicate that pyrite crystal growth is not, or not strongly, affected by As(III).

1. Introduction

Pyrite is the most stable and ubiquitous authigenic iron(II) sulphide phase in the Earth surface environment. Many different reactions for pyrite, FeS_2 , formation at ambient conditions have been suggested (e.g., Morse et al., 1987 and references therein; Wilkin and Barnes, 1997) but detailed mechanistic investigations have only been reported by Rickard (1975), Luther (1991), Rickard (1997) and Rickard and Luther (1997). A general conclusion is that the formation of the relatively oxidised $\text{S}_2(-\text{II})$ disulphide ion is obviously a prerequisite for any pyrite forming reaction. Nucleation of pyrite occurs on existing pyrite surfaces (Harmandes et al., 1998, Butler et al., submitted), on organic surfaces (Grimes et al., 2001) and, possibly, on defects on the precursor FeS_{am} surface (Wang and Morse, 1996).

Extensive scavenging of trace elements by pyrite has been reported by for example Huerta-Díaz and Morse (1992) and Morse and Luther (1999). Through this scavenging, pyrite plays an important role in retarding the migration of trace elements in the anoxic environment. Huerta-Díaz and Morse (1992) found concentrations of As in marine sedimentary pyrites to be ranging up to 0.93 wt%. Their results indicated that sedimentary pyrite is an important sink for As, even if only minor pyrite formation has taken place.

Table 1. Arsenic concentrations in natural waters. [1] Andreae (1980); [2] Scudlark and Church (1988); [3] Barbaris and Betterton (1996); [4] Andreae et al. (1983); [5] Froelich et al. (1985); [6] Seyler and Martin (1991); [7] Azcue et al. (1994, 1995); [8] Azcue and Nriagu (1995); [9] Seyler and Martin (1989); [10] Baur and Onishi (1969); [11] Reuther (1992); [12] Abdullah et al. (1995); [13] Peterson and Carpenter (1983); [14] Seyler and Martin (1990); [15] Cullen and Reimer (1989); [16] Yusof et al. (1994); [17] Navarro et al. (1993); [18] Maher (1985); [19] Widerlund and Ingri (1995); [20] Yan et al. (2000); [21] Sullivan and Aller (1996) (from Smedley and Kinniburgh, 2002)

Water body	Range ($\times 10^{-6}$ M)	References
Rain water	<0.01	[1]–[3]
River water	0.002–0.028	[4]–[6]
Lake water	0.001–0.123	[7]–[11]
Estuarine water	0.009–0.051	[6], [12]–[14]
Seawater	0.007–0.049	[15]–[18]
Sediment pore water	0.017–4.005	[19]–[21]

In chapter 5, the association of As(V) and As(III) with FeS_{am} was studied in batch experiments. It was shown that, with increasing initially added As(III) concentrations, the transformation of FeS_{am} to mackinawite and pyrite is inhibited by stabilisation of the precursor FeS_{am} surface and (or) prevention of the essential intermediate aqueous FeS cluster complex (cf. Rickard and Luther, 1997; Butler and Rickard, 2000; Rickard et al., 2001). Sorption onto the FeS_{am} surface was suggested as a control on the uptake of As(III) into the solid phase. However, as discussed in chapter 5, batch experiments are limited by reactant concentrations and uncontrolled conditions during the experiments.

In this chapter, pyrite synthesis in the presence of arsenic levels similar to those of natural sediment pore waters (Table 1) was studied under strictly controlled and monitored conditions in the continuous-flow reaction system described by Butler et al. (submitted). Arsenic was added as As(III), which is the dominant aqueous arsenic species in anoxic environments (Andreae, 1979; Andreae and Froelich, 1984; Edenborn et al, 1986; Brannon and Patrick, 1987; Sadiq, 1990; Kuhn and Sigg, 1993; Abdullah et al., 1995; Gonzalez Soto et al., 1996). Changes in the solution chemistry were monitored *in situ* via electrodes and *ex situ* by regular sampling and analyses ICP–MS and AAS. The precipitates were characterised by scanning electron microscopy (SEM), X-ray powder diffraction (XRPD) and laser-ablation ICP–MS. The results are

interpreted in terms of solution chemistry stability, pyrite textures formed, the effect of arsenic on, and the fate of As(III) during, pyrite formation.

2. Materials and methods

2.1. Materials

All chemicals were analytical grade Fisher ChemicalsTM and used without further purification. Solutions were prepared from 18 M Ω distilled deionised water. The background ionic medium was 0.2 M NaCl. Acid and base solutions, of 0.01 M concentration, were prepared from concentrated HCl and NaOH pellets. A 2.0×10^{-3} M sulphide solution was made by dissolving Na₂S·9H₂O in 0.2 M NaCl. A 6.0×10^{-4} M Fe(II) solution was prepared by dissolving Mohr's salt (Fe(NH₄)₂(SO₄)₂·4H₂O) in the background ionic medium. A 1×10^{-2} M As(III) solution was prepared by dissolving NaAsO₂ in deionised water. The Fe(II) solution was spiked with As(III) by adding 0.1 mL of the As(III) solution. The As(III) reservoir concentration was 1.1×10^{-6} M.

Immediately after preparation, the solutions were poured into the O₂-free N₂-filled reservoirs of the chemostat (section 2.2), while vigorously purging with O₂-free N₂, and the reservoirs were sealed. Analytical grade O₂-free N₂ passed through a SupelcoTM high capacity gas purifier to remove traces of O₂ prior to flushing into the reservoirs and the chemostat (section 2.2).

Cubic pyrite crystals, purchased at R.G. Widdowson (Scarborough, U.K.), were embedded in EpotechTM resin. The resin was cut into rectangles with two cm-sized pyrite cubes per block and from each cube one (001) face was exposed by carefully cutting and polishing off the resin. Handles were attached to the sides, to facilitate removal from the reaction vessel (section 2.2). The cubes were acid-washed with a 10% HCl solution. If there were any holes in the pyrite surfaces, where calcite inclusions had been removed by the acid, they were filled up with resin. Subsequently, the surfaces were polished with a water-based 800 μ m Al-oxide slurry, then KemetTM oil-based 14 μ m diamond paste and, finally, a water-based 0.3 μ m Al-oxide slurry. Before inserting the rectangular blocks into the reaction vessel, the pyrite surfaces were cleaned by rinsing with 10% HCl and with acetone and dried. One pyrite face was covered with TeflonTM tape as a control face.

2.2. Continuous-flow reaction system

The custom-built continuous-flow reaction system, or chemostat, in the Cardiff laboratory was used (Figure 1). The design and characteristics of the chemostat were described in detail by Butler et al. (submitted). The main reaction vessel was an adapted NormschliffTM 2 L flat-bottomed vessel with a thermostatic jacket (A in Figure 1). The vessel could be sealed air-tight by pressing the greased ground-glass rims of the vessel and lid onto each other with a metal clamp. The reactant reservoirs were 2 L round-bottomed flasks with three ports (B in Figure 1) and the acid and base reservoirs were standard 1 L QuickfitTM culture vessels with five-necked lids (C in Figure 1). All connections for electrodes and tubing were air-tight clamped QuickfitTM cone-screwthread and socket connections. Via ground-glass sockets in the wall of the reaction vessel, around the top, tubings were inserted into the reaction vessel for solution inflow from the reservoirs via the peristaltic pumps.

Purified N₂ was delivered from the SupelcoTM high capacity gas purifier (granular Zr at > 300°C; F in Figure 1) to the reaction vessel and reservoirs via copper tubing connected by SwagelokTM fittings. Flow rates to the reservoirs were controlled using two NorgrenTM high flow rate control valves (G in Figure 1) and to the reaction vessel using a fine-control low-flow PorterTM precision pressure regulator (behind E in Figure 1). In the lids of the reaction vessel and reservoirs, a glass tube was incorporated through which the O₂-free N₂ flowed into the vessels via a sintered-glass block. During runs, the reaction vessel was kept at a slight over-pressure, typically 20–40 mbar above atmospheric pressure (Table 2), with purified N₂, to ensure O₂-free conditions. The pressure within the reaction vessel was monitored using an EbroTM pressure transducer incorporated in the lid. Reservoir-gas outflows ran through water traps to prevent back-flow of O₂ into the system via the outflows.

The temperature in the reaction vessel was controlled at $40 \pm 0.1^\circ \text{C}$ via the thermostatic jacket by a HaakeTM F6 water bath (Figure 1). Temperature in the reaction vessel was measured via a Pt-100 probe immersed into the solution. The solution volume was kept constant at $1.00 \pm 0.02 \text{ L}$ by a Gentech InternationalTM vertical float switch and controller connected to a 20 rpm Masterflex peristaltic pump (liquid level control in Figure 1). The solution was

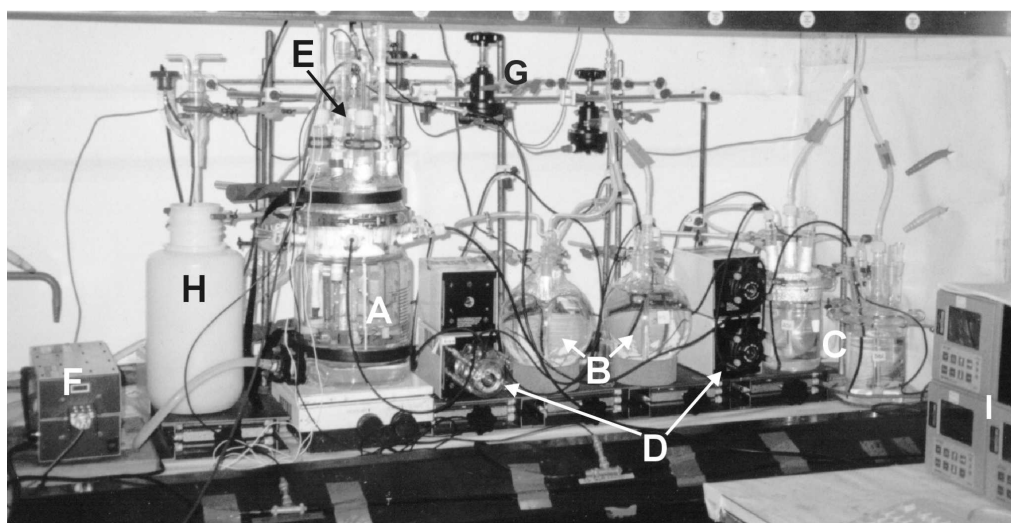
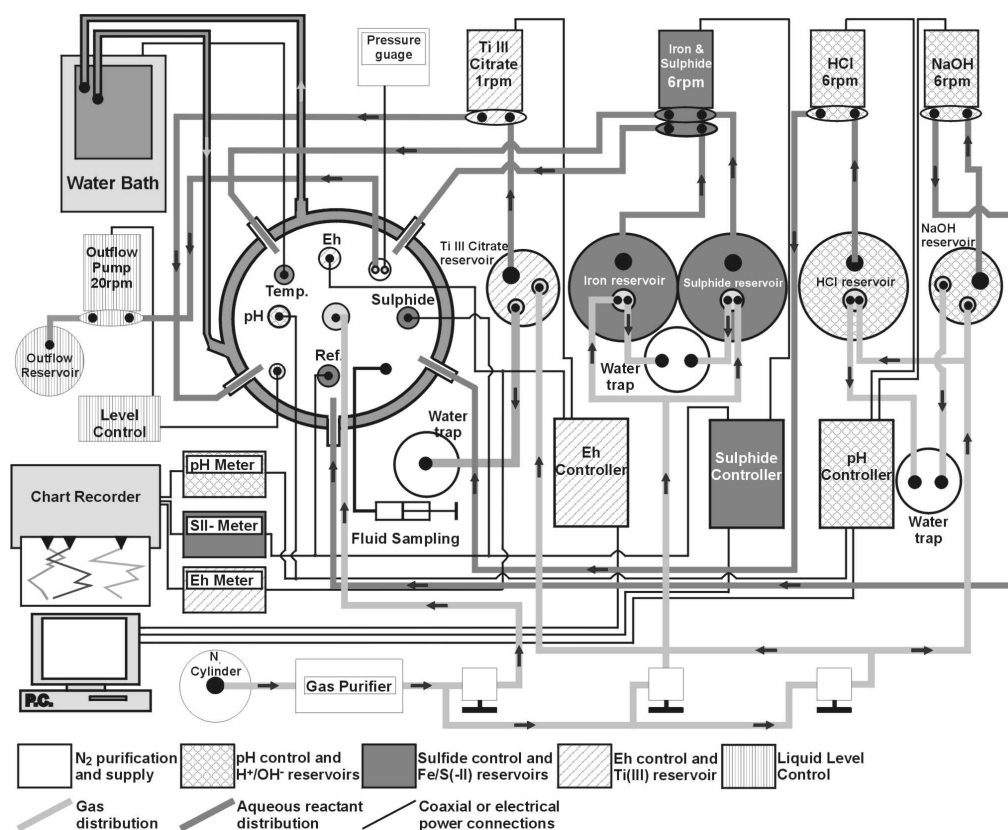


Figure 1. A schematic overview (top) and photograph (bottom) of the continuous flow reaction system (from Butler et al., submitted; used with permission). (A) reaction vessel; (B) iron(II) and sulphide reservoirs; (C) acid and base reservoirs; (D) peristaltic pumps; (E) electrode entries at reaction-vessel head; (F) O_2 -free N_2 -gas purifier; (G) O_2 -free N_2 -gas flow-rate control valves; (H) outflow reservoir; (I) process controllers. See section 2.2 for details.

kept homogenous by magnetic stirring (~60 rpm) with a TeflonTM-coated magnetic stirring bar.

The solution conditions in the reaction vessel were monitored using: (i) a gel-filled paper pulp combination pH electrode designed for reliability at high sulphide activity; (ii) a standard combination Pt electrode for redox potential measurements and; (iii) a Ag/Ag₂S sulphide specific electrode with a double-junction calomel reference electrode (E in Figure 1). The electrodes were linked to Hanna InstrumentsTM series 500 pH controller and two series 600 mV controllers (I in Figure 1). Data logging from the controllers was via RS232 output to a PC. As a back up, all electrode signals were fed into pH and mV meters with analogue outputs to a multi-pen RikadenkiTM chart recorder for real-time monitoring. The pH electrode was calibrated using HydrionTM pH 7.0 and 4.0 buffer solutions and checked for drift at the end of runs. The controller and meter were calibrated in-line. The Pt electrode was checked using Zobell's solution and the sulphide electrode was equilibrated and checked in a concentrated Na₂S·9H₂O solution.

The pH controller was set to keep the pH in the reaction vessel constant at 6.0 ± 0.05 by controlling the acid and base deliveries via the Cole-Palmer MasterflexTM low-flow (6 rpm) peristaltic pumps (D in Figure 1). The actual reaction pH varied slightly outside this range (Table 2). The redox potential was not controlled, only monitored. The sulphide controller was set to a constant slow addition of reagents to the reaction vessel at 0.36 mL min^{-1} at 6 rpm via the Cole-Palmer MasterflexTM low-flow (6 rpm) peristaltic pumps. The peristaltic-pump tubing was MasterflexTM LS13 Viton[®] tubing, which has extremely low O₂ permeability.

2.3. Continuous flow method

A day before an experiment was started, the reservoirs were filled with the reactant solutions and the reaction vessel was filled with approximately 1.5 L 0.2 M NaCl background ionic medium. Subsequently, the system was purged with O₂-free N₂ for approximately 24 hours; an hour before sealing the reaction vessel, the pyrite blocks were added to the reaction vessel. After sealing the reaction vessel, internal pressure built up and pH and liquid-level control were initiated. When both the pH and the internal pressure had stabilised, the

Table 2. Data for runs 1 and 2. p_{rv} = pressure, in mbar above ambient, in the reaction vessel; S(-II) and Eh are the uncalibrated millivolt signals from, respectively, the sulphide and redox potential electrodes; $[Fe]_{aq}$ is the total dissolved iron concentration measured by AAS; $[As]_{aq}$ is the arsenic concentration measured by ICP-MS; in the XRPD column the XRPD-identifiable products are listed, Py = pyrite. See section 2.4 for detection limits and standard deviations.

Run	Day	p_{rv} (mbar)	pH	S(-II) (mV)	Eh (mV)	$[Fe]_{aq}$ ($\times 10^{-5}$ M)	$[As]_{aq}$ ($\times 10^{-8}$ M)	XRPD	Remarks
1	0	21	6.05	-113	-222				Start of reagent pumps
	1	22	6.07	-530	-347				
	2	25	5.98	-535	-354	3.76 ± 0.07	2.7 ± 1.3	NaCl + FeS _{am}	
	3	23	6.03	-539	-359	3.12 ± 0.04	5.3 ± 1.3	NaCl	Pyrite block 1A retrieved
	4	20	6.07	-548	-356				
	5	22	6.01	-547	-356				
	6	35	6.08	-558	-363	2.04 ± 0.04	2.7 ± 1.3	NaCl	
	7	27	6.02	-550	-360	2.90 ± 0.04	5.3 ± 1.3	NaCl	
	8	27	6.09	-548	-354	2.72 ± 0.06	6.7 ± 1.3	NaCl	
	9	29	6.12	-551	-350	2.15 ± 0.03	5.3 ± 1.3	NaCl + Py	Pyrite block 1B retrieved
2	0	27	6.05	-70	-137				Start of reagent pumps
	1	35	6.02	-522	-321				
	2	28	5.98	-532	-333	4.72 ± 0.06	6.7 ± 1.3	NaCl + FeS _{am}	
	3	22	6.09	-528	-334	4.83 ± 0.02	9.3 ± 1.3	NaCl	Pyrite block 2A retrieved
	4	33	6.05	-527	-328				
	5	36	6.04	-532	-335				
	6	38	6.05	-538	-342				
	7	38	6.03	-547	-353	2.08 ± 0.01	d.l.	NaCl	
	8	37	6.05	-546	-393	2.44 ± 0.01	1.3 ± 1.3	NaCl	
	9	39	6.10	-545	-392			NaCl + Py	Pyrite block 2B retrieved

reactant pumps were started. The As(III)-doped iron(II) solution and the sulphide solution were added via the same peristaltic pump, which was fitted with two heads.

During the runs, sampling of the solution in the reaction vessel was done using a syringe and a tube which was incorporated via a socket in the wall of the vessel, near the top (Figure 1). Samples of ~40 mL were directly filtered through a Swinnex™ syringe filter-holder containing a 13 mm 0.2 µm white cellulose nitrate membrane filter disk and a cut Whatman no. 4 glass-fibre prefilter. Subsamples of the filtrate were stored in a sealed glass vial at 4°C until acidification and analysis for total Fe and As. Filter disks were freeze-dried and immediately analysed by XRPD. At the end of runs, 60 to 80 mL solution was sampled and filtered using a 0.02 µm Millipore™ filter under a N₂-filled hood. The solid was freeze-dried for ~24 hrs and stored at -18°C until XRPD analysis.

Pyrite blocks were removed from the reaction vessel, during and at the end of runs, via a port in the lid. During pyrite-block removal, the N₂-flow rate in the reaction vessel was temporarily increased. The blocks were washed with deionised water, freeze-dried and immediately Au-coated for SEM analyses. After coating, the blocks were stored in air-tight containers coating silica gel desiccant. After SEM analyses, the blocks were stored at -18°C for LA-ICP-MS analysis.

2.4. Analyses

Acidified solution samples were analysed for total dissolved arsenic using a Perkin Elmer™ Elan 5000 ICP-MS. The detection limit was 6.5×10^{-9} M (blank $\pm 5 \times$ s.d.). Total dissolved iron was measured using a Varian Spectra 300 acetylene-air-flame AAS. The detection limit was 7.4×10^{-9} M (blank $\pm 5 \times$ s.d.); errors listed (Table 2) are absolute analytical standard deviations.

SEM images and energy-dispersive X-ray (EDX) analyses of the Au-coated pyrite blocks were collected on a Leica/Cambridge Instruments S360 SEM. XRPD was carried out using a Philips™ PW170 based diffractometer (CuK α radiation, 35 kV, 40 mA). Freeze-dried samples on filter disks were loaded into a specimen holder. XRPD patterns, in the range of 3–80° 2 θ , were collected under air using the following settings: 0.1 mm receiving slit, 0.4 s/0.02° 2 θ counting time.

Laser ablation ICP–MS (LA–ICP–MS) analyses of a reacted and an unreacted pyrite block surface were performed using a MicromassTM Platform ICP equipped with a hexapole device (collision cell) for ion focussing and a quadrupole mass analyser. Samples were ablated with a MicrolasTM GeoLas 193 nm laser-ablation system, which delivers a homogenised beam at the sample surface, ideal for depth analysis. The system hardware is described in more detail by Mason and Kraan (2002). In order to work at the lowest possible ablation rate of $\sim 0.1 \mu\text{m}$ per pulse, the laser was set to 0.03 GW cm^{-2} irradiance (Mason and Mank, 2001). The laser-crater diameter was $120 \mu\text{m}$ and the pulse repetition rate was 1 Hz.

3. Results

The experimental conditions during the two runs are listed in Table 2. The electrode output signals were relatively stable after one day of reaction. The system showed a comparable stability to the experiments reported by Butler et al. (submitted). In run 1, the sulphide electrode output was $-544 \pm 14 \text{ mV}$ and in run 2 $-534 \pm 12 \text{ mV}$. The Eh closely followed the sulphide electrode signal. The total dissolved iron concentration was observed to decrease over the course of the runs. Dissolved arsenic was $(4.5 \pm 2.8) \times 10^{-8} \text{ M}$ during the runs, which is $\sim 5\%$ of the reservoir concentration. Thus, the conditions during the runs were stable and comparable between the two runs. The only significant difference was that, to keep the pH static in run 1, approximately twice the amount of acid was needed than in run 2, that is, 0.01 moles H^+ instead of 0.005 moles.

The suspended-solid concentration was generally too low to yield enough material for XRPD analyses during the runs, except at three days after reaction when the suspended FeS_{am} concentration was high enough. Usually, the only diffraction pattern observed was that of NaCl(s) (Table 2) from the background ionic medium. A larger volume, sampled from the bottom of the reaction vessel after magnetic stirring was stopped at the end of the runs, yielded enough material to show the presence of pyrite (Table 2).

SEM imaging and EDX analyses confirmed the formation of pyrite on the pyrite blocks after 9 days of reaction in runs 1 and 2. In run 1 after 3 days, precipitated FeS_{am} was found within holes in the pyrite surface (*pyrite block*

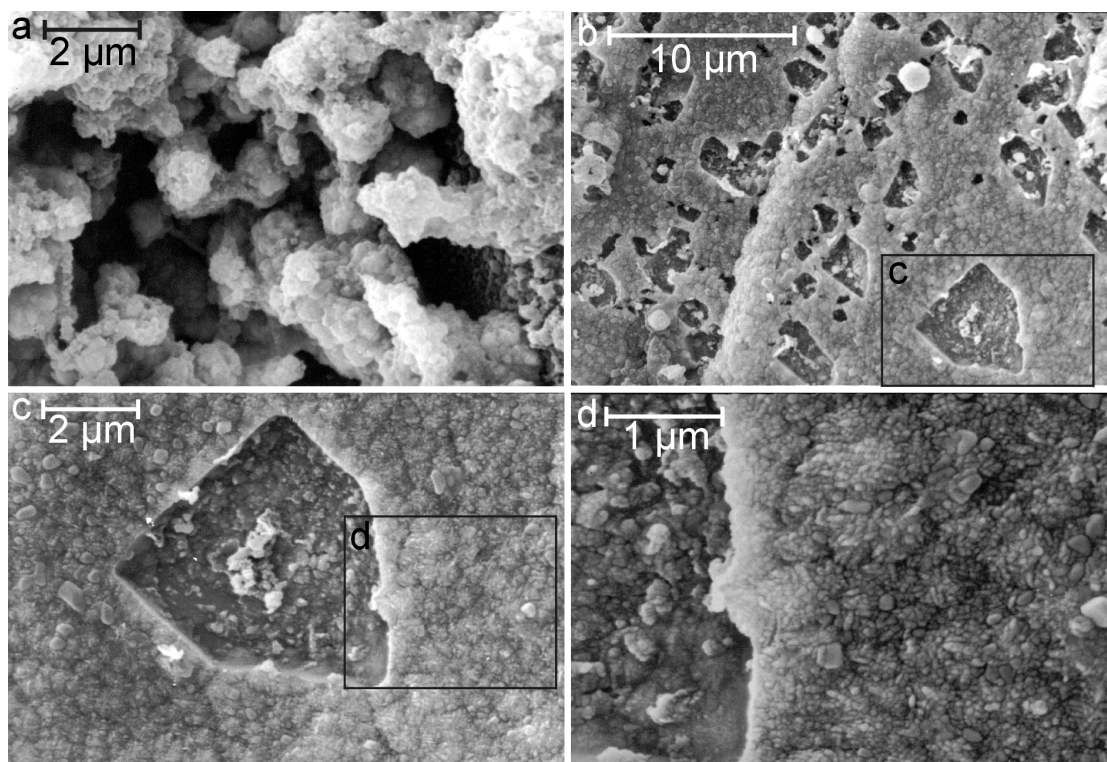


Figure 2. SEM images of (a) the unidentifiable precipitate formed on the still visible cubic pyrite surface of pyrite block 1A after 3 days of reaction in run 1. (b) subhedral pyrite formed epitaxially on the pyrite block 1B surface after 9 days of reaction in run 1.

1A, Figure 2a). EDX analysis of the precipitate returned Fe:S ratios characteristic of FeS. The block retrieved after 9 days displayed steps (*pyrite block 1B*, Figure 2b) and holes in the surface and the precipitate formed as a surface overgrowth consisted of subhedral sub-micrometer sized crystals (Figure 2d). Approximately 10% of the surface consisted of holes and cracks in the pyrite block. EDX analysis of the overgrowth (Figure 2b) returned Fe:S ratios characteristic of FeS₂. Analyses of the spherical particles formed on the overgrowth returned Na and Cl signals next to variable Fe:S ratios. Within the overgrowth, regularly shaped holes were observed (Figure 2b). In contrast, after three days in run 2, no SEM-identifiable material was formed (*pyrite block 2A*, Figure 3a). After nine days of reaction in run 2, an overgrowth of submicrometer-sized euhedral pyrite cubes on the surface of the pyrite block was formed and globular pyrite formation occurred on the overgrowth (*pyrite block 2B*, Figures 3b, 3c and 3d). Less than 1% of the surface consisted of holes and cracks in the pyrite block. EDX analysis returned ratios characteristic of FeS₂ for both the microcrystalline overgrowth and the globular pyrite.

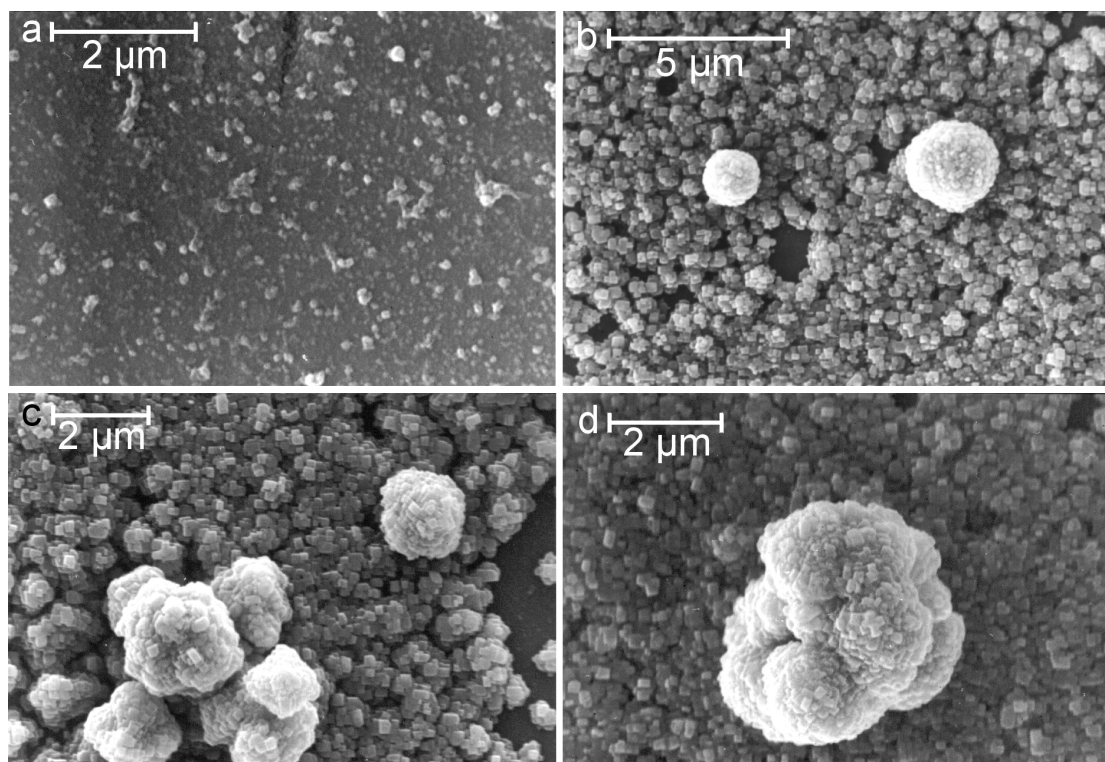


Figure 3. SEM images of products formed on (a) pyrite block 2A after 3 days and (b) – (d) on pyrite block 2B after 9 days of reaction in run 2. (a) the unidentifiable precipitate formed on the still visible cubic pyrite surface; (b) euhedral cubic pyrite overgrowth, formed epitaxially on the cubic pyrite surface, and two solitary protoframboids formed on the euhedral-pyrite overgrowth; (c) solitary protoframboid formed and protoframboid cluster in the initial stage of forming on the euhedral-pyrite overgrowth; (d) protoframboid cluster formed on the euhedral-pyrite overgrowth.

Figure 4 shows laser-ablation craters formed in the surface of reacted pyrite block 2B, which had been retrieved at the end of run 2. After approximately ten laser pulses, the boundary between the overgrowth and the underlying pyrite block was crossed (b in Figure 4). This corresponds, on the basis of the estimated ablation rate of $100 \text{ nm pulse}^{-1}$, to an overgrowth thickness of $\sim 1 \text{ }\mu\text{m}$, which agrees with an average overgrowth-thickness of $\sim 1 \text{ }\mu\text{m}$ estimated from the SEM observations (Figures 3b to 3d).

Results from the depth analyses by LA-ICP-MS are plotted in Figure 5. Figure 5a shows the depth profile for the unreacted surface of pyrite block 2B. At the start of ablation, which is marked by arrow 1 in Figure 5a, the response for $^{57}\text{Fe}^+$ rapidly increased while the response at masses (i.e., mass/charge or m/z) 30, 37 and notably 75 remained unchanged. This shows qualitatively that

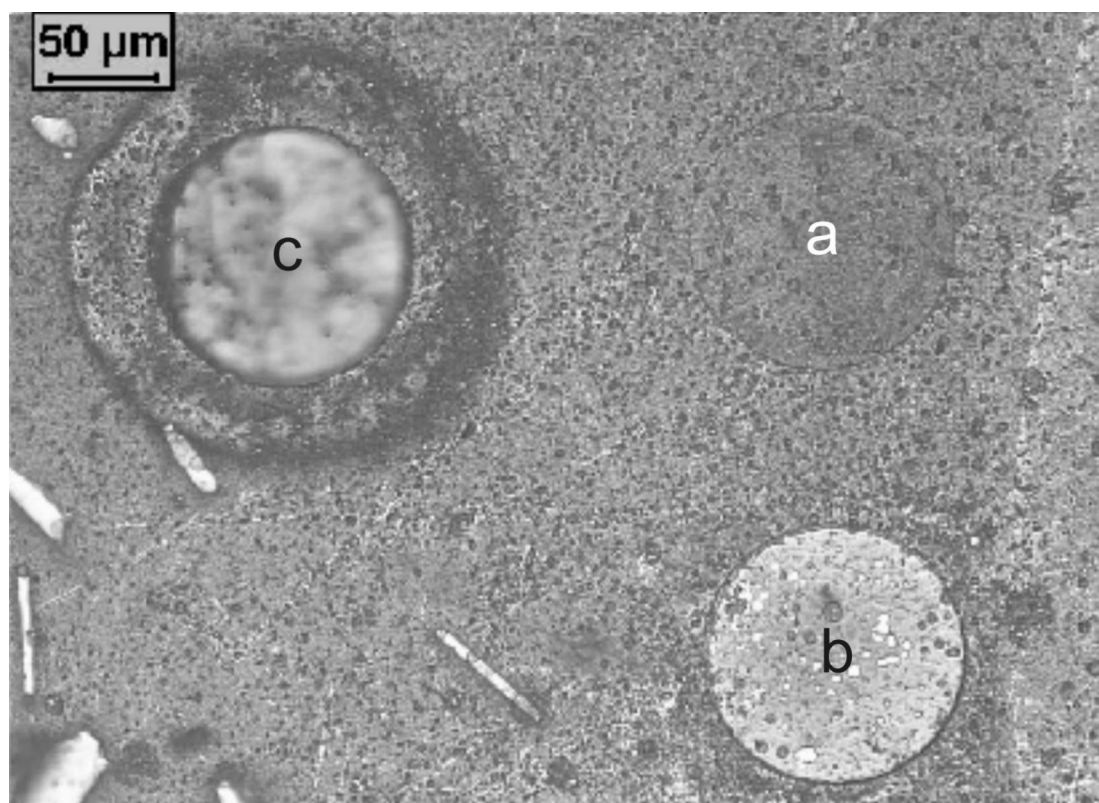


Figure 4. Laser ablation craters in the surface of pyrite block 2B (a) after 5 pulses; (b) after 10 pulses and; (c) after the analysis depicted in Figure 5b. Needle-shaped inclusions in the pyrite (bottom-left corner) are hornblende crystals (Butler et al., submitted).

no arsenic, $m/z = 75$, was present at the surface of unreacted pyrite block 2B. At $m/z = 30$, $^{30}\text{Si}^+$ was analysed simultaneously and the flat response for this isotope shows that no silicate inclusion was ablated. Depth analyses of reacted pyrite block 2B, showed a response-change for $^{57}\text{Fe}^+$ and $^{75}\text{As}^+$ at the start of ablation (arrow 1 in Figure 5b). With analysis-time and thus depth, the response for $^{57}\text{Fe}^+$ remained constant, while the response for $^{75}\text{As}^+$ dropped to the background level when the boundary between the overgrowth and the underlying pyrite was crossed (arrow 2 in Figure 5b). Isobaric interferences are possible at $m/z = 75$ from $^{40}\text{Ar}^{35}\text{Cl}^+$ polyatomic ion, which may be produced if the concentration of Cl in the system is high. To test this possibility, $^{37}\text{Cl}^+$ and $^{35}\text{Cl}^+$ were measured simultaneously during the analysis. Since there was no change in the $^{37}\text{Cl}^+$ signal and taking into account that ArCl^+ should form at 100–200 ppm level (Mason and Kraan, 2002), the $m/z = 75$ cannot be explained by the production of $^{40}\text{Ar}^{35}\text{Cl}^+$. Furthermore, at $m/z = 35$, there was a small but

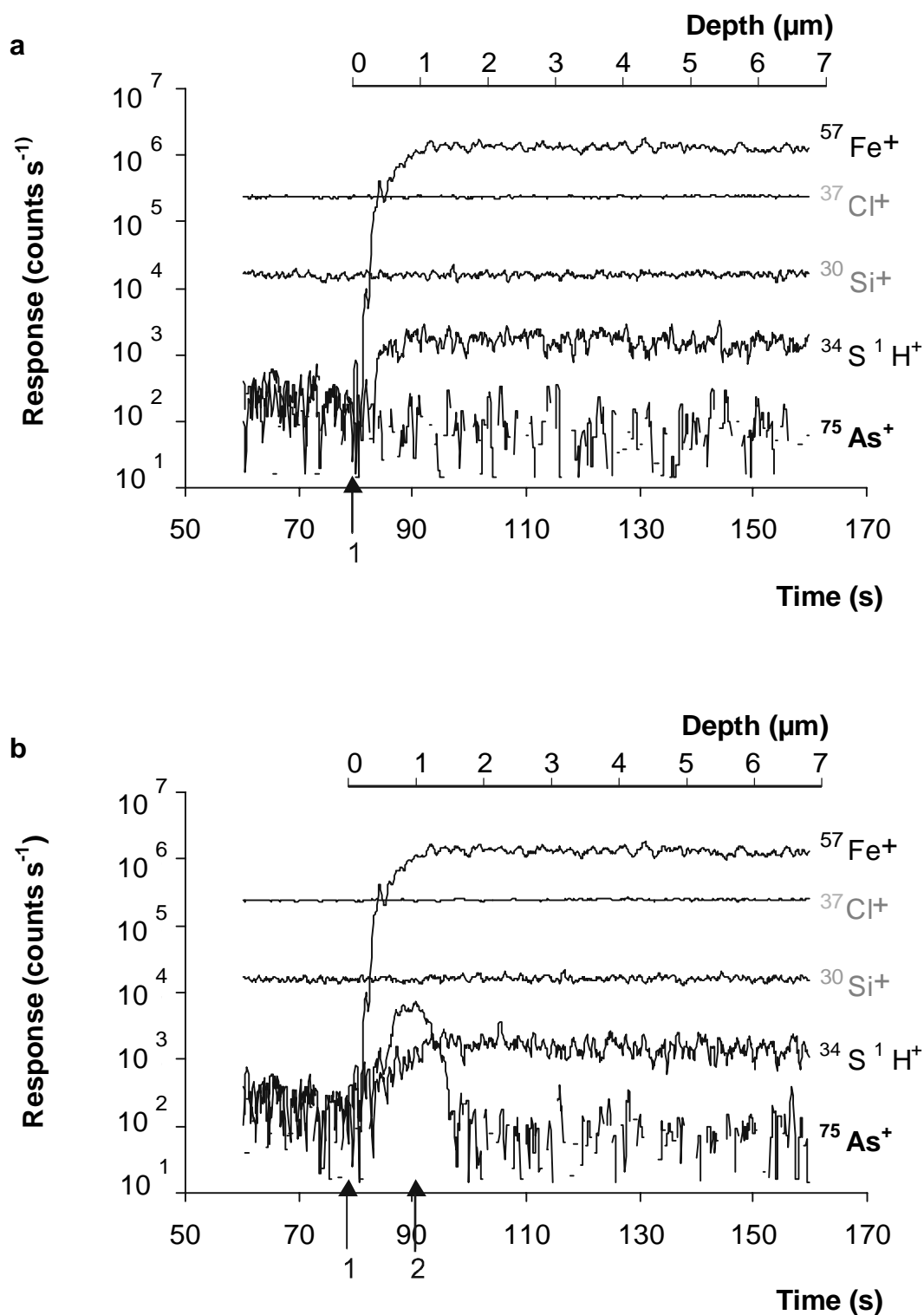


Figure 5. LA-ICP-MS depth profiles of (a) unreacted section of pyrite block 2B and; (b) reacted section of pyrite block 2B. Arrow 1 marks the start of ablation; arrow 2 marks when the boundary between the overgrowth and the underlying pyrite was crossed. The signals were smoothed by averaging 5 points at equal weight.

constant increase in signal after the start of the ablation which does not correlate with the signal at $m/z = 75$. This signal, which was also observed in the unreacted pyrite block (Figure 5a), is most likely due to the presence of $^{34}\text{S}^1\text{H}^+$ as seen in previous studies (Mason et al., 1999). Therefore, these results show qualitatively that arsenic was present in the overgrowth formed on the surface of reacted pyrite block 2B. The slopes of the curves as a response to concentration changes are not optimal, that is, not near-vertical (Mason and Mank, 2001). This is due to the large size of the pyrite block relative to the sample chamber. Such a large dead volume in the sample chamber causes imperfect mixing of the ablated material and the carrier gas and thus imperfect response times to ablation. However, the depth resolution of the system was sufficient to identify chemical differences between the 1 μm overgrowth and the underlying pyrite.

4. Discussion

4.1. Pyrite textures

XRPD analysis showed the formation of pyrite in both runs. However, the pyrite textures formed varied between the two runs. The euhedral overgrowth and globular pyrite-textures formed in run 2 after 9 days of reaction (Figures 3b to 3d) are identical to the blank runs with single crystal pyrite blocks and no arsenic present (Butler et al., submitted, their Figures 3 and 7). In contrast, the pyrite textures formed in run 1 are subhedral (Figures 2b to 2d). As the latter authors have shown, the pyrite surface and the hydrodynamics are contributing factors controlling the pyrite textures formed in the experiments. The hydrodynamics in the system are partly controlled by the imperfections at the single pyrite crystal surface (Butler et al., submitted). At the surface of block 1B, many more holes were observed than at the surface of block 2B. Furthermore, steps in the surface of block 1B were observed. Since they were not observed during SEM imaging of the surface prior to reaction, the steps may have formed by dissolution or growth of the pyrite surface during run 1. Since the surface of block 1B contained more imperfections, the surface may have had more high-energy nucleation sites. This could explain the higher density of crystals formed at the surface of block 1B relative to block 2B.

Through spatial constraints, this higher density would limit the size and shape of the crystals formed.

In addition to the relative quality of the surfaces, one significant difference between the two runs was noted: the amount of acid needed to control the pH within the set boundaries. Approximately 0.01 mole of protons was consumed overall in run 1 and ~0.005 mole in run 2. The consumption was faster over the whole period of run 1. Since solution conditions did not vary strongly between the two runs (Table 2), this proton consumption must be related to the solid phase. It could, for example, be related to dissolution inclusions in the pyrite block. The observed steps, holes and regularly shaped “windows” in the pyrite overgrowth (Figure 2b) would support such a dissolution and indicate incomplete removal and coating of inclusions in pyrite block 1B.

Other, more subtle differences between the two runs are a slightly lower redox potential as measured by the Eh electrode, and a stop of several hours in the supply of Fe(II) and sulphide on day 6 of run 1. It may be that the combination of the subtle differences with the differences in surface-quality of the pyrite blocks between runs 1 and 2 has triggered a switch from the formation of pyrite textures identical to previous experiments in the same set-up (Butler et al., submitted) to the formation of a subhedral texture.

4.2. Effect and fate of As(III)

In the batch experiments discussed in chapter 5, it was shown that: (i) As(III) concentrations higher than $\sim 1 \times 10^{-3}$ M inhibited pyrite nucleation by sorption onto the precursor FeS_{am} and (or) attack of $\text{FeS}(\text{aq})$ (cf. Rickard and Luther, 1997); (ii) lower As(III) concentrations may slow down rates of pyrite formation; (iii) arsenic, when added as As(V), is incorporated into the pyrite formed. From the results presented in this chapter, it cannot be determined if less pyrite was formed in the arsenic-doped runs compared to the blanks.

The euhedral and the globular pyrite textures formed in run 2 are identical to the textures formed in the blank runs (Butler et al., submitted), except for the lack of evidence for framboidal-pyrite formation. However, Butler et al. (submitted) have demonstrated that the formation of framboidal pyrite in the experiments is partly controlled by hydrodynamics causing diffusion-limited niches in, for example, holes in the pyrite surface. The surface

of block 2B was void of large holes in the surface, which may explain the lack of framboidal-pyrite formation. Unfortunately, the pyrite textures formed varied between the runs, therefore, there is no unequivocal evidence for an effect of As(III) on the textures formed. Nevertheless, the formation of identical textures in run 2 and in the blanks (Butler et al., submitted) suggest that As(III) has no effect on the formation of the different pyrite textures.

Depth analysis by LA-ICP-MS of the unreacted (Figure 5a) and reacted (Figure 5b) pyrite block 2B demonstrated qualitatively that As(III) was taken up into the neoformed pyrite in run 2. In chapter 5, it was proposed that the uptake of As(III) into the mixed FeS_{am} -pyrite solid phase was controlled by sorption onto the FeS_{am} surface. The conditions in the continuous-flow experiments from two days after reaction until the end of the runs are controlled by aged iron(II) monosulphide (cf. Davison, 1991; Benning et al., 2000). Thus, the uptake of As(III) into the solid phase may be controlled by iron(II) monosulphide in the continuous-flow reactions (cf. chapters 4 and 5). However, it is not unlikely that with more and more pyrite formation during the runs, while no new iron(II) monosulphide precipitates, sorption onto newly formed pyrite surfaces becomes an important uptake mechanism.

In the highly supersaturated batch experiments discussed in chapter 5, a strong effect of arsenic on nucleation was observed. In the less supersaturated continuous-flow experiments presented here, pyrite crystal growth dominated nucleation during most of the experiment time. During the continuous pyrite growth in these experiments, a continued uptake and incorporation of arsenic by pyrite is indicated by the constantly low aqueous arsenic concentration (Table 2). So, the experimental results indicate that pyrite nucleation is negatively affected by arsenic (chapter 5), while crystal growth is not, or not strongly, affected (chapter 6).

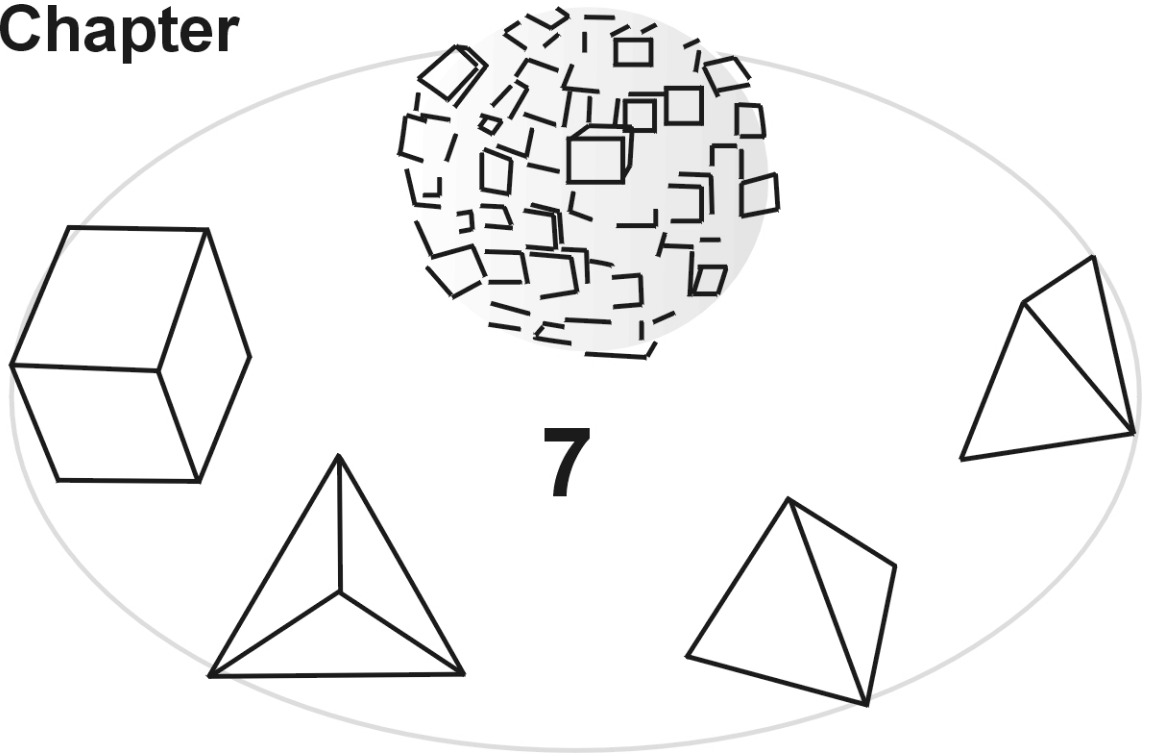
The LA-ICP-MS results confirm that arsenic is incorporated into the neoformed pyrite and, hence, that arsenian pyrite (that is, pyrite containing arsenic) is formed. Thus, the net result of the reactions in the chemostat is the continued fixation of arsenic in pyrite. The incorporation of arsenic in pyrite, suggested from the XANES results reported in chapter 5 and from the solution chemistry and LA-ICP-MS here, implies that arsenic cannot be re-released into solution, unless pyrite is oxidatively dissolved. Furthermore, the synthesis of arsenian pyrite at ambient environmental conditions is in agreement with

authigenic arsenian pyrite formed in, for example, marine sediments (Huerta-Diaz and Morse, 1992).

Acknowledgements

We thank Steve Grimes for his assistance with the chemostat and SEM, Anthony Oldroyd for general lab assistance and Sarah Goldsmith for performing the ICP-MS analyses. Cornelis Woensdrecht (Utrecht University), Cornelis H. van der Weijden (Utrecht University) and Peter van der Linde (University of Professional Education Leiden) provided insightful discussions over the course of this study. This research was supported by the Netherlands Organization of Scientific Research (NWO/ALW grant 750.197.06 to M.W.) and by NERC grant NERLS200000611 to D.R. The Utrecht LA-ICP-MS lab was supported by the NWO/GOA. This research was conducted under the program of the Netherlands Research School of Sedimentary Geology.

Chapter



Synthesis

The aim of this thesis is to contribute to the understanding of the behaviour of arsenic in suboxic and anoxic environments. This is pursued by studying arsenic sorption onto disordered mackinawite, FeS_{am} , and the association of As with Fe(II) sulphides during the formation of pyrite, FeS_2 . As a basis for this work, the bulk characteristics, crystallinity and surface properties of synthetic FeS_{am} were determined.

Synthetic FeS_{am} is nanocrystalline and displays a disordered tetragonal mackinawite structure. It has an expanded lattice, in particular along the c axis, with intercalated water molecules between the tetrahedral sheets and possibly intercalated hydroxyl groups with associated protons, cations or sulphide vacancies to balance charge. FeS_{am} can be described in terms of a mixture of two end-member phases with different average primary particle sizes and long-range ordering. The formation of two phases of FeS_{am} is consistent with competing pathways involved in its formation from aqueous solution (cf. Rickard, 1995). The reactivity of FeS_{am} is dependent on the proportion of the two end-member phases. They are, in turn, dependent on the conditions of formation, especially pH, and the age of the precipitate. These observations partly explain the reported differences in FeS_{am} reactivity in experimentation and in the environment.

The solubility of FeS_{am} in the neutral to alkaline pH-range is described by $K_s^{\text{app}} = \{\text{Fe}^{2+}\} \cdot \{\text{H}_2\text{S}(\text{aq})\} \cdot \{\text{H}^+\}^{-2} = 10^{+4.87 \pm 0.27}$. This is the first study to determine K_s^{app} at neutral to alkaline pH. Acid–base titrations show that the point of zero charge (PZC) of disordered mackinawite lies at pH ~ 7.5 . The hydrated disordered mackinawite surface is described by strong mono-coordinated and weak tri-coordinated sulphurs as the reactive sites. The mono-coordinated sulphur site determines the acid–base properties at pH $<$ PZC and has a concentration of 1.2×10^{-3} mol per gram FeS_{am} . At higher pH the tri-coordinated sulphur, which has a concentration of 1.2×10^{-3} mol per gram FeS_{am} as well, determines surface charge changes. The total site density is 4 sites nm^{-2} .

This surface model was applied to the experimental arsenic sorption data. Arsenate, As(V), sorption onto synthetic FeS_{am} , is fast. As(V) dominantly forms a monodentate complex at the surface of mackinawite, binding to the protonated mono-coordinated sulphide edge sites. Arsenite, As(III), sorption is not strongly pH-dependent and can be expressed by a Freundlich isotherm.

Sorption is fast, although slower than of As(V). Stronger sorption of As(V) than As(III) and thus a higher As(III) mobility may be reflected in natural anoxic sulphidic waters when disordered mackinawite controls arsenic mobility.

The behaviour of arsenic during the reaction of FeS_{am} to pyrite was studied in batch experiments. The uptake of arsenic into the solid phase is described by As(V) and As(III) sorption onto FeS_{am} . Nucleation kinetics plays an important role in the pyrite formation in these experiments, since the solutions are highly supersaturated with respect to pyrite (cf. Butler and Rickard, 2000). Arsenic retards and, at high concentrations, inhibits pyrite nucleation by sorption onto FeS_{am} and (or) attack of the $\text{FeS}(\text{aq})$ cluster complex (cf. Rickard and Luther, 1997); and As(V) oxidises iron(II) sulphide. In other words, arsenic strongly affects pyrite nucleation. Pyrite was also synthesised in the presence of As(III) at concentrations approaching those in ambient environments, in a continuous-flow system. In these less supersaturated experiments, pyrite crystal growth dominates nucleation during most of the experiment time. During the pyrite growth in these experiments, a continuous incorporation of arsenic in pyrite is observed. So, the results indicate that pyrite nucleation is negatively affected by arsenic, while crystal growth is not noticeably affected.

The implications of this last conclusion are two-fold. First, in environments highly supersaturated with respect to pyrite, where nucleation is fast relative to crystal growth, arsenic incorporation into pyrite will not be favourable since arsenic retards or inhibits pyrite formation. Therefore, arsenic sorption onto FeS_{am} may be a more important mechanism of arsenic removal from solution. However, arsenic sorbed onto FeS_{am} cannot be regarded as immobilised due to the metastability of its host phase and the possibility of desorption. In other words, no stable arsenic sink is formed. Secondly, in environments where pyrite grows from a solution less supersaturated with respect to pyrite, such that the rate of crystal growth is greater than the rate of nucleation, arsenic will be incorporated into pyrite in quite substantial amounts. In these environments, a relatively stable arsenic sink will be formed, which would only release incorporated arsenic during oxidative dissolution.

Several questions arise from this thesis, which should be addressed in future research. First: will the pH_{PZC} of the FeS_{am} surface change with ageing? Such a change is expected, since the pH_{PZC} of crystalline mackinawite lies

below pH 3 (Bebié et al., 1998). Furthermore, the crystal structure has been shown to change with age, with longer range ordering being formed (chapter 2). As discussed in chapter 3, such structuration causes an increase in surface site acidity and, hence, a downward shift in pH_{PZC} for silicates. Such a shift would be important for environmental studies, since a surface with different charge will have different specific sorption capacities, preferentially sorbing cations or anions. Secondly: what is, or are, the FeS_{am} -solubility controlling mechanism(s) in the neutral to alkaline pH range? A detailed study on the aqueous iron-sulphide speciation in relation to the FeS_{am} solubility is required, since the results presented in chapter 3 show that the controlling dissolution mechanism changes with pH. Thirdly: what is the reduction mechanism of As(V) and As(III) in iron(II)-sulphide systems? This question can be answered by conducting arsenic sorption studies onto FeS_{am} and pyrite with equilibration times up to several weeks, combined with both macro-scale analyses and X-ray absorption spectroscopy studies of the surface complexes formed. As discussed in chapter 5, reduction may occur via intermediate thioarsenate and thioarsenite species within four weeks at pH 6. Reduction of arsenic to As(-I) and incorporation into pyrite is an important step in forming the most stable arsenic sink in suboxic and anoxic environments. Lastly: can the incorporation of arsenic in pyrite during continuous-flow experiments be quantified? To answer this question, more continuous-flow experiments should be performed, with additional detailed analyses of the solution species, which may include iron-sulphide complexes, thioarsenate and thioarsenite species or iron-arsenic-sulphide species. The best way forward in this direction would be to work at natural concentration levels and study the solution speciation with polarographic techniques. In this way, the ambient environmental conditions for the formation of arsenian pyrite are most closely simulated.

References

- Abdullah M.I., Shiyu Z., Mosgren K., 1995. Arsenic and Selenium species in the oxic and anoxic waters of the Oslo fjord, Norway. *Mar. Poll. Bull.* 31, pp 116–126.
- Andreae M.O., 1979. Arsenic speciation in seawater and interstitial waters: The influence of biological–chemical interactions on the chemistry of a trace element. *Limnol. Oceanogr.* 24, pp 440–452.
- Andreae M.O., 1980. Arsenic in rain and the atmospheric mass balance of arsenic. *J. Geophys. Res.* 85, pp 4512–4518.
- Andreae M.O., Byrd T.J., Froelich P.N., 1983. Arsenic, antimony, germanium, and tin in the Trejo Estuary, Portugal: modelling a polluted estuary. *Envir. Sci. Techn.* 17, 731–737.
- Andreae M.O., Froelich P.N., 1984. Arsenic biogeochemistry in the Baltic Sea. *Tellus* 36B, pp 101–117.
- Appelo C.A.J., Postma D., 1994. *Geochemistry, Groundwater and Pollution*. A.A. Balkema, Rotterdam.
- Arakaki T., Morse J.W., 1993. Coprecipitation and adsorption of Mn(II) with mackinawite (FeS) under conditions similar to those found in anoxic sediments. *Geochim. Cosmochim. Acta* 57, pp 9–14.
- Azcue J.M., Murdoch A., Rosa F., Hall G.E.M., 1994. Effects of abandoned gold mine tailings on the arsenic concentrations in water and sediments of Jack of Clubs Lake, B.C. *Envir. Sci. Techn.* 15, pp 669–678.
- Azcue J.M., Murdoch A., Rosa F., Hall G.E.M., Jackson T.A., Reynolds T., 1995. Trace elements in water, sediments, porewater, and biota polluted by tailings from an abandoned gold mine in British Columbia, Canada. *J. Geochem. Explor.* 52, pp 25–34.
- Azcue J.M., Nriagu J.O., 1995. Impact of abandoned mine tailings on the arsenic concentrations in Moira Lake, Ontario. *J. Geochem. Explor.* 52, pp 81–89.

- Barbaris B., Bettertin E.A., 1996. Initial snow chemistry survey of the Mogollon Rim in Arizona. *Atmos. Environ.* 30, pp 3093–3103.
- Bard A.J., Parson R., Jordon J., 1985. *Standards Potentials in Aqueous solution*, Marcel Dekker, New York, 834 p.
- Basu A., Mahata J., Gupta S., Giri A.K., 2001. Genetic toxicology of a paradoxical human carcinogen, arsenic: a review. *Mutation Res/Rev. Mutation Res.* 488, pp 171–194.
- Baur W.H., Onishi B.-M.H., 1969. Arsenic. In: K.H. Wedepohl (Ed.) *Handbook of geochemistry*. Springer-Verlag, Berlin, pp 33-A-1 – 33-O-5.
- Bayliss P., 1989. Crystal chemistry and crystallography of some minerals within the pyrite group. *Am. Min.* 74, pp 1168–1176.
- Bebie J., Schoonen M.A.A., Fuhrman M., Strongin D.R., 1998. Surface charge development on transition metal sulfides: An elektrokinetic study. *Geochim. Cosmochim. Acta* 62, pp 633–642.
- Belzile N., Lebel J., 1986. Capture of arsenic by pyrite in near-shore marine sediments. *Chem. Geol.* 54, pp 279–281.
- Benning L., Wilkin R.T., Barnes H.L., 2000. Reaction pathways in the Fe–S system below 100°C. *Chem. Geol.* 167, pp 25–51.
- Berner R.A., 1964. Stability fields of iron minerals in anaerobic marine sediments. *J. Geol.* 72, pp 826–834.
- Berner R.A., 1967. Diagenesis of iron sulfide in recent marine sediments. *Estuaries* [papers of a conference on estuaries, Jekyll Island, 1964], Lauff, George H. (ed), publ. Washington, American Association for the Advancement of Science, pp 268–272.
- Berner R.A., 1970. Sedimentary pyrite formation. *Am. J. Sci.*, 268, pp 1–23.
- Berner R.A., 1981. A new geochemical classification of sedimentary environments. *J. Sed. Petrol.* 51, 359–365.
- Berner R.A., 1974. Iron sulfides in Pleistocene deep Black Sea sediments and their paleo-oceanographic significance. In: E.T. Degens and D.A. Ross (Editors), *The Black Sea: Geology, Chemistry and Biology*. MPG Memoir 20, pp. 524–531.

- Binsted N., Strange R.W., Hasnain S.S., 1992. Constrained and restrained refinement in EXAFS data analysis with curved wave theory. *Biochem.* 31, pp 12117–12125.
- Boyle R.W. and Jonasson I.R., 1973. The geochemistry of arsenic and its use as an indicator element in geochemical prospecting. *J. Geochem. Expl.* 2, pp 251–296.
- Brannon J.M., Patrick Jr. W.H., 1987. Fixation, transformation, and mobilization of arsenic in sediments. *Envir. Sci. Techn.* 21, pp 450–459.
- Brindley, G.W., 1980. Order–disorder in clay mineral structures. In: *Crystal Structures of Clay Minerals and Their X-ray Identification*, G.W. Brindley and G. Brown, eds., Mineralogical Society London, pp 125–195.
- Broecker W.S., Peng T–H., 1982. *Tracers in the sea*. Palisades (publ) New York, 690p.
- Browne, P.R.L. and Wood, C.P., 1974. Mackinawite and pyrite in a hot springs deposit, Mohaka River, New Zealand. *Neues Jahrb. Mineral. Monatsh.* 10, pp 468–475.
- Butler I.B., Grimes S.T., Rickard D., Oldroyd A. (submitted). Pyrite synthesis at ambient temperatures in a continuous–flow chemostat.
- Butler I.B., Rickard D., 2000. Framboidal pyrite formation via the oxidation of iron (II) monosulfide by hydrogen sulphide. *Geochim. Cosmochim. Acta* 64, pp 2665–2672.
- Canfield D.E., Raiswell R., Bottrell S., 1992. The reactivity of sedimentary iron minerals toward sulfide. *Am. J. Sci.* 292, pp 659–683.
- Charlet L., Wersin P., Stumm W., 1990. Surface charge of MnCO_3 and FeCO_3 . *Geochim. Cosmochim. Acta* 54, pp 2329–2336.
- Cullen W.R., Reimer K.J., 1989. Arsenic speciation in the environment. *Chem. Rev.*, 89, pp 713–764.
- Dang M.–Z., Rancourt D.G., Dutrizac J.E., Lamarche G., Provencher R., 1998. Interplay of surface conditions, particle size, stoichiometry, cell parameters, and magnetism in synthetic hematite-like materials. *Hyperfine interactions* 117, pp 271–319.

- Davison W., 1991. The solubility of iron sulphides in synthetic and natural waters at ambient temperature. *Aquat. Sci.* 53, pp 309–329.
- Davison W., Philips N., Tabner B.J., 1999. Soluble iron sulfide species in natural waters: reappraisal of their stoichiometry and stability constants. *Aquat. Sci.* 61, pp 23–43.
- Dekkers M.J., Schoonen M.A.A., 1994. An electrokinetic study of synthetic greigite and pyrrhotite. *Geochim. Cosmochim. Acta* 58, pp 4147–4153.
- Dellwig O., Böttcher M.E., Lipinski M., Brumsack H-J., 2002. Trace metals in Holocenec coastal peats and their relation to pyrite formation (NW Germany). *Chem. Geol.* 182, pp 423–442.
- Ding M., de Jong B.H.W.S., Roosendaal S.J., Vredenberg A., 2000. XPS studies on the electronic structure of bonding between solid and solutes: adsorption of arsenate, chromate, phosphate, Pb^{2+} , and Zn^{2+} ions on amorphous black ferric oxyhydroxide. *Geochim. Cosmochim. Acta* 64, pp 1209–1219.
- Dixit S., Van Cappellen P., 2002. Surface chemistry and reactivity of biogenic silica. *Geochim. Cosmochim. Acta* 66, pp 2559–2568.
- Dzombak D.A., Morel F.M.M., 1990. *Surface Complexation Modelling, Hydrous Ferric Oxide*, Wiley & Sons, NY, 393 p.
- Eary L.E., 1992. The solubility of amorphous As_2S_3 from 25 to 90°C. *Geochim. Cosmochim. Acta* 56, pp 2267–2280.
- Eary L.E., Schramke J.A., 1990. Rates of Inorganic Oxidation Reactions Involving Dissolved Oxygen (chapter 30). In: *Chemical Modeling of Aqueous Systems II*, ACS Symposium Series 416, ACS, Washington, pp. 379–396.
- Edenborn H.M., Belzile N., Mucci A., Lebel J., Silverberg N., 1986. Observations on the diagenetic behavior of arsenic in a deep coastal sediment. *Biogeochem.* 2, pp 359–376.
- Evans, Jr., H.T., Milton, C., Chao, E.C.T., Adler, I., Mead, C., Ingram, B. and Berner, R.A., 1964. Vallerite and the new iron sulfide, mackinawite. USGS Prof. Paper 475–D: 64–69.
- Farquhar M.L., Charnock J.M., Livens F.R., Vaughan D.J., 2002. Mechanisms of arsenic uptake from aqueous solution by interaction with goethite, lepidocrocite, mackinawite, and pyrite: an X-ray absorption spectroscopy study. *Envir. Sci. Technol.* 36, pp 1757–1762.

- Fendorff S., Eick M.J., Grossl P., Sparks D.L., 1997. Arsenate and chromate retention mechanism on goethite. 1. Surface structure. *Envir. Sci. Technol.* 31, pp 315–320.
- Ferguson J.F., Gavis J., 1972. A review of the arsenic cycle in natural waters. *Water Res.* 6, pp 1259–1274.
- Fleet M.E., Chryssoulis S.L., MacLean P.J., Davidson R., Weisener C.G., 1993. Arsenian pyrite from gold deposits: Au and As distribution investigated by SIMS and EMP, and color staining and surface oxidation by XPS and LIMS. *Can. Min.* 31, pp 1–17.
- Fleet M.E., Mumin A.H., 1997. Gold-bearing arsenian pyrite and marcasite and arsenopyrite from Carlin Trend gold deposits and laboratory synthesis. *Am. Min.* 82, pp 182–193.
- Fleischer M., 1955. Minor elements in some sulfide minerals. *Econ. Geol.* 50, pp 970–1024.
- Foissy A., Persello J., 1998. Chapter 4B, Surface group ionization on silicas. In: A.P. Legrand (Ed.), *The surface properties of silicas*, Wiley & Sons, New York, pp 365–414.
- Froelich P.N., Kaul L.W., Byrd J.T., Andreae M.O., Roe K.K., 1985. Arsenic, barium, germanium, tin, dimethyl-sulfide and nutrient biogeochemistry in Charlotte Harbour, Florida, a phosphorous-enriched estuary. *Estuar. Coast. Shelf Sci.* 20, pp 239–264.
- Gabriel U., Gaudet J.P., Spadini L., Charlet L., 1998. Reactive transport of uranyl in a goethite column: an experimental and modelling study. *Chem. Geol.* 151, pp 107–128.
- Gonzalez Soto E., Villa Lojo M.C., Alonso Rodrigues E., Neira Dourado J., Prada Rodriguez D., Fernandez Fernandez E., 1996. Speciation of inorganic and organic arsenic in marine sediments from La Coruna estuary. *Fresenius' J. Anal. Chem.* 355, pp 713–715.
- Griffin W.L., Ashley P.M., Ryan C.G., Sie S.H., Suter G.F., 1991. Pyrite geochemistry in the North Arm epithermal Ag–Au deposit, Queensland, Australia: a proton-microprobe study. *Can. Min.* 29, pp 185–198.

- Grimes S.T., Brock F., Rickard D., Davies K.L., Edwards D., Briggs D.E.G., Parkes R.J., 2001. Understanding fossilization: experimental pyritization of plants. *Geology* 29, pp 123–126.
- Grundy P.J., Jones G.A., 1976. Electron microscopy in the study of materials. In: B.R. Coles (Ed.), *The structure of solids* 7, Arnold, London.
- Gulens J., Champs D.R., Jackson R.E., 1979. Influence of redox environments on the mobility of arsenic in groundwater. In: E.A. Jenne (Ed.), *Chemical Modelling of Aqueous systems*. A.C.S., pp 81–95.
- Harmandas N.G., Fernandez E.N., Koutsoukos P.G., 1998. Crystal growth of pyrite in aqueous solutions. Inhibition by organophosphorus compounds. *Langmuir* 14, pp 1250–1255.
- Harvey C.F., Swartz C.H., Badruzzaman A.B.M., Keon-Blute N., Yu W., Ali M.A., Jay J., Beckie R., Niedan V., Brabander D., Oates P.M., Ashfaque K.N., Islam S. Hemond H.F., Ahmbed M.F., 2002. Arsenic mobility and groundwater extraction in Bangladesh. *Science* 298, pp 1602–1606.
- Helz G.R., Tossell J.A., Charnock J.M., Patrick R.A.D., Vaughan D.J., Garner C.D., 1995. Oligomerization in arsenic(III) sulfide solutions: theoretical constraints and spectroscopic evidence. *Geochim. Cosmochim. Acta* 59, pp 4591–4604.
- Herbert Jr. R.B., Benner S.G., Pratt A.R., Blowes D.W., 1998. Surface chemistry and morphology of poorly crystalline iron sulfides precipitated in media containing sulfate-reducing bacteria. *Chem. Geol.* 144, pp 87–97.
- Hickmott D.D., Baldrige W.S., 1995. Application of PIXE microanalysis to Macerals and sulfides from the Lower Kittanning Coal of Western Pennsylvania. *Econ. Geol.* 90, pp 246–254.
- Hiemstra T., Van Riemsdijk W.H., 1999. Surface structural ion adsorption modeling of competitive binding of oxyanions by metal (hydr)oxides. *J. Colloid Interf. Sci.* 210, pp 182–193.
- Hiemstra T., Venema P., Van Riemsdijk W.H., 1996. Intrinsic proton affinity of reactive surface groups of metal (hydr)oxides: the bond valence principle. *J. Coll. Interface Sci.* 184, pp 680–692.

- Hingston J.A., Moore J., Bacon A., Lester J.N., Murphy R.J., Collins C.D., 2002. The importance of the short-term leaching dynamics of wood preservatives. *Chemosphere* 47, pp 517–523.
- Huerta-Diaz M.A., Morse J.W., 1992. Pyritization of trace metals in anoxic marine sediments. *Geochim. Cosmochim. Acta* 56, pp 2681–2702.
- Hurtgen M.T., Lyons T.W., Ingall E.D., Cruse A.M. 1999 Anomalous enrichments of iron monosulfide in euxinic marine sediments and the role of H₂S in iron sulfide transformations: examples from Effingham Inlet, Orca Basin, and the Black Sea. *Am. J. Sci.* 299, 556–588.
- Isenbeck–Schröter M., Höhn R., Stadler S., Jann S., Davis J., Kent D., Niedan V., Scholz C., Tretner A., Jakobsen R., 2002. Tracer test with As(III) and As(V) at the Cape Cod Site. *Geochim. Cosmochim. Acta* 66, A356 (abstr).
- Keith M.L. and Degens E.T., 1959. Geochemical indicators of marine and fresh-water sediments. In: Abelson (Ed.) *Researches in geochemistry*, V5, , NY Wiley and Sons, pp38–61.
- Kjekshus A., Nicholson D.G. and Mukherjee A.D., 1972. On the bonding in tetragonal FeS. *Acta Chem. Scand.* 26, pp 1105–1110.
- Kolthoff I.M., Griffith F.S., 1938. Studies in ageing and properties of precipitates. XXIII. The postprecipitation of ferrous sulphide with cupric sulphide. *J. Am. Chem. Soc.* 60, pp 2036–2039.
- Kornicker W.A. and Morse J.W., 1986. The surface chemistry of mackinawite and pyrite. *Abstr. w. progr.* 18, pp 661.
- Kornicker W.A., 1988. Interactions of divalent cations with pyrite and mackinawite in seawater and sodium–chloride solutions. Ph.D. thesis Texas A&M University.
- Kornicker W.A., Morse J.W., 1991. Interactions of divalent cations with the surface of pyrite. *Geochim. Cosmochim. Acta* 55, pp 2159–2171.
- Korte N.E., Fernando Q., 1991. A review of arsenic (III) in groundwater. *Crit. Rev. in Envir. Control* 21, pp 1–39.
- Krauskopf K.B., 1955. Sedimentary deposits of rare metals. *Econ. Geol.* 50, pp 411–463.

- Kuhn A., Sigg L., 1993. Arsenic cycling in eutrophic Lake Greifen, Switzerland: influence of seasonal redox processes. *Limnol. Oceanogr.* 38, pp 1052–1059.
- Kullerud G., Yoder H.S., 1959. Pyrite stability relations in the Fe–S system. *Econ. Geol.*, 54 pp 533–572.
- Kuo S., McNeal B.L., 1984. Effects of pH and Phosphate on cadmium sorption by a hydrous ferric oxide. *Soil Sci. Soc. Am. J.* 48, pp 1040–1044.
- Kuovo O., Vuorelainen Y., Long J.V.P., 1963. A tetragonal iron sulfide. *Am. Min.* 48, pp 511–524.
- Langmuir D., 1997. *Aqueous environmental geochemistry*. Prentice Hall, New York.
- Lennie A.R. and Vaughan D.J., 1996. Spectroscopic studies of iron sulfide formation and phase relations at low temperatures. *Min. Spectr.*, special publ. 5, pp 117–131.
- Lennie A.R., Redfern S.A.T., Champness P.E., Stoddart C.P., Schofield P.F., Vaughan D.J., 1997. Transformation of mackinawite to greigite: An in situ X-ray powder diffraction and transmission electron microscopy study. *Am. Min.* 82, pp 302–309.
- Luther G.W., Ferdelman T.G., 1993. Voltammetric characterization of iron(II) sulfide complexes in laboratory solutions and in marine waters and porewaters. *Envir. Sci. Technol.* 27, pp 1154–1163.
- Luther III G.W., 1991. Pyrite synthesis via polysulfide compounds. *Geochim. Cosmochim. Acta* 55, pp 2839–2849.
- Luther III G.W., Rickard D., Theberge S., Olroyd A., 1996. Determination of Metal (Bi)Sulfide Stability Constants of Mn^{2+} , Fe^{2+} , Co^{2+} , Ni^{2+} , Cu^{2+} and Zn^{2+} by Voltammetric Methods. *Envir. Sci. Technol.* 30, pp 671–679 .
- Luther III G.W., Rozan T.F., Taillefert M., Nuzzio D.B., Di Meo C., Shank T.M., Lutz R.A., Cary S.C., 2001. Chemical speciation drives hydrothermal vent ecology. *Nature* 410, pp 813–816.
- Luther III G.W., Theberge S.M., Rickard D.T., 1999. Evidence for aqueous clusters as intermediates during zinc sulfide formation. *Geochim. Cosmochim. Acta* 63, pp 3159–3169.

- Maher W.A., 1985. Arsenic in coastal waters of South Australia. *Water Res.* 19, pp 93–934.
- Mason P.R.D., Kaspers K., Van Bergen M.J., 1999. Determination of sulfur isotope ratios and concentrations in water samples using ICP–MS incorporating hexapole ion optics. *J. Anal. At. Spectrom.* 14, pp 1067–1074.
- Mason P.R.D., Kraan J.W., 2002. Attenuation of spectral interferences during laser ablation inductively coupled plasma mass spectrometry (LA–ICP–MS) using an rf only collision and reaction cell. *J. Anal. At. Spectrom.* 17, pp 858–867.
- Mason P.R.D., Mank A.J.G., 2001. Depth-resolved analysis in multi-layered glass and metal materials using laser ablation inductively coupled plasma mass spectrometry (LA–ICP–MS). *J. Anal. At. Spectrom.* 16, pp 1381–1388.
- McEwan D.M.C., Ruiz A.A., Brown G., 1961. Interstratified clay minerals. In: *Crystal Structures of Clay Minerals and Their X-ray Identification*, G.W. Brindley and G. Brown, eds., Mineralogical Society London, pp 393–445.
- Meyer I., Heinrich J., Lippold U., 1999. Factors Affecting Lead, Cadmium, and Arsenic Levels in House Dust in a Smelter Town in Eastern Germany. *Envir. Res.* 81, pp 32–44.
- Milonjić S.K., 1987. Determination of surface ionization and complexation constants at colloidal silica/electrolyte interface. *Colloids Surf.* 23, pp 301–312.
- Mok W.M., Wai C.M., 1994. In: *Arsenic in the environment, Part I: Cycling and characterization*, J.O. Nriagu (Ed.), Wiley NY, pp 99–118.
- Morel F.M.M., Hering J.G., 1993. *Principles and applications of aquatic chemistry*. Wiley and Sons, New York, 588p.
- Morse J.W., Arakaki T., 1993. Adsorption and coprecipitation of divalent metals with mackinawite (FeS). *Geochim. Cosmochim. Acta* 57, pp 3635–3640.
- Morse J.W., Casey W.H., 1988. Ostwald processes and mineral paragenesis in sediments. *Am. J. Sci.* 288, pp 537–560.
- Morse J.W., Luther III, G.W., 1999. Chemical influences on trace metal-sulfide interactions in anoxic sediments. *Geochim. Cosmochim. Acta* 63, pp 3373–3378.

- Morse J.W., Millero F.J., Cornwell J.C., Rickard D., 1987. The Chemistry of the Hydrogen Sulfide and Iron Sulfide Systems in Natural Waters. *Earth–Sci. Rev.* 24, pp 1–42.
- Mullet M., Boursiquot S., Abdelmoula M., Génin J.–M., Ehrhardt J.–J., 2002. Surface chemistry and structural properties of mackinawite prepared by reaction of sulfide ions with metallic iron. *Geochim. Cosmochim. Acta* 66, pp 829–836.
- Murowchick J.B., Rickard D.T., 1997. Structural changes during ripening of synthetic mackinawite formed by corrosion of alpha-iron. *Abstr. w. Progr. – GSA.* 29, p 402.
- Navarro M., Sanchez M., Lopez H., Lopez M.C., 1993. Arsenic contamination levels in waters, soils, and sludges in southeast Spain. *Bull. Envir. Contam. Toxicol.* 50, pp 356–362.
- Oremland R.S., Dowdle P.R., Hoefft S., Sharp J.O., Schaeffer J.K., Miller L.G., Switzer Blum J., Smith R.L., Bloom N.S., Wallschlaeger D., 2000. Bacterial dissimilatory reduction of arsenate and sulfate in meromictic Mono Lake, California. *Geochim. Cosmochim. Acta* 64, pp 3073–3084.
- Parfitt R.L., Van der Gaast S.J., Childs C.W., 1992. A structural model for natural siliceous ferrihydrite. *Clays Clay Min.* 40, pp 675–681.
- Park S.W., Huang C.P., 1987. The surface acidity of hydrous CdS. *J. Colloid and Interface Sci.* 117, pp 431–441.
- Parkhurst D.L., Appelo C.A.J., 1999. User's guide to PHREEQC (version 2)—A computer program for speciation, batch-reaction, one-dimensional transport, and inverse geochemical calculations. *Water-Resources Invest. Report 99–4259*, USGS, p 312.
- Passier H.F., Middelburg J.J., de Lange G.J., Böttcher M.E., 1997. Pyrite contents, microtextures, and sulfur isotopes in relation to formation of the youngest eastern mediterranean sapropel. *Geology* 25, pp 519–522.
- Pauling L., 1939, 1960. *The nature of the chemical bond*, 1st and 3rd editions, Cornell Univ Press.
- Pauling L., 1970. Crystallography and chemical bonding of sulfide minerals. *Min. Soc. Am. Spec. Pap.* 3, pp 125–131.

- Pauling L., 1978. Covalent chemical bonding of transition metals in pyrite, cobaltite, skutterudite, millerite and related minerals. *Can. Mineral.* 16, pp 447–452.
- Penrose W.R., 1974. Arsenic in the marine and aquatic environments: analysis, occurrence, and significance. *CRC Crit. Rev. Environ. Control* 1974, pp 465–482.
- Peterson M.L., Carpenter R., 1983. Biogeochemical processes affecting total arsenic and arsenic species distribution in an intermittently anoxic fjord. *Mar. Chem.* 12, pp 295–321.
- Pierce M.L., Moore C.B., 1982. Adsorption of arsenite and arsenate on amorphous iron hydroxide. *Water Res.* 16, pp 1247–1253.
- Pokrovski G., Gout R., Schott J., Zotov A., Harrichoury J–C., 1996. Thermodynamic properties and stoichiometry of As(III) hydroxide complexes at hydrothermal conditions. *Geochim. Cosmochim. Acta* 60, pp 737–749.
- Pokrovski G.S., Zakirov I.V., Roux J., Testemale D., Hazemann J.–L., Bychkov A.Y., Golikova G.V., 2002. Experimental study of arsenic speciation in vapor phase to 500°C: implications for As transport and fractionation in low-density crustal fluids and volcanic gases, *Geochim. Cosmochim. Acta* 66, pp 3453–3480.
- Pósfai M., Buseck P.R., 1997. Modular structures in sulfides: sphalerite/wurzite-, pyrite/marcasite-, and pyrrhotite-type minerals. In: S. Medino (Ed.), *European Mineralogical Union Notes in Mineralogy*, 1. Eotvos University press, Budapest, pp 193–235.
- Prasad B., 1976. Charge characteristics and phosphate adsorption on ferruginous soils and synthetic iron oxides. Ph.D. Thesis, Univ. Minnesota, St. Paul Minn.
- Raiswell R., Plant J., 1980. The Incorporation of Trace Metals into Pyrite during Diagenesis of Black Shales, Yorkshire, England. *Econ. Geol.* 75, pp 684–699.
- Rancourt D.G., Fortin D., Pichler T., Thibault P.–J., Lamarche G., Morris R.V., Mercier P.H.J., 2001. Mineralogy of a natural As-rich hydrous ferric oxide coprecipitate formed by mixing of hydrothermal fluid and seawater:

Implications regarding surface complexation and color banding in ferrihydrite deposits. *Am. Min.* 86, pp 834–851.

Raven K.P., Jain A., Loeppert R.H., 1998. Arsenite and arsenate adsorption on ferrihydrite; kinetics, equilibrium, and adsorption envelopes. *Envir. Sci. Technol.* 32, pp 344–349.

Renders P.J., Seward T.M., 1989. The adsorption of thio gold(I) complexes by amorphous As_2S_3 and Sb_2S_3 at 25 and 90°C. *Geochim. Cosmochim. Acta* 53, pp 255–267.

Reuther R., 1992. Geochemical mobility of arsenic in a flow-through water-sediment system. *Envir. Sci. Technol.* 13, 813–823.

Rickard D., 1989. Experimental concentration–time curves for the iron(II) sulphide precipitation process in aqueous solutions and their interpretation. *Chem. Geol.* 78, pp 315–324.

Rickard D., 1995. Kinetics of FeS precipitation: Part 1. Competing reaction mechanisms. *Geochim. Cosmochim. Acta* 59, pp 4367–4379.

Rickard D., 1997. Kinetics of pyrite formation by the H_2S oxidation of iron (II) monosulfide in aqueous solutions between 25 and 125°C: The rate equation. *Geochim. Cosmochim. Acta* 61, pp 115–134.

Rickard D., Butler I.B., Oldroyd A., 2001. A novel iron sulphide mineral switch and its implications for Earth and Planetary science. *Earth Planet. Sci. Lett.* 189, pp 85–91.

Rickard D., Luther III G.W., 1997. Kinetics of pyrite formation by the H_2S oxidation of iron (II) monosulfide in aqueous solutions between 25 and 125°C: The mechanism. *Geochim. Cosmochim. Acta* 61, pp 135–147.

Rickard D., Oldroyd A., Cramp A., 1999. Voltammetric evidence for soluble FeS complexes in anoxic estuarine muds. *Estuaries* 22, pp 693–701.

Rickard D.T., 1968. The geological and microbiological formation of iron sulfides. Ph.D. thesis, London Univ., 283 p.

Rickard D.T., 1969. The chemistry of iron sulphide formation at low temperatures. *Stockh. Contrib. Geol.* 20, pp 67–95.

Rickard D.T., 1975. Kinetics and mechanism of pyrite formation at low temperatures. *Am. J. Sci.* 275, pp 636–652.

- Rittle K.A., Drever J.I., Colberg P.J.S., 1995. Precipitation of arsenic during bacterial sulfate reduction. *Geomicrobiol. J.* 13, pp 1–11.
- Rochette E.A., Bostick B.C., Li G., Fendorf S., 2000. Kinetics of As(V) reduction by dissolved sulfide. *Envir. Sci. Technol.* 34, pp 4714–4720.
- Rönngren L., Sjöberg S., Sun Z., Forsling W., Schindler P.W., 1991. Ion exchange and acid/base reactions at the ZnS–H₂O interface. *J. Colloid and Interface Sci.* 145, pp 396–404.
- Roos J.H.T., Price W.J., 1971. *Spectrochim. Acta* 26B, pp 279–284.
- Rosso K.M., 2001. Structure and reactivity of semiconducting mineral surfaces: convergence of molecular modeling and experiment. In: Cygan R.T. and Kubicki J.D. (Eds) *Rev. Mineral. Geochem.* 42, Molecular modeling theory: applications in the geosciences, pp 199–271.
- Sadiq M., 1990. Arsenic chemistry in marine environments: a comparison between theoretical and field observations. *Mar. Chem.* 31, pp 285–297.
- Sander J.E., Wilson J.L., Bush P.B., Rowland G.N., 1994. Severe pododermatitis in broiler breeder hens housed on pressure-treated slats. *Avian Diseases* 38, pp 172–176.
- Savage K.S., Tingle T.N., O'Day P.A., Waychunas G.A., Bird D.K., 2000. Arsenic speciation in pyrite and secondary weathering phases, Mother Lode Gold District, Tuolumne County, California. *Appl. Geochem.* 15, pp 1219–1244.
- Schoonen M.A.A., Barnes H.L., 1991a. Reactions forming pyrite and marcasite from solution: I. Nucleation of FeS₂ below 100°C. *Geochim. Cosmochim. Acta* 55, pp 1495–1504.
- Schoonen M.A.A., Barnes H.L., 1991b. Reactions forming pyrite and marcasite from solution: II. Via FeS precursors below 100°C. *Geochim. Cosmochim. Acta* 55, pp 1505–1514.
- Scudlark J.R., Church T.M., 1988. The atmospheric deposition of arsenic and association with acid precipitation. *Atmos. Envir.* 22, pp 937–943.
- Seyler P., Martin J.M., 1989. Biogeochemical processes affecting arsenic species distribution in a permanently stratified lake. *Envir. Sci. Technol.* 23, pp 1258–1263.

- Seyler P., Martin J.M., 1990. Distribution of arsenite and total dissolved arsenic in major French estuaries: dependence on biogeochemical processes and anthropogenic inputs. *Mar. Chem.* 29, pp 277–294.
- Seyler P., Martin J.M., 1991. Arsenic and selenium in a pristine river-estuarine system: the Krka, Yugoslavia. *Mar. Chem.* 34, pp 137–151.
- Smedley P.L., Kinniburgh D.G., 2002. A review of the source, behaviour and distribution of arsenic in natural waters. *Appl. Geochem.*, 17, pp 517–568.
- Spadini L., Bott M., Wehrli B., Manceau A., submitted. Analysis of the major Fe bearing phases in recent lake sediments by EXAFS spectroscopy.
- Sposito G., 1984. *The surface chemistry of soils*. Oxford U.P., New York, p 234.
- Steeffel C.I., Van Cappellen P., 1990. A new kinetic approach to modeling water-rock interaction: the role of nucleation, precursors, and Ostwald ripening. *Geochim. Cosmochim. Acta* 54, pp 2657–2677.
- Strazhesko D.N., Strelko V.B., Belyakov V.N., Rubanik S.C., 1974. Mechanism of cation exchange on silica gels. *J. Chromatogr.* 102, pp 191–195.
- Stumm W., Wehrli B., Wieland E., 1987. Surface complexation and its impact on geochemical kinetics. *Croat. Chem. Acta* 60, pp 429–456.
- Stumm W., 1991. *Chemistry of the solid–water interface, processes at the mineral–water and particle–water interface in natural systems*. Wiley & Sons, NY, 428 p.
- Stumm W., Morgan J.J., 1995. *Aquatic Chemistry: chemical equilibria and rates in natural waters*. Wiley-Interscience, New York.
- Suleimonov O.M., Seward T.M., 1997. A spectrophotometric study of hydrogen sulphide ionisation in aqueous solutions to 350°C. *Geochim. Cosmochim. Acta* 61, pp 5187–5198.
- Sullivan K.A., Aller R.C., 1996. Diagenetic cycling of arsenic in Amazon shelf sediments *Geochim. Cosmochim. Acta* 60, pp 1465–1477.
- Sun Z.X., Forsling W., Rönngren L., Sjöberg S., Schindler P.W., 1991. Surface reactions in aqueous metal sulphide systems. 3. Ion exchange and acid/base properties of hydrous lead sulphide. *Colloids and Surf.* 59, pp 243–254.

- Swedlund P.J., Webster J.G., 1999. Adsorption and polymerisation of silicic acid on ferrihydrite, and its effect on arsenic adsorption. *Wat. Res.* 33, pp 3413–3422.
- Sweeney R.E. and Kaplan I.R., 1973. Pyrite framboid formation: laboratory synthesis and marine sediments. *Econ. Geol.* 86, pp 618–634.
- Taylor L.A., Finger L.W., 1970. Structural refinement and composition of mackinawite. *Carnegie Inst. Washington Geophys. Lab. Ann. Rep.* 69, pp 318–322.
- Taylor P., Rummery T.E., Owen D.G., 1979. On the conversion of mackinawite and greigite. *J. Inorg. Nucl. Chem.* 41, pp 595–596.
- Theberge S.M., Luther III G.W., 1997. Determination of the electrochemical properties of a soluble aqueous FeS species present in sulfidic solutions. *Aquat. Geochem.* 3, pp 191–211.
- Tingle T.N., Waychunas G.A., Bird D.K., 1996. X-ray absorption spectroscopy (EXAFS) of arsenic solid solution in pyrite, Clio Mine, Mother Lodge gold district, Tuolumne county. *Abstr. w. Progr. – Geol. Soc. Am.* 28 (7), p 518.
- Tossell J.A., 1997. Theoretical studies on arsenic oxide and hydroxide species in minerals and in aqueous solution. *Geochim. Cosmochim. Acta* 61, pp 1613–1623.
- Tossell J.A., Vaughan D.J., Burdett J.K., 1981. Pyrite, marcasite and arsenopyrite type minerals: crystal chemical and structural principles. *Phys. Chem. Min.* 7, pp 177–184.
- Tournassat C., Charlet L., Bosbach D., Manceau A., 2002. Arsenic(III) oxidation by birnessite and precipitation of manganese(II) arsenate. *Envir. Sci. and Technol.* 36, pp 493–500.
- Uda M., 1968. *Zeitschrift für Anorganische und Allgemeine Chemie* 361, p 94.
- Van Cappellen P., Charlet L., Stumm W., Wersin P., 1993. A surface complexation model of the carbonate mineral–aqueous solution interface. *Geochim. Cosmochim. Acta* 57, pp 3505–3518.
- Van der Gaast S.J., Mizota C., Jansen J.H.F., 1986. Curved smectite in soils from volcanic ash in Kenya and Tanzania: a low-angle X-ray powder diffraction study. *Clays & Clay Min.* 34, pp 665–671.

- Van der Gaast S.J., Wada K., Wada S.I., Kakuto Y., 1985. Small-angle X-ray powder diffraction, morphology, and structure of allophane and imogolite. *Clays & Clay Min.* 33, pp 237–243.
- Vaughan D.J., 1970. Nickelian mackinawite from Vlakfontein: a reply. *Am. Min.* 55, pp 1807–1808.
- Vaughan D.J., Craig J.R., 1978. Mineral chemistry of metal sulfides. Textbook, Cambridge University Press, 493 p.
- Vink B.W., 1996. Stability relations of antimony and arsenic compounds in the light of revised and extended Eh-pH diagrams. *Chem. Geol.* 130, pp 21–30.
- Viollier E., Inglett P.W., Hunter K., Roychoudhury A.N., Van Cappellen P., 2000. The ferrozine method revisited: Fe(II)–Fe(III) determination in natural waters. *Appl. Geochem.* 15, pp 785–790.
- Wagman D.D., Evans W.H., Parker V.B., Schumm R.H., Halow I., Bailey S.M., Churney K.I., Nuttall R.I., 1982. The NBS tables of chemical thermodynamic properties: selected values for inorganic and C1 and C2 organic substances in SI units. *J. Phys. Chem. Ref. Data* 11, suppl. 2, 392 p.
- Wang Q., Morse J.W., 1996. Pyrite formation under conditions approximating those in anoxic sediments I. Pathway and morphology. *Mar. Chem.*, 52, pp 99–121.
- Ward J.C., 1970. The structure and properties of some iron sulfides. *Rev. Pure Appl. Chem.* 20, pp 175–206.
- Watson J.H.P., Cressey B.A., Roberts A.P., Ellwood D.C., Charnock J.M., Soper A.K., 2000. Structural and magnetic studies on heavy-metal-adsorbing iron sulphide nanoparticles produced by sulphate-reducing bacteria. *J. of Magn. and Magn. Materials* 214, pp 13–30.
- Watson J.H.P., Cressey B.A., Roberts A.P., Ellwood D.C., Charnock J.M., Soper A.K., 2000. Structural and magnetic studies on heavy-metal-adsorbing iron sulphide nanoparticles produced by sulphate-reducing bacteria. *J. of Magn. and Magn. Materials* 214, pp 13–30.
- Waychunas G. A., 2001. Structure, aggregation and characterization of nanoparticles. In: *Rev. in Min. & Geochem.* 44, Nanoparticles and the environment, Banfield J.F. and Navrotsky A. (Eds.), Min. Soc. Am..

- Waychunas G.A., Fuller C.C., Rea B.A., Davis J.A., 1996. Wide angle X-ray scattering (WAXS) study of "two-line" ferrihydrite structure: effect of arsenate sorption and counter ion variation and comparison with EXAFS results. *Geochim. Cosmochim. Acta* 60, pp 1765–1781.
- Wei D., Osseo-Asare K., 1995. Formation of iron monosulfide: a spectrophotometric study of the reaction between ferrous and sulfide ions in aqueous solutions. *J. Coll. Interf. Sci.* 174, pp 273–282.
- Westall J., Zachary J.L., and Morel F. (1976). MINEQL: A computer program for the calculation of chemical equilibrium composition of aqueous systems. Technical Note 18, Dept. of Civil Eng., Massachusetts Institute of Technology, Cambridge, Massachusetts.
- Wharton M.J., Atkins B., Charnock J.M., Livens F.R., Patrick R.A.D., Collison D., 2000. An X-ray absorption spectroscopy study of the coprecipitation of Tc and Re with mackinawite (FeS). *Appl. Geochem.* 15, pp 347–354.
- Widerlund A., Ingri J., 1995. Early diagenesis of arsenic in sediments of the Kalix River estuary, northern Sweden. *Chem. Geol.* 125, pp 185–196.
- Widler A.M., Seward T.M., 2002. The adsorption of gold(I) hydrosulphide complexes by iron sulphide surfaces. *Geochim. Cosmochim. Acta* 66, pp 383–402.
- Wilkin R.T., Barnes H.L., 1997. Formation processes of framboidal pyrite. *Geochim. Cosmochim. Acta* 61, pp 323–339.
- Yan X-P., Kerrich R., Hendry M.J., 2000. Distribution of arsenic(III), arsenic(V) and total inorganic arsenic in porewaters from a thick till and clay-rich aquitart sequence, Saskatchewan, Canada. *Geochim. Cosmochim. Acta* 64, pp 2637–2648.
- Yusof A.M., Ikhsan Z.B., Wood A.K.H., 1994. The speciation of arsenic in seawater and marine species. *J. Radioanal. Nucl. Chem.-Articles* 179, pp 277–283.
- Zehnder A.J.B., Wuhrman K., 1976. Titanium(III) citrate as a non-toxic oxidation–reduction system for the culture of obligate anaerobes. *Science* 192, pp 1165–1166.

Zhang J.-Z, Millero F.J., 1994. Investigation of metal sulfide complexes in sea water using cathodic stripping square wave voltammetry. *Analyt. Chim. Acta* 284, pp 497–504.

Curriculum vitae

Mariëtte Wolthers werd geboren op zondag 9 juni 1974 te Opmeer. In 1992 behaalde zij haar gymnasium diploma aan de Openbare Scholengemeenschap in Hoorn, waarna zij in datzelfde jaar begon met haar studie Geologie aan de Faculteit der Aardwetenschappen van de Vrije Universiteit in Amsterdam. Binnen de doctoraalfase deed zij onderzoek bij de vakgroep Petrologie/Isotopengeologie naar de rubidium–strontium en kalium–argon isotopenouderdommen en de geochemie van hydrothermale kleien in de Troodos ophioliet op Cyprus. Daarnaast verrichtte zij bij de vakgroep Tektoniek en Structurele Geologie, in samenwerking met het Department of Geology van de University of Zimbabwe, een kort onderzoek op het gebied van de structurele geologie van de Bindura–Shamva groensteengordel in Zimbabwe. In augustus 1997 studeerde zij af bij de vakgroep Petrologie/Isotopengeologie. Aansluitend werd zij door de Nederlandse Organisatie voor Wetenschappelijk Onderzoek aangesteld als Onderzoeker in Opleiding bij de projectgroep Geochemie van de Faculteit Aardwetenschappen aan de Universiteit Utrecht. Het promotieonderzoek voerde zij uit in nauwe samenwerking met de sulfide-onderzoeksgroep van Cardiff University in Groot-Brittannië. Dit is onder andere vormgegeven in een werkbezoek van een jaar. Het onderzoek leidde uiteindelijk tot de in dit proefschrift uitgewerkte resultaten.

